UMBC

DISSERTATION APPROVAL SHEET

Title of Dissertation: The Hyper-Angular Rainbow Polarimeter: Pre-Launch Calibration, Validation, and Advancements in Cloud Science

Name of Candidate: Brent McBride
mcbride1@umbc.edu
Doctor of Philosophy, 2022
Graduate Program: Atmospheric Physics

Dissertation and Abstract Approved:

Jose Vanderlei Martins

Jose Vanderlei Martins
martins@umbc.edu
Atmospheric Physics Program
Department of Physics
12/1/2022 | 12:41:50 AM EST

NOTE: *The Approval Sheet with the original signature must accompany the thesis or dissertation. No terminal punctuation is to be used.

ABSTRACT

Title of Document: The Hyper-Angular Rainbow Polarimeter: Pre-Launch Calibration, Validation, and Advancements in Cloud Science

Brent A. McBride, Doctor of Philosophy in Atmospheric Physics, 2022

Directed By: Dr. Jose Vanderlei Martins, Professor, Physics

Studying the climate requires comprehensive, accurate, and global measurements of the atmosphere and surface. Small, economical, and powerful platforms, like the Hyper-Angular Rainbow Polarimeter (HARP), are part of a new paradigm in Earth observation. HARP is a wide field-of-view imaging polarimeter that is uniquely capable of sampling the Earth from 120 co-located views, four visible channels (440, 550, 670, and 870 nm), and three distinct polarization states. The HARP instrument is low-cost (<$5 million), compact (10x10x30 cm), continues the heritage of earlier, successful space missions, while also expanding the information content possible in a single set of measurements.

This dissertation connects the instrument science of the HARP mission to unprecedented cloud property retrievals from HARP polarization data. A robust, physics-based calibration pipeline is developed for HARP and is shown to be accurate to 0.5% degree of linear polarization (DOLP) across all channels in the lab, a climate community requirement for modern aerosol and cloud retrievals. Calibrated measurements are compared to co-located data from the Research Scanning Polarimeter

(RSP) during a field campaign in 2017 to validate the calibration across the entire HARP FOV. HARP and RSP agree within 1% in reflectance and DOLP over two desert and two ocean scenes, relative to their error models.

These advancements also allow spatially resolved retrievals of liquid water cloud droplet size distributions (DSDs). The hyper-angular, wide swath measurement enables *spatial maps* of cloud droplet effective radius (CDR) and variance (CDV) for HARP resolutions < 1 km from aircraft and < 10 km from space. This work shows that high resolution DSD retrievals are essential to understanding the correlation between reflectance, CDR and CDV, which have connections to cloud growth processes, and ultimately, radiative balance.

With the upcoming launch of the NASA Plankton-Aerosols-Clouds-ocean Ecosystem (PACE) mission and the release of HARP CubeSat L1B data to the scientific community, the same calibration and cloud retrieval concepts discussed in this work may be used to help connect cloud microphysical properties to global radiative forcings. Current and future HARP datasets may provide strong rationale for including high-resolution, hyper-angle imaging polarimetry and small satellite technology on future major Earth science space missions.

THE HYPER-ANGULAR RAINBOW POLARIMETER: PRE-LAUNCH CALIBRATION, VALIDATION, AND ADVANCEMENTS IN CLOUD SCIENCE

By

Brent A. McBride

Dissertation submitted to the Faculty of the Graduate School of the
University of Maryland, Baltimore County, in partial fulfillment
of the requirements for the degree of
Doctor of Philosophy in
Atmospheric Physics
2022

Dedication

This dissertation is dedicated to Maria and Charles Booth, Darl and Hilda McBride, and Emma Jane Fielding.

Acknowledgements

This dissertation would not be possible without the scientific and/or social support from my committee, fellow graduate students, and family.

I thank my advisor, Dr. J. Vanderlei Martins, for the opportunity to follow a satellite mission from the initial proposal, though the assembly and calibration, field campaigns, data processing, to scientific analysis of the data and interpretation. Very few students have that kind of exposure and breadth during their PhD research, and technically, I got to do it twice with AirHARP and HARP CubeSat. HARP engineers Dominik Cieslak, Dr. Roberto Fernandez-Borda, and Dr. Lorraine Remer were wonderful teachers and friends throughout my journey with HARP, as well. My committee, Dr. Zhibo Zhang, Dr. Pengwang Zhai, Dr. Graham Feingold, and Dr. Henrique Barbosa made sure I had everything I needed to get over the line and were patient and understanding about my timeline and resources. I also acknowledge the financial support from the Joint Center for Earth Systems Technology (JCET), NASA, NOAA, and UMBC throughout the past seven years.

I will remember the laughs, regular outings with my cohort, and fruitful discussions with other close friends and students: Dr. Brian Carroll, Dr. Anin Puthukuddy, Dr. Chamara Rajapakshe, Dr. Jaron Kropp, Anthony Bratt, Noah Sienkiewicz, Erik Crowe, Dr. Reed Espinosa, Dr. Daniel Miller, and Dr. Eddie Strobach. There is something about going through the same process together that makes it easier, if not in a physical way, a mental one. Seeing the Dr. prefix in front of some of their names is a testament to how committed we all were to finish, despite all the wild challenges along the way. I hope I left an impression on their time at UMBC as they did mine.

My parents, Mary Jo and Rob, siblings Austin and Carly, and my partner Juliana were there since the very beginning. They supported me unconditionally, regardless of if I was away at NOAA in Boulder, communicating my research to colleagues in France, Brazil, or Israel, or at UMBC, calibrating AirHARP into the early hours of the morning on weekends. My relationship with Juliana was especially tested during my PhD, and I am grateful for her endurance and strength when mine was running low – my success in this program is also hers, in no small way. I also acknowledge the support from Juliana's family: Angela, Julio, Martin, and Tracey. They lifted me up in different ways throughout the years, and together with my nuclear family, I am blessed to have the support system I have.

.

Table of Contents

Dedication ii
Acknowledgements iii
Table of Contents v
List of Tables viii
List of Figures ix
Chapter 1: Introduction 1
Section 1: Climate, aerosols, and the big picture 1
Subsection 1.1: Climate and prediction 1
Subsection 1.2: Radiative forcing of aerosols and clouds 3
Subsection 1.3: Cloud Feedbacks 5
Subsection 1.3.1: Low cloud feedbacks 5
Subsection 1.3.2: High cloud feedbacks 6
Subsection 1.3.3: Coupled radiative forcings 7
Subsection 1.4: Current challenges with global climate and sub-climate models 8
Subsection 1.5: Current challenges with cloud microphysics 9
Section 2: Spaceborne satellite instrument design 13
Subsection 2.1: Active remote sensing 13
Subsection 2.2: Passive remote sensing 15
Subsection 2.2.1: Introduction 15
Subsection 2.2.2: Imaging systems 18
Subsection 2.2.3: Multi-angle imaging instruments 22
Subsection 2.2.4: Multi-angle polarimetry 23
Subsection 2.2.5: Improvements to Earth-observing MAP design 26
Subsection 2.2.5.1: Photoelastic modulation 26
Subsection 2.2.5.2: Amplitude-splitting polarimeters 27
Subsection 2.2.5.3: Spectral modulation 28
Subsection 2.3: MAIPs, climate needs, and uncertainty 30
Section 3: Thesis of this dissertation 35
1. Development and validation of an adaptable, physics-driven polarimetric calibration for a small-satellite hyper-angular imaging polarimeter 35
2. Development and validation of a novel spatial cloud droplet size distribution retrieval algorithm from co-located hyper-angular imaging polarimeter cloud datasets 36
Chapter 2: The Hyper-Angular Rainbow Polarimeter 38
Section 1: General concept 38
Subsection 1.1: Optical design 38
Subsection 1.2: Wavelength selection 41
Section 2: Significance of the HARP design for Earth science 44
Section 3: HARP sampling and measurement 48
Section 4: AirHARP, HARP CubeSat, HARP2, and beyond 51
Chapter 3: Pre-launch calibration and validation of Hyper-Angular Rainbow Polarimeter (HARP) measurements 56
Section 1: Description of the system light path 56

Section 2: Calibration pipeline for the HARP instrument 59
Subsection 2.1: Detector specifications and background correction 59
Subsection 2.2: Flatfielding 61
Subsection 2.3: Non-linear correction 65
Subsection 2.4: Detector relative alignment 67
Subsection 2.5: Relative polarimetric calibration 70
Subsection 2.5.1: Theoretical description 70
Subsection 2.5.2: Application in the laboratory 73
Subsection 2.6: Radiometric calibration 77
Subsection 2.6.1: Relative spectral response 77
Subsection 2.6.2: Absolute radiometric calibration 81
Section 3: Validation of calibrated measurements 83
Subsection 3.1: Validation of nadir coefficients 83
Subsection 3.2: Full FOV intercomparisons with field data 86
Subsection 3.2.1: AirHARP participation in the Aerosol Characterization with Polarimeter and LIDAR (ACEPOL) campaign 86
Subsection 3.2.2: Results and discussion 89
Section 4: Conclusions 95
Section 5: Acknowledgements 97
Chapter 4: Spatial distributions of cloud droplet size properties from Hyper-Angular Polarimeter (HARP) measurements 99
Section 1: Introduction 99
Subsection 1.1: Cloud microphysics and climate relevance 99
Subsection 1.2: Retrievals of cloud droplet effective radius, optical thickness, and effective variance 101
Subsection 1.3: Measurement requirements for cloud DSD retrieval 103
Section 2: Cloud retrieval framework 108
Section 3: AirHARP measurement relative to cloudbows 114
Section 4: Retrieval validation 119
Section 5: Resolution and scale analysis of retrieval products 121
Subsection 5.1: Spatial correlations between intensity, CDR, and CDV 121
Subsection 5.2: Information content retrieved at different scales 126
Section 6: Validation using large-eddy-simulated clouds and an AirHARP measurement simulator 128
Section 7: Discussion and conclusions 136
Section 8: Acknolwedgements 140
Chapter 5: Summary and Outlook 142
Section 1: Calibration and validation 142
Section 2: Spatial distributions of cloud properties, interpretation, and validation 146
Section 3: Legacy and extensions of this work 150
Subsection 3.1: Cross-track retrieval of cloud properties 150
Subsection 3.1.1: Joint spectral application 150
Subsection 3.1.2: Application to flatfield characterization 152
Subsection 3.2: Cross-comparison with SPEXone for cloud retrievals 153
Subsection 3.3: Extensions on the along-track cloud DSD retrieval 157

Section 4: Conclusions 161
Appendix 163
Bibliography 165
Section 1: Complete Reference List 165
Section 2: Figure Licensing Statements and Notices 182

List of Tables

Table 1. Mission characteristics of POLDER and ACEPOL MAPs.

Table 2. Desired modern MAP design requirements for upcoming climate missions.

Table 3. Specifications of the HARP TrueSense KAI-04070 CCD detectors.

Table 4a. Characteristic matrix elements, C_{ij}, for the 670 nm AirHARP band, vis Eq. (12).

Table 4b. Instrument-relative parameters for the 670 nm AirHARP band, vis Eq. (13).

Table 5. Derived AirHARP pre-launch SRF parameters.

List of Figures

Figure 1. Top of the atmosphere reflectance spectra for a variety of Earth targets.

Figure 2. Schematic of MODIS on-orbit and Earth-view sampling swath characteristics.

Figure 3. Daily coverage of Aqua-MODIS Collection 6 corrected reflectance, retrieved aerosol optical depth, and Chlorophyll-A concentration for all granules on July 12, 2020.

Figure 4. Artist rendering of the Terra-MISR nine-camera pushbroom sampling technique.

Figure 5. Simulated retrieval uncertainties for aerosol optical thickness and single scattering albedo as a function of spectral range and co-located viewing angles for multi-angle polarimetric data over land.

Figure 6. Description of the HARP instruments: HARP CubeSat, AirHARP, and HARP2.

Figure 7. Comparison of the four HARP spectral response functions with compatible space radiometers.

Figure 8. Simplified Zemax model of the HARP CubeSat optical train.

Figure 9a-b. Time-lapse of an AirHARP live capture during NASA LMOS on May 25, 2017.

Figure 9c-d. A continuation of the AirHARP live capture timelapse from Figure 9a-b.

Figure 10. Press kit distribution of HARP CubeSat's first light image over southern Europe.

Figure 11. Schematic of the NASA PACE spacecraft and a cross- and vicarious calibration plan outlined from the perspective of the HARP2 detector.

Figure 12. The Phillips prism is made of three elements: A, B, and C.

Figure 13. AirHARP captures a full-field raw image in each detector of the aperture of the NASA GSFC "Grande" integrating sphere and a dark capture with the lens cap on.

Figure 14. The flatfield is performed by submerging the wide field front lens into the aperture of a stable integrating sphere.

Figure 15. Non-linear correction evaluation for AirHARP 670 nm.

Figure 16. Full-size full-resolution imagery of the LED X form the HARP CubeSat during pre-launch testing at the Space Dynamics Laboratory (Feb 7 2018).

Figure 17. Alignment results from a feature detection algorithm on HARP CubeSat data pre- and post-vibrational testing at SDL in August 2018.

Figure 18. Malus curves for each of the four AirHARP channels.

Figure 19. Examples of AirHARP images taken at different in-band Ekspla wavelengths to show the distribution of illuminated stripes.

Figure 20. The absolute gain calibration of the HARP CubeSat instrument.

Figure 21. The POLBOX system generates partial polarization by rotating two glass blades.

Figure 22. Multi-angle, co-located comparison between AirHARP and RSP for ACEPOL targets.

Figure 23. Direct comparison plot of AirHARP and RSP reflectance and DOLP for 550 nm, 670 nm, and 870 nm data over the two ocean and two desert ACEPOL cases shown in Figure 22.

Figure 24. The phase space of the radiometric bi-spectral retrieval of CDR and COT.

Figure 25. The angular structure of the polarized cloudbow as described by Mie simulations.

Figure 26. HARP CubeSat 670 nm total reflectance nadir observation over Lake Titicaca, South America on May 5 2020.

Figure 27. The scattering angle coverage typical of an instantaneous AirHARP wide FOV capture of a marine stratocumulus cloud field.

Figure 28. An example of how a wide FOV cloudbow measurement in a single snapshot translates into single angle pushbrooms.

Figure 29. AirHARP forward pushbroom (~38° nadir VZA) RGB composite for total reflectance and polarized reflectance for the June 19, 2017 LMOS cloud case.

Figure 30. Several examples of the parametric fit retrieval applied to AirHARP cloudbow measurements at 200 m superpixel resolution.

Figure 31. Nadir pushbroom images for 670 nm of total intensity and polarized intensity, as well as the retrieved CDR and CDV for 200 m gridded superpixels with the requisite scattering angle geometry.

Figure 32. A zoom of heterogeneous and homogeneous sectors of the LMOS cloud field observed by AirHARP.

Figure 33. Analysis of intensity, CDR, and log(CDV) anomalies from the mean along the black transect for a segment of the cloud field measured by AirHARP.

Figure 34. Scale analysis for the scene in Figure 31 at 200 m and 600 m resolutions.

Figure 35. DYCOMS-II bulk microphysical cloud field simulated off the coast of California with constant geometric standard deviation 1.105.

Figure 36a-b. Example ‘cloud core’ DSD retrievals over a DYCOMS-II marine stratocumulus cloud simulation with bin microphysics

Figure 36c-d. Example ‘cloud side’ DSD retrievals over the same domain as Figure 36.

Figure 37. Joint spectral retrieval of cloud DSD properties for a cross-track line-cut of pixels in the AirHARP observation of the LMOS cloud field.

Figure 38. Schematic of HARP-like and SPEXone-like cloudbow sampling

Figure 39. Spectral separation typical of cloudbow signals at a single geometry.

Figure 40. Same study as Figure 39 but the expected polarized phase function for a given CDV for a narrow DSD cloudbow signal observed at 147 and 155 degrees.

Figure 41. Sampling resolution required to resolve cloudbow signals for a given CDR and wavelength.

Figure 42. Mie simulations for 0.67 μm and 1.64 μm cloudbow observations for increasing CDR 8μm, 15μm, and 30μm.

Chapter 1: Introduction

Section 1: Climate, aerosols, and the big picture

Subsection 1.1: Climate and prediction

The sustainability of our climate is one of the most important goals of humanity. Life on Earth, as we know it, depends on a fragile window of temperatures to survive. While we can adapt, alarming trends in climate models and real data suggest that humans are accelerating global warming. Global land and ocean areas have warmed differently over time and year-on-year. Projections of *climate sensitivity*, or the temperature change of the climate due to increasing carbon dioxide (CO_2) concentrations, suggest a global sea surface temperature (SST) rise of anywhere from 1-10 degrees Celsius by the year 2100 (USGCRP 2017). Last year, the National Oceanic and Atmospheric Administration (NOAA) estimated a +1.35ºC (+0.65ºC) global land (ocean) surface temperature increase relative to the 1880-2020 average. This result placed 2021 among the top 10 warmest years on record, all of which occurred in the last decade (NOAA 2021). These results are important on a global scale but can be misleading. Certain regional areas of the globe are projected to cool in the future, like the southern ocean off the coast of Greenland due to ice sheet melt (Fox-Kemper et al. 2021). Sea level rise may submerge low-lying areas, such as Chesapeake Bay in Maryland (~1.2 m) and the Louisiana region of the United States (1.8+ m) by 2100 (UGSCRP 2017). These changes and others can be local, regional, and global, and may impact the livelihood of millions of people, threaten property, and disrupt ecosystems. The rise of anti-climate populist politics across the world has also complicated climate mitigation efforts and perception (Lockwood and Lockwood 2022, Yan et al. 2021). Even so, the state of climate science today is more robust than ever in the face of adversity. Scientists across the world are developing new technologies, advancements in miniaturization, modern policy proposals, and new scientific understanding

to tackle this climate crisis. Global satellite measurements and physics-based models are major drivers of climate policy. Satellites, like NASA's A-Train constellation (Anderson et al. 2005), include a host of complementary instruments and sensors that probe aerosol, cloud, land, ocean, and molecular signals for hints of a changing world. Some are radiometric cameras with broad swaths. Others are spectrometers that span a wide range of wavelengths and lasers that measure backscattered and polarized signals. There are also a few radars in space that can peer through the clouds straight to the Earth's surface and others that are completely saturated by cloud reflectances. This global data is taken daily and over a span of decades. With this massive dataset, information like refractive index, sphericity, and single-scattering albedo of pollution particles, size distributions of cloud droplets, and reflectance distribution functions of the land or ocean surface can be used to help characterize our biomes and their changes. These are indicators that we use to monitor the health of our world, too. Global climate models (GCMs) use these variables as inputs to project our current climate years into the future. Several GCMs are brought together into *integrated assessment models* (IAMs) that inform global policy decisions on climate. The famous Representative Concentration Pathways (RCPs), now reframed as the Shared Socio-Economic Pathways (SSEC), are IAMs that simulate the kind of warming we may see if humans intervene (or not) with political action (O' Neill et al. 2016). The results of these scenarios inform the Intergovernmental Panel on Climate Change (IPCC) decadal assessments, advise new space missions in the NASA Decadal Survey (NAMES 2018), and guide the recent 2016 international Paris Agreement accords (Paris Agreement 2015). The link between satellite measurements, climate models, and policy decisions is non-linear but extremely critical.

Specifically, we need to improve the way we characterize the parts of the Earth system that contribute to warming and cooling over time. In theory, the Earth is a closed system with a net zero surplus of energy, down to internal climate fluctuations. Self-contained systems, such as the carbon and water cycle, produce a net zero impact on the environment,

without human involvement. Rapid industrialization and human population growth led to increased consumption of food and production of livestock, fossil fuel and land use, and waste. These factors generate energy, pollution, and have de-stabilized the Earth system in a measurable way (Steffen et al. 2007). Our ability to track these changes depends on how well we can answer the following questions. How do we track these imbalances from space? How do we connect them to the properties of the atmosphere, land, ocean, clouds, and aerosols? Finally, how can we use these properties and teleconnections to project future climates?

Subsection 1.2: Radiative forcing of aerosols and clouds

Scientists approach this problem by measuring how much energy these different factors add or remove from the Earth system on a yearly basis. This metric is called *global radiative forcing* (RF) and is measured in flux units, watts-per-meter-squared (W m^{-2}). Figure 1a shows the breakdown of the latest globally averaged RF estimates, as attributed to different anthropogenic and natural contributions.

Carbon dioxide (CO_2) is the largest warming agent, producing an estimated +2.16 W m^{-2} relative to 1750. Other absorbing compounds such as methane (CH_4), nitrous oxide (N_2O), ozone (O_3), and halogens have smaller but notable warming impacts, and together with CO_2, these compounds can have lifetimes in the stratosphere anywhere from minutes to 100+ years (Szopa et al. 2021). These species, with CO_2, contribute an estimated +3.79 W m^{-2} and are the major net positive influences on global RF. However, the IPCC discusses that the global impact of CO_2 may be partially offset by cooling agents: aerosols, clouds, and cloud-adjustments due to aerosols.

So far, the estimated negative RF of aerosols and clouds carries an uncertainty larger than the predicted impact (Forster et al. 2021). The major reason for this is that aerosols comprise a wide range of particles with different radiative impacts. Aerosols interact with both

longwave and shortwave radiation and can influence cloud development, which in turn, has a separate radiative adjustment. Sulphate (SO_4^{-2}), a highly reflective particle produced by volcanic eruptions and industry, is a dominant aerosol considered in RF studies (Myhre et al. 2013). The direct RF of sulphate is estimated between -0.26 and -0.86 W m^{-2}. Unlike the greenhouse gases, aerosols like sulphate are not well-mixed horizontally or vertically in the atmosphere, and their direct RF is coupled to their sources, transport, and aging processes (Putaud et al. 2010, Samset et al. 2013). Also, low aerosol signals are challenging to measure from space, especially over bright or complex surfaces like deserts, coastal areas, and polar caps and certain times of year (Levy et al 2003, Remer et al. 2005, Boucher et al. (2013), Tomasi et al. (2015)). Still, their impact on global RF is significant – the current high bound for sulphate RF could offset more than half of CO_2's net positive RF alone. Other aerosol species, such as organic and anthropogenic black carbon, nitrates, biomass burning, and mineral dust, and sea salt have their own complexities and are considered individually in RF studies (Forster et al. 2021).

Aerosols are well-known *cloud condensation nuclei* (CCN) and indirectly contribute to the growth of liquid water clouds. When ambient water vapor is supersaturated (RH > 100%), it will condense on CCN and release latent heat. If local supersaturation is maintained, more water vapor condenses until a cloud droplet is formed. In the presence of heavy aerosol loading, this process leads to more smaller droplets, which are efficient scatterers of shortwave (SW) radiation. Recent studies estimate the indirect RF of CCN on clouds is between -0.4 to -1.14 W m^2 (Gryspeerdt et al. 2017, Hasekamp et al. 2019, Diamond et al. 2020). This range is for the *albedo effect* which is a brightness enhancement due to an increase of smaller droplets at constant liquid water path (Twomey 1974). Other aerosol-cloud interactions include cases where smaller droplet sizes extend the lifetime of the cloud and delay precipitation (Albrecht 1989) and absorbing aerosols promote evaporation; these are trickier to quantify (Ackerman et al. 2000, Johnson, Shine, and Forster 2004). Time-trends of

global climate models (GCMs) are required, which introduce their own assumptions and uncertainties. Of these, a poor understanding of how to parametrize clouds smaller than the GCM grid cell, difficulties in modeling certain types of clouds, and a lack of well-recorded historical aerosol properties are major limitations.

Subsection 1.3: Cloud Feedbacks

Though the global RF of clouds can be discussed relative to aerosol-droplet interactions, clouds can affect the climate system in a series of large-scale feedback mechanisms as well. Low and high cloud feedbacks are currently considered to generate a net positive radiative forcing, estimated at +0.42 W m^{-2} $C^{\circ-1}$ (Szopa et al. 2021). However, the errorbar on this estimate is the largest of any contribution considered by the IPCC in 2021, -0.1 to 0.94 W m^{-2} $C^{\circ-1}$. Therefore, the sign of cloud feedback RF is currently unknown and represents the "most important" cloud-related influence on climate, according to the 2017 NASA Decadal Survey (NAMES 2017). The uncertainty on the total RF estimate is tied to a mixture of impacts that grow, deplete, and maintain water and ice clouds. Cloud feedbacks also vary in strength and distribution globally and recent studies have identified cloud amount, altitude, and optical depth as critical observables for low and high clouds (Zelinka, Zhou, and Klein 2016).

Subsection 1.3.1: Low cloud feedbacks

Low cloud feedback is related to the expansion or depletion of warm and liquid water clouds found in the low to mid-troposphere, such as marine stratocumulus. As our climate warms, increased sea surface temperatures (SST) may lead to horizontal and vertical cloud reduction. This may be balanced by a stronger and more stable capping inversion, brought upon by reduced mixing of the boundary layer, and other so called "cloud controlling factors" (Qu et al. 2015, Klein et al. 2017). This may increase cloud amount and optical depth (COD), which in turn may increase longwave (LW) and shortwave (SW) reflection to space. COD

may also increase due to a change in thermodynamic phase, which may occur as the isotherms shift higher in warmer climates, changing ice particles to more reflective water droplets (Zelinka, Klein, and Hartmann 2012). Broader and brighter low clouds may have a significant SW cooling due to the albedo effect, as well. Therefore, observables such as cloud fraction, COT, thermodynamic phase, and the cloud droplet size distribution (DSD) are the key global measurements we need to monitor low cloud feedbacks. As of IPCC AR5, it was assumed that the effect of SW scattering on RF is the largest negative (cooling) contributor in future climates, but this depends on the extent and appearance of large-scale marine stratocumulus clouds. As of AR6, advancements in cloud modeling suggest that the LW impact likely dominates (Forster et al. 2021). Even so, geoengineers are currently considering the ramifications of "marine cloud brightening" (MCB) MCB is the process of regularly seeding the areas of the world where these low stratocumulus clouds appear to generate an aggressive cooling RF. Much of MCB research is interdisciplinary (involving GCMs, high resolution microphysical and fluid flow models, and field measurements), though there are serious concerns about the unknown and coupled impacts this could have on other parts of the Earth system (Lanham et al. 2012).

Subsection 1.3.2: High cloud feedbacks

Low cloud feedback is only one part of the overall cloud impact on global RF, however. Towering cumulus and cirrus clouds in the high troposphere can produce a *high cloud feedback* as well. This radiative impact is positive (warming) and tied to longwave fluxes and cloud height. The main contributor, the Fixed Anvil Temperature (FAT) hypothesis, suggests that the reduction in the longwave emission of water vapor in the vicinity of tropical high-level clouds may keep the cloud top temperature constant even while the clouds rise and increase the barrier between the surface and space (Hartmann and Larsen 2002). Water vapor becomes less and less radiative at higher altitudes, creating a gradient in cooling RF of the

clear sky. Convective detrainment, the process of warmer air from the inside of clouds moving into the environment, balances this effect and the resulting cirrus clouds form at a fixed temperature. The FAT suggests that these clouds may develop regardless of the surface temperature response they produce. Observational studies can reproduce FAT-like processes (Eitzen et al. 2009), though trends in global cloud height are difficult to decouple from regular oscillations like La Niña (Davies et al. 2017). High cloud feedbacks are currently estimated to contribute +0.22 W m^{-2} C^{-1}, which is due to model adjustments relative to AR5 (+0.5 W m^{-2} C^{-1}, Boucher et al. 2013). Finally, the global RF of thin cirrus clouds, including contrails, and recent hypothesis related to reduction in anvil cloud amount (Saint-Lu et al. 2020) is not well understood due to modeling limitations (Forster et al. 2021).

Subsection 1.3.3: Coupled radiative forcings

Aerosol, cloud, and their coupled impacts on climate are understood by separating their direct and indirect influence on radiative forcing. Outside of the first and second indirect effects, several working groups including those for the NASA Decadal Survey, IPCC, NASA Plankton-Aerosol-Cloud-ocean Ecosystem (PACE, Werdell et al. 2019) and Aerosol-Cloud-Ecosystem (ACE, Mace et al. 2013, da Silva et al. 2020), and the upcoming Atmosphere Observing System (AOS) mission (da Silva et al. 2021) consider studying the effects of aerosols on cloud formation, height, and other feedback-related properties a high priority. The IPCC segregates these impacts into several parts: aerosol direct effects on radiative forcing (RFari), RFari plus semi-direct effects (ERFari), indirect cloud adjustments due to aerosols (ERFaci), and the total aerosol-cloud RF impact (ERFaci+ari). These values are often derived using GCMs alone that simulate liquid phase stratus-like, mixed, or convective cloud processes. The RFari is well constrained (driven by CMIP5 studies), though ERFaci carries the bulk of the uncertainty for reasons explained above (Boucher et al. 2013). Satellite measurements have helped to constrain the range of the ERFaci+ari to the range of -1 to 0 W m^{-2}, but future

improvements will likely come with stronger parametrizations of cloud processes in global climate models (GCMs) and enhanced satellite measurements (Boucher et al. 2013). In the remainder of this dissertation, aerosols will only be discussed in the context of clouds, though the impact of aerosols on global RF, measurements, and models are a highly active area of research and an equally curious source of uncertainty in our understanding of climate change.

Subsection 1.4: Current challenges with global climate and sub-climate models

Our ability to predict future climates relies on accurate GCMs and satellite measurements. GCMs are three-dimensional climate simulations that resolve cloud and other atmospheric processes at large-scale resolutions and over decadal time scales. To simulate clouds in GCMs, a careful mixture of radiative transfer, convection and mixing, and microphysical modules are required. However, it is challenging to balance computational run time, grid cell resolution, and the scales of the relevant cloud processes (Schar et al. 2020). Figure 4a shows important processes, such as collision/coalescence, scavenging, entrainment, and ice formation and nucleation, operate on the order of minutes to hours, on a scale of meters or less, and are not well-mixed vertically or horizontally in a cloud or in the atmosphere. Typical GCM grid cells, by comparison, can be 50 km or more, meaning that coarse parametrizations are often used to capture the relationship between them and RF. This can lead to biases, however. Cloud microphysical processes are coupled to aerosols, are phase-dependent and distributed vertically throughout the cloud and may not directly translate to RF at larger scales (Murray, Carslaw, and Field 2021, Kay et al. 2016, Komurcu et al. 2014). Other models that run at narrower resolutions can decouple or better simulate some of these processes. Large-eddy simulations (LES) are physics-based cloud models that use fluid flow equations to drive the evolution of cloud microphysical properties over a small domain (typically <50km, Kazil et al. 2017, Stevens et. al 2005). LES can be three-dimensional, and each pixel can be discretized into dozens of droplet mass and number bins, but they can be computationally expen-

sive at larger scales, as well. Global cloud-resolving models (GCRMs) exist somewhere in-between GCMs and LES. GCRMs balance parametrization, resolution, and efficiency by running on monthly timescales, grid cell resolutions <50km, and at times, coupled into the grid cells of larger GCMs (USGCRP 2017).

Even so, as of the upcoming IPCC AR6, resolving cloud processes in models at scales relevant for climate prediction remains a serious challenge. Modern, global satellite instruments that can measure these properties accurately and over decadal scales will help improve assumptions and parametrizations, as well. Current and future reflectance-based imaging radiometers and multi-angle polarimeters (MAPs) that measure these properties may allow scientists to track the development of cloud droplets and aerosols in specific areas of the world, connect their development to the direct, indirect, and semi-direct effects, and finally to changes in cloud RF predicted by climate modeling. The next section will go into more detail about the specific cloud microphysical processes that satellites instruments measure and models use to predict future climates.

Subsection 1.5: Current challenges with cloud microphysics

Many of the formative processes of clouds occur at the sub-micron scale and over various vertical regimes in the atmospheric column. When a parcel of air is warmer than its surrounding environment, it rises, carrying energy with it. The troposphere is cooler at higher altitudes, so the ambient environment will cool the parcel as it rises. This creates a gradient in relative humidity (RH) between the parcel and the environment. If enough cooling occurs such that the parcel pressure matches the saturation vapor pressure of the environment, the water vapor in the parcel will condense into droplets via *heterogeneous nucleation*. This occurs at supersaturation (RH ~100.1%) in the presence of aerosol particles, like sulphate. The CCN eventually dissolves in the droplet and creates a solute, which reduces the efficiency of evaporation. If the rate of condensation is maintained with supersaturated conditions, runa-

way condensation occurs (Farmer, Cappa, and Kreidenweis 2015). The relationship between droplet size and relative humidity (or supersaturation) during this process is called the Kohler curve (Kohler 1936). Heterogeneous nucleation typically first occurs at the *lifted condensation level* (Craven, Jewell, and Brooks 2002), which is the location in the atmosphere where the ambient temperature meets the dewpoint. Coalescence, usually via Brownian motion or turbulence grow the droplets to micron sizes as they rise, to their largest non-precipitate sizes at cloud top.

Droplets may undergo further mixing processes due to turbulence, longwave radiative cooling, aerosol and moist air entrainment, and updraft velocities inside the cloud and at cloud top (Tao et al. 1996, Sullivan et al. 2016, Lu and Seinfeld 2006, Devenish et al. 2012). The nature of the droplet size distribution in different regions of the cloud can help tease out the impact of these individual processes. Liquid water clouds generally follow lognormal or gamma distributed DSDs, with one or more size modes (Miles, Verlinde, and Clothiaux 2000, Feingold and Levin 1986). Condensation creates narrow DSDs, but this can be modulated in several ways. Chandrakar et al. (2021) suggests that DSD broadening can occur due to entrainment, and Chen et al. (2018) add that a similar effect can be produced by in-cloud turbulence, which increases collision rates. Though there is some debate, droplets between 40um and 0.5mm are considered *drizzle* (Gilenke et al. 2017), and droplets that reach radii around 15 um are large enough to start colliding with others (Pinksy and Khain 2002b). However, the presence of aerosol can be a determining factor in how a cloud matures and whether it will precipitate at all. At high loadings, there is evidence to suggest that an abundance of smaller droplets can delay or halt precipitation entirely (Khain, Rosenfeld, and Pokrovsky 2005, Andreae et al. 2004). Increasing CCN can also invigorate cloud systems, and increase lightning frequency, local precipitation rates, and cloud cover (Rosenfeld et al. 2008, Bell, Rosenfeld, and Kim 2009, Kaufman et al. 2005). Fan et al. (2013) suggests that CCN contribute differently to cloud properties and growth depending on the age of the cloud, as well. The effect of

aerosol loading on clouds has a tipping point, though, and may inhibit the growth of clouds instead (Koren et al. 2004). There is also a subtle correlation between the size of the CCN and onset of precipitation. Most CCN that contribute to cloud development fall within the Aitken regime (0.06-0.2 um) (Yin et al. 2000) and so called, "giant CCN" (> 2 um) can accelerate the onset of precipitation when Aitken-dominated aerosol loading is high. These giant CCN also correlate to a reduction in cloud albedo in stratocumulus clouds (Feingold et al. 1999).

In clouds nearing precipitation, drizzle drops may become *collector drops*. These droplets take up smaller droplets in their path as they fall at a rate that is correlated to their size (Stephens and Haynes 2007). When droplets reach their terminal velocity, which is associated with millimeter radii, they fall out as rain. Rain efficiently scavenges and removes suspended aerosol in the atmosphere beneath the cloud, as well (Chate et al. 2003). This is the general growth and depletion process of liquid water clouds, which generally form in near the PBL and temperatures warmer than 0º C. Therefore, several different droplet size regimes, development processes, and meteorology can complicate how we model liquid water clouds in global climate models or derive macro- and microphysical properties from satellite measurements.

Clouds like these can be wide spanning marine stratocumulus, which are thin in the vertical (1 km+) compared to a wide horizontal spread (1000 km+), or popcorn cumulus, which are localized, sub-kilometer clouds that are comparable in height and width. As was discussed with high cloud feedbacks, if the moist cloud parcel continues to rise into sub-zero Celsius regimes, liquid water may become *supercooled*, which is controlled by a completely different set of processes. Water vapor in the parcel may sublimate onto ice nuclei, which can be an ice crystal or a suitable irregular surface, such as aerosol. Though there is significant debate, airborne particles such as black carbon, such as those from aircraft exhaust (Gorbunov et al. 2001), dust and fly ash (Richardson et al. 2007), volcanic ash (Schill, Genareau, and Tolbert 2015), silver iodide (DeMott 1995), biogenic particles (Burrows et al. 2013), and

specific bacteria species (Bowers et al. 2009) may be suitable surfaces for ice formation. Because pure water does not freeze in the atmosphere above approximately -40°C, this *heterogeneous freezing* is the primary ice formation mechanism in clouds (Wright and Petters 2013). Ice crystals may also grow via evaporation and sublimation of supercooled water onto nearby ice crystals (the Wegener-Bergeron-Findeisen process, Korolev et al. 2017), a series of melting and freezing in the presence of supercooled water droplets may rime the crystal via *accretion*, and crystals may stick to each other via *aggregation.* These processes occur because the saturation vapor pressure over ice is lower than over water vapor. These pathways can be helped along by ionization of the air, as well (DeMott et al. 2011). Depending on the temperature, saturation, and other factors, ice crystals can take on several different shapes, such as quasi-spheres, columns, plates, and rosettes. Each shape has a different aspect ratio and surface features, which correlate to unique scattering and absorption properties (Yang et al. 2013, van Diedenhoven et al. 2012, Parol et al. 2004). If icy crystal growth is unimpeded, graupel, millimeter-size ice crystals, may form. In particularly strong convection, updrafts may cycle the graupel through a range of temperatures, which forms a hailstone in a continued melting-freezing riming process. The largest hailstones can reach centimeters in diameter. Gravity will pull ice crystals out of suspension if they are large enough. The ambient temperature below the cloud determines the form the ice crystal takes when it precipitates: rain, freezing rain, graupel, or snow. Precipitating ice crystals can be efficient scavengers of aerosol, as well.

In summary, complexity in global cooling and warming for clouds and aerosols is challenging to characterize because of the scales, processes, and coupling involved. The reader is directed to recent review articles that further discuss the difficulty in measuring and modeling liquid water (Ghan et al. 2016), ice (Baumgartner et al. 2012), and mixed-phase clouds (McCoy et al. 2016) that are beyond the scope of this dissertation. In the next section, the history of satellite-based remote sensing of the Earth system, relative to the microphysical

properties that drive cloud and aerosol feedbacks and growth processes, is discussed. Active instruments, such as lidar and radar, are then compared with passive instruments, like radiometers and polarimeters. Advanced passive remote sensors, such as MAPs, are well-suited to continue our current climate record and improve the inputs to GCMs. This section will then make a case for the modern MAP and conclude with a look towards the *multi-angle imaging polarimeter* (MAIP), the Hyper-Angular Rainbow Polarimeter (HARP), which is the topic of this work.

Section 2: Spaceborne satellite instrument design

Subsection 2.1: Active remote sensing

Earth-observing instruments are one of two categories: active or passive. Active instruments, like Light Detection and Ranging (lidar) and Radio Detection and Ranging (radar) instruments send a pulse of light into the atmosphere and measure the signal that returns. Some of these instruments, like Cloud Aerosol Lidar with Orthogonal Polarization (CALIOP) on the Cloud-Aerosol Lidar and Infrared Pathfinder Suite (CALIPSO) (Winker et al. 2009) and the Cloud Profiling Radar (CPR) on CloudSat (Stephens et al. 2008, Tanelli et al. 2008) in the NASA A-Train, use these high-frequency pulses to generate a "curtain", which is a continuous measurement of total column backscatter as the instrument flies over the Earth. Scientists use the relative strength of the signals in a curtain as a function of height to differentiate aerosol, cloud, molecule, land, and ocean layers (Frances et al. 2020). The CALIPSO lidar uses two wavelengths, 532 and 1064 nm, which have different penetration depths and scattering efficiencies in the atmosphere. Two important lidar products is the *lidar ratio* and *depolarization ratio*, which are derived from the backscatter return from these pulses. The lidar ratio can help differentiate aerosol type and loading (Kim et al. 2018), though is typically limited to scenes with lofted aerosol. The depolarization ratio compares horizontally over vertically polarized pulse returns, which encodes information about cloud thermodynamic

phase, ice orientation, and aerosol sphericity, which can help identify dust species (Hu et al. 2009, Liu et al. 2008). These properties are directly tied to radiative forcing and cloud feedbacks, as mentioned above. Instruments like CALIPSO that survey the Earth over decades can build a sophisticated climate record of these products and track their changes over a variety of scenes.

Radar systems, like the CPR on CloudSat, are similar, though use specific frequencies (94 GHz) to penetrate deeper into the clouds or study water vapor transport over the Earth (Im, Wu, and Durden 2005). The frequency channels used by radar are sensitive to a larger particle size than lidar instruments. The size parameter dictates the kind of scattering (Rayleigh, Mie, or geometric optics for example) that occurs when light of a given wavelength interacts with a particle of a given size. Lidar instruments with visible channels are sensitive to smaller particles or droplets (5-20um, though can saturate on clouds), but radar signals encode the properties of precipitation-size particles on the order of millimeters. Therefore, radars are also useful in weather forecasting. They can be used to estimate the strength and trajectory of storms from aircraft and ground stations (Smith et al. 2016) and infer precipitation type as well as global distribution (Stephens et al. 2018).

Both lidar and radar can be exceptionally accurate instruments and their calibration is relatively straightforward compared to imaging systems (Hunt et al. 2009, Tanelli et al. 2008) Lidar payloads in space have been traditionally limited to those with a strong lidar focus, such as IceSat, CALIPSO, and Aeolus missions (Abdalati et al. 2015, Winker et al. 2009, Endemann 2017) or those with larger spacecraft (and budget) that can accommodate other instruments, such as EarthCare or the upcoming Atmosphere Observing System (AOS) (J. P. do Carmo et al. 2021, da Silva 2021). Recent small-satellite technology demonstrations, such as the Cloud-Aerosol-Transport System (CATS, Yorks et al. 2016) have shown that compact, small-satellite designs can produce high-quality lidar observations of the atmosphere – a general theme that will continue throughout this dissertation. Finally, comprehensive lidar sys-

tems like the High Spectral Resolution Lidar (HSRL, Hair et al. 2008) are popular in aircraft campaigns, where access to the instrument is easier, there is dedicated space for the payload, and cross-validation with other instruments on the aircraft or satellite platforms is desired (Knobespiesse et al. 2020).

Lidar and radar instruments are also limited by spatial and signal resolution compared to other remote sensors. As a light pulse travels through the atmosphere, it is attenuated by molecules, clouds, and aerosols and the signal spreads out due to diffraction. The return pulse is often order of magnitudes dimmer than the original pulse, depending on the time of day and movement of the planetary boundary layer (PBL). Lidar like CALIPSO track a nadir path in their orbit and at narrow ground resolution (100 m spot size). This is excellent for highly resolved aerosol or wind speed retrievals, but makes it challenging to infer the spatial context of the atmosphere around the nadir point, which is important for aerosol sourcing and aerosol-cloud interactions. This is another benefit of CALIPSO and CloudSat flying in the NASA A-Train constellation with other imagers that are capable of similar and complementary retrievals (L'Ecuyer and Jiang 2010).

Subsection 2.2: Passive remote sensing

Subsection 2.2.1: Introduction

Global Earth observation is synonymous with passive remote sensing. These instruments do not generate their own source of radiation. Instead, they use scattered sunlight at the top of the atmosphere as their light source. This can greatly reduce development cost and size and lead to a wide variety of designs and instrument concepts. Passive remote sensors, such as the Advanced Very High Resolution Radiometer (AVHRR, Bhatt et al. 2016), make Earth measurements inside specific spectral windows, called *passbands*. Unlike lidar or radar that use a very narrow spectral pulse, each passband covers a wider range of wavelengths. Each meas-

urement is an integrated estimate of the reflected or emitted radiation arriving at the detector in this wavelength range.

Passbands are designed to study specific Earth phenomena, as shown in Figure 1. These typically take advantage of *atmospheric windows*, spectral regions without strong molecular or water vapor absorption. Molecules in the atmosphere, such as ozone (O_3) and nitrogen (N_2) strongly scatter light in the shortwave visible range of the spectrum due to vibrational and rotational excitations (Young 1981 and references therein). Passive spectrometers like the Ozone Monitoring Instrument (OMI, Levelt et al. 2018) and the Ozone Mapping Profiler Suite (OMPS, Flynn et al. 2014) have passbands in this 300-400 nm range. In these bands, the Earth surface appears hazy due to the heavy Rayleigh signal at the top of the atmosphere (TOA). This region is also sensitive to aerosol index, total column ozone abundance, and nitrous oxides (NO_x) and volatile organic compounds (VOCs) that can affect public health, such as formalehyde (HCHO). Fine mode aerosol can also scatter light in the Rayleigh regime in longer wavelength bands, such as 670-870 nm. Scientists can leverage this information and Earth data from wide-swath imaging radiometers, such as the Moderate-resolution Imaging Spectro-radiometer (MODIS), for *atmospheric correction* (Vermote, Saleous, and Justice 2002). This is the process of "removing the atmosphere" to expose dimmer land or ocean signals. Passbands in the 550 nm range represent the peak of the solar blackbody spectrum and are useful for ocean color retrievals, as well as intercomparison of aerosol retrieval products with AERONET and global circulation models (Kinne 2003, Remer et al. 2005). The 670 nm region is useful for deriving cloud and aerosol properties over dark ocean and in the absence of molecular Rayleigh scattering and water vapor absorption (King et al. 1997). 870 nm passbands can help differentiate vegetation on land and ocean from clouds and deserts, leading to categorical indices such as the Normalized Difference Vegetation Index (NDVI, Fensholt et al. 2009, Schucknecht et al. 2013).

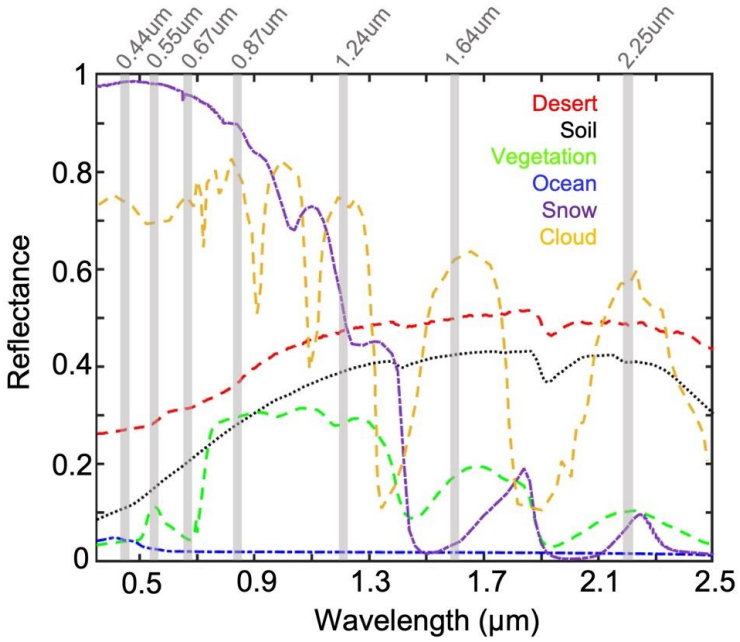

Figure 1. Top of the atmosphere reflectance spectra for a variety of Earth targets. Popular passive remote sensing passbands are overlaid in grey blocks, with the corresponding center wavelength shown at the top. Note the brightening of vegetation beyond 0.7um. The 1.24, 1.64. and 2.25um bands all see bright cloud but lower signal from snow due to increasing absorption. Water absorption bands appear as dips in the cloud profile around 0.9, 1.1, 1.38, and 1.9μm. This figure is adapted from Ding et al. (2021) under the CC-BY-4.0 license. Modifications: axis labels, legend, and passband labels, and grey bands.

Shortwave-infrared passbands such as 1.24, 1.6, and 2.2 um can be used alongside visible passbands to infer cloud droplet properties. Several instruments also have a 1.38 um passband for cirrus cloud detection (Gao and Kaufman 1995). Oxygen and water vapor absorption is strong around 765 (O_2 A-band) and 900 nm, which can contaminate aerosol signals in these bands (Weigner and Gastieger 2015), though sometimes these bands are added specifically for characterizing these gases. Thermal infrared passbands are used to identify cold targets, such as deep convective clouds (DCC) or cirrus, and are used to infer cloud height, precipitation, and thermodynamic phase (Menzel, Frey, and Baum 2015). Given the wide array of sensitivities and climate-relevant Earth phenomena, passive remote sensors are solicited for many Earth science missions. Those with a variety of passbands that span several spectral regions (UV, VIS, NIR, TIR, etc.) are especially useful for decadal missions.

Subsection 2.2.2: Imaging systems

Passive remote sensors can also *map* the Earth. For example, AVHRR, MODIS, and VIIRS contain a rotating optical element that sweeps the Earth scene onto a detector array (Xiong and Butler 2020, Rao 1987). For a given passband, the detector is a single pixel, but the rotation of the mirror continually exposes that pixel to new Earth scene information. In the case of AVHRR, this scan mirror is a single plate that rotates at 45 degrees in front the detector array. MODIS (and VIIRS) use a two-sided mirror to achieve a similar effect, as shown in Figure 2. After this mirror finishes a half-rotation, the detector has captured a line of data that represents the portion of the Earth that was covered during that sweep. Then, the second mirror side sweeps out the next scan and so on. A two-dimensional image, or *granule*, of the scene is made when these individual scans are stacked sequentially in time. Instruments like these are called *whisk-broom sensors*. This capability allows for full global coverage in two days. The two MODIS instruments, on NASA's Aqua and Terra satellites, were specially designed for daily global coverage between them – Aqua orbits the Earth from the South Pole to the North Pole (*ascending*) and Terra does the reverse (*descending*). Many aspects of MODIS and VIIRS missions in terms of vicarious calibration, instrument design, and orbit characteristics adapt the AVHRR heritage.

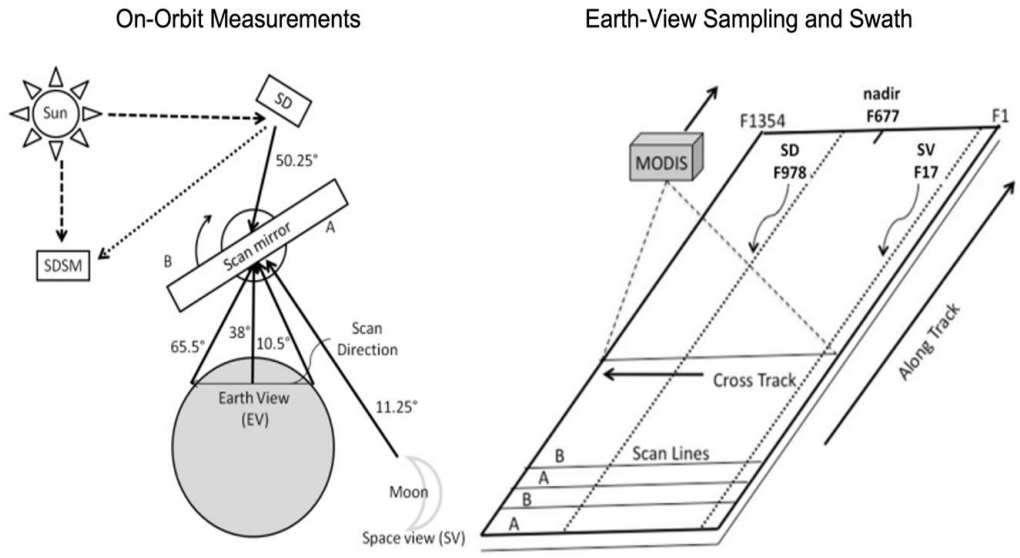

Figure 2. Schematic of the MODIS on-orbit (left) and Earth-view sampling swath characteristics (right). Half of the MODIS scan cavity has on-orbit calibrators (OBC), including a solar diffuser (SD), space view (SV) port for lunar views, and a Solar Diffuser Stability Monitor (SDSM) for tracking the degradation of the SD in different spectral channels. These objects are observed by the MODIS detector at different AOI as the scan mirror rotates (AOIs given in the diagram). These elements provide a regular assessment of the absolute gain (m_1) and AOI-dependent response of the scan mirror sides (RVS) for the 21 MODIS reflective solar bands. The other half of the cavity is dedicated to Earth view data capture, which spans 10.5 to 65.5º AOI. As the MODIS instrument flies over a scene, the scan mirror sweeps Earth signals over the detector in the cross-track direction (right). The scans correspond to alternating mirror sides (denoted A and B) and the AOI are mapped one-to-one into 1354 segments called *frames* (designated by F). Some portions of the Earth view scan represent the same AOI as the on-board calibrators (ie. SD and SV frames). Therefore, Earth view data at these AOI from stable or well-characterized targets can be used for vicarious calibration and support the OBC results. This figure is adapted from Lyapustin et al. (2014), under the CC-BY-4.0 license. Modifications: titles.

During a single scan, the scan mirror reflects the Earth scene onto the detector at different angles-of-incidence (AOIs) as well. Each pixel in the scan represents a unique viewing and solar geometry on the ground. While AVHRR, MODIS, and VIIRS view the Earth from a single angle in the along-track, or instrument-heading, direction, they image a swath that spans thousands of kilometers in the cross-track direction (see Figure 3). For example, the MODIS 2330 km swath corresponds to a 45.5° field-of-view (FOV) in a single scan. This angular coverage allows for multiple views on a single target over a period of a time

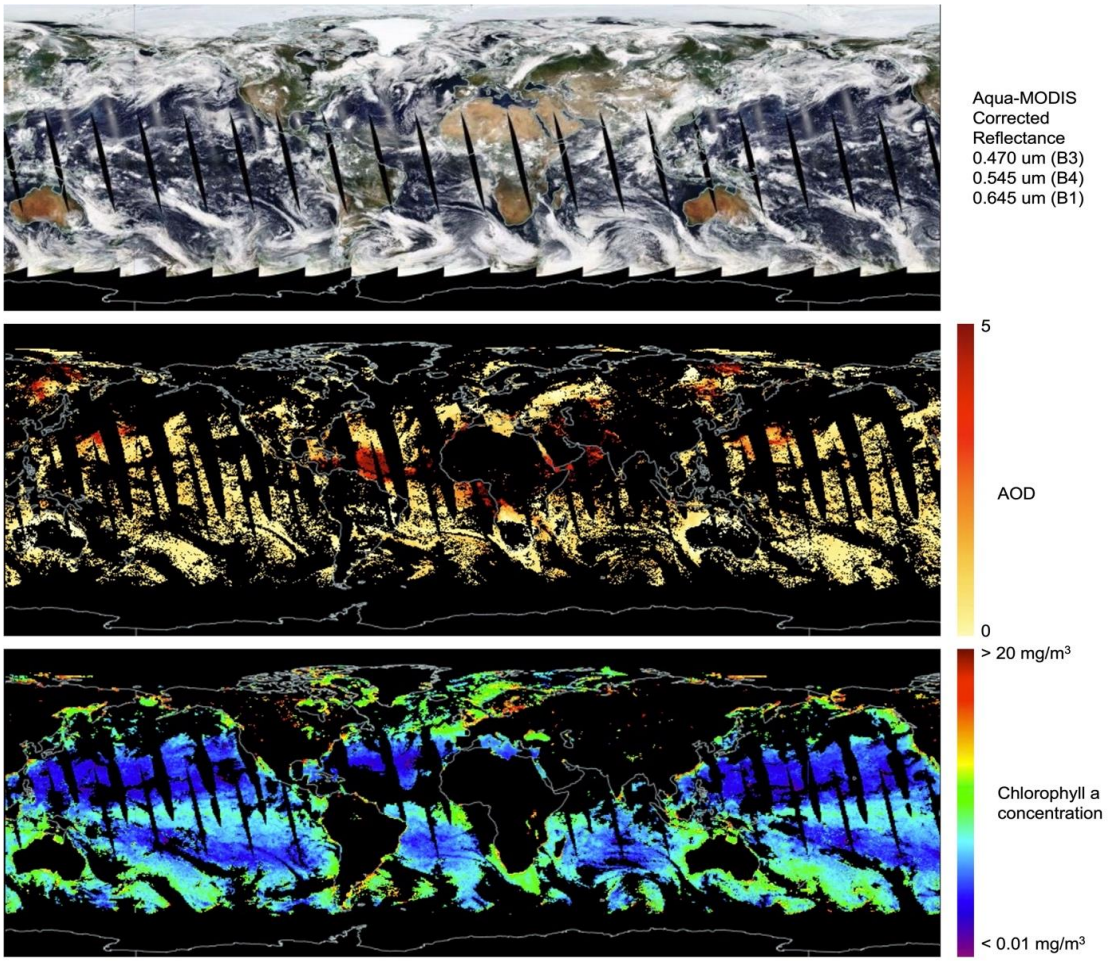

Figure 3. Daily coverage of Aqua-MODIS Collection 6 corrected reflectance (top) and retrieved aerosol optical depth (AOD, middle) and Chlorophyll-a (Chl-a) concentration (bottom) for all granules from July 12, 2020. The reflectance data is a composite of visible bands that most closely represent the human eye spectral response (bands 3, 4, and 1). The AOD shows a significant dust plume over the Atlantic Ocean and Caribbean Sea. Regions of heavy pollution exist in eastern Russia, the middle East and western Pacific, as well. Chl-a is a proxy for phytoplankton populations. Blooms (data in cyan to red) are visible in coastal areas, northern Europe, Oceania, and along the Inter-Tropical Convergence Zone (ITCZ). Data retrieved from NASA Worldview (https://worldview.earthdata.nasa.gov/) on 14 Aug 2022.

(~weekly), and from several different AOI. MODIS re-visits the same target at the same AOI every 16 days. This is significant for two reasons. Earth targets, like land and ocean surfaces, scatter light asymmetrically as a function of angle, and some of their properties are encoded in this information. For example, MODIS measurements have been used to validate bi-directional reflectance distribution functions (BRDF) of land and ocean environments (Schaff et al. 2002), retrieve globally resolved cloud, aerosol, and ocean properties (see Figure 3) over decadal periods, including cloud droplet effective radius, Chlorophyll-a concentrations,

and aerosol optical depth (Remer et al. 2005, Platnick et al. 2016), and help discriminate and categorize global biomes (Sulla-Menashe and Friedl 2018). Corrected digital counts and reflectance data can also be used for vicarious calibration over well-characterized targets, such as the Northern African Sahara, Dome Concordia plateau in Antarctica, clear open ocean scenes over the Equator and Northern Atlantic, and deep convective clouds in the Tropics (Wu et al. 2017, Xiong et al. 2009, Twedt et al. 2021).

Imaging systems like these are not the only ones to make considerable contributions to Earth mapping. The Landsat program, with on-board imaging cameras such as the Operational Land Imager (OLI, Knight and Kvaran 2014), has continued to provide land use and mapping data from low-earth orbit since 1975. New follow-on missions, such as Landsat 9, are still being solicited based on the success and utility of prior systems. Geostationary instruments have also made impressive strides in Earth remote sensing. The GOES-R Advanced Baseline Imager (ABI, Schmit et al. 2005) can capture larger regions of the Earth in a single capture and at a higher frequency than polar-orbiting imagers. GEO payloads are incredibly useful in weather prediction and land use change tracking (Chaves, Picoli, and Sanches 2020 and references therein). GOES-R ABI takes

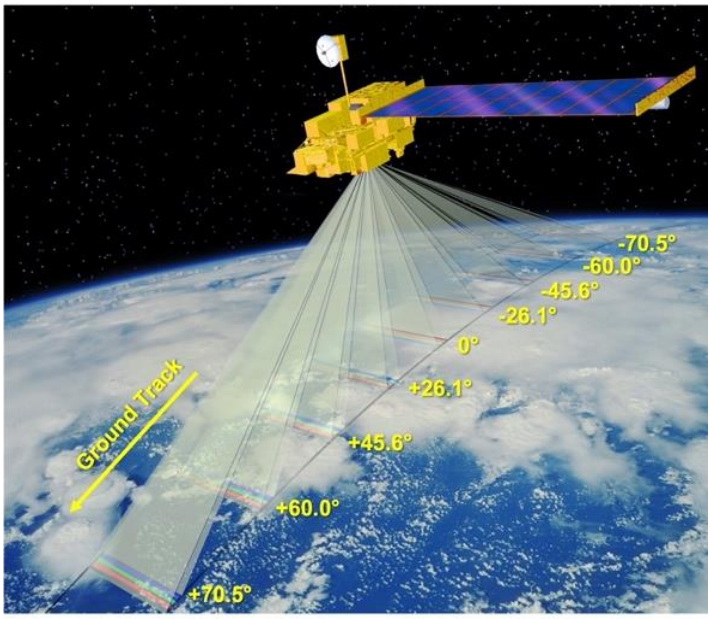

Figure 4. Artist rendering of the Terra-MISR nine-camera pushbroom sampling technique. Each transparent triangle that connects the Earth's surface to the satellite is a single MISR view (with nominal view zenith angle given in yellow). Positive (negative) degree labels signify forward (backward) views. Each view is captured simultaneously. The instrument is heading toward the bottom left of the image. This figure is adapted from https://misr.jpl.nasa.gov/, courtesy of NASA/JPL-Caltech. Modifications: angle and ground track labels.

images of the full Earth disk every 5 minutes and shares many heritage bands in common with MODIS, VIIRS, and current GOES platforms. Its data is used to retrieve Level 2 aerosol and cloud products at a similar 1km resolution as MODIS (Khan et al. 2021). There are many other successful legacy instruments and geostationary imagers, such as EPIC on the DSCOVR satellite, but further discussion is largely outside the scope of this work.

Radiometers like these are all considered "single-angle imagers" because they view Earth targets from one viewing angle per orbit (along-track by cross-track) or full-disk capture in the case of GEO (each target is always viewed from the same viewing geometry). This limits their access to certain scattering angles and information content depending on orbit/image. For the polar orbiters, it also requires several orbits (and a series of days) to collect data over the same target at different geometries. Despite these limitations, these instruments have contributed significantly to our current climate record for aerosols, clouds, land, and ocean properties and weather monitoring. They will be used as a foundation to discuss advanced instrument designs in the next section.

Subsection 2.2.3: Multi-angle imaging instruments

Multi-angle Imaging Spectro-Radiometer (MISR, Diner et al. 1998) instrument on NASA's Terra spacecraft was the first in space to sample a single target from multiple, co-located along-track views. The MISR payload included nine identically calibrated cameras with nadir view zenith angles from ±70º. Unlike the cross-track scanning of MODIS, the nine MISR detectors take a simultaneous image of a 4-row focal plane at fast intervals as it flies over the Earth, as shown in Figure 4. Each image capture slightly overlaps with the last and in post-processing, the images of the Earth taken in a single camera and spectral channel can be stitched together, sequentially, to form *pushbrooms* of the Earth scene below. The data in each camera is geolocated to a common lat-lon grid using the nadir view, and the time it takes a single target to pass from the furthest forward to furthest aft camera is approximately 7

minutes. Multi-angle MISR reflectances led to several improvements in microphysical retrievals and modeling of three-dimensional phenomena. MISR data improved our understanding and modeling of aerosol plume transport and rise and trends in air pollution over urban centers (Kahn et al. 2007, Scollo et al. 2010, Liu et al. 2009). MISR data increased measurements of the total phase function of aerosols and clouds to nine discrete points, which could be further improved by aggregating pixels for scattering angle coverage. Therefore, aerosol species are separated by composition much more easily (Frouin et al. 2019). The multi-angle aerosol record of MISR that comprises global retrievals of AOD, and other properties was recently enhanced to 4.4km, from 17.6 km, as well (Garay et al. 2017). Cloud height derived using stereo photogrammetry (Marchand, Ackerman, and Moroney 2007), which does not rely on absolute calibration, is complementary to and independent of the legacy MODIS CO_2-slicing technique (Mitra et al. 2020). MISR CTH retrievals can distinguish multi-layer clouds as well, in specific scenarios (Naud et al. 2007). The added information content in multiple views allow for joint retrievals of ocean and aerosol properties (Limbacher and Kahn 2017). While MISR continues to fly on NASA's Terra spacecraft as of this work, its success led to the development of advanced multi-angle systems that included polarization and more spectral channels and viewing angles (Dubovik et al. 2019). If an instrument includes all three, it is considered a MAP, one of the most comprehensive passive remote sensing instrument concepts to date (Dubovik et al. 2021).

Subsection 2.2.4: Multi-angle polarimetry

So far, the discussion has focused on pulsed (single-view, single-pixel), single-angle (single-view, multi-pixel), or multi-angle (multi-view, multi-pixel) reflectance data for Earth science applications. Polarimeters, instruments that can measure the orientation of the electric field of incoming photons, were first developed for Earth remote sensing in the late 1990s,

after several decades of modeling and observation of the scattering of Earth and other planets and the cosmic microwave background of the universe (Coffeen 1979, Kowosky 1995, Mischenko and Travis 1997). The Polarization and Directionality of the Earth's Reflectances (POLDER, Deschamps et al. 1994), an instrument developed by the Centre National d'Etudes Spatiales (CNES), was launched on the ADEOS satellite in 1996. Polarimeters like POLDER can infer the full Stokes vector, which includes the total and linearly polarized reflectances from an Earth target. Polarization is another dimension of information content that can be used to retrieve size, shape, and compositional properties of clouds and aerosols, and surface-layer properties of the land and ocean (Hansen and Travis 1974). This information is often independent and complementary to reflectance-based measurements. POLDER-1 (1996-1997) and POLDER-2 (2002-2003) were fraught with satellite payload failures and had truncated missions. The third iteration, POLDER-3, flew successfully from 2004-2013 on the Polarization and Anisotropy of Reflectances for Atmospheric Sciences coupled with Observations from Lidar (PARASOL) satellite as part of the NASA A-Train from 2004-2011. The instrument was then lowered into a different orbit and continued operations until its eventual decommission in 2013. The remainder of this section will focus on POLDER-3 on PARASOL.

POLDER measured three unique states of linear polarization and selected wavelengths (9 passbands from 490 – 1024 nm) using a rotating filter wheel placed in front of the detector focal plane array (FPA). As the instrument flew over the Earth scene, the filter wheel rotated quickly to move through the passbands and cycle through the three polarization states (0, 60, and 120°) in the three bands sensitive to polarization (490, 670, and 865 nm). The polarization data taken by the three orientation angles can be recombined in post-processing to recover the original polarization state (I, Q, U) of the ground scene. Scientists can now access the *polarized scattering phase function* of particles, which contains independent information about sphericity, refractive index, and the size distribution of particle and droplets (Parol et

al. 2004, Gerard et al. 2005). Comparing the polarized signal of liquid water and ice particles is enough to discriminate thermodynamic phase, as well (Reidi et al. 2010). Therefore, microphysical retrievals can be improved using reflectance and polarization data, rather than reflectance alone. Unlike total reflectance, which includes both diffuse and direct scattering signals, polarization is dominated by single-scattered photons. This leads to a fundamental difference in *where* the retrieved information is coming from. Multiple scattering of photons contains sub-surface information, while polarization typically encodes surface or skin-layer properties. POLDER-3 and simulated proxy data also led to improvements in vicarious and cross-calibration over Rayleigh, sunglint, and deserts (Fougnie et al. 2007, Djelalli et al. 2019), advanced aerosol retrieval algorithm development (GRASP, Dubovik et al. 2011, SRON, Fu and Hasekamp 2018), cloud microphysical properties (Shang et al. 2015, 2019) BRDF and BDPF modeling at a wide variety of solar and viewing angles and IGBP regions (Breon and Maignan 2017), and the development of modern polarimeter designs that specifically targeted angular, spectral, and/or spatial signals (Cairns et al. 1999, Diner et al. 2013, Martins et al. 2018, Hasekamp et al. 2019). The Directional Polarimetric Camera series (DPC, Li et al. 2018) and the upcoming Multi-Angle, Multi-Imaging, Multi-Polarization (3MI, Fougnie et al. 2018) instrument are Earth remote sensing polarimeters that have similar capabilities to POLDER.

Sampling and accuracy are major considerations when designing a polarimeter. These two concepts, and the fact that the atmosphere produces negligible circular polarization (Hansen and Travis 1974), led to a wide variety of different polarimeter designs. For example, the POLDER instrument is a *division of time* polarimeter. These use sequential measurements to sample an orthogonal basis set of polarization states. Because the mechanism of polarization is a filter wheel, instrument designs like POLDER that use a single detector, simple optical assembly, and a wide FOV, are attractive in space. However, the major drawback of this polarimeter design is time-related misregistration. If the target travels outside the pixel in

the time it takes to measure all polarization states, the Stokes vector recovery will be biased. Sharp targets like coastlines or cloud edges can appear artificially bright if they move too quickly across the FPA as the filters swap. This is called “false polarizations”. The POLDER and upcoming 3MI processing accounted for this using a mixture of motion compensation and interpolation/geo-registration techniques to account for this (Hioki, Reidi, and Djellali 2020). However, scientists often estimated a 2% (1%) polarization accuracy of POLDER over land (ocean), and vicarious techniques have shown an uncertainty range in total reflectance between 1.5 to 4% depending on the spectral band and target used (Fougnie et al. 2007). This polarimetric uncertainty is considered too large for modern aerosol microphysical retrievals of refractive index, which differentiates aerosol type (Hasekamp and Landgraf 2007, Wu et al. 2015), though is still considered valid for atmospheric correction, cloud microphysical retrievals over cloudbow, and constraining aerosol retrievals (NASA 2015).

Subsection 2.2.5: Improvements to Earth-observing MAP design

Subsection 2.2.5.1: Photoelastic modulation

The Multi-Spectral Polarimetric Imager (MSPI) uses photoelastic modulation (PEM) to get around the limitations of time-related polarization sampling (Diner et al. 2013). Even though it is still technically a division of time polarimeter, its polarization measurement is so quick that all polarization states are imaged effectively simultaneously. Two PEMs in series put stress on a glass plate, which generates a time-dependent retardance at frequencies higher than 42000 Hz. This signal is sampled 23 times for every exposure. In post-processing, the signal captured by sectors of the detector overlaid with polarizing filters is transformed into I and Q and I and U pairs. The PEM approach allows for high polarimetric accuracy (<0.005, van Harten et al. 2018) which is further improved by binning pixels (van Harten and Diner 2017). Instead of a wide FOV like POLDER, MSPI has a programmable gimble to access

viewing angles up to ±67° along-track. This gimble can be programmed in two modes: *step-and-stare* and *continuous sweep*. In step-and-stare, the gimble snaps to a specific view angle and creates a pushbroom over a target. The gimble moves to a different view angle and again forms a pushbroom over the same target. In this way, MSPI step-and-stare data generates a co-located and discrete reflectance and polarization data over a single target. During the NASA ACEPOL campaign, the MSPI gimble was programmed to the same viewing angles as the SPEX polarimeter for ease of cross-calibration and validation (Knobelspiesse et al. 2020). If scattering angle coverage is desired, MSPI may use the *continuous sweep* mode, which slowly drags the detector over a scene. The detector is continually exposed and a single pushbroom is made of the ground scene. This time, there is no co-located information, but large-scale features, like the polarized cloudbow or aerosol plumes, can be imaged over a wide swath. MSPI data has advanced coupled liquid water cloud and aerosol retrieval algorithms (Xu et al. 2017, 2018) and volumetric cloud tomography (Levis et al. 2017), which takes advantage of narrow spatial resolution (e.g. 10m from 20km altitude). MSPI is the precursor to the Multi-Angle Imager for Aerosols (MAIA) mission, which will sample the polarimetric information content of urban pollution for the purpose of public health (Diner et al. 2018).

Subsection 2.2.5.2: Amplitude-splitting polarimeters

There are other ways to image polarization states simultaneously and with high accuracy. *Division of amplitude* polarimeters use refractive optics to split the polarization components of a single beam. These beams fall onto individual FPAs (often the same number as independent polarization measurements). The FPAs are timed together to ensure they are spatially and temporally identical. Because these designs rely on more than one detector, maintaining detector co-alignment in the image space can be a major source of uncertainty. This is

the concept behind the Research Scanning Polarimeter (RSP, Cairns et al. 1999) and the Hyper-Angular Rainbow Polarimeter series (HARP, Martins et al. 2018), which is the topic of this dissertation and detailed in later chapters. The RSP instrument is a single-pixel scanner capable of 152 along-track viewing angles across nine passbands (470 – 2250 nm). Incident light onto the RSP boresight is split by a Wollaston prism and dichroic beamsplitters into two light paths and detectors. One detector measures I and Q, the other I and U reflectances. Single pixel sampling avoids the detector co-alignment issues that could impact two-dimensional FPAs. RSP is among the most accurate polarimeter instruments to date, with polarization uncertainty at 0.2% maintained by on-board calibration during field campaigns and frequent lab calibrations over decades (van Harten et al. 2018, Knobelspiesse et al. 2019). RSP data led to improvements in cloud droplet distribution retrievals, including for multi-mode DSDs and drizzle (Alexandrov et al. 2016, Sinclair et al. 2021), ice discrimination and habit (van Diedenhoven et al. 2013), ocean color and CDOM (Chowdhary et al. 2012), joint aerosol retrievals and comparisons with lidar (Knobelspiesse et al. 2011, Wu et al. 2016, Stamnes et al. 2018, Schlosser et al. 2022), and intercomparisons with other polarimeters (Knobelspiesse et al. 2019, Smit et al. 2019). The RSP instrument was designed for aircraft, though a spaceborne version, the Aerosol Polarimetry Sensor (APS, Peralta et al. 2007), was developed in the late 2000s for the NASA A-Train Glory mission. Unfortunately, the APS launch failed in 2011 and Glory was lost. RSP-1 and RSP-2 continue to fly in targeted campaigns and RSP data is often referenced in support of future polarimetric space missions.

Subsection 2.2.5.3: Spectral modulation

Another successful polarimetric design, the SPEX concept from the Netherlands Institute for Space Research (SRON) uses division of amplitude optics combined with a diffraction grating to achieve a polarized measurement in up to 109 narrow channels from 385 to

770 nm (van Amerongen et al. 2019). The polarizing optics split the incident beam into two components and imbue a retardance on each, such that the linear combination of these signals at a given wavelength is correlated to the intensity (I) and degree of linear polarization (DOLP) for that target. SPEX nominally measures at five viewing angles from ±50º, including a nadir view (0º), and has a relatively narrow swath of ~100km from 700km altitude (this correlates to a cross-track FOV ~7º). An aircraft demonstration, SPEX airbone, flew during the ACEPOL campaign (Knobelspiesse et al. 2019) and scientists demonstrated its ability to perform compatible aerosol retrievals against other MAPs, such as RSP and AirMSPI, and the HSRL-2 lidar (Fu et al. 2020). SPEX is also highly accurate, with a polarimetric (radiometric) uncertainty of 0.25% (2%) (Smit et al. 2019, Remer et al. 2019). A small-satellite version of SPEX airborne, called SPEXone, has been integrated on-board the NASA PACE spacecraft as of this writing. Alongside OCI and HARP2, its data is expected to advance aerosol microphysical retrieval techniques and algorithms, in line with new accuracy requirements suggested in the literature (Hasekamp and Landgraf 2007, Hasekamp et al. 2019). OCI and HARP2 will share a portion of their swaths with SPEXone. Synergistic aerosol and cloud retrievals improved atmospheric correction for OCI, and intercalibrations over common targets is anticipated from all three PACE instruments (Werdell et al. 2019).

In Table 1 below, the mission characteristics for the above airborne polarimeters and POLDER-3 are shown. However, other Earth-observing MAPs exist with varying designs, capabilities, and data availablilty. To limit the scope of this dissertation, the reader is encouraged to seek out the comprehensive review article on the topic, Dubovik et al. (2019).

Table 1. Mission characteristics of POLDER and ACEPOL MAPs[e]

Mission	Swath (along/cross)	Viewing Angles	Spectra, nm (# total, # pol.)	Spatial Res. at nadir (altitude)	DoLP Accuracy[d]	Agency	Heritage
POLDER	±51°/±43°	14	443-1020 (9,3)	6 x 7 km (700 km)	<= 0.02	CNES	ADEOS-1/-2, 3MI
RSP	±60°/[a]	152	410-2250 (9,9)	277 m (20 km)	<= 0.002	GISS	APS
AirMSPI	±67°/varies[b,c]	varies[b,c]	355-931 (8,3)	10 m[b], 25 m[c] (20km)	<= 0.005	JPL	GroundMSPI, MAIA
AirHARP	±57°/±47°	120	440-870 (4,4)	20 m (20 km)	<= 0.005	UMBC	AirHARP, HARP2
SPEX airborne	±57°/±3.5°	9	385-770 (109,109)	250 m (20 km)	<= 0.004	SRON	GroundSPEX, SPEXone

[a]The cross-track swath of RSP is 14 millirad (pixel IFOV).
[b]AirMSPI step-and-stare mode (±15° cross track swath, programmable views)
[c]AirMSPI continuous sweep mode (cross-track swath varies along the sweep)
[d]Demonstrated degree of linear polarization (DoLP) measurement accuracy as of this work.
[e]Data from Knobelspiesse et al. (2019), van Harten et al. (2018), Smit et al. (2019), and Dubovik et al. (2019).

Subsection 2.3: MAIPs, climate needs, and uncertainty

To narrow uncertainties in radiative forcing of clouds and aerosols, highly accurate, comprehensive measurements of our atmosphere and surface are needed. Specifically, the strongest candidate instruments will be those that can (1) help improve the inputs to our climate models that describe processes at relevant scales, (2) maintain continuity and accuracy of measurement over time, and (3) increase information content and reduce large-scale assumptions in retrievals. MAP instruments of varying designs can make meaningful improvements to all three. They also benefit from increases in technology for data processing and continuity of measurement over long periods in space (Dubovik et al. 2021). To narrow the scope of this dissertation, only MAP specs and desired requirements related to global measurements of aerosols and clouds will be considered.

Over the last few decades, several studies were done to assess the information content in Earth observations using a mixture of sampling characteristics: channels, discrete view angles, and polarization. The utility of polarimetric remote sensing for Earth observation was convincingly discussed in Mischenko and Travis (1997) related to aerosols and ocean measurements. Later work helped to define the kinds of MAPs that could best sample aerosol, cloud, land, and ocean properties, test these designs in targeted campaigns, and develop formal uncertainty requirements for future space missions.

Hasekamp and Landgraf (2007) developed a framework to compare different kinds of remote sensors and their ability to retrieve critical aerosol properties, such as SSA, effective radius, effective variance, refractive indices, and AOD. They found that multiple, co-located angles, combined with measurements in reflectance and polarization were optimal, particularly over land. Radiometry, regardless of angular capability, is limited in information content by comparison. For modern aerosol microphysical retrievals using MAP data, 3 viewing angles are required, but 5 viewing angles produces the lowest possible error in retrieved

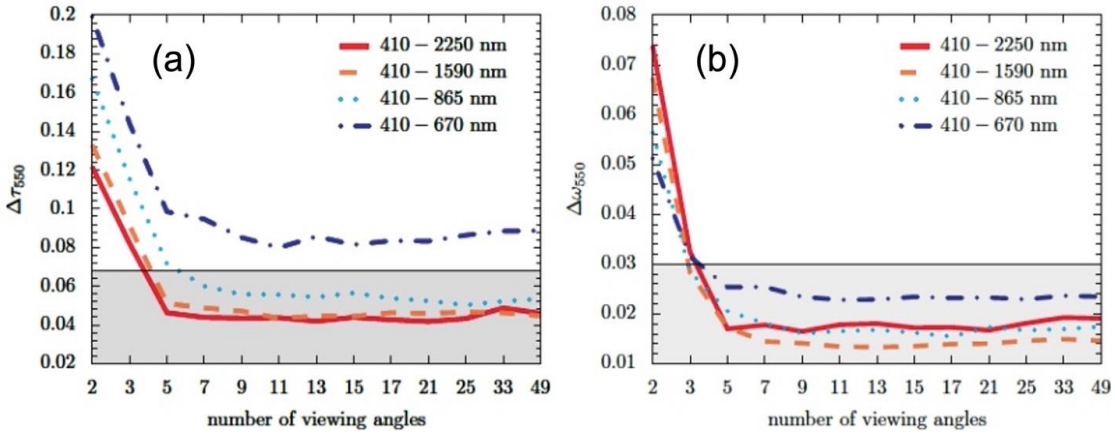

Figure 5. Simulated retrieval uncertainties for aerosol optical thickness (AOT, a) and single-scattering albedo (SSA, b) as a function of spectral range and co-located viewing angles for multi-angle polarimetric data over land. The community benchmark uncertainty level is given by the grey block (0.07 in AOT and 0.03 in SSA). Data inside the gray block meets community requirements. In both cases, the uncertainty is minimized at five co-located views. This figure is adapted from Wu et al. (2015) under the CC-BY-4.0 license. Modifications: figure letter labels.

SSA(550 nm), effective radius, effective variance, real and imaginary parts of the reftactive index, and AOD(550 nm). The major conclusion from this work, which was published after most modern MAPs were built, is that there is a tradeoff between angular and spectral information content in aerosol microphysical retrievals. This suggests that a variety of potential MAP designs may produce compatible aerosol retrieval capability. This work was directly validated by Wu et al. (2015), who used a mixture of simulated datasets and field measurements from RSP and AERONET during the NASA SEAC^{4}RS campaign. The authors studied the impact of viewing angles and spectral range on aerosol retrieval accuracy. The authors suggested that while five viewing angles is the minimum requirement to hit the community accuracy benchmark for several aerosol retrieval products (SSA, AOT, fine mode effective radius, coarse mode real refractive index), a spectral range that *includes* SWIR bands is required, as shown in Figure 5. Spectral coverage between 410 and 670 nm alone did not contain enough information content to hit the required accuracy levels, regardless of number of angles, for many products. These two studies helped to narrow the acceptable range of MAP instrument designs for modern aerosol retrievals.

Further support for MAPs as the highest accuracy aerosol-retrieving passive remote sensors was provided by Knobelspiesse et al. (2012). The authors simulated the information content in aerosol retrievals that used intensity and/or DOLP signals in APS/RSP, POLDER, and MISR-like designs at a range of viewing angles. The authors found that the uncertainty in retrieved parameters, such as SSA, AOT, and refractive indices, were minimized over ocean and land scenes when both intensity and DOLP are used in the retrieval, and with measurements at as many available viewing angles as possible (maximum simulated was 255). The calibration uncertainties for radiance of all instruments were simulated at 3% but polarization varied considerably, with 2% estimated for POLDER and 0.2% used for APS/RSP over land scenes. Notably, the addition of intensity and DOLP in retrievals appeared to benefit instruments with lower accuracy (i.e., POLDER), but had less of an impact on retrievals from high-

er accuracy instruments (i.e., RSP/APS) due to the extra constraints required to correct surface reflectance.

Several other sensitivity studies were performed that demonstrate the advantage of certain polarimeter designs or data on the uncertainty of or information content in retrievals. Some examples concern ocean color and CDOM (Chowdary et al. 2012), aerosol vertical distribution (Kolashnikova et al. 2011), atmospheric correction (Knobelspiesse et al. 2018), and cloud microphysical properties and 3D effects (Miller et al. 2018, Rajapakshe et al. 2020). For climate science retrievals of these properties, a modern MAPs must achieve a DOLP accuracy of 0.005 or smaller and a corresponding a total radiance uncertainty of 3-5% (NASA 2015, NASA 2009). Several modern MAPs meet these requirements (Cairns et al. 1999, Smit et al. 2019, McBride et al. 2022, van Harten et al. 2018).

For clouds, MAP instruments can access information about the cloud DSD independently of reflectance. The polarized cloudbow is a single-scattering structure that appears in the presence of liquid water clouds. Spherical droplets that are compatible in size with the interacting wavelength give off Mie resonances in a range of backwards scattering angles. If the MAP angular sampling density is fine enough, these resonances can be sampled and compared with Mie theory to retrieve a uni- or multi-modal cloud top DSD. As in the aerosol discussion above, there is a trade-off between information content, angular density of the measurement, and spectral channel (Miller et al. 2018). The angular structure of the polarization generated by the droplets depends on the *size parameter*, so a channel twice as large as another (i.e., 1.6 μm vs. 0.67 μm) may allow retrievals of droplet sizes twice as big, if angular measurement density is kept constant. This is useful for retrieving larger drizzle mode droplet signals (>20 μm), which may suggest the onset of precipitation and is of critical interest in upcoming space missions (NASA 2015, NASA 2009). If the wavelength is kept constant, larger CDR retrievals may be possible by increasing the angular sampling resolution of the measurement (Sinclair et al. 2021). Because of the importance and uncertainty of resolving

cloud properties in GCMs as discussed in earlier sections, MAPs that can measure at high resolution (<10 km), at over 50+ co-located viewing angles in a single visible/SWIR channel, and at least 0.02 DOLP accuracy are sufficient to characterize global polarimetric liquid water cloud DSDs. Like aerosols, five angles are considered the minimum requirement for characterizing ice scattering properties as well, given the signal of ice as a function of scattering angle in backscattering is featureless (NASA 2015, van Diedenhoven et al. 2012b). Further details about the utility of polarimetric measurements for clouds will be discussed in context in Chapter 4. Of those discussed in this chapter, RSP/APS and HARP instruments meet these criteria at PACE altitudes (700 km) or lower (Alexandrov et al. 2016, McBride et al. 2020).

These considerations help define the necessary accuracies required for climate-relevant retrievals. The needs for clouds, aerosols, land, ocean, and atmospheric characterization are combined, and Table 2 summarizes these recommendations for major upcoming climate missions.

Table 2. Desired modern MAP design requirements for upcoming climate missions

Performance Marker	PACE	AOS
Spectral Coverage	400-2200nm	360-2260nm
Spectral Ranges (# of channels)	400-1600nm (4), 2200 (1)	360-410nm (1), 440-870 nm (3), 1000-2260nm (2)
Cross-Track Swath (º or km)	± 25°†, ± 15°‡	> 100 km
Nadir Spatial Resolution	< 5 km	< 1 km
Along-Track Coverage (# views)	± 50° (6+)	± 55° (5+)
Radiometric Accuracy	< 5%	< 3%
Polarimetric Accuracy (DoLP)	< 1%	< 0.5%

†Atmospheric correction
‡Aerosol, cloud
Data from NASA (2015) and NASA (2021).

Note the similar requirements between NASA PACE and AOS missions, which speaks to the convergence of literature studies. Each desires an imaging swath, multi-angle sampling with

significant angular separation, coverage across a broad spectral range, narrow spatial resolution, and sensitivity to and high accuracy in radiometry and polarization.

Section 3: Thesis of this dissertation

Therefore, there is a strong interest in the climate community for instruments capable of measuring the same target from multiple angles and at narrow resolution, with sensitivity to intensity and polarization, and an imaging swath with the potential for global coverage and spatial context. The last part of that sentence is what distinguishes a MAP from a MAIP. A MAIP with wide swath FOV is attractive for the globally resolved passive remote sensing observations that the community desires. This dissertation focuses on a new MAIP instrument with these specs, the Hyper-Angular Rainbow Polarimeter (HARP) series, a wide FOV, amplitude-splitting imaging polarimeter. This work proposes the HARP instrument as the next generation MAIP that can address the climate needs above for both aerosols and clouds and with requisite accuracy and design characteristics. This dissertation has two main components:

1. *Development and validation of an adaptable, physics-driven polarimetric calibration for a small-satellite hyper-angular imaging polarimeter*

Chapter 2 discusses the HARP instrument and its design, emphasizing its small size (10x10x30cm), low-cost development (< $6M USD), and comprehensive sampling in reflectance, polarization, angles, spectra, and swath. Chapter 3 develops a comprehensive calibration of the HARP instrument that takes advantage of the telecentric optical design. Using the detector flatfields, calibration coefficients derived at any location in the FOV can be spread to all others, with no sacrifice in accuracy. The performance of all spectral channels is validated to the 0.005 level in DOLP in the laboratory. The field performance of HARP is validated against the RSP instrument to <1% in DOLP over land and water targets observed during the

NASA Aerosol Characterization from Polarimeter and LiDAR (ACEPOL) field campaign. The results of this section demonstrate that HARP meets community accuracy requirements for modern aerosol (and cloud) retrievals, which is 0.5% in DOLP (NASA 2015, NASA 2021). This capability is desired by several major upcoming missions that the HARP is either a part (PACE) of or under consideration for (AOS).

2. *Development and validation of a novel spatial cloud droplet size distribution retrieval algorithm from co-located hyper-angular imaging polarimeter cloud datasets*

Chapter 4 discusses the application of this calibration to liquid water cloud DSD retrievals. The very first polarized, co-located cloud DSD retrieval at narrow resolution (200 m) and over a wide spatial field can be done using HARP data at 0.67 μm and a legacy algorithm (Breon and Goloub 1998). The HARP cloud data was taken during the NASA Lake Michigan Ozone Study (LMOS) in 2017. This retrieval provides a measure of cloud droplet effective radius (CDR), like those retrieved from radiometric bi-spectral methods, but also the cloud droplet effective variance (CDV), a measure of the width of the size distribution. Direct sensitivity to CDV is unique to polarimetric cloud data. Data from instruments like HARP, that have the potential produce a spatial map of CDV values for global clouds, may enhance information-limited radiometric DSD retrievals and improve our current climate record of cloud properties.

HARP multi-angle imagery allows for cloud property retrievals across and along the swath and at resolutions narrow enough to tease out correlations in the local microphysics. This result is extended to DSD retrievals at multiple scales (i.e., 600 m) to understand how the retrieval performs relative to HARP sampling and in different regions of the cloud field. These results are validated against similar cloud studies in the literature. To validate this, a simulation of HARP-like sampling characteristics was developed to measure simulated polarized cloudbows produced by a DYCOMS-II LES marine stratocumulus cloud domain. The

information content and quality of HARP cloud retrievals from LMOS not only agree with literature studies and LES simulated-polarization fields, but also show that HARP is sensitive to a predicted range of CDR (Miller et al. 2018).

This work concludes that the HARP concept (1) meets community accuracy requirements for modern climate science, (2) provides an unprecedented dataset for new cloud retrieval science, and (3) is a compelling example of high science quality and potential at a low taxpayer burden. Chapter 5 summarizes this work and looks ahead to future applications of HARP data, including the upcoming NASA PACE mission, extensions of the instrument design into the SWIR for drizzle mode sensitivity, cross-validation of cloud products with SPEXone, and multi-spectral retrievals of cloud DSD properties. This work is the foundation that positions the HARP instrument is an accurate, attractive, and economical MAIP that can meet current and future needs of climate science and Earth observation.

Chapter 2: The Hyper-Angular Rainbow Polarimeter

The AirHARP concept, and the HARP family of polarimeters in general, was developed with a wide swath, fine angular resolution, and high polarization accuracy to address some of the limitations of modern polarimeters. This chapter will discuss the design and rationale for the HARP relative to the needs of the climate community.

Section 1: General concept

The HARP concept was designed and developed at the University of Maryland Baltimore County (UMBC) in Baltimore, MD by the Earth and Space Institute (ESI), led by principal investigator Dr. J. Vanderlei Martins. It was proposed to NASA as a technology demonstration of new instrumentation to advance remote sensing and our understanding of the Earth's atmosphere. The NASA Earth Science and Technology Office (ESTO) funded the HARP proposal through an In-Space Validation of Earth Science Technologies (InVEST) grant in 2014. The two instruments described in this work, AirHARP and HARP CubeSat, were developed over the next five years by UMBC faculty, students, and external subcontractors. The Space Dynamics Laboratory (SDL) in Logan, Utah, USA, continues to provide flight and engineering support to the HARP CubeSat mission.

Subsection 1.1: Optical design

The HARP instrument observes the Earth with a wide field-of-view aspherical front lens. This lens projects view angles on the ground that range from ±57° along-track and ±47° cross-track relative to nadir. This correlates to a ~1000 km ground swath in a single image from ISS altitude of 400 km. A physical baffle on the front lens helps to limit stray light on the detector focal plane array (FPA) and defines the edges of the active science area. Even so,

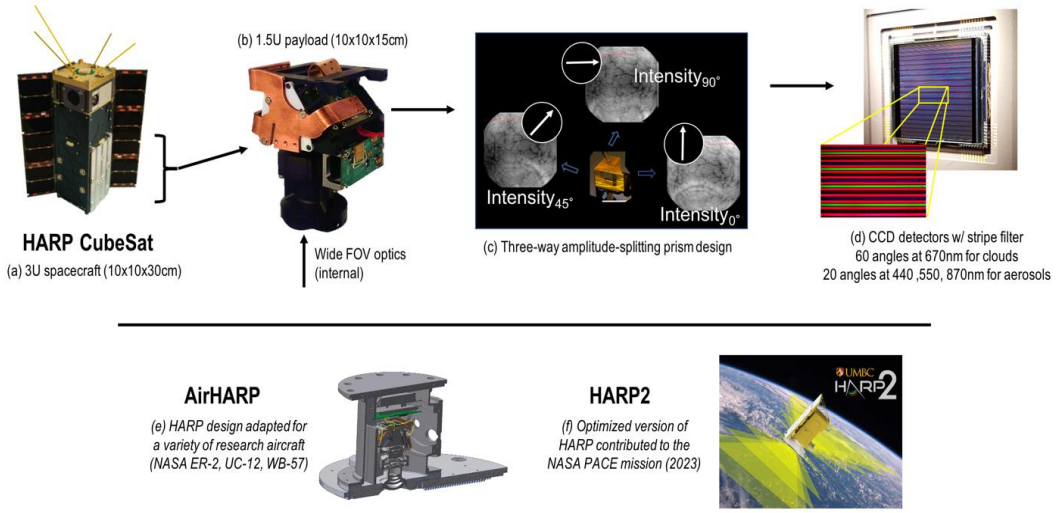

*Figure 6***.** Description of the HARP instruments: HARP CubeSat, AirHARP, and HARP2. The size (a), payload (b), polarization properties (c), and wavelength selection (d) are compatible between the three instruments. AirHARP (e) is sub-orbital only and HARP2 (f) will launch as part of NASA PACE spacecraft in 2023. Image credits: UMBC/ESI.

active science pixels can reach view zenith angles up to 64°. The front lens has a notable pin-cushion distortion, which grows a ground target by a factor of 3.3 in the furthest forward or aft directions relative to nadir. The differential resolution across the detector is accounted for in the design by a custom spectral filter on the detector, on-board binning schemes in the case of HARP CubeSat, and in post-processing. With this wide FOV, a spaceborne polar-orbiting HARP can achieve global coverage in two days, which is the current standard for globally resolved and climate-relevant measurements (McBride et al. 2020, Puthukkudy et al. 2020).

The HARP concept, shown in Figure 6, is an amplitude-splitting polarimeter. These instruments use a glass interface to cut a light beam into two or more components. These beams are separately and simultaneously measured by a detector along each light path, which is shown in Figure 8. In HARP, this is done by three individual FPAs. These images are later recombined to recover the properties of the original beam. The beamsplitter in the HARP design is a modified Phillips prism (Figure 6c). These are typically chromatic beamsplitters that are made of smaller triangular and trapezoidal prisms. In HARP, the Phillips prism splits the *polarization state* of the incident beam, not color. Custom thin-film coatings at the interface

between prism elements help to balance the spectral and radiometric content of the reflected and transmitted beams. These elements are also designed with acute angles to minimize internal polarization. This prism ensures that all light passing through the system encounters an even number of reflections, too. Therefore, an image taken by any detector is spatially identical to the others and upright on the FPA.

The three charge-coupled device (CCD) detectors in HARP (Figure 6d) are commercial sensors. Each pixel in the silicon FPA has a microlens to focus electrons onto the photovoltaic surface. The detector has a negligible dark current at operational exposure times (3 e-/s) and is broadly efficient in the HARP visible-to-near-infrared (VNIR) range. Each of the 4 million pixels have a 0.055 degree instantaneous FOV, which translates to a 400 m nadir ground resolution from a 400 km altitude. This ground resolution scales linearly with altitude, as well. AirHARP on-board the NASA ER-2, which flies at 20 km, had a 20 m nadir resolution and the upcoming HARP2 on NASA PACE will observe the Earth at 700 m nadir resolution. Compared to the last spaceborne polarimeter, POLDER-3, HARP2 may resolve Earth targets by a factor of 8 or more. This is particularly notable for the cloud droplet size distribution retrievals discussed in Chapter 4.

The CCD detectors cannot natively measure the polarization state (Q and U) of a target. They can measure polarization if that information is somehow encoded into the intensity signal that reaches the detector. In HARP, the prism ensures that the radiation at the detector represents a single polarization state, even though the detector itself cannot measure the actual electric field orientation. By combining the data from the three detectors, we can reproduce the Stokes vector of the incident beam. The mathematical treatment of this is given in Borda et al. (2009) and detailed further in Chapter 3. This prism allows for wide-FOV polarization measurements inside a compact CubeSat housing (10x10x30cm, Figure 6a), though the actual instrument is half that size (10x10x15cm, Figure 6b).

A linear sheet polarizer in front of each detector helps boost the polarization efficiency of the light path. These polarizers are offset by 45-degrees relative to one another to maximize the discrimination between polarization states (Tyo et al. 2006, Schott 2009). Other instruments, POLDER-3 for example, used an optimal 60° separation between polarization angles. However, these designs tend to use simpler optical assemblies and moving parts, such as filter wheels (Deschamps et al. 1994). 45-degree separations minimize retardances and circular polarization generated by this custom prism and splitting coatings. Therefore, the 45-degree separation reduces the degrees of freedom in the design and calibration. The polarizers on HARP are commercially available and chosen specifically for high contrast and comparable efficiency over a broad visible and near-IR spectrum.

Subsection 1.2: Wavelength selection

HARP measures wide-FOV polarization in four spectral channels: 440 (15), 550 (12), 670 (18), and 870 (39) nanometers (nm). The bandwidths are given in parentheses next to the nominal center wavelength of each band. The measured values to three significant digits are given in Chapter 3. A custom stripe filter on the detector assigns specific pixel rows in the FPA to the four channels. The rows that correspond to a single channel are, together, called a *view sector*. There are 120 view sectors distributed in a regular, along-track pattern across the filter, shown in Figure 6d. The 670 nm band corresponds to 60 of them and justify HARP as "hyper-angular". The other three channels have 20 each. Each 670 nm view sector is separated from the next by approximately 2° in view zenith angle (VZA), and the other channels have a 6° separation. These view sectors are largest at nadir and taper in the along-track direction to account for the barrel distortion of the front lens. Depending on how we bin cross-track pixels (i.e., binning aggressively at nadir and minimally far forward and aft), we can maintain a similar ground resolution across the entire sensor.

The four spectral channels of HARP were chosen for compatibility with current space sensors (i.e., MODIS, MISR, VIIRS, ABI) and the phenomena suited to those bands (Puthukuudy et al. 2022, IAC). Figure 7 shows the HARP spectral response function against MODIS, VIIRS, and several other compatible space radiometers. The 440 nm region is sensitive to chlorophyll concentration, molecular scattering, and aerosol sensitivity, 550 nm is the peak of the solar spectrum and useful in ocean color studies, 670 nm was chosen specifically for polarized cloudbow measurements with minimal Rayleigh contamination, and 870 nm is particularly useful for aerosol and vegetation studies alongside 670 nm. All bands are expected to be used in multiple ways over a variety of targets, and in vicarious and intercalibration studies. The multi-angle, polarized sampling in each channel increases the information content relative to traditional, single-wavelength, single angle measurements (Knobel-

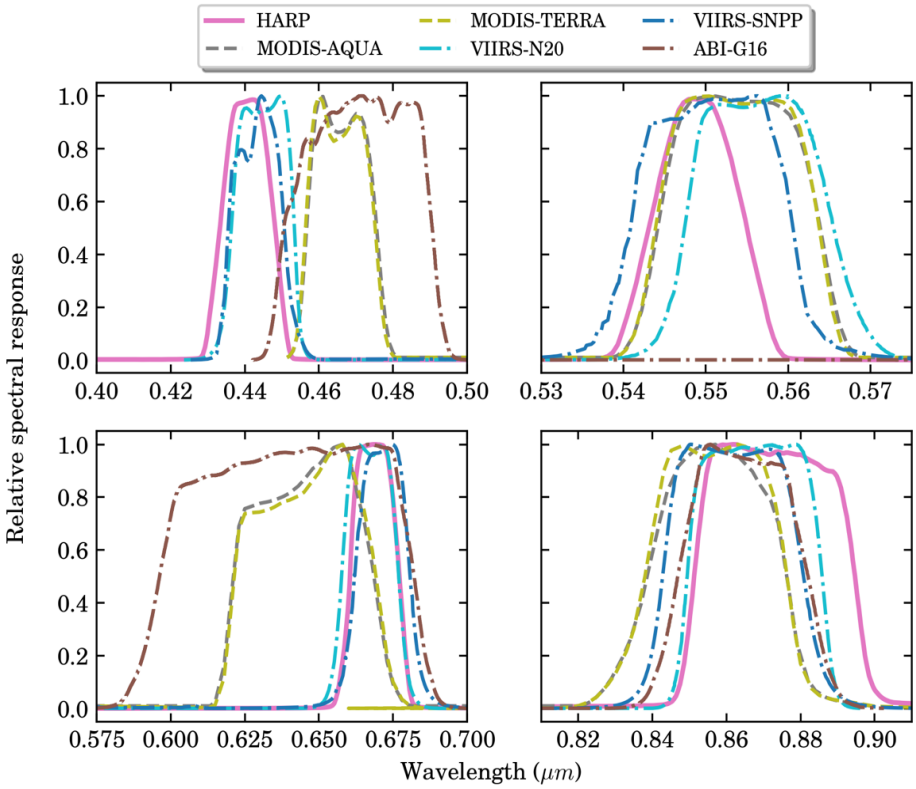

Figure 7. Comparison of the four HARP spectral response functions (pink) with compatible space radiometers. The HARP SRF is shown for 440 (upper left), 550 (upper right), 670 (lower left), and 870 nm (lower right) spectral regions. Image provided by A. Puthukuddy, UMBC/ESI.

spiesse et al. 2012, 2018).

The stripe filter spectral response function (SRF) is broad in all four bands for flexibility in the design of the prism splitting coatings and overall system SRF. The 870 nm band was specially constructed to avoid strong water vapor absorption lines around 750nm and 905nm. A neutral density multi-bandpass filter, located further into the optical assembly, is much narrower in each channel and defines the HARP SRF. The combination of both of these filters are shown in Figure 7 for each HARP spectral band (pink curves). Details on SRF characterization are in Chapter 3.

Finally, we can downsample the detector as needed using *linetables* that screen out certain view sectors and wavelengths. Depending on the flight altitude, flight speed, and data storage capacity on-board, we may decide to save a subset of view sectors instead of the entire full-size, full-resolution image. A smaller image size also allows for longer and/or more Earth scene captures in a single campaign flight. More images per live capture correlates to a larger overlap region between all 120 pushbrooms when they are all mutually gridded, and therefore more science potential. The HARP CubeSat has four different standard compression schemes, which are much more aggressive due to the limited downlink capacity from space (5 Mbps during a 15-minute window over the ground station). The AirHARP data was also compressed during field campaigns, but modifications could be done in real-time and had expanded data storage for images. Regardless, no compression scheme for any HARP instrument sacrificed any less than 60 views at 670 nm for clouds and nine views at the other three bands for aerosol coverage. Several studies in the literature suggest that five views on an aerosol target is optimal for microphysical retrievals (Hasekamp and Landgraf 2007, Wu et al. 2015). Hyper-angular cloud sampling is critical for droplet size distribution retrievals (McBride et al. 2020, Alexandrov et al. 2016, Miller et al. 2018). The hyper-angular 670 nm band is also useful for aerosol retrievals and intercomparison studies (Puthukuddy et al. 2020, Gao et al. 2021).

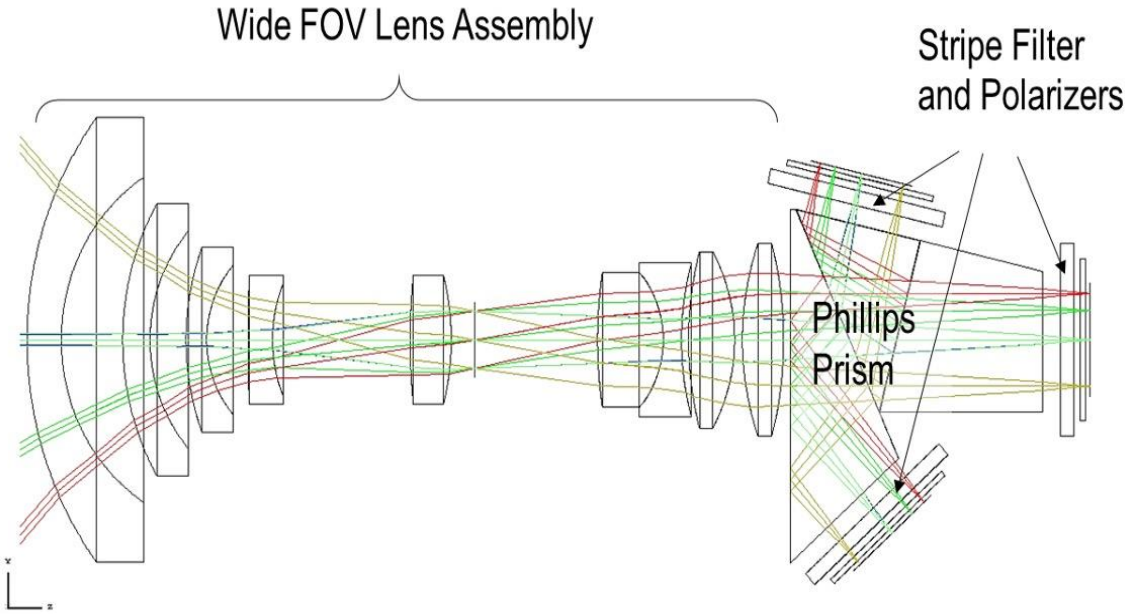

Figure 8. Simplified Zemax model of the HARP CubeSat optical train**.** The front lens and the following eight elements create a light path that is telecentric in the image space. The beam enters the Phillips prism at 0° AOI and maintains this collimation all the way to the detector FPA.

Section 2: Significance of the HARP design for Earth science

Altogether, the HARP instrument is one of the most comprehensive Earth-observing instruments to date. The instrument measures 3 polarization states, in 4 spectral channels, across 120 different viewing angles, and 3 detectors, and does so within a tiny 10x10x15cm housing. There are three

major advancements in the design of HARP, beyond these mentioned, that make it an attractive concept for future space missions.

First, HARP measures polarization accurately without any moving parts. In space, moving parts introduce risk of failure or degraded performance. For example, the solar diffuser door on MODIS Terra failed open in 2003 (Erives et al. 2004). This door was designed to be opened during solar calibrations and closed during science mode. Since the failure, the performance of several of the reflective solar bands (RSB), especially the 412, 443, 470, and

490 nm channels, have degraded faster than expected (Aldoretta et al. 2020). Most of the RSBs now require an aggressive calibration, including new vicarious techniques and polarization correction (Twedt et al. 2021). These issues may translate to extensive and exhaustive work on the part of science and calibration teams, reduced data accuracy/reliability, and a larger taxpayer burden. This was a major consideration when designing the HARP concept. Moving parts can also affect the accuracy of science products during nominal operation. POLDER-3 is a classic example, as discussed in Chapter 1. POLDER-3's polarization accuracy of 1% over ocean and 2% over land is, in part, due to "false polarizations" created by the temporal misregistration of the polarizing filters (Kokhanovsky and Leeuw 2009). Imaging instruments with no moving parts, like HARP, demonstrate polarization uncertainties at or lower than 0.5% and may aggregate pixels to reduce this further (McBride et al. 2022). Other modern polarimeters with moving parts related to the polarization measurement, such as the Research Scanning Polarimeter (Cairns et al. 1999) and AirMSPI (Diner et al. 2013), have other advancements to sampling or accuracy that improve upon the POLDER-3 design in their own way.

Second, the HARP optical assembly is telecentric in the image space. The chief rays that pass through the front lens all the way to the FPA arrive at the detector at 0º angle-of-incidence. This property holds for any target imaged at least three meters away from the front lens. Any target beyond this point is considered "in the infinite" and is in-focus on the FPA. This also means that spatially homogeneous targets, like integrating spheres, can be used to map the internal optical performance of the instrument, with no focus- or AOI-related artifacts in the images.

Telecentricity also simplifies our calibration from space, aircraft, or in the lab. Gain coefficients can be derived at any location in the FOV and spread to all others using the detector flatfields alone. In the lab, these coefficients may be derived in a convenient area, such as nadir or along the optical axis. In space, we can use a mixture of vector radiative transfer

(VRT) modeling and measurements to re-derive these coefficients wherever a target appears in the FOV (Puthukuddy et al. 2022). This design removes the need for complex calibrators or moving parts. Therefore, our calibration coefficients can be maintained and updated using a variety of sources, targets, and dynamic ranges over the lifetime of a mission and regardless of how degraded certain areas of the sensor are.

Finally, the HARP mission is an example of high science quality at a low taxpayer burden. One of the largest considerations when developing any space mission is the overall cost. This may cover support personnel, procurement, quality assurance, launch, post-launch maintenance and science, and incidentals. Small satellite missions like HARP can offset some of these expenses by opting for commercial or off-the-shelf detectors, filters, polarizers, or other materials. Development costs can be further reduced by designing and assembling the instrument with external sub-contractors and employing students for major engineering and science support. This work and others, including McBride et al. (2020) and Puthukuddy et al. (2020), show that the AirHARP instrument can match and, at times, exceed the capabilities of current space instruments. AirHARP and HARP CubeSat missions, including assembly, field campaigns, data processing, launch, and science output were both achieved under six million USD. Also, the small CubeSat size and low cost lends well to constellations of CubeSats. These can expand the spatial and temporal measurement coverage and overall sampling statistics over different Earth targets.

By comparison, larger space missions with larger procurements, federal oversight, and support personnel can cost upwards of 1 billion USD per mission. The current estimated budget of the NASA PACE mission is 805 million (Bontempi et al. 2022). Despite a high cost, legacy missions such as Aqua (952 million USD, NASA 2004), Aura (752 million USD, NASA 2005), and OCO-2 (467 million USD, NASA 2014) continue to produce an unparalleled, confident, and continuing climate record. However, these missions put such an impact on our federal budget that they are sometimes considered by name by Congress during yearly

negotiations with the President (Anderson 2017, in the case of NASA PACE). Given the NASA budget as remained relatively constant over the past five years (within 0.5%, NASA 2021), a more aggressive balance of mission cost and science impact can be socio-economically attractive. HARP-like smallsats may offer comparable science quality to current platforms, and while they typically last few years in space, they may be used as high-reward demonstrations of new technology, especially when funding is limited.

Section 3: HARP sampling and measurement

HARP is a pushbroom imager. As the instrument flies over a target, HARP takes sequential images at two frames per second. Along with our compression scheme, this ensures that the same view sector from image A overlaps slightly with same view sector in the next image B. Therefore, a continuous pushbroom is created for this single view sector as HARP takes data. Because the HARP detector contains 120 view sectors, 120 unique pushbrooms are generated per detector per continuous live capture.

Figures 19a-d show an example of an AirHARP live data capture over Milwaulkee, Wisconsin during the NASA LMOS field campaign in June 2017. The full-size, full-resolution AirHARP image (far top left, Figure 9a) shows horizontal lines across the detector. These are the boundaries of the view sectors. An elliptical darkness on the outer edge of the image comes from a physical mask over the front lens that shields the detector from stray light and non-science content. A cartoon aircraft is positioned at nadir. Four red lines on this image represent the four respective view sectors shown on the right (nadir VZA and channel given in the titles). As these images are taken, these four view sectors take data, and each new image adds a new row of data to the long form imagery to the right. At the end of the data capture, each view sector produces a continuous pushbroom of the ground scene. The final step is not shown here, but all the pushbrooms are adjusted to fit a common lat-lon grid. After geo-registration, any mutual target to all or a subset of the pushbrooms has a multi-angle scattering profile in reflectance and polarization.

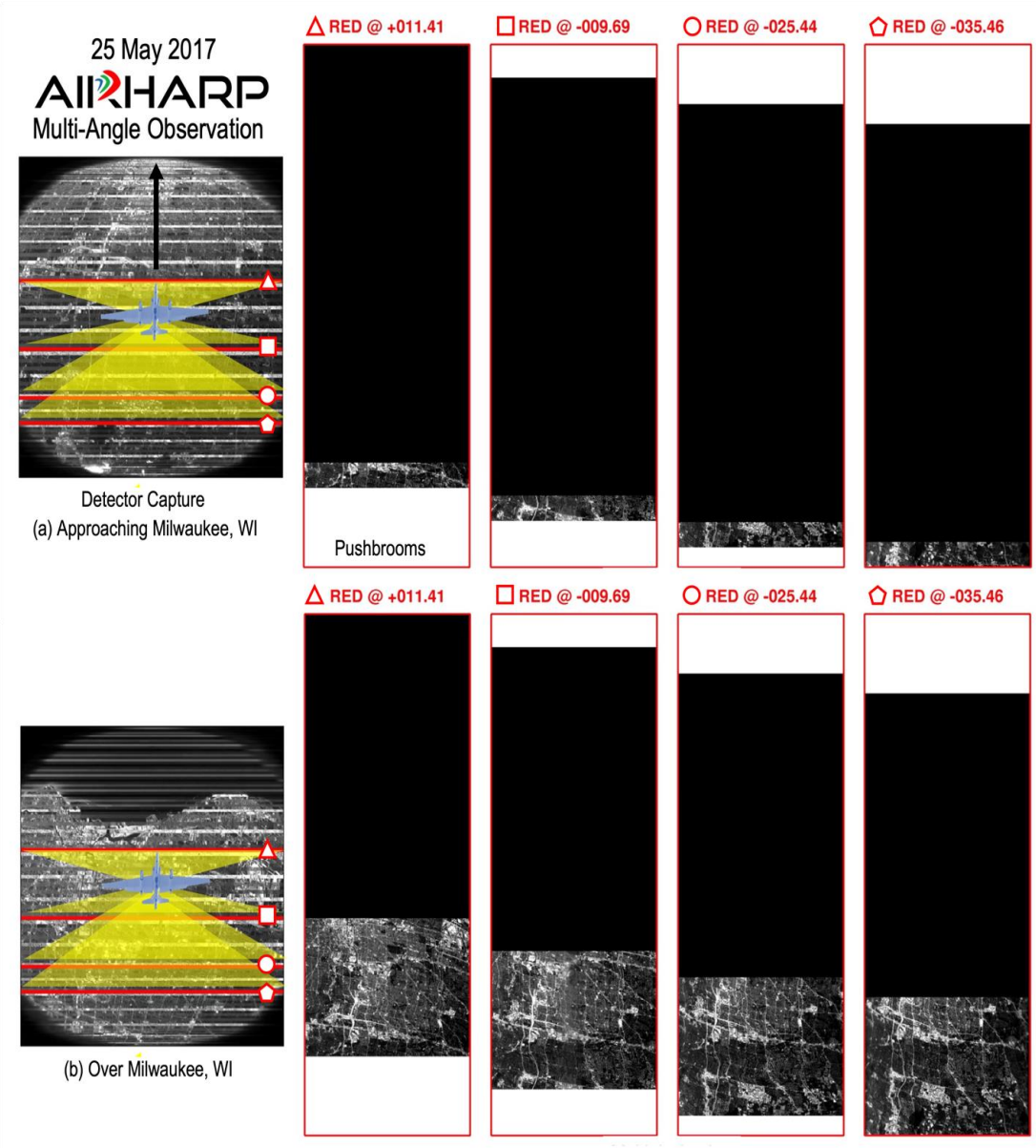

Figure 9a-b. Time-lapse of an AirHARP live capture during NASA LMOS on May 25, 2017. The left-most image is a full-size, full-resolution detector capture. The airplane is at nadir, the instrument is flying in the direction of the black arrow, and the horizontal lines on the image are view sectors. Each view sector corresponds to a spectral channel and specific set of along- and cross-track views. The four view sectors highlighted in red correspond to nadir VZA of +11.41 (triangle), -9.69 (square), -25.44 (circle), and -35.46 degrees (pentagon). As the instrument flies, pushbrooms are made by each of these view sectors (long-form images). The data capture is just starting in (a), but a substantial pushbroom has built up as the instrument flies over Milwaulkee, WI (b).

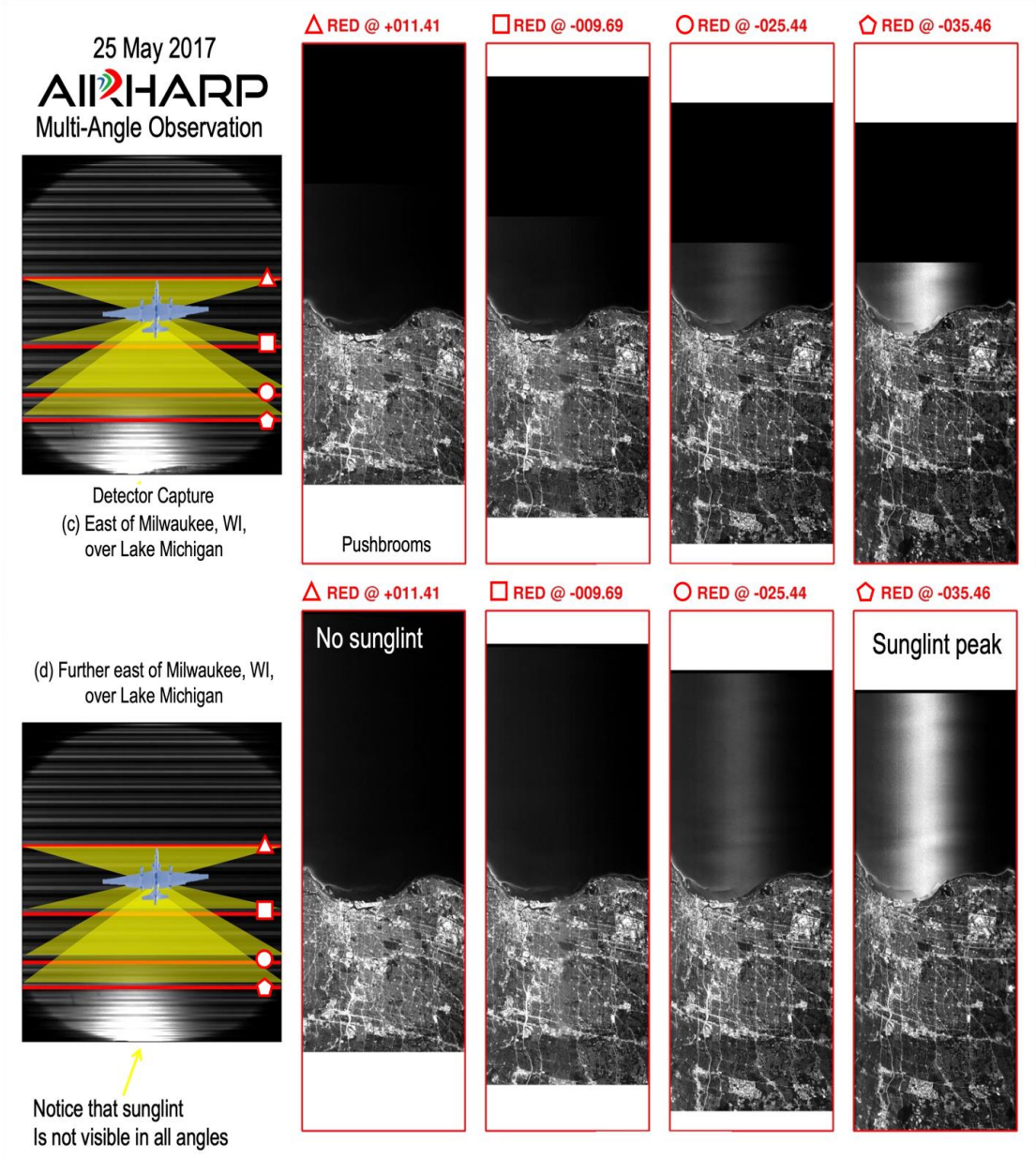

Figure 9c-d. A continuation of the AirHARP live capture timelapse from Figure 9a-b. As the instrument flies over Lake Michigan in (c), the angular signal of sunglint appears at specific angles. Later in the same flight, shown in (d), the difference in information content between the view sectors is clear. Note that in the detector raw capture, sunglint only appears at the base of the image. This corresponds to the large bright band that we see in the 35.46 degree view sector, which is located in that area of the detector. In post-processing, these pushbrooms are geo-registered to the same lat-lon grid. Therefore, any pixel in common to the pushbrooms contains a multi-angle signal from that target.

Figure 9d shows how much information is contained in multiple views. Note that Lake Michigan is dark in the forwardmost view sector (second from left), but as we transition to nadir and in the aft directions of the sensor (moving right across the pushbrooms), the lake becomes brighter. This is the signal from sunglint scattering off the lake at different angles. Whisk-broom instruments like MODIS and VIIRS can make one of these long-form images only, per overpass. The added information from the many HARP views can provide closure and context in retrievals, models, and intercomparisons with other instruments

A target, either on the ground or in the atmosphere, may be viewed from a subset of the 120 view sectors with its reflected apparent *I*, *Q*, and *U* measured in each view sector and wavelength. From these measurements, the polarized reflectance as a function of scattering angle can be compared with theoretical radiative transfer or modeled calculations to retrieve atmospheric parameters. Note that because AirHARP is an imager, each pixel in the image is a potential target viewed by multiple angles. Therefore, each pixel in the image will produce its own polarized reflectance and may be used in a retrieval. If a large number of pixels in the image are viewed at the requisite geometry, then a spatial map can be made of microphysical or surface parameters. Depending on the observation altitude and binning scheme, less than 0.2 km retrieval resolutions are possible. For example, the microphysics of individual fair-weather cumulus clouds can be retrieved across a cloud field stretching tens to hundreds of kilometers. This capability is unprecedented for any existing multi-angle polarimeter instrument. Details on this retrieval and its implications are given in Chapter 4.

Section 4: AirHARP, HARP CubeSat, HARP2, and beyond

The HARP instruments are currently active, and the HARP science team is soliciting future campaigns, as well. The AirHARP instrument was flown on two NASA campaigns in 2017: the Lake Michigan Ozone Study (LMOS) in the summer and the Aerosol Characterization from Polarimeter and Lidar (ACEPOL) in the fall. As of this writing, data from

ACEPOL is publicly available with an accompanying data quality statement and user guide (NASA LARC Data Archive 2022). Datasets from NASA LMOS were used internally for engineering and calibration but have not been processed through L1B. AirHARP is the centerpiece of this work. The calibration and validation of the instrument is discussed in Chapter 3 and the first polarized cloud retrievals from LMOS are explored in Chapter 4. Because AirHARP is the similar in design to HARP CubeSat and comparable to HARP2, the calibration and science framework developed here is compatible with all three instruments and their data.

The HARP CubeSat satellite was launched on November 2, 2019, to the International Space Station (ISS) on a Space-X Dragon re-supply mission. Astronauts deployed HARP into orbit, from the Nanoracks pod in the ISS, in February 2020. HARP was expected to see a 6-month to 1-year mission life, but HARP was released from the ISS at a high-point in the orbit (~420km) and will have a longer mission life than expected. However, the launch was not graceful, the instrument spent its first moments in orbit in an uncontrolled wobble. HARP successfully communicated with the ground station at Wallops Space Flight Center in Wallops, VA, USA and downlinked a first light capture on April 16, 2020. This capture is shown

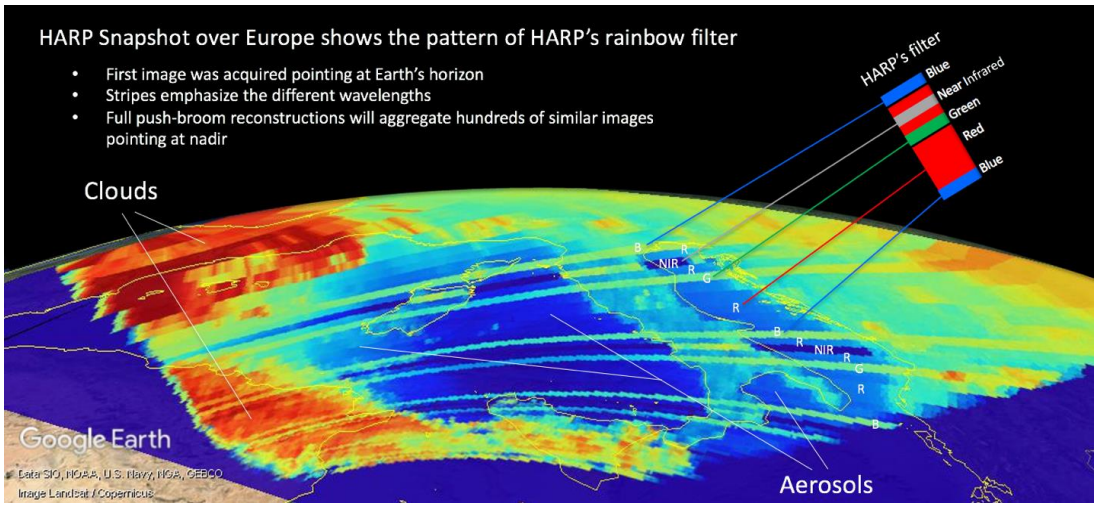

Figure 10. Press kit distribution of HARP CubeSat's first light image over southern Europe. The Italian mainland and Cyprus shown bright in all wavelengths against the dark Mediterranean Sea, which helped geolocate this rare limb view. This figure is reprinted from https://esi.umbc.edu.

in Figure 10. It was a limb view over southern Europe, and the difference in the spectral response of land, ocean, clouds, and the atmosphere helped us to geolocate these images. In the days following, the 3-axis stabilization on the spacecraft helped to orient the front lens nadir.

As science data started to come in, the HARP science team built a simulator to track co-incident overpasses with other satellites (N. Sienkiewicz, private communication) and prioritized targets of opportunity in the data captures (i.e. large aerosol events, phytoplankton blooms, wide-scale marine stratocumulus, sunglint scenes, desert calibration sites, etc). Planning out the captures minimized risk and optimized the science content, given the limited data storage capacity of the CubeSat. Preliminary vicarious calibrations show acceptable agreement in reflectance between HARP CubeSat, MODIS and VIIRS over common targets (Puthukuddy et al. 2022). The first polarized cloud retrieval from HARP CubeSat was done over the west coast of South America at ~9 km resolution (see Figure 26 in Chapter 4) and is the first space demonstration of this science at sub-40km spatial resolutions. As of this writing, HARP CubeSat has taken over 60 individual datasets and is still in space taking Earth data. HARP CubeSat data is still undergoing quality assurance and limited L1B data is available upon request.

A third HARP concept, HARP2, is currently under development for the NASA PACE mission to launch in 2023 (see Figure 11a). HARP2 is larger than HARP CubeSat (~10kg) and has a large baffle fixed around the front lens to minimize stray and tangential light from the sun when the PACE spacecraft is flying over the poles of the Earth. Unlike HARP CubeSat, HARP2 will be bolted to the side of the PACE spacecraft. HARP2 will be constantly co-incident with the other two instruments, the Ocean Color Instrument (OCI), a hyper-spectral radiometric imager, and SPEXone, a hyper-spectral multi-angle polarimeter smallsat. During the dark side of the orbit, HARP2 will offload data to on-board storage on the spacecraft and will return to real-time data captures about 11° before the Earth's terminator. This allows HARP2 to take real-time, full-orbit data that does not require the same pre-

planning as the HARP CubeSat. The PACE mission is a polar-orbiting, sun-synchronous 676 km mission, which means that the HARP2 wide FOV will produce two-day global coverage with a minimum nadir spatial resolution of ~700 m.

Another major difference between HARP2 and HARP CubeSat is on-orbit calibration. Planned HARP2 calibration events are shown in Figure 11b, from the perspective of the detector. HARP2 will join OCI during scheduled solar calibrations. HARP2 will get a limited custom maneuver to get the sun into the corner of the detector during these events (Figure 11b lower right). An on-board solar diffuser will actuate and spread sunlight to all FOVs. HARP2 will view the sun on a weekly basis during commissioning, then monthly for trending exercises. During the OCI lunar slews, HARP2 will also perform lunar calibrations. The moon will appear in the HARP2 FOV at 10x10 pixel square (0.5° size in the sky) over 9 minutes, entering and exiting out the same corner. OCI and HARP2 will be co-incident over Earth targets at the ± 20° VZA in the HARP FPA and SPEXone along the nadir track, with a mutual swath of 7° VZA. This will allow HARP2 and SPEXone to "remove" the highly polarized atmosphere from the OCI ocean measurements. Constant co-incidence will also lead to interesting synergy and inter-calibration between the three instruments. HARP2 is currently being assembled and calibrated at the UMBC ESI facilities in Baltimore, MD.

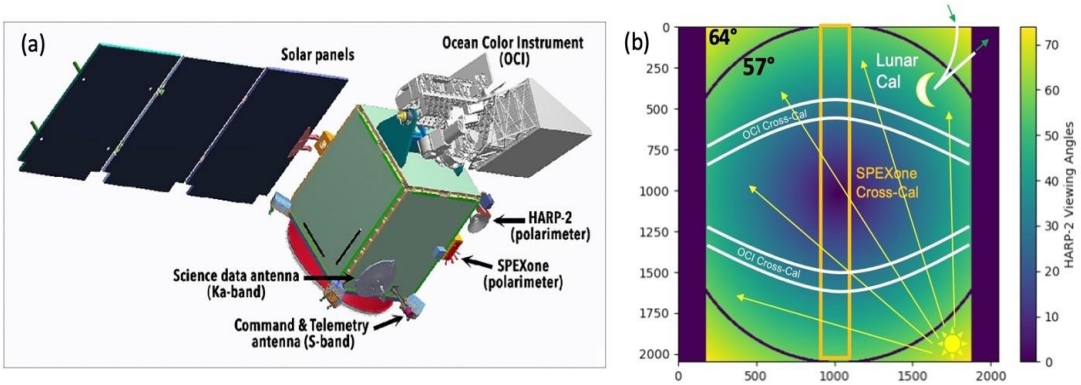

Figure 11. Schematic of the NASA PACE spacecraft (a) and a cross- and vicarious calibration plan outlined from the perspective of the HARP2 detector. In (a), note the small size of HARP2 relative to OCI and the OCI Earth shield (large triangular object). In (b), note the locations of the lunar calibration (upper right), solar calibration (lower right), and cross-calibration opportunities with SPEXone and OCI. Image (a) adapted from NASA PACE (https://pace.oceansciences.org). Modifications: image label.

The HARP concept is larger than AirHARP, HARP CubeSat, and HARP2, however. Hyper-angular sampling could be extended to the ultraviolet, for stronger atmospheric correction and aerosol retrievals, or further into the shortwave infrared, for enhanced thermodynamic phase and cloud retrievals, water vapor, or snow characterizations. Adding several HARP cameras to the same payload, or developing a constellation of HARPs, would increase the effective FOV and spectral range, polarization capability, and global coverage in a "single observation". Several HARP-like designs are currently in development for enhanced standalone or multi-satellite missions. Some of these future applications are discussed in Chapter 5.

Chapter 3: Pre-launch calibration and validation of Hyper-Angular Rainbow Polarimeter (HARP) measurements

This chapter will detail the engineering development of the HARP instrument, an efficient calibration technique demonstrated in the lab and field, an error assessment, and discussion of limitations in the design of AirHARP specifically. The results shown here demonstrate that the HARP calibration is adaptable for lab, field, and potential space applications. The performance of the HARP (and future HARP-like designs) is demonstrated to meet the 0.5% DOLP requirement for modern aerosol property retrievals (NASA 2015, NASA 2021).

The results and discussion in this section refer to the AirHARP instrument, unless otherwise noted, though the general calibration pipeline and instrument design is valid for all HARP-like designs. In some cases, HARP CubeSat data is shown instead of AirHARP for variety when the results are comparable or when a particular difference between the two instruments is important to emphasize.

Section 1: Description of the system light path

In this section, we will first discuss the optical design of the HARP concept and how it helps define the calibration theory in later sections. The core of the HARP design, shared by both AirHARP, HARP CubeSat, and HARP2, is a custom Phillips prism beamsplitter, shown in Figure 12. This prism is typically designed to split colors, but the AirHARP prism splits the *polarization content* of the original signal into the three AirHARP detectors. The prism is made of three individual glass elements, A, B, and C, of equal index of refraction. The prism is the major component of a telecentric optical train made up of eight other sequential elements and the 114° wide field front lens. Most importantly, this compact, refractive design allows wide-field of view measurements in a 3U CubeSat housing (10x10x30cm).

The modified Phillips prism alters each detector's light path in a specific way. The incident beam enters the prism at the front face of Element A and meets the boundary be-

tween Elements A and C. Here, a custom splitting coating reflects 33% of the incident light back into Element A. Reflections like this reduce P-polarization and preserve S-polarization. Transmissions do the reverse. To boost the efficiency of the final polarization measurements, we align the Detector A polarizer with this S-polarization state during assembly. The light path defined by the wide FOV front lens, optical train, the prism, the 0° polarizer, and the Detector A FPA is called *Sensor A.* The convention of our polarimetric calibration is relative to this Sensor, and its polarization angle is defined as 0º. Two other light paths, shown in Figure 12, define *Sensors B* and *C* (with sensor letter matching the prism element).

The light that passes through this coating then meets the Element B-C interface. Another thin-film coating splits the light intensity 50%-in-reflection and 50%-in-transmission. So far, the polarization content of this beam has changed by a transmission through the Element A-C interface and a reflection at the B-C interface. Therefore, the light incident on Detector C is a weak mixture of S- and P-states. The detector polarizer can be set at any angle with minimal impact to polarization efficiency. During optimization testing, we found the best orientation to be 90° for the Detector C polarizer, and likewise 45° for the Detector B polarizer. This 45° relative separation between the polarizers is optimal to discriminate measured states of polarization in our design (Tyo et al. 2006). Sensors B and C each account for 33% of the intensity of the incident beam. Therefore, the AirHARP optics splits the incident light intensity equally among the three Sensors, each Sensor images a spatially identical scene, and each Sensor is sensitive to a different angle of polarized light.

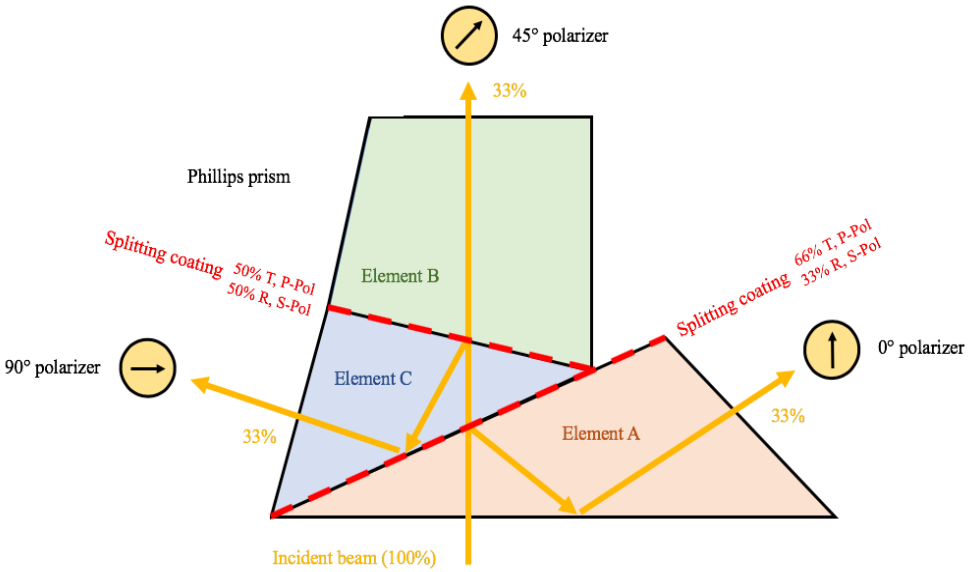

Figure 12. The Phillips prism is made of three elements: A, B, and C. Two splitting coatings split polarization states by transmission (T) and reflection (R). The coatings ensure that each HARP detector sees ~33% of the incident beam. The angle of the detector polarizer boosts the polarization efficiency of the prism along that light path.

Light that passes through the prism and detector polarizer is categorized by a custom interferometric filter. Each detector pixel maps to a specific spectral band, defined by one of the 120 *view sectors* in the filter. These sectors span a range of viewing angles (zenith and azimuth) defined by their reverse ray trace through the front lens. The 440, 550, and 870 nm channels measure at 20 view sectors each with 6° separation, and the 670 nm band measures at 60 view sectors with 2° separation. The design of the filter allows the AirHARP instrument to form a pushbroom of a ground scene in a single view sector by flying over the scene and acquiring images one after the other. This co-located information from multiple view sectors can provide high angular coverage on the Earth targets, clouds, and aerosols (McBride et al. 2020, Hasekamp and Landgraf 2007, Hasekamp et al. 2019, Puthukuddy et al. 2020, Gao et al. 2021), and is useful for atmospheric correction (Frouin et al. 2019). Aerosol and cloud properties retrieved by AirHARP (and future HARP instrument) measurements will complement our existing climate record and advance our understanding of climate change uncertainties, feedbacks, and forcings (Boucher et al. 2013).

The following section will discuss the steps in our calibration of the AirHARP optical train, specifically how we translate detector counts to calibrated, polarized radiances for all pixels in the detector system. We will first step through background correction, flatfielding, and non-linear corrections before detailing the relative polarimetric, spectral, and absolute radiometric calibration. We will end the discussion with lab and field validations of AirHARP calibrated measurements and comment on the application of these results to science products.

Section 2: Calibration pipeline for the HARP instrument

Subsection 2.1: Detector specifications and background correction

The HARP detectors are monochrome CCDs with a 4 megapixel active focal plane array (FPA) (Semiconductor Components Industries 2015). Relevant properties, such as quantum efficiency, read noise, and dark current, are given in Table 3.

Table 3. Specifications of the HARP TruSense KAI-04070 CCD detectors

Specification	Value
Number of Active Pixels	2048x2048
Pixel Size	7.4 x 7.4 µm
Quantum Efficiency (Max R, G, B, Pan)	0.38, 0.42, 0.43, 0.52
RMS Read Noise	12 e^-
Dark Current	3 e^-/s (<0.2 e^- below 20ms)
Operational Integration Time	20 ms (AirHARP), 10 ms (HARP CubeSat)

The typical image taken by HARP detectors are shown in Figure 13a. The detector stripe filter creates the cross-track striping in the images. The far left and right detector pixels are masked, which defines the active science area of the FPA. The pixel values in these areas are compatible with a *dark image*, which is an image taken when the entire FOV is blocked from illumination, shown in Figure 13b.

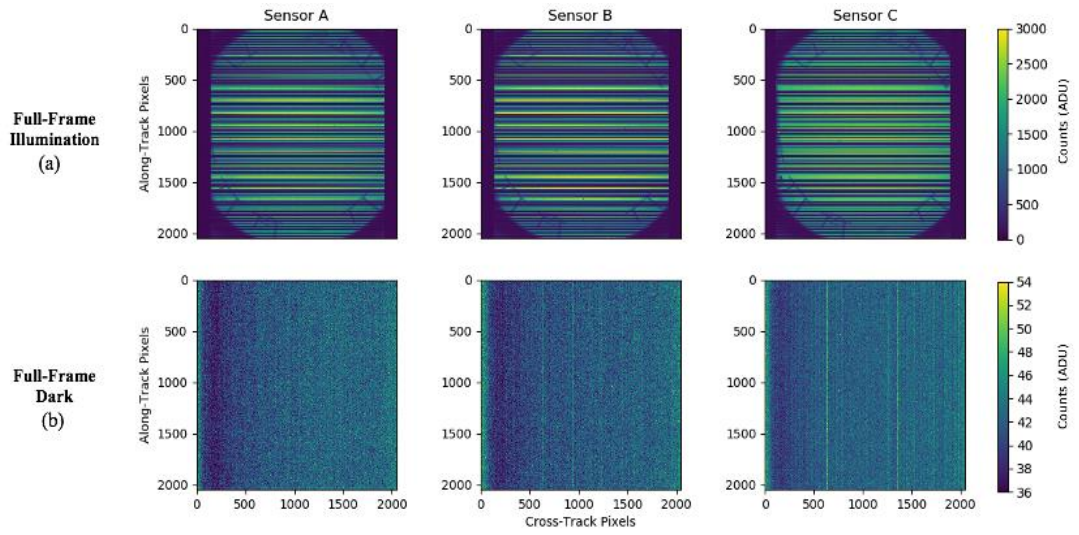

Figure 13. AirHARP captures a full-field raw image in each detector of the aperture of the NASA GSFC "Grande" integrating sphere (a) and a dark capture with the lens cap on (b). The dark shown here can be normalized and used as a template for any live data capture.

The first step in the HARP calibration begins at the detector level. Detectors generate a stable electrical bias across the FPA when they operate. To measure this, we block all illumination from reaching the front lens (i.e. with a lens cap or internal shutter) and take 10 or more sequential images in each detector. These images are averaged together into a *dark template*. Creating a template image in this way is called the *standard process* in this work going forward. The typical distribution of the dark template is given in Figure 13b. The region of lower pixels on the left-hand side of the image is typical of CCDs and occurs as photoelectrons move toward the serial register. A typical dark signal for the HARP detectors is 40 counts when operating at room temperatures. In general, the background correction is as follows:

$$DN_{BC} = DN_{raw} - DN_{dark}, \tag{1}$$

where DN_{BC} is the background corrected image *digital numbers* or counts, DN_{raw} are the raw image counts, and DN_{dark} represents the dark template counts. Whenever the term *raw* is used it refers to any HARP image, whereas subscripts other than *raw* will describe an image captured in a specific environment or counts data processed through a certain step. Furthermore, counts may be called *analog-digital units* (ADU) in this work, when relevant. In sensi-

tivity studies on AirHARP dark image data, the dark counts do not depend on integration time, but are sensitive to operating temperature.

This dark template is normalized by the vignetted area of the detector (cross-track pixel indices 0-200 or 1848-2048). If we cannot take dark captures on-orbit or during field campaigns for any reason, we could create a synthetic dark by scaling the normalized dark template by the measured counts in the vignetted areas of a live data capture:

$$DN_{dark} = \alpha \, DN_{raw\,[0-200,1848-2048]} \quad (2)$$

where DN_{dark} is the estimated dark image counts and α is the normalized dark template image. $DN_{raw\,[0-200,1848-2048]}$ represents pixels in the vignetted area of a raw image capture (Figure 13a). Eq. (2) creates a full-field dark image for each sensor that is used in the following calibration steps and in the Level 1B processing of AirHARP flight imagery. If Eq. (2) is required, i.e. the DN_{dark} here is substituted into Eq. (1). This technique is currently used to correct AirHARP L1B datasets in Version 002 and accounts for the possibility of internal shutter failure on-orbit. In the following sections, we limit our discussion to the 670 nm channel, unless otherwise noted. Similar performance for the other three channels can be found in official ancillary basis documents (NASA LARC Data Archive 2018).

Subsection 2.2: Flatfielding

Next, we characterize the pixel-to-pixel relative response of each detector. Any system with sequential optical elements will vignette photons toward the edge the FPA. Individual pixels may have a relative differential gain, as well. Both effects must be corrected. To account for this, images are taken of a homogenous target in a process is called *flatfielding*. Integrating spheres are typical sources. They create uniform illumination over their aperture. Those with a < 5% port fraction, the ratio of total area covered by portholes to the total sphere surface area, and 10 or more sphere multiplier, a measure of the increase in reflectance due to the

sphere compared to a planar diffuser, are considered suitable (Taylor 2013). Integrating spheres also depolarize the output light to a level below 0.5% in visible wavelengths (McClain et al. 1994). Therefore, any heterogeneity in the images is due to the instrument, not the source. This work uses measurements of the "Grande" 101.6cm NIST-tracable integrating sphere at NASA GSFC for flatfielding and radiometric calibration and a portable LED hemisphere at UMBC for similar calibrations during field campaigns or outside of UMBC. To form the flatfield template, the full-FOV of the AirHARP instrument images the aperture of an illuminated integrating sphere, at an integration time where all channels are below saturation. The images are full-size, full-resolution and resemble Figure 13a. A template image, cre-

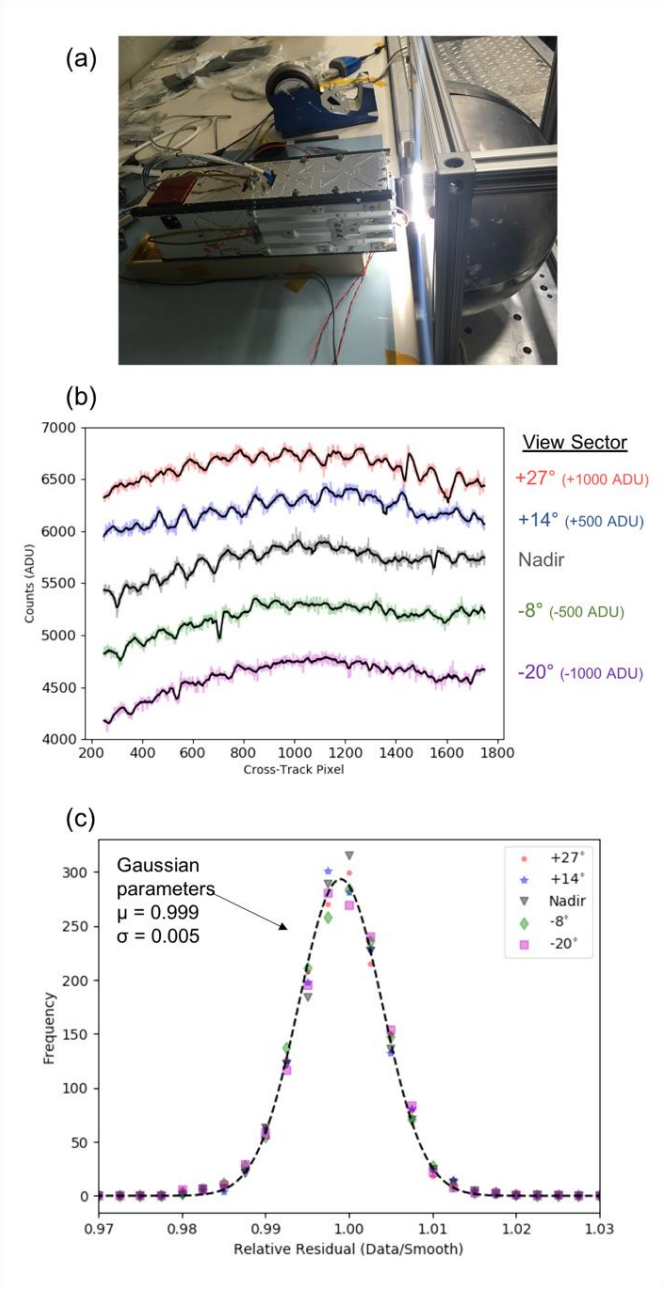

Figure 14. The flatfield is performed by submerging the wide field front lens into the aperture of a stable integrating sphere (HARP CubeSat shown, a). This creates a full-field image like Figure 13a. In (b), the cross-track signal for several detector rows (colored data) is smoothed (black curves). After Eq. (3) is applied, only the SNR remains, which is normally distributed within 0.5% across the FOV. Data shown for AirHARP 670 nm in (b) and (c).

ated using the standard process, is background corrected via Eq. (1) and (2). This template is then interpolated by a smoothing algorithm, row-by-row. This step captures the structure of vignetting and other potential artifacts, such as optical etaloning and defects or hot pixels in the detector (Oxford Instruments 2020).

Figure 14b shows a cross-track line-cut for several 670 nm view sectors: +27º (red), +14º (blue), nadir (grey), -8º (green), and -20º (magenta) are shown. The x-axis is cross-track pixel index, starting with 200 at the image far left and 1800 on image far right. This region represents the active science area of the detector. The y-axis is detector counts (ADU). Each curve is artificially offset by +/- 500 or 1000 ADU for clarity, though the nadir curve corresponds directly to the y-axis values. Without these offsets, each of the curves would overlap with the nadir curve. The counts data for each row is smoothed using a 15-pixel sliding window average (black). The smoothing process also captures other stable artifacts in the images (i.e. oscillations due to optical etaloning). We repeat this smoothing process for each channel and detector row until we arrive at a smoothed full-field template image, at the same size and resolution as the original data. We then normalize the smoothed signal of each channel by the respective pixels in that channel that lie closest to the optical axis of the detector ([y,x] = [1024,1048] for AirHARP). This normalized, smoothed signal becomes the flatfield correction, *f*, for this channel and detector. Normalization is done so that the flatfield is scalable to any reflectance level in a field measurement. Each pixel in the FOV has a different value of *f*, and the optical axis is chosen specifically as the location of $f = 1$ in order to simplify the later steps in the calibration process that also use optical axis pixels. We apply the flatfield correction at the pixel-level:

$$DN_{flat} = \frac{DN_{BC}}{f}, \tag{3}$$

where *f* is the value of the flatfield correction for that pixel, and the numerator of Eq. (3) is the same as Eq. (1). To verify the flat correction, we apply the flatfield to its generating dataset via Eq. (3). Figure 14c shows a histogram of the residuals after flatfielding all pixels in each Figure 14b view sector. The data point colors in Figure 14c map to the same view sector colors in Figure 14b. The original signal is successfully corrected down to signal-to-noise (SNR) variations at the 0.005 level (1-sigma) for each view sector. Figure 14c shows that this method is robust across the FOV and accurately removes all systematic artifacts in the data. On-orbit, the flatfield can be created from solar calibration data (i.e. viewing the sun through a solar diffuser essentially simulates a full-field integrating sphere measurement)/ Other techniques, such as amassing a large amount of Earth scene imagery such that averaging over the randomness of the scenes reveals the overall structure of the flatfield at the detector level, may be used to characterize the flatfield vicariously. This method is currently underway for MODIS L1A calibration for the equivalent response-versus-scan-angle (RVS, K. Twedt, private communication) and was used to characterize the flatfield of the Earth Polychromatic Imaging Camera (EPIC, X. Xu, private communication).

The flatfield serves another critical role in the AirHARP calibration. AirHARP optics are telecentric in the image space, and so all incident rays on the detector arrive at 0° angle-of-incidence (AOI). This design prevents AOI- and focus-related artifacts in Earth view data. Our flatfield represents the entire internal optical behavior of the system and simplifies our next calibration steps in the process. We can derive channel-dependent coefficients at any location in the FPA and spread that result to the rest of the FOV using the detector flatfields. This *telecentric technique* is the method used in the following steps presented here. We also verify these coefficients using lab techniques and across the full FOV using field data in later sections.

Subsection 2.3: Non-linear correction

The AirHARP CCDs may have non-linearities in their analog-to-digital conversion (ADC) by design, that must be corrected. For very bright targets, like sunglint, the Earth's limb, or direct solar exposure, pixels may saturate the detector well. This limit corresponds to 44,000 electrons, or 2^{14} counts (14-bit). Saturated pixels cannot convert any extra photoelectrons to counts and CCDs are known to have non-linear gain coefficients near saturation and potentially at very low light levels (Semiconductor Components Industries 2015). The detectors must have a well-characterized gain for accurate science retrievals and as a baseline for on-orbit trending of calibration coefficients during a space mission.

Non-linearity is characterized by taking images of a stable source at a single illumination level. Each image is taken at a longer integration time than the last, and the testing ends when all sensors and channels are saturated. To perform this test, the AirHARP instrument was placed before the aperture of the NASA GSFC "Grande" sphere. The AirHARP detector integration times are set near 4ms to start. The integration times of each sensor are increased, and images are taken until all three sensors saturate. The stability of the source is

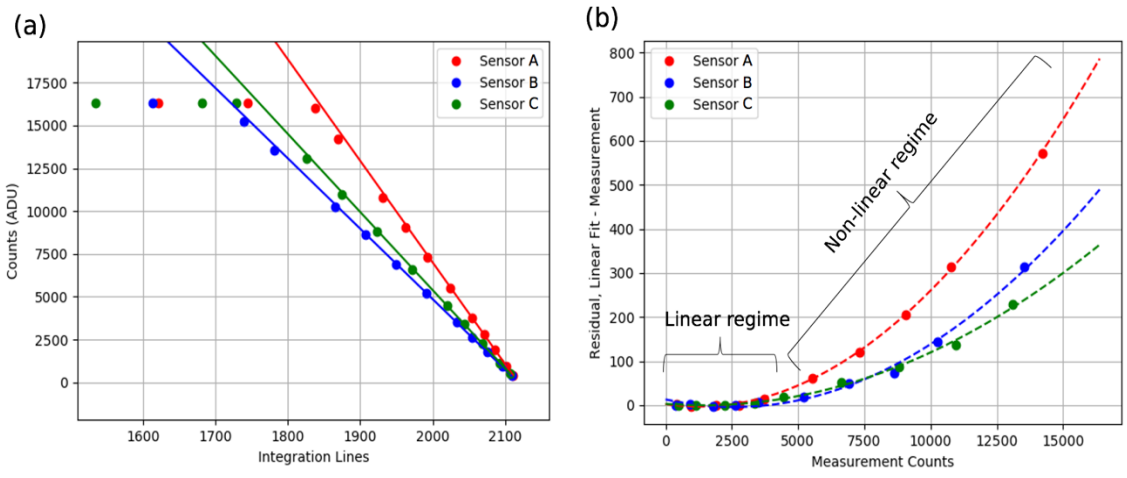

Figure 15. Non-linear correction evaluation for AirHARP 670 nm. AirHARP detector integration time (compatible with "lines") is varied while imaging a stable light source (670 nm channel shown). The counts in the linear regime (<3000 ADU) are fit in (a) for all sensors. This linear fit is compared to the entire dataset, and the residual is fit to a three parameter quadratic (b), which can now correct any raw measurement > 3000 ADU.

tracked over the testing window using a current monitor. The standard process is used, and a template image is made at each integration time and for each detector. We take a small pixel bin (~4x4) along the optical axis in the templates and plot those values against their integration times. This process is performed for each channel and sensor. An example for the 670 nm channel is shown in Figure 15a, for the three AirHARP detectors (Sensor A in red, Sensor B in blue, Sensor C in green). Instead of using integration times, we plot detector counts against *integration lines*, which are the exact exposure settings used by the AirHARP timing board. Integration lines convert to times via 0.237 ms * (2117 – Lines). Larger integration line values correspond to shorter integration times. There is a monotonic, positive relationship between integration lines and detector counts, up until the saturation point, 2^{14} ADU. In this example, Sensor B saturates earlier than Sensors A or C, due to the ratio of integration times between detectors. We then fit all counts in the linear region of the detector, defined by values < 3000 ADU. Note that there is no evidence in the data of low light non-linearity in these detectors. We then compare this fit curve to the rest of the data and form a counts-to-counts correction, shown in:

$$DN_{corr} - DN_{flat} = n_0\, DN_{flat}^2 + n_1 DN_{flat} + n_2, \quad (4)$$

where DN_{corr} is the non-linear corrected counts data, DN_{flat} is the counts data derived from Eq. (3), and fit parameters n_0, n_1, and n_2 are free parameters. Eq. (4) is explicitly separated into two terms for trending of the non-linear coefficients. In our Figure 15b example, the residual ($DN_{corr} - DN_{flat}$) is the y-axis and the x-axis is DN_{flat}. In this example, the maximum non-linear deviation is 4% in Sensor A, found by taking the ratio DN_{corr}/DN_{flat}. This ratio agrees with the 6% non-linearity limit in KAI-04070 detector spec, and similar agreement is found for other channels and sensors. The three above tests occur before any other step in the Level 1B processing pipeline for HARP data. Non-linearity is characterized early in the calibration pipeline to check detector-level anomalies, though other instruments, like

MODIS, can be characterized for non-linearity at the same time as the radiometric gain calibration (Aldoretta et al. 2020). On-orbit, we may be able to use a variety of Earth targets, ADU values, and integration times for each detector to reproduce these curves and regularly update n_x coefficients as needed.

Subsection 2.4: Detector relative alignment

The above calibration exercises are performed for individual detectors, however, the mechanism to produce polarized radiances in AirHARP requires accurate, co-located pointing knowledge between all three in the image space. This means that the detectors need to be mechanically aligned such that an Earth target, like a cloud edge or coastline, appears at the same pixel location in all three detectors.

In the lab, this alignment is verified by comparing images of a mutual, well-lit target and retrieving any new translational and rotational offsets needed to match the image of one detector with another. This process is iterated until all detectors are aligned in the image space to ½ a pixel or less. However, on-orbit, well-defined Earth features can be used to align the detectors. Without proper co-alignment, HARP will produce false polarization spikes when observing small or thin features, like coastlines, cloud edges, and cities. With proper align-

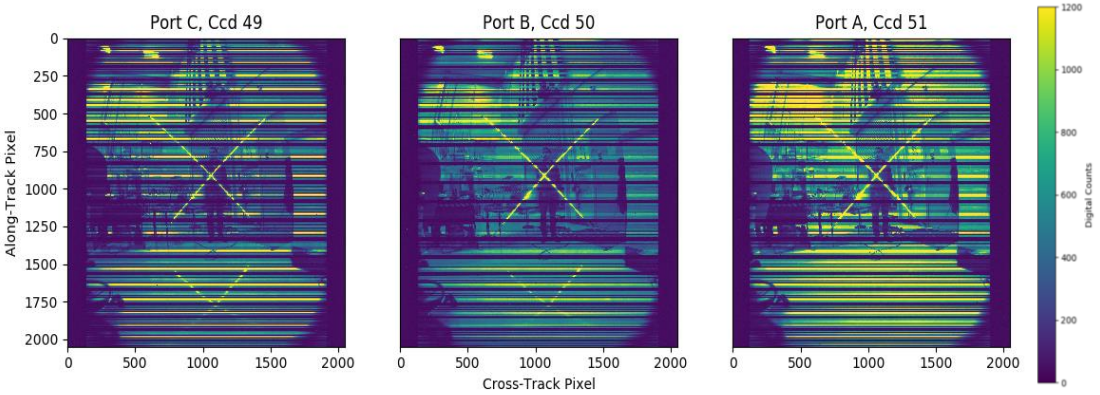

Figure 16. Full-size full-resolution imagery of the LED X from the HARP CubeSat during pre-launch testing at the Space Dynamics Laboratory (Feb. 7 2018).

ment, HARP can maintain DOLP accuracy within the current community recommendation, 0.5% (details in Section 3.1).

Verifying the detector alignment in the lab comes with challenges. The effective focal length of the AirHARP optical train is three meters, and due to the telecentric optics, anything beyond this point is considered “in the infinite” and well-resolved. Therefore, any calibration feature with well-defined edges observed by AirHARP must be at least three meters away and broad enough to cover a significant portion of the wide FOV. Therefore, we developed a large 2-meter diameter “X” of PVC piping and attached strips of white light-emitting diodes (LEDs) along the length of the pylons, shown in Figure 16. The LEDs-in-a-row along each axis of the X created a well-illuminated line of light and the size of the X spanned a broad range of viewing angles in the detector. The AirHARP detectors were set at integration times outside of saturation so that the lines of light were well resolved on the X. It is not necessary to know the spectral character or absolute calibration of these LEDs though, only that they are visible in the AirHARP images and unsaturated.

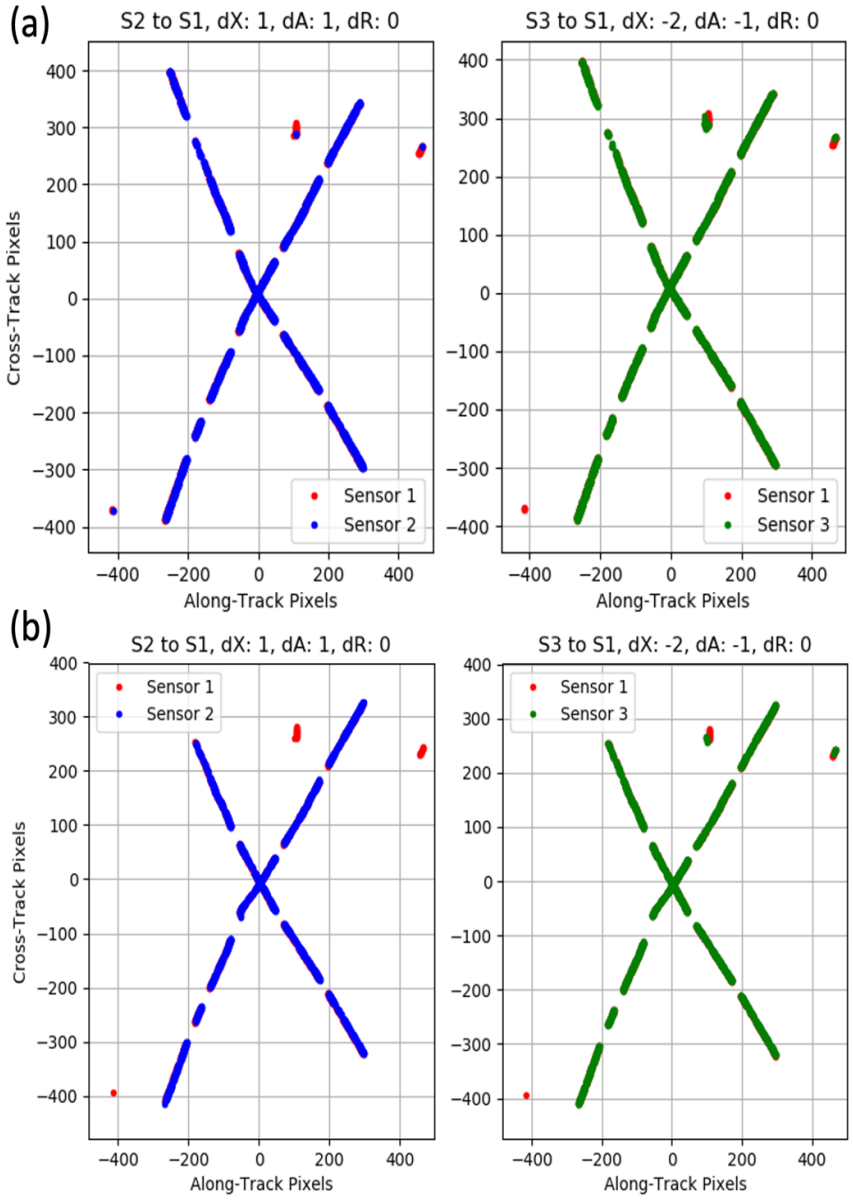

Figure 17. Alignment results from a feature detection algorithm on HARP CubeSat data pre- (a) and post- (b) vibrational testing at SDL in August 2018. Sensor 2 and 3 ADU (blue and green) were thresholded and features of the LED X wer globally compared to Sensor 1 (red). dX and dA refer to cross- and along-track translational offsets and dR to any rotational offsets in pixel units. Negative dX means the first sensor is misregistered by that many pixels to the left of the second sensor. Negative dA means an upward relative offset.

We developed several techniques to correlate the images of the LED X and retrieve the rotational and translational offsets required to synthetically align the images. The simplest was to image process the X in each sensor and run a feature detection routine on the pixel grid, shown in Figure 16. Using Sensor A as a reference, the distribution of lit pixels in the X were compared and offsets were retrieved within ½ of a pixel. This accuracy is comparable to the accuracy of mechanical alignment during assembly. Because HARP CubeSat data required compression before downlink, the image co-alignment was done on-board using offsets derived in pre-launch testing. These values were accurate to the pixel. Larger storage, easier access, and no aggressive image compression meant that co-alignment of the AirHARP detectors could be done at the sub-pixel level in AirHARP L1B image processing, however. Other statistical methods of cross-correlation were tested on lab and field data with comparable results (Barbosa and Martins 2019, private communication). On-orbit, long coastlines or islands, such as Madagascar or the Baja California region of Mexico, could serve the same role as the LED X for detector cross-correlation. Vicarious alignment could be done whenever these targets are observed over the course of the mission.

Subsection 2.5: Relative polarimetric calibration

Subsection 2.5.1: Theoretical description

After the images are corrected and properly aligned, the instrument is ready for quantitative polarization calibration. Here, relative states of polarization are converted to co-located counts in the three detectors and vice versa. The theory of this calibration is given in Borda et al. (2009), though a brief treatment is discussed here. The polarization state of a light beam is described by the Stokes column vector, which is a time-average (designated by the enclosing brackets) of the real and imaginary components of the electric fields (Jackson 1962):

$$S = \begin{bmatrix} I \\ Q \\ U \\ V \end{bmatrix} = \begin{bmatrix} \langle E_{\parallel} E_{\parallel}^{*} + E_{\perp} E_{\perp}^{*} \rangle \\ \langle E_{\parallel} E_{\parallel}^{*} - E_{\perp} E_{\perp}^{*} \rangle \\ \langle E_{\parallel} E_{\perp}^{*} + E_{\perp} E_{\parallel}^{*} \rangle \\ i\langle E_{\parallel} E_{\perp}^{*} - E_{\perp} E_{\parallel}^{*} \rangle \end{bmatrix}, \quad (5)$$

where $E_{\parallel}$ and $E_{\perp}$ the parallel (S) and perpendicular (P) real components of the electric field (with their imaginary counterparts designated by *). The Stokes parameters represent total, linearly polarized, and circularly polarized radiance, which all carry units of W m^{-2} nm^{-1} sr^{-1}. The total radiance (*I*) is the sum of the parallel and perpendicular intensities of the beam. The linearly polarized radiances represent excesses of 0° over 90° polarization angles (*Q*), and 45° over 135° polarization angles (*U*), and the circularly polarized radiance represents the excess of left-circular over right-circular polarization (*V*). These four parameters fully describe the polarization state of a light beam and are related with two equations:

$$I^2 \geq Q^2 + U^2 + V^2, \quad (6)$$

and

$$DOP = \frac{\sqrt{Q^2 + U^2 + V^2}}{I}, \quad (7)$$

where *DOP* is the degree of polarization, a dimensionless ratio between 0 and 1 that represents the amount of polarized light in the total intensity measurement. Note that in the absence of V, Eq. (7) becomes the *degree of linear polarization* (*DOLP*). We will neglect the V parameter in this study, as it is negligible at the top of the atmosphere (Hansen and Travis 1974).

Ray traces through optical media, like lenses and prisms, are sequential and can be described by linear algebra. A polarized beam traveling through an optical interface is related to the output beam by a Mueller matrix:

$$\begin{bmatrix} I \\ Q \\ U \end{bmatrix}_{sca} = \begin{bmatrix} M_{11} & M_{12} & M_{13} \\ M_{21} & M_{22} & M_{23} \\ M_{31} & M_{32} & M_{33} \end{bmatrix} \begin{bmatrix} I \\ Q \\ U \end{bmatrix}_{inc}, \quad (8)$$

where subscripts *inc* and *sca* represent the Stokes vector for the incident beam and scattered beam, respectively. The M_{ij} elements describe how the medium changes the nature this beam. The M-matrix in Eq. (8) may be a single optical element, or an optical train. This matrix is a product of several matrices that describe the sequential optical elements of the AirHARP system:

$$\begin{bmatrix} I \\ Q \\ U \end{bmatrix}_{det} = M_{polarizer}\, M_{prism}\, M_{train} \begin{bmatrix} I \\ Q \\ U \end{bmatrix}_{inc} = \boldsymbol{M_{system}} \begin{bmatrix} I \\ Q \\ U \end{bmatrix}_{inc}, \quad (9)$$

where the subscript *det* now corresponds to the Stokes vector incident on the detector FPA, and the subscripts *polarizer*, *prism*, and *train* correspond to the Mueller matrices of the detector polarizer, the optical path through the Phillips prism, and the optical lens train in the housing. In theory, each of these M-matrices defined in Eq. (9) contain internal Mueller matrices for coating interfaces, lenses, and prism elements, but these are difficult to characterize individually after assembly. Therefore, these are combined into one global M-matrix (M_{system}) that characterizes the system.

The HARP detectors only register intensity values. It is not possible to measure the Q_{det} and U_{det} information directly in Eq. (9). However, because each detector linear polarizer is oriented at a different angle, the intensity measured at the FPA encodes information about the polarization state. The original polarization of the Earth scene can be retrieved by combining the intensity information from the three detectors. The matrix components from the Eq. (9) matrix that contribute to I_{det} , for each detector form a relationship between detector counts and the incident Stokes state:

$$\begin{bmatrix} DN_{corr,det\ A} \\ DN_{corr,det\ B} \\ DN_{corr,det\ C} \end{bmatrix} = \begin{bmatrix} M_{11,det\ A} & M_{12,det\ A} & M_{13,det\ A} \\ M_{11,det\ B} & M_{12,det\ B} & M_{13,det\ B} \\ M_{11,det\ C} & M_{12,det\ C} & M_{13,det\ C} \end{bmatrix} \begin{bmatrix} I \\ Q \\ U \end{bmatrix}_{inc} = \boldsymbol{M}^* \begin{bmatrix} I \\ Q \\ U \end{bmatrix}_{inc}, \quad (10)$$

where the $M_{1j,\ det\ X}$ coefficients represent the first row of the Mueller matrix for the light path through the optical system into that specific detector (j = 1, 2 or 3) and $DN_{corr,\ det\ X}$ represents

the corrected detector counts from Eq. (5), where X could be A, B, or C. This matrix with M_{1X} coefficients is **M***. Note that **M*** is *not* a Mueller matrix.

Subsection 2.5.2: Application in the laboratory

The purpose of the polarimetric calibration of the AirHARP instrument is to derive **M*** and/or its inverse using Eq. (10). To do this, an integrating sphere is used, and a 1-inch Moxtek wire-grid linear polarizer is rotated at the aperture of this sphere to cycle the Q and U distribution of the output. The Moxtek is a high efficiency, high contrast polarizer suitable for the 400-900nm wavelength range. The polarizer is set in a Thorlabs rotational mount and accurately control the angle of polarization entering the AirHARP instrument to 0.001°. The Moxtek is highly reflective, so the polarizer is tilted 10° relative to the AirHARP optical axis to avoid retroreflections (van Harten et al. 2018). The polarizer is characterized before any testing and its starting orientation is verified by an external reference polarizer.

The optical axis of the HARP instrument is placed along the axis between the center of the Moxtek polarizer and the aperture of the integrating sphere such that the HARP image is illuminated at nadir. The integrating sphere is set to a lamp level below the saturation limit of all HARP channels. The Moxtek is mechanically rotated at intervals of 10°. Simultaneous images are taken at each detector and Moxtek angle. The relative Stokes state at each angle is well-known, with $Q/I = \cos 2\vartheta$ and $U/I = \sin 2\vartheta$ (Kliger et al. 1999), where ϑ is the rotation angle.

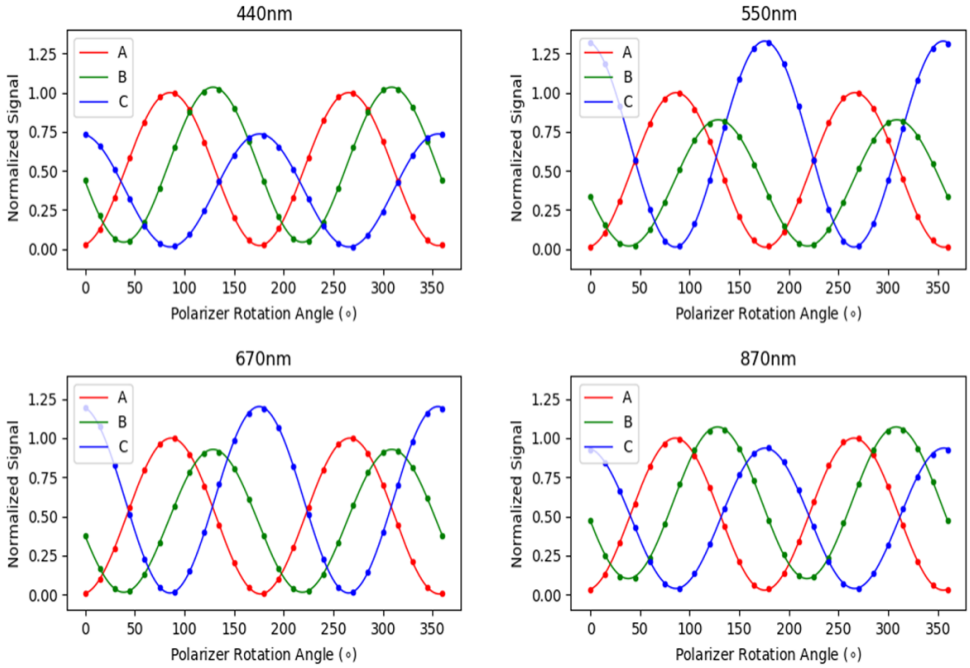

Figure 18. Malus curves for each of the four AirHARP channels. Each plot corresponds to an AirHARP channel, with data from Sensors A (red), B (green), and C (blue) fit to Eq. (12). These curves are normalized to the Sensor A maximum and represent the closest 4x4 nadir pixel bin, in each channel, to the AirHARP optical axis. Note the polarizer rotation angle is offset by -90° as shown.

The optical path from the HARP front lens to a single FPA creates a single partial polarizer (i.e., Eq. 9). Therefore, this test creates a two-polarizer system. Malus' law explains the observed counts at each detector as a function of ϑ. To account for optical complexity of HARP, a general fit is used:

$$DN_{corr,det\ X}(\vartheta) = \alpha\ cos^2[\vartheta - (\vartheta_X - \beta)]\ +\ \gamma, \tag{11}$$

where the subscript *corr*, *det X* represents the corrected counts in a single detector (i.e. X could be A, B, or C) during this test and α, β, and γ are fit parameters. ϑ_X is the nominal polarizer angle for a detector X, determined during AirHARP pre-assembly testing. Figure 17 shows examples of Malus curves for the three detectors, using co-located Moxtek data along the optical axis for the 670 nm channel.

Note that the amplitude of the curves is related to the α and γ parameters, the phase to β, and the extinction ("lift" off the zero line) to γ. Any global bias due to the Moxtek polarizer itself is negligible or removable for reasons stated above. Surface inhomogeneities on the polarizer may impart higher-order frequencies in the signal, which are accounted for by Fourier decomposition (Cairns et al. 1999). A separate sensitivity study using a reference polarimeter and a rotating polarizer in our lab suggests that Fourier modes at the 0.005 level ($\sin 4\vartheta$ and $\cos 4\vartheta$) come from surface variations. After normalizing each Malus curve by the maximum of the curve in *det A* for each channel and detector, and inverting the matrix in Eq. (10), we come to a final relationship that completely represents this step:

$$\begin{bmatrix} 1 \\ -cos\ 2\vartheta \\ sin\ 2\vartheta \end{bmatrix}_{inc} = \begin{bmatrix} C_{11,} & C_{12} & C_{13} \\ C_{21} & C_{22} & C_{23} \\ C_{31} & C_{32} & C_{33} \end{bmatrix} \begin{bmatrix} DN_{corr,det\,A}(\vartheta) \\ DN_{corr,det\,B}(\vartheta) \\ DN_{corr,det\,C}(\vartheta) \end{bmatrix} (max(DN_{corr,det\,A}(\vartheta))^{-1}, \qquad (12)$$

where the Stokes parameters (I, Q, U) are replaced with their theoretical forms and the matrix $\mathbf{C} = (\mathbf{M}^{*})^{-1}$ from Eq. (10). This **C** is defined in Borda et al. (2009) as the *characteristic matrix*. The **C** translates normalized, corrected detector counts to normalized Stokes parameters. The $\mathbf{C}^{-1}$ has an analytic form based on the angle of the polarizers used for the three detectors (Schott 2009):

$$C^{-1} = \begin{bmatrix} f_A & f_A\, g_A\, cos\, 2(\theta_A - \beta_A) & f_A\, g_A\, sin\, 2(\theta_A - \beta_A) \\ f_B & f_B\, g_B\, cos\, 2(\theta_B - \beta_B) & f_B\, g_B\, sin\, 2(\theta_B - \beta_B) \\ f_C & f_C\, g_C\, cos\, 2(\theta_C - \beta_C) & f_C\, g_C\, sin\, 2(\theta_C - \beta_C) \end{bmatrix}, \qquad (13)$$

where coefficients define the transmission of the light through the system (f_X), polarizing efficiency (g_X), and phase offset (β_X) relative to the nominal detector polarizer angles (θ_X) from Eq. (11). This characteristic matrix (and/or its inverse) can be solved using a least-squares approach using data from at least three Moxtek polarizer angles.

Table 4a gives the characteristic matrix coefficients with relative uncertainties and Table 4b gives example values with uncertainties for the inverse characteristic matrix. Both tables shown below represent a 4x4 nadir pixel bin for the 670 nm channel for AirHARP.

Table 4a. Characteristic matrix elements, C_{ij}, for the 670 nm AirHARP band, vis Eq. (12).

C_{ij}	j = 1	j = 2	j = 3
i = 1	1.020 ± 0.108%	-0.053 ± 3.214%	0.848 ± 0.083%
i = 2	-0.843 ± 0.107%	-0.309 ± 0.454%	0.938 ± 0.062%
i = 3	-1.257 ± 0.051%	2.230 ± 0.044%	-0.689 ± 0.060%

Table 4b. Instrument-relative parameters for 670 nm AirHARP band, vis Eq. (13).

	f (%/100)	g (%/100)	β(°)
Sensor A ($\theta_A = 0°$)	0.501 ± <0.001	0.994 ± 0.002	-3.261 ± 0.060
Sensor B ($\theta_B = 45°$)	0.471 ± <0.001	0.970 ± 0.002	-6.115 ± 0.048
Sensor C ($\theta_C = 90°$)	0.605 ± <0.001	0.985 ± 0.003	-4.608 ± 0.060

Table 4b shows that the nominal AirHARP polarizer angles (θ_X) deviate from their expected values (β_X). Note that $\theta_X - \beta_X$ is the perceived polarization orientation of the entire light path from the perspective of each FPA. Retardances induced by the prism and/or detector polarizer will contribute to β_X. Note that the coefficients are significantly different from the Pickering matrix, the ideal C-matrix for a AirHARP-like system (Schott 2009). The characteristic matrix coefficients shown in Table 4a use the polarizer datasets alone, though current AirHARP L1B processing through Version 002 includes input from low DOLP sources (integrating spheres, partial polarization generators) for closure on the entire DOLP range. Those matrix values may deviate slightly from those shown here, and will continue to be updated with on-orbit trending exercises. The errors and values in Table 4a can be used to calculate the propagated uncertainty in the Stokes parameters, which is derived from Eq. (12):

$$\sigma_{S_j}{}^2 = (max(DN_{corr,det\,A}(\vartheta))^{-2} \sum_{i=1}^{3} \left[\left(DN_{corr,i}\, \sigma_{C_{ij}} \right)^2 + \left(C_{ij}\, \sigma_{DN_{corr,i}} \right)^2 \right], \qquad (14)$$

where σ_{S_j} is the 1-sigma standard deviation of the Stokes parameters (denoted generally by subscript *S*). We use the j iterant to define the Stokes parameter: [1,2,3] corresponds to [I,Q,U] and can be used interchangeably. $DN_{corr,i}$ is the result from Eq. (5) where the i iter-

ant [1,2,3] corresponds to sensors [A, B, C]. $\sigma_{C_{ij}}$ is the uncertainty quoted in Table 4b for the C_{ij} matrix element, and $\sigma_{DN_{corr,i}}$ is the propagated uncertainty of the detector counts measurement:

$$\sigma_{DN_{corr,i}}{}^2 = (B\sigma_{shot})^2 + (B\sigma_{read}G)^2 + (B\sigma_{dc}\Delta tG)^2 + \sigma_{ext}^2, \quad (15)$$

where B is the total number of binned pixels, G is the detector ADC gain (~2 e^-/ADU), Δt is the detector integration time, the parameter with subscript *shot* (Poisson noise) scales with the counts measurement, and the others, *read* (read noise) and *dc* (dark current), are provided in Table 1. The parameter with subscript *ext* includes uncertainties due to background correction, flatfielding, non-linearity, pixel crosstalk, and noises that are difficult to decouple or model, including stray light. At the integration times we use, the *read* and *dc* terms are negligible compared to shot noise. We can substitute Eq. (15) for a 1-sigma standard deviation of data in a real AirHARP superpixel. This is equivalent to Eq. (15) without the need to explicitly define σ_{ext}^2 and in field data, the shot and ext components will dominate the dark and read terms.

Finally, the propagated uncertainty in the DOLP L1B polarization product can be written with the Stokes parameters and their errors:

$$\sigma_{DOLP}{}^2 = \frac{\left(Q\ \sigma_Q\right)^2 + (U\ \sigma_U)^2}{(Q^2 + U^2)^2} + \left(\frac{\sigma_I}{I}\right)^2, \quad (16)$$

Subsection 2.6: Radiometric calibration

Subsection 2.6.1: Relative spectral response

The radiometric calibration, of AirHARP requires knowledge of spectral response. The AirHARP instrument uses several filters to define the four nominal wavelength channels, with bandwidths in parentheses: 440 (15), 550 (12), 670 (18), and 870 (39) nm. The spectral

response function (SRF) is defined by a multi-bandpass filter (MBPF) and the stripe filter on top of each detector.

To validate these filter specs, the AirHARP instrument was placed in the aperture of a 25.6cm integrating sphere at NASA GSFC, which was illuminated by an Ekspla laser source. The Ekspla is a scanning monochromator capable of 1 nm precision in wavelength, over a 200-1000nm range. The Ekspla source was set at a given wavelength and each output channel and bandwidth was verified using an external Avantes spectrometer. The spectrometer output was used to correct the AirHARP measurements for any variation in Ekspla laser power over the course of the testing period.

The standard process is used on AirHARP images that are taken at each Ekspla wavelength setting. The Ekspla channels were chosen using *a priori* knowledge of the filter spectra from the manufacturer. A higher density of images was acquired in-band than out-of-band to capture the structure of the in-band SRF. Figure 19a shows AirHARP images of the integrating sphere, illuminated by four in-band Ekspla wavelengths. When the Ekspla is set to an in-band channel near 670 nm, the 60 AirHARP red view sectors are illuminated. For the other AirHARP channels, the sparser distribution of 20 view sectors appears whenever the Ekpsla is in-band. For Ekpsla wavelengths rejected by the AirHARP system, the images are compatible with dark signal (Figure 13b).

Using the telecentric technique, we take a small region of nadir pixels, correct their values via the process leading up to Eq. (5), and plot them against Ekspla wavelength for a single HARP channel. Figure 19b shows the SRF for AirHARP Sensor 1 (blue dots), Sensor 2 (green dots), and Sensor 3 (orange dots) for 440 nm (left), 550 nm (left-center), 670 nm (right-center), and 870 nm (right). Because the SRF data is noisy, even after correction from an external spectrometer, we use a general super-Gaussian fit of order 6 (plotted in gray) to simplify the following analysis. Note that the edges of the in-band response are well-defined, and the 870 nm channel shows the aggressive narrowing of the leading edge of the SRF as discussed earlier. Figure 19b also shows a differential SRF for the AirHARP 440 nm band, which is likely due to manufacturer error in the thin-film coating design of the AirHARP prism interfaces or detector stripe filters. This difference may impact AirHARP 440 nm L1B radiances in field data that is calculated using lab-derived coefficients. Because Rayleigh scattering is so strong in the 440 nm range, offsets in the L1B data at 440 nm can be treated

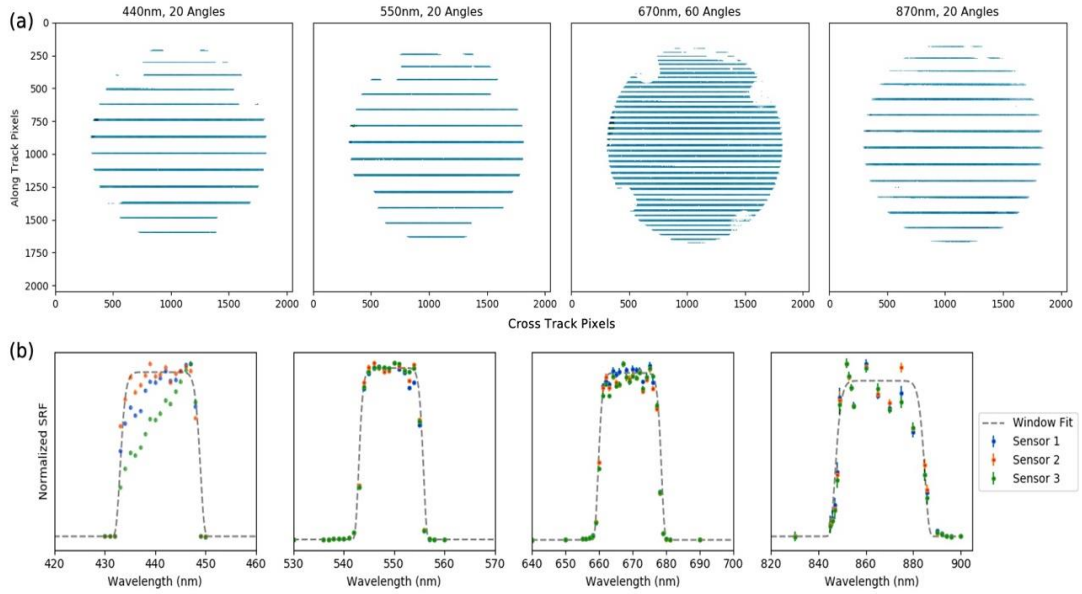

Figure 19. Examples of AirHARP images taken at different in-band Ekpsla wavelengths to show the distribution of illuminated stripes (a). The AirHARP SRF for the three sensors and the super-Gaussian SRF fit (gray) is shown in (b). All data shown in (b) is normalized to 1 for each channel individually. The AirHARP 440 nm differential SRF is a manufacturing defect and efforts to account for this in the L1B reflectance product are currently under investigation.

like stray light, which correlates with the signal (and therefore the SRF). A simple Rayleigh-like SRF adjustment in each sensor may correct for this SRF differential. This 440 nm SRF differential is unique to AirHARP; we see no evidence of this in the HARP CubeSat (Puthukuddy et al. 2022) or HARP2 440 nm designs.

This testing benefits two studies: (1) calculation of extraterrestrial solar irradiance, used to convert radiance measured at TOA to reflectance, and (2) radiometric calibration. To perform (1), the solar spectrum (NREL 2000) is integrated inside the SRF for each HARP wavelength:

$$F_0(\lambda) = \frac{1}{\Delta\lambda} \int_{\lambda_i}^{\lambda_f} B(\lambda)\, SRF(\lambda)\, d\lambda, \tag{17}$$

where λ is the wavelength (subscripts i and f denoting the trailing and leading edges of the spectral band) in nm, $\Delta\lambda$ is the bandwidth in nm, $B(\lambda)$ is the solar spectral irradiance in W m^{-2} nm^{-1} and SRF(λ) is the spectral response function. Only the structure of the in-band channel is used in Eq. (17), and each window is fit to a 6^{th} order super-Gaussian function, due to unexplained noise in the dataset larger than the uncertainty of each data point. Analysis of the second-order in-band differences relative to this theoretical fitting are ongoing but are not expected to contribute significantly to the L1B data product (AirHARP 440 nm notwithstanding). The limits of integration for Eq. (17) typically span ± infinity to account for any contributions from other spectral ranges, though in a separate sensitivity study, it was determined that the out-of-band rejection for AirHARP was at or below the 0.001 level from 300 to 1050 nm. Therefore, reducing the limits of integration to the leading and trailing edges of the in-band response properly defines the F_0 for each channel. Table 3 shows the details of our spectral response testing and the extraterrestrial solar irradiance calculated using Eq. (17), for each channel.

Table 5. Derived AirHARP pre-launch SRF parameters

Nominal Channel (nm)	Center (nm)	Bandwidth (nm)	F_0 (W m^{-2} nm^{-1})
440 nm	441.4	15.7	1.855
550 nm	549.8	12.4	1.873
670 nm	669.4	18.1	1.534
870 nm	867.8	38.7	0.965

The final column of this chart is used to normalize measured radiances as per:

$$\rho(\lambda) = \frac{\pi L(\lambda)}{F_0(\lambda)}, \tag{18}$$

where $\rho(\lambda)$ is the reflectance and $L(\lambda)$ is radiance in units of W m^{-2} nm^{-1} sr^{-1}, assuming a Lambertian scattering distribution of light in the pixel. It is convention to sometimes include an extra term in the denominator of Eq. (18) to account for the view zenith a ut it is omitted here to remain consistent with later discussions.

Subsection 2.6.2: Absolute radiometric calibration

Our radiometric calibration translates the normalized Stokes parameters to calibrated radiances (W m^{-2} nm^{-1} sr^{-1}). This step gives scientific weight to our measurements and allows us to retrieve radiative properties about the atmosphere and surface. Again, integrating spheres are optimal for this testing. For example, the radiometrically calibrated NASA GSFC "Grande" sphere is traceable to the National Institute of Standards and Technology (NIST) with calibration uncertainties publicly available for a comparable sphere (Cooper and Butler 2020). The spectral sensitivity of "Grande" peaks around 1 μm and the illumination of the nine lamps is linear. Our study uses all nine lamp levels, plus a measurement of the final lamp at 50% attenuation, to capture a wide range of illumination.

The AirHARP instrument is set under the same conditions as the polarimetric calibration, discussed in Section 2.5.2, except with no polarizing element between the instrument and integrating sphere. Because the lamps are incandescent sources, the AirHARP detector integration times are adjusted to capture enough signal in the blue channel and beneath saturation in the NIR. The standard process is used at each lamp level to create template images. Using the telecentric technique, we select a small nadir pixel bin for a given wavelength, correct the values using the process leading up to Eq. (4), and apply the characteristic matrix for that channel to the co-located data in each detector. The sphere output is depolarized, so the resulting Stokes parameters Q and U are statistically zero and the total intensity, I, contains all the information content. As per Eq. (12), the resulting I is in counts, yet represents the band-weighted signal measured by a particular AirHARP channel. To find the equivalent radiance levels as observed by AirHARP, the solar spectrum, B(λ), is replaced by the Grande SRF in Eq. (17) (Cooper and Butler 2020) and this calculation is performed for each lamp and wavelength. The radiometric calibration derives the slope (W m^{-2} nm^{-1} sr^{-1} ADU^{-1}) that translates the normalized AirHARP intensities to the calibrated radiances:

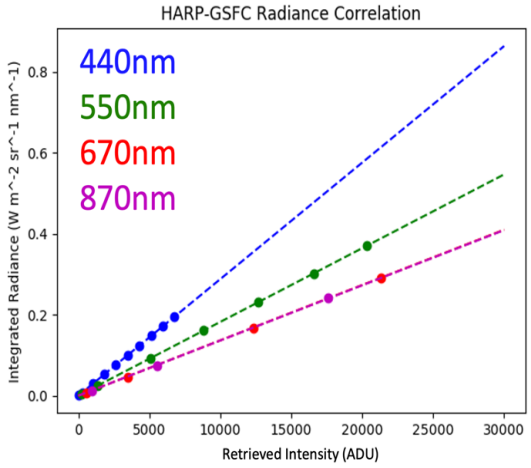

λ	k *10^{-5}	R^2
440nm	2.8 ± 0.1%	0.99
550nm	1.8 ± 0.1%	0.99
670nm	1.4 ± 0.3%	0.99
870nm	1.4 ± 0.4%	0.99

Figure 20. The absolute gain calibration of the HARP CubeSat instrument. Data and linear fits (left). The above table shows the gain coefficient, uncertainty, and fit correlation for each channel.

$$L_{lamp} = k\,(C_{11}DN_{corr,det\,A} + C_{12}DN_{corr,det\,B} + C_{13}DN_{corr,det\,C}) + \gamma, \qquad (19)$$

where *L(lamp)* is the calibrated irradiances (W m^{-2} nm^{-1} sr^{-1}) at that lamp level, *k* is our gain factor (W m^{-2} nm^{-1} sr^{-1} ADU^{-1}), and γ is a linear bias (W m^{-2} nm^{-1} sr^{-1}). The equivalent Grande

radiances and measured counts share the same pixel solid angle as observed by AirHARP, so this is implicitly factored into Eq. (19). For all channels, the linear bias γ is compatible with zero within 3-sigma. The results, derived from the HARP CubeSat instrument using the NASA Grande sphere, are shown in Figure 20. Note that, because we performed the non-linear correction at the detector level early in the pipeline and the source illumination is linear and stable, a linear fit describes the correlation well ($R^2 = 0.99$ for all channels). This allows us to formulate the general calibration equation for the AirHARP instrument:

$$\begin{bmatrix} I \\ Q \\ U \end{bmatrix} = k \begin{bmatrix} C_{11} & C_{12} & C_{13} \\ C_{21} & C_{22} & C_{23} \\ C_{31} & C_{32} & C_{33} \end{bmatrix} \begin{bmatrix} DN_{corr,det\ A} \\ DN_{corr,det\ B} \\ DN_{corr,det\ C} \end{bmatrix}, \tag{20}$$

and the complete, propagated uncertainty of the Stokes parameters:

$$\sigma_{S_j}{}^2 = \sum_{i=1}^{3} k^2 \left[\left(DN_{corr,i}\, \sigma_{C_{ij}} \right)^2 + \left(C_{ij}\, \sigma_{DN_{corr,i}} \right)^2 \right] + \left(C_{ij}\, DN_{corr,i}\, \sigma_k \right)^2, \tag{21}$$

where the subscripts follow the same convention as Eq. (14). Note that if the signal-to-noise ratio of each detector is preferred, $\sigma_{DN_{corr,i}}$ can be substituted for $DN_{corr,i}\, SNR_i^{-1}$ and further consolidation of terms is possible.

Section 3: Validation of calibrated measurements

Subsection 3.1: Validation of nadir coefficients

Before we evaluate the calibration over the entire FOV, it is important we validate the same lens locations that we used to calibrate the instrument. Here, we evaluate the nadir coefficients for a range of partially polarized DOLP signals, like those AirHARP observes in field data. In the atmosphere, DOLP measurements close to 1 occur only at certain geometries with sunglint over dark ocean or Rayleigh scattering in the ultraviolet. More often, a complex atmosphere-land-ocean scene generates partially polarized light ($0 < DOLP < 1$). To simulate this, a partial polarization generator box (POLBOX), a Fresnel device comprised of

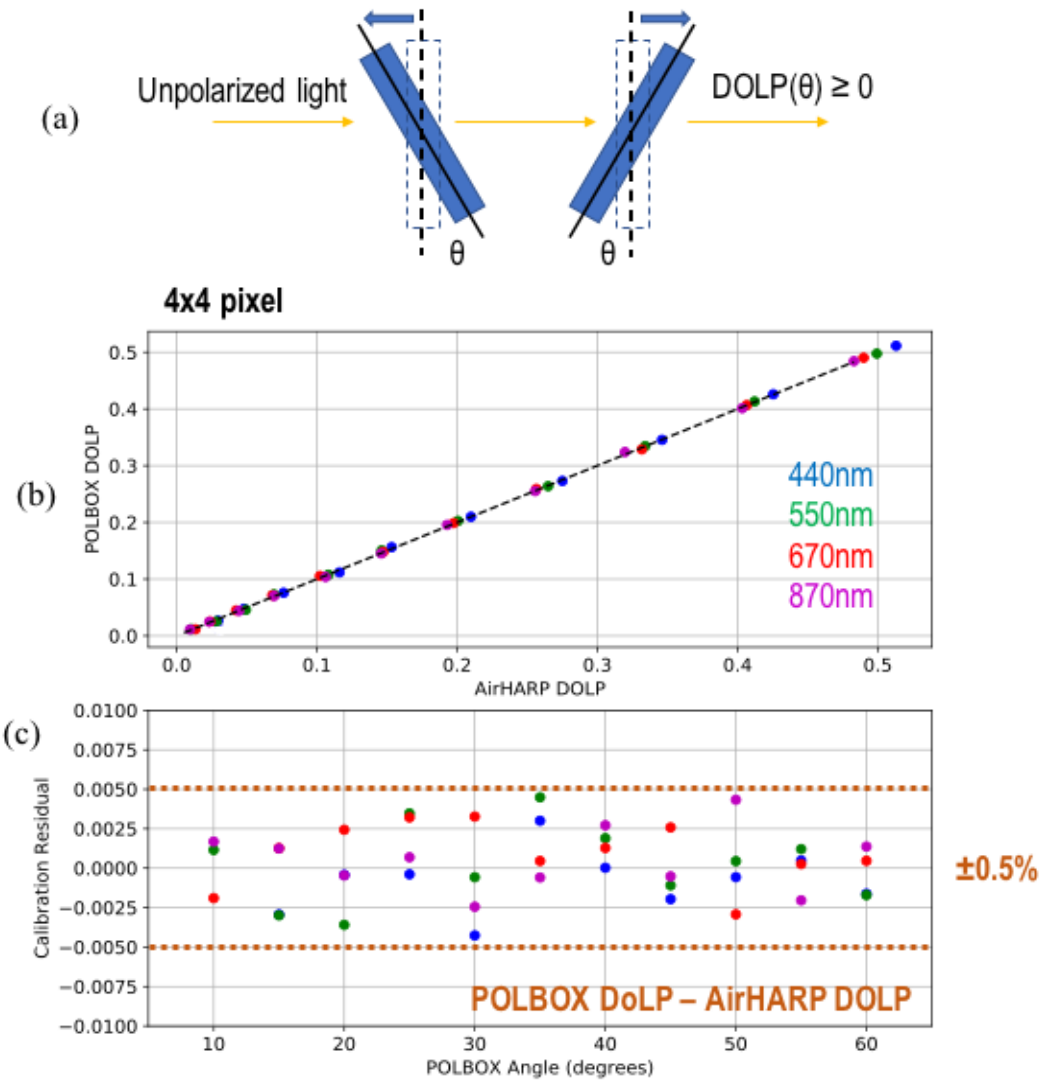

Figure 21. The POLBOX system generates partial polarization by rotating two glass blades (a). When comparing the DOLP theory to AirHARP measurement in all channels (b), we see AirHARP reproduces the entire POLBOX range within ± 0.5% DOLP (c). The lamp reflectance for this measurement was > 0.09 in all channels.

two rotatable glass blades at equal index of refraction, is used (Figure 21a). This polarization state generator is widely used for lab validation of spaceborne polarimeters (van Harten et al. 2018, Li et al. 2018, Smit et al. 2019). This POLBOX system is unique in that it *conserves DOLP*: when the entire POLBOX system rotates along its center axis, any DOLP measured at fixed blade angle remains the same, while the absolute values of Q and U will change. At a fixed global rotation angle, steeper inclinations of the glass blades will increase the DOLP up to ~60%, due a rotation limit of the blades. Any deviation in the DOLP retrieval gives the lab

calibration uncertainty of the HARP system, after systematic POLBOX uncertainty is accounted for. The POLBOX DOLP is analytic and the values at each blade setting can be determined by the sequential Fresnel interactions at each air-glass interface:

$$DoLP_{POLBOX} = \frac{\alpha(n,\lambda)\cos^2(2\theta) + \beta(n,\lambda)\cos(2\theta) + \gamma(n,\lambda)}{\varepsilon(n,\lambda)\cos^2(2\theta) + \mu(n,\lambda)\cos(2\theta) + \omega(n,\lambda)} \tag{22}$$

where $\alpha, \beta, \gamma, \varepsilon, \mu,$ and ω are glass-specific coefficients, dependent on refractive index, n, and wavelength, λ, and θ is the glass blade angle. For our test, we keep the POLBOX glass blades perpendicular to the table and take HARP images at increasing blade angles. The angle of the blades is controlled by a fine micrometer dial, and the angle is known within 0.25°. The data is corrected through the process leading up to Eq. (4), and the pre-computed calibration matrices are applied for each wavelength and image in the dataset. As mentioned above, the characteristic matrix used in this validation includes Moxtek polarizer data and input Stokes vectors that represent unpolarized light for closure over the entire DOLP range. Using the same nadir pixel bin that was used for calibration, the measured Stokes parameters at each POLBOX blade angle are processed into the DOLP via Eq. (7) and these results are compared to Eq. (22) for each blade angle and wavelength.

The measured DOLP from the HARP system is within ±0.5% (RMS ~0.25%) of the true POLBOX values for all wavelengths, given a 4x4 pixel nadir bin, as shown in Figure 21b-c. Glass blade angles (<5˚) that create back reflections in the wide HARP FOV are neglected from the comparison. Removing these angles has a negligble impact on the comparison, as the theoretical DOLP at 10˚ is still quite low (~4%) and still represents a depolarized environment. The POLBOX itself imparts a static DOLP uncertainty of 0.0015, related to the uncertainty in the glass blade angle (Li et al. 2018) and is the only error contribution as long as the source field is unpolarized. This experiment is only limited by the intensity of the integrating sphere, which here was no less than 0.09 in reflectance (440 nm). This level is a bit higher than the typical aerosol signal used in theoretical experiments (L_{typ}), but it is challeng-

ing to balance integration time, saturation, and SNR in a single lab measurement when all channels are simultaneously exposed. POLBOX testing at different levels of reflectance are anticipated during the HARP2 pre-launch baseline testing later this year. Even so, we conclude that the HARP design allows for an accurate pre-launch DOLP baseline for all channels, relative to recommended cloud and aerosol science uncertainty benchmarks (NASA PACE 2015).

Subsection 3.2: Full FOV intercomparisons with field data

Subsection 3.2.1: AirHARP participation in the Aerosol Characterization with Polarimeter and LIDAR (ACEPOL) campaign

Sensitivity tests in the lab allow us to characterize the HARP instrument in a well-controlled setting. However, these environments can be limited by resources and time, and this can impact how much of the FOV, spectral channels, and dynamic range are characterized. To validate the full FOV calibration, we take field data and compare how the HARP instrument measures the multi-angle reflectance and polarized signal with a similar MAP over a common target.

AirHARP participated in two NASA aircraft campaigns in 2017: the Lake Michigan Ozone Study (LMOS) and Aerosol Characterization from Polarimeter and Lidar (ACEPOL). LMOS took place over Lake Michigan and eastern Wisconsin from May 25 to June 19 2017 and ACEPOL over the southwestern United States and eastern Pacific Ocean from October 23 to November 9 2017. LMOS was AirHARP's debut and was the only instrument of its kind taking measurements during this period. ACEPOL, on the other hand, included two lidar and four polarimeter instruments on the aircraft, including AirHARP. A major goal of the ACEPOL campaign was to compare different polarimeter concepts over common targets, improve cross-calibration studies, and develop new synergistic algorithms for retrieving aerosol, cloud, land, and ocean properties.

During ACEPOL, these six instruments observed over 30 scenes including urban cities, coastal oceans, dry lakes, cloud decks, and prescribed wildfire smoke. Two of these targets are best suited for reflective solar band calibration and validation: sunglint over dark ocean and the Rosamond Dry Lake, a flat desert site in California. Sunglint is highly polarized at some geometries, reaching DOLP of nearly 1 in the optical regime. Off-glint, polarization is reduced and low ocean albedo is useful to validate dim reflectances. The sunglint signal can be modeled accurately, if the viewing and solar geometry are known and aerosol and Rayleigh scattering are removed. The appearance of sunglint depends on the ocean surface wind speed, which can roughen the surface and break up the signal (Cox and Munk 1954). Even despite strong surface winds, the ocean surface is considered flat from a viewing altitude of 20km and requires no special topography correction to the data. Multi-angle polarimeters, like AirHARP, measure the way the sunglint signal varies with viewing angle, and can reproduce a discrete intensity and polarization profile with angle. Therefore, sunglint datasets are very convenient to use for calibration validation. The Rosamond Dry Lake is also a useful calibration target: it is a pseudo-invariant, highly reflective surface with a low DOLP profile. Targets similar to Rosamond in northern Africa have been used for decades as vicarious calibration targets for these reasons and others (Wu et al. 2007, Wu et al. 2017). We will use two sunglint (10/23/2020) and two Rosamond Dry Lake (10/25/2020) scenes from the campaign to show that our telecentric technique captures the expected performance of the AirHARP instrument across the entire FOV.

Because the focus of this work is calibration and not data intercomparisons, we will present the following study in a limited sense, only for the purpose of proving our calibration technique in the field. For this study, the Research Scanning Polarimeter (RSP) instrument was chosen as our validator because it best matches the along-track angular sampling of HARP, shared the same wing of the ER-2 with AirHARP during ACEPOL, and has the longest history of accurate, validated measurements. The following describes the process used to

co-locate AirHARP and RSP measurements at similar viewing angles and spectral channels. We follow these steps in generating the co-located data for I and DOLP:

1. A target of interest and reference lat-lon pair is identified and the closest scan in the RSP data is found. The average lat-lon pair of this scan becomes the new reference lat-lon point.
2. The AirHARP angular data is cross-correlated with its own nadir image to correct for any pushbroom misregistration.
3. The algorithm finds the closest matching view zenith angles between AirHARP and RSP within 0.5° over this common target.
4. For each matching view angle, an 8x8 pixel search window is defined in the AirHARP granule around the lat-lon point for that RSP view angle. Using each pixel in the search window as a new "target", the AirHARP data is binned 8x8 around this pixel to approximately match RSP 220 m ground resolution. A cost function is used to calculate the error-normalized difference between the AirHARP-RSP measurements for that view angle. The closest matching AirHARP superpixel measurement will minimize the cost function.
5. The angular data of the RSP is interpolated to the exact scattering angle range measured by AirHARP.
6. This process is repeated for all relevant spectral channels.

We use a search method in this comparison to reduce the differences in pointing between the two instruments, which can be complicated by wing flex, differences in inertial monitoring, vibrations and thermal changes, and geolocation references used between both science teams. The cost function used to minimize the closest match between the two instruments is driven by total and polarized reflectances and their variances:

$$\chi^2 = \frac{(R_{RSP} - R_{AirHARP})^2}{(\Delta R)^2_{RSP} + (\Delta R)^2_{AirHARP}} + \frac{(P_{RSP} - P_{AirHARP})^2}{(\Delta P)^2_{RSP} + (\Delta P)^2_{AirHARP}}, \quad (23)$$

where R and P are total and polarized reflectances (the top term in Eq. 7). The delta terms represent the respective measurement uncertainty using the error model for the instrument in question. These models are given in the Appendix. This cost function as written is robust against scenes with a notable difference in DOLP and reflectance. Desert (high reflectance and low DOLP) and ocean (low reflectance and high DOLP) measurements will be compared similarly with no preferential weighting toward either term in Eq. 23. Both total and polarized reflectances are considered in Eq. 23 as the closest matching pixel measurement between AirHARP and RSP will be the same location on the ground for both products. Because this paper uses these intercomparisons to prove our full FOV calibration, we only need a few datasets over different viewing and solar geometries to make our case. The following will discuss the results of the AirHARP and RSP intercomparison over both ocean and desert sites during the ACEPOL campaign.

Subsection 3.2.2: Results and discussion

The full FOV comparison with RSP uses two ocean cases from October 23, 2020 and two desert cases from October 25, 2020, taken during the ACEPOL campaign. The ocean captures occurred 30 minutes apart off the coast of California: the first at 20:10 UTC over 35.12° N 124.75° W and the second at 20:49 UTC over 31.75° N 122.38° W. We will identify the earlier as Ocean 1 and the later as Ocean 2 going forward, and both are parallel to and slightly off the solar principal plane. The desert cases were taken on October 25, 2020 over the Rosamond Dry Lake site in California, also 30 minutes apart: the first at 17:28 UTC and the second at 17:57 UTC. These captures will be identified as Desert 1 and Desert 2, and both targeted the general region around 34.83° N 118.07° W.

The AirHARP and RSP data were ordered for these dates, times, and locations, and the co-location procedure described in Section 3.2.1 was followed for each of the sites and the three spectral channels in common to both instruments: 550, 670, and 870 nm. We do not show a comparison with the AirHARP 440 nm band because there is no comparable RSP channel and for SRF reasons mentioned above that could complicate the interpretation of the results. The difference in the spectral shapes between AirHARP and RSP are not significantly different for these bands, so we did not perform any spectral matching in this work.

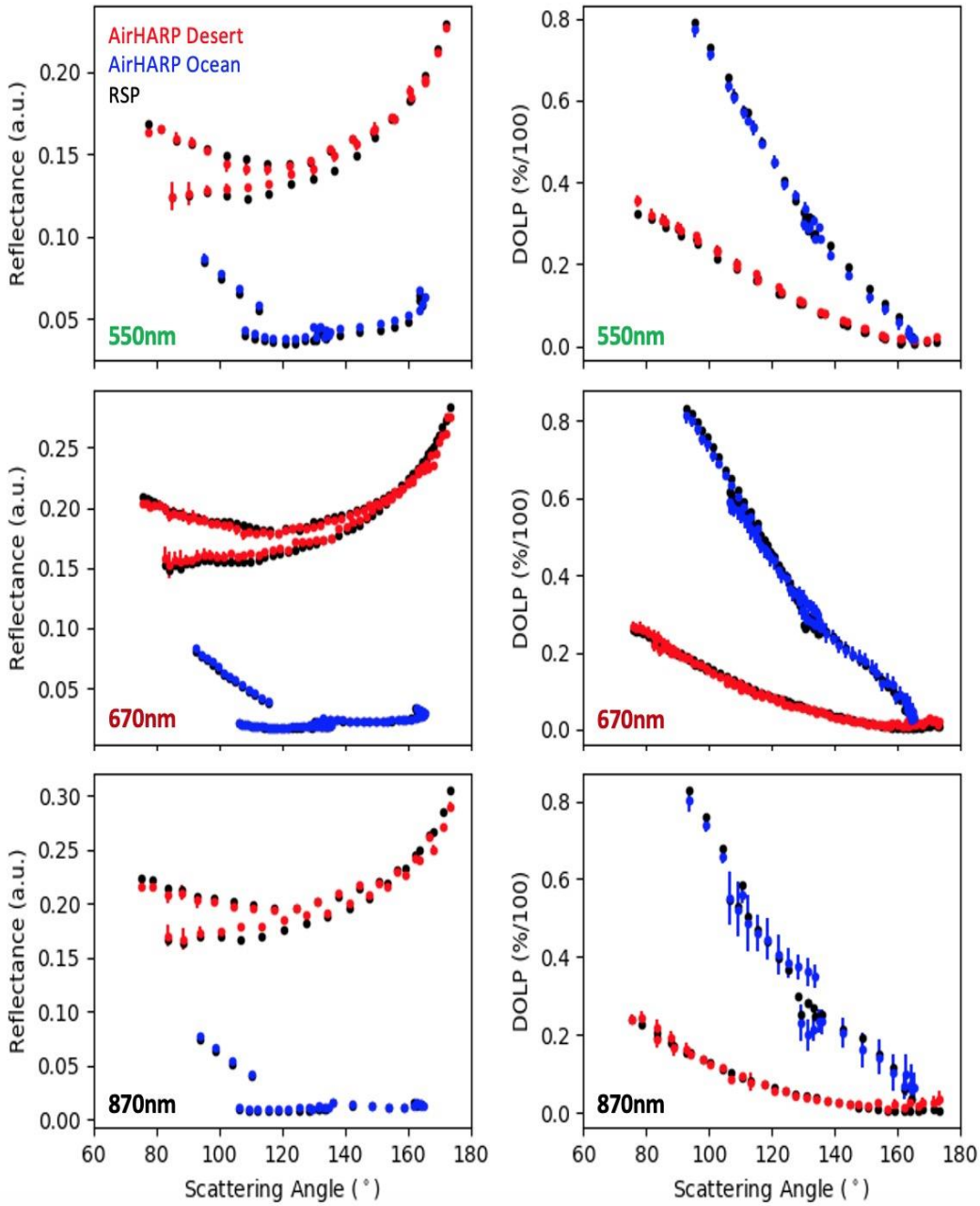

Figure 22. Multi-angle, co-located comparison between AirHARP and RSP for ACEPOL targets. Reflectance (left column) and DOLP (right column) are compared for three compatible spectral channels: 550 nm (top), 670 nm (middle), and 870 nm (bottom). AirHARP data in the colors and RSP is black, with red signifying Rosamond Dry Lake and blue data as ocean/glint cases. Error bars on the AirHARP data represent a 1-sigma standard deviation of the superpixel bin.

Figure 22 shows a multi-angle co-located comparison AirHARP and RSP for the four ACEPOL datasets. RSP data is in black and the AirHARP desert (red) and ocean (blue) for both reflectance (first column) and DOLP (second column). Three compatible channels are shown: 550 nm (top row), 670 nm (middle row), and 870 nm (bottom row). The error bar on the AirHARP points is the sub-pixel standard deviation of the superpixel at each angle. For the ocean cases, the reflectance is lower than 0.1 in all channels, but the DOLP range is wide, 0 to ~0.8. The desert cases were chosen specifically to contrast with sunglint. The desert cases represent the same target viewed from two different headings. The dependency on viewing geometry is clear in the separation of the desert reflectance curves in all channels. These cases provide a range of geometry for intercomparison and adequate contrast in reflectance and DOLP to validate our calibration.

Figure 23 shows a one-to-one comparison of co-located AirHARP and RSP reflectance and DOLP, across their three common spectral bands, and four ACEPOL targets. The plots are log-scaled to show differences for dim reflectance and low DOLP. The AirHARP data matches the global structure of the RSP for all sites in all channels, within statistical uncertainty. For AirHARP, the errorbar represents a 1-sigma standard deviation of the AirHARP superpixel and an assumed 3% relative calibration uncertainty in reflectance and absolute 0.25% RMS uncertainty for DOLP (see Figure 21). The RSP uncertainty is calculated using their error model and *a priori* inputs to reflectance and DOLP equations (Knobelspiesse 2015). The instruments agree within 1% in reflectance and DOLP for most VZA up to ~35°. Beyond ~35° VZA, there is a systematic difference between AirHARP and RSP, which may be tied to a variety of error sources.

First, AirHARP did not have an on-board calibrator, mechanism of temperature regulation, or dry purge during ACEPOL. If the field data was impacted by ascent-descent humidity changes, differences in temperature between the aircraft pod and the outside environment, condensation of water and aggregation of ice particles on the front lens, and any thermal flexing of the optical train, these impacts may be difficult to characterize. These may have asymmetric impacts on the data at different FOVs as well.

Specifically, Figure 22 shows some deviations between the AirHARP-RSP measurements, especially at larger scattering angles at 670 nm and 870 nm. This deviation may also be connected to georegistration at the widest angles, pointing misregistration between RSP and AirHARP, and/or interpolation at the AirHARP L1B stage. The HARP front lens distorts the ground projection by a factor of 4 at the furthest angles relative to nadir, so the amount of interpolation needed to fit the data on a common L1B grid is much more intense there than at nadir. The AirHARP sampling and data compression is also sensitive to "pitch surfing" of the ER-2. In several cases during ACEPOL, the ER-2 hit slight turbulence during

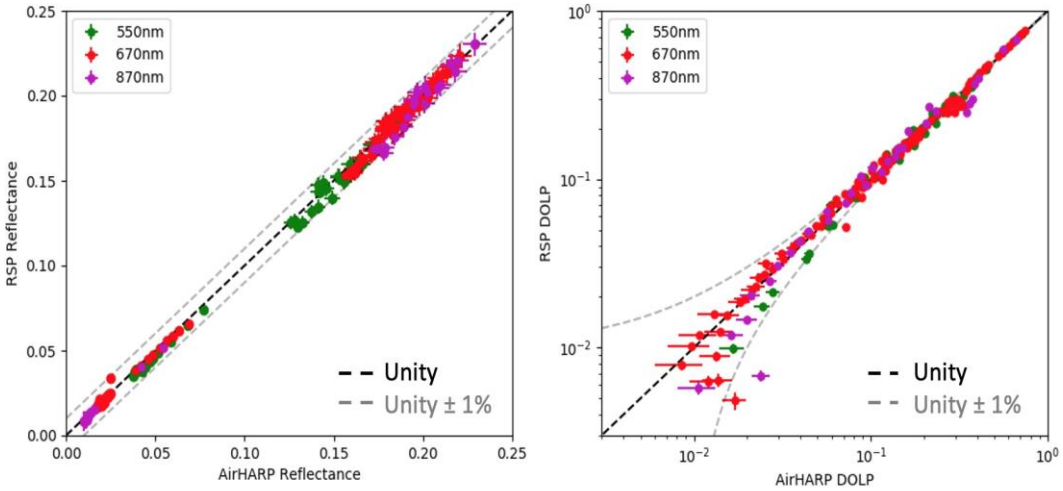

Figure 23. Direct comparison plot of AirHARP and RSP reflectance (left) and DOLP (log-scaled, right) for 550 nm (green), 670 nm (red), and 870 nm (magenta) data over the two ocean and two desert ACEPOL cases shown in Figure 22. The dashed black line is unity, and the gray lines represent a 1% deviation from unity. Errorbars represent uncertainty relative to the error models of both instruments explained in the text. All data shown represents co-located VZA < = 35°.

flight, which briefly tilted the AirHARP instrument off-nadir. Pitch surfing may grow the pixel projection at far angles and adds uncertainty in our interpolation of these angles in the gridding stage. It is also suggested that the RSP pointing knowledge is no better than 1° (Alexandrov et al. 2012), so intercomparisons at further angles may be complicated by larger projections, angular misregistrations, and any surface variations. The wider angles that disagree beyond 1% in the Figure 22 comparison are desert cases (red in Figure 22). If pointing misregistration is a major factor, the angular signals from the ocean may be more robust against slight changes in pointing, than desert surfaces. Figure 22 does not show the same differences in the ocean scenes (blue) for these angles and channels.

There may be other, minor impacts to the data that are also affecting the comparison in general. For one, the lab flatfield calibration is less robust at large VZA. Far-forward/aft detector stripes are much narrower than those around nadir (by a factor of 5 at narrowest) and more challenging to illuminate in a full FOV capture. In order to image the full aperture of the traceable integrating sphere at NASA GSFC, the AirHARP instrument also images some of the baffle structure inside the sphere that covers the incandescent bulbs. These structures appear at the edges of the FOV and limit the amount of usable pixels for flatfield characterization.

Furthermore, the AirHARP 870 nm DOLP measurements carry a larger uncertainty in general due to lower quantum efficiency than the other channels. Even so, the overall structure of the RSP signal is reproduced by AirHARP instrument across two different scenes, a wide range of view angles, and within statistical uncertainty for most angles. However, even despite these challenges, these results show the strength of our simple and efficient telecentric technique. The accuracy of this calibration is demonstrated indirectly in AirHARP Level 2 aerosol and cloud retrieval studies in Puthukuddy et al. (2021) and McBride et al. (2020), as well.

It is also important to note that cross-validation between instruments cannot determine which instrument is "more correct", just how well they both agree over the range of angles, channels, and targets they measured. There is inherently some error associated in treating RSP as a reference, however, the RSP instrument is considered a community standard MAP, given its long-term stability in DOLP (van Harten et al. 2018) and successful comparisons with other instruments and models (Alexandrov et al. 2016, Knobelspiesse et al. 2018, Smit et al. 2019, Gao et al. 2020). The community anticipates a third-party intercomparison study that compares the measurements of all ACEPOL polarimeters with each other, vector radiative transfer models, and other co-located satellite instruments.

Section 4: Conclusions

The AirHARP calibration scheme generates a polarization accuracy of 0.5% DOLP in lab settings and reproduces the structure of natural targets relative to other co-located polarimeters. The telecentric calibration scheme is as effective as it is simple. It is also possible in a variety of environments: in space, where physical access is impossible, and during field campaigns, where time and access to the instrument is limited. If a flatfield measurement is done regularly and consistently, the performance of the entire FPA can be traced through a range of temperatures and humidity environments. The upcoming HARP2 instrument on the NASA PACE mission will include an internal calibrator to validate the full FOV performance throughout the life of the mission.

The telecentric technique can be used for vicarious calibration with field data alone, too. In the lab calibration, we used a rotating polarizer-sphere setup and pixels at the center of the lens to calculate the characteristic matrix. This is a special case. In general, any polarized target viewed from at least three different angles may provide enough information to trend the characteristic matrix. It is important that the target is viewed from significantly different geometry (optimally with views parallel and perpendicular to the solar plane, and/or at attack

angles 60° apart). This achieves the highest discrimination between polarization states and therefore the highest calibration accuracy (Tyo et al. 2006). Therefore, sunglint, cloudbow, dry lake, salt flat, aerosol plume, polar ice, and other natural targets can be excellent homogeneous and/or stable vicarious calibration targets. Measurements of these targets, combined with an internal flatfield measurement, allows for an effective and efficient trending of the instrument. It is very important that these are well-modeled though, as these corrections will take on any uncertainty related to assumptions made about the atmosphere.

The telecentric technique can also be used to cross-calibrate HARP against other polarimetric instruments. For example, any bias in the comparison of reflectance in Figure 22 could generate a radiometric correction factor that could be applied to the characteristic matrix in Eq. (20). Because the radiometric *k-factor* applies to the entire matrix, a single co-located intercomparison between like instruments is enough to correct the measurement. Using co-located instruments in this way also transfers their uncertainty in geolocation, measurement accuracy, and pointing. Nevertheless, it is invaluable over ill-modeled targets and/or validating against solar or lunar views. The HARP science team is currently evaluating how this telecentric technique can improve the in-flight calibration of AirHARP and HARP CubeSat data. We anticipate these methods will be used during the HARP2 deployment in 2023 and beyond.

In conclusion, this chapter develops and demonstrates an adaptable and physics-based HARP calibration pipeline for use in the lab, field, and in space. The mathematical treatment of the calibration is informed by the optical design and the lab validation of the calibration coefficient and a simple field example of wide FOV intercomparison is discussed. This chapter demonstrated that the AirHARP instrument measures DOLP to a 0.5% accuracy level (0.25% RMS) in the lab. This chapter shows that HARP meets current community requirements for modern aerosol retrievals, and in particular, upcoming missions such as NASA PACE and AOS, which have solicited the HARP design as a potential candidate for

cloud/aerosol measurements. In the field, wide FOV AirHARP measurements are compatible with a similar multi-angle polarimeter to 1% in both reflectance and DOLP. These results are reasonable given the challenges of the field environment. However, this work can be improved and optimized, especially relative to the limitations presented in Section 3.2.2. In the next chapter, we explore how this calibration allows for an unprecedented spatial retrieval of cloud droplet size distribution properties over marine stratocumulus clouds and the implications those results on current and future Earth remote sensing

Section 5: Acknowledgements

The work presented in this chapter is part of a forthcoming publication in AMT, in open access format (anticipated citation below, to be submitted no earlier than December 2022):

McBride, B. A., Martins, J. V., Cieslak, J. D., Fernandez-Borda, R., Puthukkudy, A., Xu, X., Sienkiewicz, N., Cairns, B., and Barbosa, H. M. J., *Pre-launch calibration and validation of the Hyper-Angular Rainbow Polarimeter (HARP) instruments*, Atmospheric Measurement Techniques, 2023 (in prep).

I would like to personally thank J. Vanderlei Martins, J. Dominik Cieslak, Roberto Fernandez-Borda, and Lorraine A. Remer for fantastic discussions, insights, and contributions to this work over the years. Special thanks to Henrique M. J. Barbosa for supporting AirHARP in the field with me during the ACEPOL campaign and helping with field calibration, flight planning, and mid-flight troubleshooting. RSP data used in this study is available at the NASA ACEPOL Data Archive (https://www-air.larc.nasa.gov/missions/acepol/index.html) and I acknowledge the RSP PI, Brian Cairns, for public access to this data. Kirk Knobelspeisse, Richard Ferrare, and Sharon Burton were

instrumental in planning and organizing the ACEPOL campaign and we thank the flight staff at the NASA Armstrong Research Center for steady flights and AirHARP in-flight operation. I graciously thank John Cooper and Jim Butler at NASA GSFC for their continued support of the HARP missions and allowing the HARP team to use the GSFC calibration facilities for radiometric, polarimetric, and spectral calibration over the years. I also thank Anin Puthukkudy, Noah Sienkewicz, and Xiaoguang Xu for excellent discussions on HARP on-orbit/vicarious calibration and data processing. Finally, UMBC students Kailas Mehta, Jesse Sheldon, Frank Harris, Gordon McDonnell, and Tuvia Rappaport made substantial contributions to the early development of the concepts in this chapter and lab testing of AirHARP.

This work was supported by the NASA Earth and Space Science Fellowship (grant no. 18-EARTH18R-40) under the NASA Science Mission Directorate from 2016 to 2019.

Chapter 4: Spatial distributions of cloud droplet size properties from Hyper-Angular Polarimeter (HARP) measurements

In the previous chapter, an efficient and robust HARP calibration was demonstrated. The AirHARP instrument can achieve community benchmark accuracy requirements in the lab. On-orbit, this calibration produces a reasonable level of agreement across the entire FOV, compared to measurements from a like polarimeter. These calibrated reflectances can be used to infer microphysical information about our atmosphere, too. This chapter explains how HARP measurements can provide a detailed characterization of the cloud droplet size distribution (DSD). The wide HARP swath, hyper-angular, polarized sampling in the 670 nm channel and the calibration developed in Chapter 3 help frame the unprecedented cloud retrievals that are possible with HARP datasets.

Section 1: Introduction

Subsection 1.1: Cloud microphysics and climate relevance

Clouds are one of the most uncertain aspects of our climate system. Clouds are highly variable and well-dispersed across the globe. They play a dual role in distributing energy: they trap infrared radiation in our atmosphere and reflect shortwave radiation back to space. This energy distribution is the key unknown in our understanding of climate change. As the planet warms, the way clouds interact with longwave and shortwave radiation may change. Cloud properties control these impacts. Measurables such as optical thickness (COT), thermodynamic phase, cloud-top temperature, height, cloud fraction, liquid and ice water path and content, and DSDs can help scientists track and decouple cloud feedbacks and growth from scattering and absorption. For climate applications, scientists need to measure these properties in a global context and over long temporal scales.

Clouds have a close relationship with aerosols, too. Aerosols drop the energy barrier required for condensation and serve as nucleation sites (Petters and Kreidenweis, 2007) for liquid water and ice clouds in our atmosphere. When aerosols are entrained into a cloud, they can set off a positive condensation feedback loop. In some cases, the opposite occurs: they dry out the local atmosphere and evaporate smaller droplets (Hill et al., 2009; Small et al., 2009). Aerosols can invigorate convective clouds (Altaratz et al., 2014) and suppress the development of other clouds (Koren et al., 2004), depending on the aerosol and meteorological properties of the local atmosphere. This complexity is a major source of uncertainty related to understanding global radiative forcing and predicting climate change (Boucher et al., 2013; Rosenfeld et al., 2014; Penner et al., 2004; Coddington et al., 2010). The remainder of this chapter will focus on liquid water clouds, but ice and aerosol-cloud interaction may be discussed where relevant.

A major link between the radiative and microphysical climate impacts of liquid water clouds is the DSD. The liquid water cloud DSD is often represented with two or more driving parameters (Feingold and Levin 1986; Alexandrov et al., 2015). The cloud droplet *effective radius* (CDR or r_{eff}) and *effective variance* (CDV or v_{eff}; Hansen and Travis, 1974) are popular ones. These describe a unimodal gamma DSD and represent the mean droplet size and dispersion relative to the scattering cross section of the droplet. The mathematical description of these parameters is discussed in later sections.

Aerosol effects on cloud microphysics are strongly tied to the CDR (Twomey, 1977, Albrecht, 1989). In a general example, aerosol loading generates competition for condensation sites and leads to smaller droplets (if liquid water content is kept constant). This process can delay rainout and extend the lifetime of the cloud. In regions of heavy aerosol loading, the number of smaller droplets increase, leading to a brighter cloud compared to a low loading scene. Finally, excess SW scattering due to a brighter, longer-lived cloud may result in a

net cooling of the planet (Haywood and Boucher, 2000; Lohmann et al., 2000, and references therein).

Typically, studies that connect the microphysical and radiative properties of clouds do so by tracking changes in CDR only, with no direct sensitivity to CDV (Feingold et al., 2001; Platnick and Oreopoulos, 2008). CDV is a proxy for the breadth of the DSD and may encode information on cloud growth processes such as collision–coalescence, aerosol or dry air entrainment, evaporation, and the initiation of precipitation in different parts of a cloud. Not all clouds share the same relationship between microphysics and radiation, but the key to understanding the connection lies in the microphysics of size distributions. Only satellite instruments allow us to make long-term radiative-microphysical links for different cloud types, over large and small spatial and temporal periods, and without empirical assumptions. Also, satellite measurements of cloud DSDs enhance global models that predict future climate scenarios and cloud feedbacks (Stubenrauch et al., 2013).

Subsection 1.2: Retrievals of cloud droplet effective radius, optical thickness, and effective variance

There are currently two methods used to retrieve CDR from spaceborne instruments. The first is the widely used radiometric bi-spectral retrieval, first proposed by Nakajima and King (1990). This retrieval is main operational algorithm used with MODerate resolution Imaging Spectroradiometer (MODIS) and other multi-band radiometer data (Platnick et al., 2003, 2017; Walther and Heidinger, 2012). The bi-spectral retrieval uses the difference in cloud information content observed by shortwave infrared (i.e., 1.6, 2.1, or 3.7 μm) and visible (i.e., 0.67 or 0.87 μm) channels to retrieve CDR and COT simultaneously for a cloud target. Figure 24 shows a bi-spectral retrieval of CDR for a partial MODIS Terra granule over the Pacific Ocean. The CDR-COT phase space shown in Figure 24a is pre-computed for a wide array of geometries using a radiative transfer model. In the retrieval, the VIS-SWIR re-

flectance pair maps to a location in CDR-COT phase space. A spatial map of CDR and COT is possible if a granule contains a multi-pixel cloud field with suitable geometry (Figure 24c). This allows for context and further analysis of cloud structure, ambient aerosol, and cloud typing and phase.

A spatially resolved cloud DSD retrieval is also possible using multi-angle polarimetric measurements. This algorithm compares polarimetric measurements of the liquid water cloudbow to pre-computed Mie polarized phase functions. The result is a direct retrieval of CDR and CDV from the best matching Mie profile. Notably, the polarimetric method is the only one that can retrieve CDV at the pixel (Breon and Goloub, 1998; Alexandrov et al., 2015; Di Noia et al., 2019), though both methods are sensitive to CDR. COT may be retrieved with assistance from an external radiative transfer simulation (Alexandrov et al., 2012). More details on this retrieval technique are discussed in Section 4.5.

The radiometric and polarimetric methods are not always compatible, though.

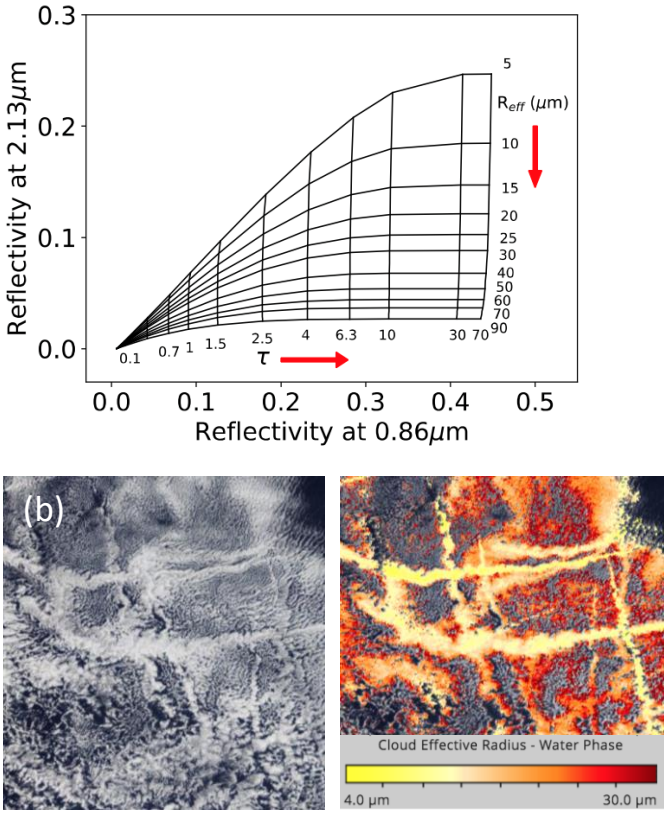

Figure 24. The phase space of the radiometric bi-spectral retrieval of CDR and COT, shown in (a). For a total reflectance image with specific geometry (MODIS Terra over the Pacific Ocean on October 21, 2019, b), each 0.87um-2.13um reflectance pair maps to a CDR and COT in (a). The resulting product is a spatial map of CDR over the cloud field (c), COT not shown. The legend is valid for LW CDR between 4 and 30um. The top figure is reprinted from from Yang et al. (2018) under the CC-BY-4.0 license. The bottom two panels are retrieved from NASA Worldview (https://worldview.earthdata.nasa.gov/)

The bi-spectral method is more sensitive to multiple-scattering of photons in the cloud layer. Three-dimensional cloud effects, including shadowing and illumination (Marshak et al., 2006; Varnai and Marshak, 2002), can bias radiometer retrievals of CDR and COT done on clouds observed at high latitudes and large solar zenith angles. The polarimetric retrieval is sensitive to scattered photons from a COT up to ~3, lessening the impact of this effect (Miller et al., 2018). Sub-pixel clouds and spatial heterogeneities can affect both methods, as discussed in later sections (Zhang and Platnick, 2011; Breon and Doutriaux-Boucher, 2005; Shang et al., 2015). Furthermore, the bi-spectral technique is not sensitive to CDV and uses a pre-established value (typically from 0.1 to 0.15, Arduini et al. 2005) that may not be valid for all liquid water cloud targets and all regions of the world. CDV values in the literature have been retrieved as low as 0.003 and as high as 0.4 for marine stratocumulus targets (McBride et al. 2020, Alexandrov et. al 2016, Shang et al. 2019). Finally, the polarimetric technique requires a target observed over many along-track scattering angles, whereas the bi-spectral method only requires a single view angle. This distinction typically drives the design of cloud-measuring polarimeters, since this might mean more cameras, a wide FOV, or a scanning element that can sweep through a wide range of view angles.

Subsection 1.3: Measurement requirements for cloud DSD retrieval

Multi-angle polarimetric measurements have other advantages for cloud characterization beyond the retrieval of these two DSD parameters. Retrievals of cloud thermodynamic phase (Riedi et al., 2010; Goloub et al., 2000), ice crystal asymmetry (van Diedenhoven et al., 2013), aerosol above cloud (Waquet et al., 2013), and COT (Xu et al., 2018; Cornet et al., 2018) are considerably improved with the addition of polarized observations. At the time of this writing, only POLDER and HARP CubeSat instruments have demonstrated the polarized retrieval of cloud DSD properties from space. However, several aircraft instruments, including the AirMSPI, the RSP, and the subject of this paper, the Airborne Hyper-Angular Rain-

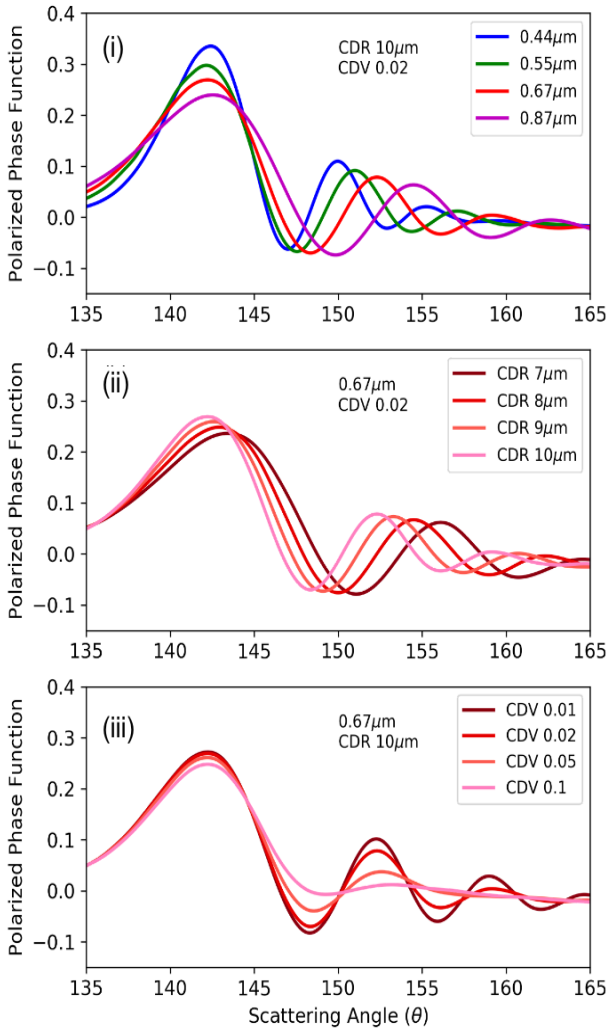

Figure 25. The angular structure of the polarized cloudbow as described by Mie simulations. Details described in text. This figure is reprinted from McBride et al. (2020) under the CC-BY-4.0 license.

bow Polarimeter AirHARP, have demonstrated improved sampling schemes, resolution, and accuracy.

Not all polarimetric measurements will achieve a high-quality retrieval of cloud DSDs. Multi-angle sampling at high angular density and moderate pixel resolution is necessary for an accurate single-wavelength retrieval. To resolve the cloudbow patterns from space and retrieve the CDR and CDV of the cloud, the multi-angle polarimetric instruments must satisfy a minimum viewing angle density (Miller et al., 2018). This density is related to scattering angle coverage and the range of droplet sizes present in the target pixel. Figure 25 shows theoretical Mie simulations for liquid water cloud droplets, which mimic the polarized cloudbow for values of CDR, CDV, and wavelength. The *location* of the supernumerary peaks in scattering angle encodes CDR, as shown in Figure 25 (ii). To resolve the CDV, the *amplitude* of the supernumerary peaks must be detected (Figure 25 (iii)). Polarimeters with coarser viewing angle separation for a single wavelength (i.e., >2° at 0.67 µm for typical droplets <24 µm; Miller et al., 2018) may not distinguish these features.

Instruments like POLDER, which samples at 14 unique viewing angles separated by 10°, may not have the native angular resolution to identify wide versus narrow DSD clouds at specific geometries (Miller et al., 2018, Shang et al., 2015). POLDER retrievals must aggregate pixels to 100 km+ sizes to access the full scattering angle coverage in Figure 25 and perform an accurate retrieval (Breon and Goloub, 1998). However, this limits their retrievals to large-scale, homogenous marine stratocumulus clouds with narrow DSDs. A study by Breon and Doutriaux-Boucher (2005) that compared POLDER polarized and MODIS radiometric retrievals showed a CDR bias of 2 μm that could not be decoupled from the large POLDER superpixel. A later study by Alexandrov et al. (2015), with the RSP and the Autonomous Modular Sensor spectrometer, found that the CDR values retrieved by the two methods agree at narrower resolution. Shang et al. (2015) improved the POLDER retrieval by reducing the superpixel to 42 km. Even though sampling at higher resolution produced gaps in cloudbow coverage, they still found heterogeneity inside the original 150 km superpixel. In a follow-up paper, Shang et al. (2019) showed that the POLDER retrieval is sensitive to a wider CDR and CDV range and can be done at a lower 40–60 km resolution when considering all three polarized wavelengths (490, 670, and 865 nm) in the retrieval. Until 2021, no instrument had performed a polarimetric cloud retrieval from space with both co-located pixel resolution less than 40 km and high native angular density (<10◦). The Figure 26 example from a May 5 2020 observation from the HARP CubeSat over South America shows an 8x8km retrieval of cloud droplet DSDs using this technique. Although the results are still preliminary, HARP will reduce POLDER's retrieval footprint by a factor of 5 or more. These goals are essential to studying the spatial distribution of DSDs for other clouds such as heterogeneous, broken, and popcorn cumulus cloud scenes.

Aircraft instruments like RSP, AirMSPI, and AirHARP have demonstrated new technologies that improve upon the POLDER retrieval heritage. RSP samples at 150+ viewing angles, separated on average by ~0.8°, and does so for a 250 m along-track pixel (Alexandrov et al., 2012b, 2015, 2016b). This advancement removes any large-scale homogeneity assumptions and allows for a *rainbow Fourier transform* on the data, one that retrieves the DSD itself, including multiple modes, without any assumptions on the distribution shape (Alexandrov et al., 2012b). RSP can sample other kinds of clouds, including broken and popcorn cumulus clouds, with this high angular and spatial resolution. The single-pixel cross-track swath of RSP, however, restricts its spatial coverage. RSP cannot form an intuitive image of the scene, requires specific solar angles for cloudbow coverage (Alexandrov et al., 2012b), and input from other coincident instruments for off-nadir context (Alexandrov et al., 2016a). The AirMSPI instrument is a highly accurate push-broom imager capable of discrete, programmable viewing angles on the same target, but it has the same angular limitations as POLDER

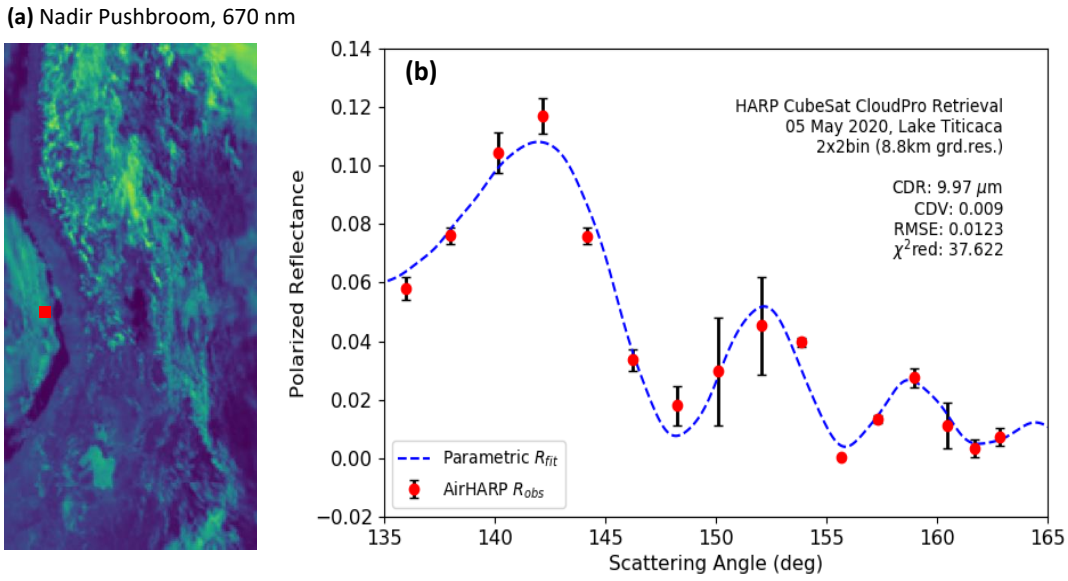

Figure 26. HARP CubeSat 670 nm total reflectance nadir observation over Lake Titicaca, South America on May 5 2020 shown in (a). The red square is the general location of the cloud retrieval in (b), size not to scale. Co-located, multi-angle polarized reflectance data (red points) with 1-sigma superpixel standard deviation (errorbars) are fit to pre-computed Mie profiles and the closest match is found (blue curve).

in this *step-and-stare* mode. AirMSPI also samples in a *continuous sweep* mode that trades co-located information for scattering angle coverage (Diner et al., 2013). This mode gives full visual coverage on the cloudbow but limits the retrieval to a line cut of binned pixels along the solar principal plane. A study by Xu et al. (2018) extended the AirMSPI line-cut retrieval to the entire continuous sweep image of the cloudbow with assistance from image-specific empirical correlations between COT, CDR, and CDV. This line-cut polarimetric technique requires a droplet size homogeneity assumption over the full line cut of the cloudbow, which may steer the retrieval towards wider DSDs. Imaging polarimeters, like POLDER, the 3MI (Fougnie et al. 2018) successor to POLDER, AirMSPI, and HARP have larger access to cloudbow geometry with less dependency on flight track or time of day. This kind of sampling could provide global coverage from a polar orbit within a few days. This coverage is an invaluable asset to tracking, comparing, and modeling trends in global aerosol-cloud distribution or cloud type.

Despite these advances, polarimetric cloud information is not yet a part of our climate record. POLDER, which performed Earth science measurements on three platforms from 1995 – 2011, is the only spaceborne polarimeter with decadal observations. Even so, none of its polarized retrieval products are operational. Our current satellite record is dominated by radiometric retrieval products which may be complemented and extended by upcoming polarimeter missions (Remer et al. 2019, Hasekamp et al. 2019, Fougnie et al. 2018).

There is a strong interest in the Earth science community in a multi-angle polarimeter concept like AirHARP for cloud retrievals with a wide swath for global coverage, high accuracy in polarization, high angular density for cloudbow retrieval, and narrow ground resolution (Remer et al., 2019; Dubovik et al., 2019). An instrument of this kind in space for decadal periods could greatly benefit our climate record and the science of clouds of different shapes, sizes, and source regions.

This chapter will detail the cloud droplet retrieval framework in Section 2, followed by applications of the retrieval on a stratocumulus cloud deck observed by AirHARP during the NASA Lake Michigan Ozone Study field campaign in 2017 in Section 3. Section 4 and 5 The fine spatial resolution of the retrieved DSD parameters is used to explore the information content of the retrieval itself and relate the spatial variability of the results to cloud processes in Section 4 and 5. Section 6 discusses the uncertainties and current limitations of the retrieval. This study is extended in Section 7: an AirHARP simulator is developed to validate the LMOS results in general over large-eddy-simulated (LES) marine stratocumulus cloud fields. The chapter concludes with a look ahead to HARP CubeSat and HARP2 deployment and data content. The study below refers specifically to AirHARP datasets, but the HARP term may be used when discussing general performance expected from any of the HARP instruments.

Section 2: Cloud retrieval framework

A simple treatment of the parametric retrieval is described below, with main components derived from Breon and Goloub (1998), Alexandrov et al. (2015), and Diner et al. (2013). A scattering matrix (below) describes how incident light is transformed after interacting with a medium, like an aerosol particle or cloud droplet,

$$\begin{bmatrix} I \\ Q \\ U \\ V \end{bmatrix}_{sca} = \frac{\sigma_{sca}}{4\pi R^2} \begin{bmatrix} P_{11} & P_{12} & P_{13} & P_{14} \\ P_{21} & P_{22} & P_{23} & P_{24} \\ P_{31} & P_{32} & P_{33} & P_{34} \\ P_{41} & P_{42} & P_{43} & P_{44} \end{bmatrix} \begin{bmatrix} I \\ Q \\ U \\ V \end{bmatrix}_{inc}, \tag{24}$$

where a Stokes column vector describes the incident beam (subscript "inc"), in total radiance (I) and polarized radiance (Q, U, V), and the scattered beam by a similar vector with subscript "sca". The P_{ij} matrix elements [1/sr units] scale by the scattering cross section (σ_{sca}) of the particle, weighted by the inverse of its surface area. These P_{ij} elements encode size, shape, and composition information about an arbitrary medium. Eq. (24) can be simplified for liquid water droplets observed at cloud top because they are spherical, randomly oriented, and mir-

ror symmetric (Hansen and Travis, 1974). Also, circular polarization at the top of the atmosphere (TOA) is negligible and not measured by AirHARP, so the fourth column and row are neglected. With these changes, Eq (24) is reduced to

$$\begin{bmatrix} I \\ Q \\ U \end{bmatrix}_{sca} = \frac{\sigma_{sca}}{4\pi R^2} \begin{bmatrix} P_{11} & P_{12} & 0 \\ P_{12} & P_{22} & 0 \\ 0 & 0 & P_{33} \end{bmatrix} \begin{bmatrix} I \\ Q \\ U \end{bmatrix}_{inc} . \quad (25)$$

Because sunlight incident on the atmosphere is unpolarized (*Qinc*, *Uinc* = 0), Eq. (25) further simplifies to

$$I_{sca} = \frac{\sigma_{sca}}{4\pi R^2} P_{11} I_{inc}, \quad (26)$$

and

$$Q_{sca} = \frac{\sigma_{sca}}{4\pi R^2} P_{12} I_{inc}. \quad (27)$$

For single-scattered photons, the scattered intensity (I_{sca}) is proportional to the first matrix element, P_{11} and its polarization (Q_{sca}) to the second, P_{12}, called the *polarized phase function*. U_{sca} does not contain any structural information in the scattering plane, though it may show a weak linear slope in the presence of non-cloud scatterers (Alexandrov et al., 2012a). For this reason, Q_{sca} in the scattering plane represents the entire polarized signal. Note that dividing Eq. (27) by Eq. (26) removes dependence on the incident intensity. Therefore, the *signed degree of linear polarization* (Q/I) is ratio of polarized to total phase functions (P12/P11) in the scattering reference plane.

At the top of the atmosphere (TOA), remote sensors do not observe the scattering from individual droplets but the bulk signal from the droplet distributions. This limitation is due to measurement resolution and scale. The bulk Mie polarized phase function, $\langle P_{12} \rangle$, is a weighted sum of optical properties:

$$\hat{P}_{12}(\lambda) = \frac{\sum_i P_{12,i} \omega_i C_{ext,i}}{\sum_i \omega_i C_{ext,i}}, \quad (28)$$

where ω is the single-scattering albedo (SSA, 1 for water droplets), and C_{ext} is the scattering cross section, which itself is composed of the scattering efficiency (Q_{ext} = 2 for cloud droplets, Hansen and Travis 1974) and a size distribution weighted by droplet scattering cross section. Non-precipitating cloud droplets at cloud top are often described by a unimodal gamma size distribution (Breon and Goloub 1998):

$$n(r) = N_0 \left(\frac{r}{r_{eff}}\right)^{3v_{eff}-1} \exp\left(\frac{1}{v_{eff}}\left[\left(\frac{r}{r_{eff}}\right) - ln\left(\frac{r}{r_{eff}}\right) + 1\right]\right), \tag{29}$$

where N_0 is the droplet number, r stands for droplet radius (a range of values). The other two parameters are free and describe the scattering properties of the DSD: the effective radius (r_{eff}), and the effective variance (v_{eff}). These are defined in Hansen and Travis (1974) as weighted integrals:

$$r_{eff} = \frac{\int_0^\infty \pi\, r^3\, n(r)\, dr}{\int_0^\infty \pi\, r^2\, n(r)\, dr}, \tag{30}$$

and

$$v_{eff} = \frac{\int_0^\infty \pi\, (r - r_{eff})^2\, r^2\, n(r)\, dr}{r_{eff} \int_0^\infty r^2\, n(r)\, dr}, \tag{31}$$

The effective radius is the droplet volume weighted by surface area. Note that the effective variance goes to zero when $r = r_{eff}$. In this format, polarized cloud retrievals are compatible to the description of r_{eff} and v_{eff} that is currently used in the radiometric bi-spectral retrieval discussed above. These definitions are easily converted to the geometric standard deviation and radius used in large-eddy simulations of cloud fields (Kazil et al. 2017) and other DSD models. Therefore Eq. (29), (30), and (31) are convenient and suitable for comparing to and complementing cloud products in our current and future climate record.

Polarized reflectance observed at TOA from liquid water cloud droplets at cloud top, assuming single-scattering, is proportional to P_{12}:

$$\mathcal{R}_{obs} = \frac{4}{\pi}(\mu_0 + \mu)\left[\frac{-\pi Q_{sca}}{\mu_0 F_0}\right], \tag{32}$$

where the cosines of the view zenith angle (μ_0) and solar zenith angle (μ) and the band-weighted extraterrestrial solar irradiance (F_0) rescale the polarized radiance (Q_{sca}). The bracketed term is the *polarized reflectance* (ρ_P), and a similar expression gives the total reflectance (ρ) using the Stokes parameter I_{sca} in place of $-Q_{sca}$. Eq. (32) comes from a simplification of the radiative transfer equation for non-absorptive media (SSA = 1). Subsequent figures use $L_{670\,nm}$ for I_{sca} and $L_{P,670\,nm}$ for Q_{sca} radiances, where applicable, and anytime the term *intensity* is used, it corresponds to a radiance measurement, not reflectance, unless explicitly noted. Radiance and reflectance are interchangeable in terms of the information content shown in the figures because this work only uses a single spectral channel. Corrections to Eq. (32) for Rayleigh scattering at observation height are performed in prior studies, equivalently before or during the fitting step (Breon and Goloub, 1998; Diner et al., 2013, Alexandrov et al., 2015). This study accounts for Rayleigh effects in a cosine term in the fitting step.

The retrieval compares Eq. (32) to a parametric model and infers the CDR and CDV from the best-fitting P_{12} simulations:

$$\mathcal{R}_{fit}(\lambda, \vartheta_{scat}) = \alpha P_{12}(\lambda, \vartheta_{scat}, CDR, CDV) + \beta\, cos^2\, \vartheta_{scat} + \gamma. \tag{33}$$

The parametric fit scales the theory, Eq. (32), to observations, Eq. (27), inside the polarized cloudbow scattering angle range ($135° < \vartheta_{scat} > 165°$; Di Noia et al., 2019; Shang et al., 2015) with three free parameters (α, β, γ). Corrective factors for aerosol above cloud, cirrus, sun glint, molecular scattering, and surface reflectance signals are weak functions of scattering angle (Diner et al., 2013; Alexandrov et al., 2015). The parameter α is related to cloud fraction (Breon and Goloub, 1998) and the droplet number, N_0, from the Eq. (29) DSD. Therefore, explicit knowledge of N_0 and/or cloud fraction is not required, and COT is not retrievable without assistance from an external radiative transfer simulation.

A prescribed lookup table (LUT) in CDR and CDV drives the parametric fit, ranging between 5 and 20 μm in CDR (Δ=0.5 μm), and CDV values of 0.004 to 0.3 at variable intervals, like Alexandrov et al. (2015), with Δ values indicating the step size. The LUT is dense for CDV<0.1: most of the supernumerary bow sensitivity exists below this level and is considerably reduced for CDV>0.1, as shown in Figure 24b. Polarized reflectance measurements are corrected via Eq. (32) and fit in a nonlinear least-squares process to Eq. (33), checking all possible combinations of CDR and CDV in the LUT. The root mean square error (RMSE) and reduced chi-square statistic (χ^2) of the least-squares process verify all LUT comparisons:

$$RMSE = \sqrt{\frac{1}{n}\sum_i^n \left(\mathcal{R}_{fit,i} - \mathcal{R}_{obs,i}\right)^2} \tag{34}$$

and

$$\chi^2 = \frac{1}{n-5}\sum_i^n \frac{\left(\mathcal{R}_{fit,i} - \mathcal{R}_{obs,i}\right)^2}{{\sigma_{obs,i}}^2}. \tag{35}$$

The χ^2 verifies that the data are best described by the fit in Eq. (33) with $n-5$ degrees of freedom (for three fit parameters, CDR, and CDV), where n is the number of measurements in the cloudbow scattering angle range for that pixel. Like Alexandrov et al. (2015), a fine-scale interpolation is performed on the LUT at 10 times the original resolution in CDR and CDV. Retrievals are accepted immediately for χ^2 values 0.5 to 1.5. In this range, our error estimate is consistent with the minimized fit. However, a χ^2 outside this range does not always mean the fit is poor. The physics of the cloud field may justify solutions with χ^2 beyond 1.5. Therefore, the fit must also satisfy an RMSE threshold of 0.03. If not, the fit is rejected, and the pixel is masked. These diagnostics were found in a sensitivity study on synthetic AirHARP cloudbow retrievals and an estimation of the error in the actual data.

There are several reasons for this two-factor diagnostic. First, the signal-to-noise ratio of the superpixel is not the only measurement error. Optical etaloning (Oxford Instruments 2020) in this AirHARP dataset will also add uncertainty. This effect is weak compared to the

signal and nearly random angle to angle, which contributes an extra 1σ contribution in each superpixel. Therefore, the superpixel uncertainty, σ_{obs}, used in Eq. (35) is two times the standard deviation of the superpixel bin.

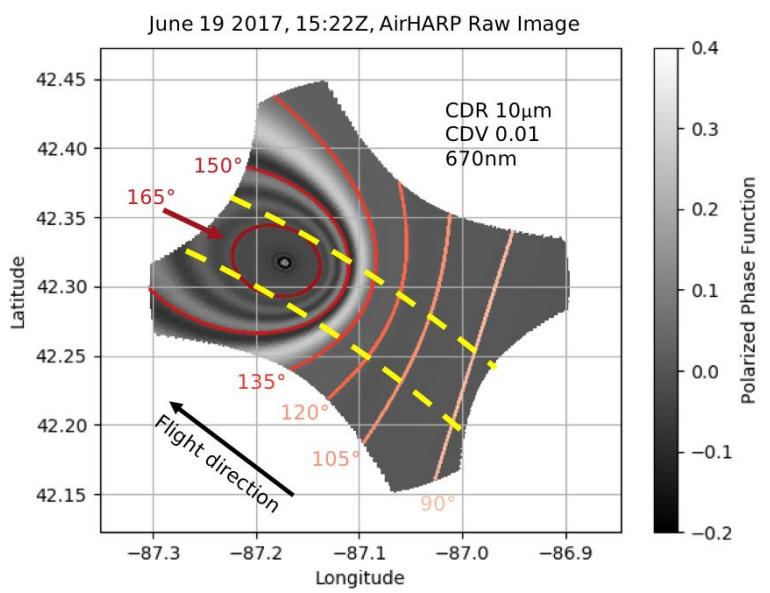

Figure 27. The scattering angle coverage typical of an instantaneous AirHARP wide FOV capture of a marine stratocumulus cloud field. Because AirHARP captures hyper-angle data along-track, only the pixels inside the yellow dashed lines may have the required scattering angle geometry for the retrieval. This figure is reprinted from McBride et al. (2020) under the CC-BY-4.0 license.

Second, when multiple DSDs exist inside a superpixel, the polarized signal may not agree with a signal that represents a single DSD (Shang et al., 2015). This retrieval will still try to find a representative DSD in the measurement and typically retrieves a wider DSD relative to the sub-pixel variability. Here, the χ^2 may be higher than 1.5, but the RMSE threshold may still allow a solution. This may also occur for observations of multi-layer cloud fields. Because the χ^2 depends on the uncertainty of the individual measurements, there is also a possibility of χ^2 values beyond 1.5 for narrow DSD retrievals. Figure 30a is an example where the AirHARP data clearly captures the cloudbow pattern but the χ^2 is 2.52. The RMSE threshold can preserve these cases.

Third, Breon and Goloub (1998) found that secondary and tertiary scattering events in the primary bow region (137–145° in scattering angle) can widen the polarized signal here relative to Mie simulations. Again, the RMSE may preserve a strong fit in the supernumerary region, where most of the DSD information content lies, even if primary bow structure is not consistent with our errorbars. These diagnostics also account for any artifacts that arise from

rotating our reference frame of polarization into the scattering plane and retrievals that converge artificially to the edges of the LUT. The retrieval will be rejected if both values exceed their expected ranges. More details on some of these effects are discussed in Section 6.

Section 3: AirHARP measurement relative to cloudbows

As the AirHARP instrument flies over a scene, each view sector captures a range of scattering angles unique to each of the 120 view sectors and wavelengths. Figure 27 shows an example of the AirHARP instantaneous scattering angle coverage for a simulated observation at 15:22 UTC over Lake Michigan on 19 June 2017 during the NASA Lake Michigan Ozone Study (LMOS) field campaign. The sub-solar geometry here allows for retrievals across the swath and along the entire length of the granule. Figure 27 shows how a simulated cloudbow would look in a single AirHARP snapshot if the entire detector could sample at 670 nm. This cloud field represents a CDR of 10 μm and CDV of 0.01, with the same solar and viewing geometry of the LMOS observation. Note that this is the scattering angle coverage for a single snapshot, and when AirHARP flew over this cloud deck, it took two snapshots every second. The target travels from the front of the detector to the back during this full angle observation. While clouds span the entire AirHARP image, only along-track pixel columns inside the yellow dotted lines in Figure 27 contain pixels that are eligible for the retrieval. This work does not perform a retrieval on any targets outside these lines. The reduced scattering angle coverage outside the yellow lines will truncate the signal from the supernumerary bows. It is important that the full scattering angle range is preserved in this retrieval because the supernumerary bows (145–165°) contain the majority of DSD information.

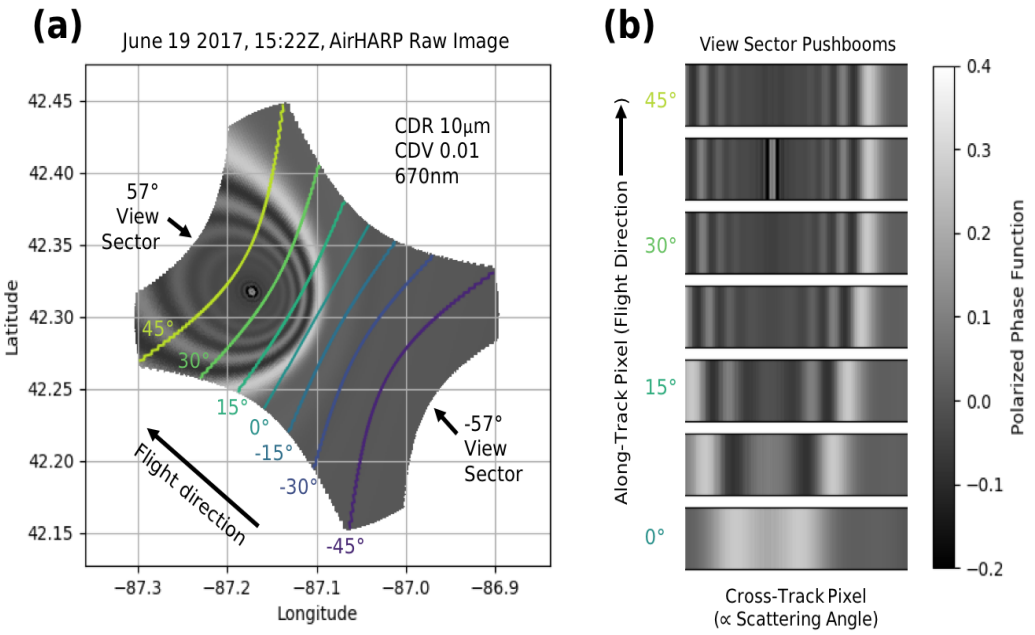

Figure 28. An example of how a wide FOV cloudbow measurement in a single snapshot (a) translates into single angle pushbrooms (b). The colored lines in (a) are constant along-track VZA and correspond to a pushbroom rectangle in (b). When all pushbrooms are georegistered to a common grid, a single pixel in common to all views can reproduce the cloudbow structure, if those pixels have the requisite geometry (see Figure 27). This figure is reprinted from McBride et al. (2020) under the CC-BY-4.0 license.

Figure 28 shows the view sector isolines of AirHARP over the same snapshot from Figure 27. The AirHARP wide FOV covers view sectors from ±57◦ but note that the cloudbow only covers a subset of these. Pushbrooms are made from individual view sectors as the instrument flies over the cloud field. Figure 28b shows examples of push brooms built from cloudbow content in Figure 28a isolines. The concentric cloudbow in the wide FOV capture transforms to a linear one in the pushbrooms. This occurs because each view sector only observes a specific cross-section of the cloudbow at any one time (Figure 28b). The structure of the cross section is maintained due to the viewing geometry of a single view sector and the uniformity of the cloud DSD in space. Figure 29 shows the actual AirHARP observation during LMOS, in total (top) and polarized reflectance (bottom), at view sectors near +38◦ during the same time and day used to simulate Figures 27 and 28. The red–green–blue (RGB) composite image of the polarized reflectance displays a similar cross-track cloudbow structure as

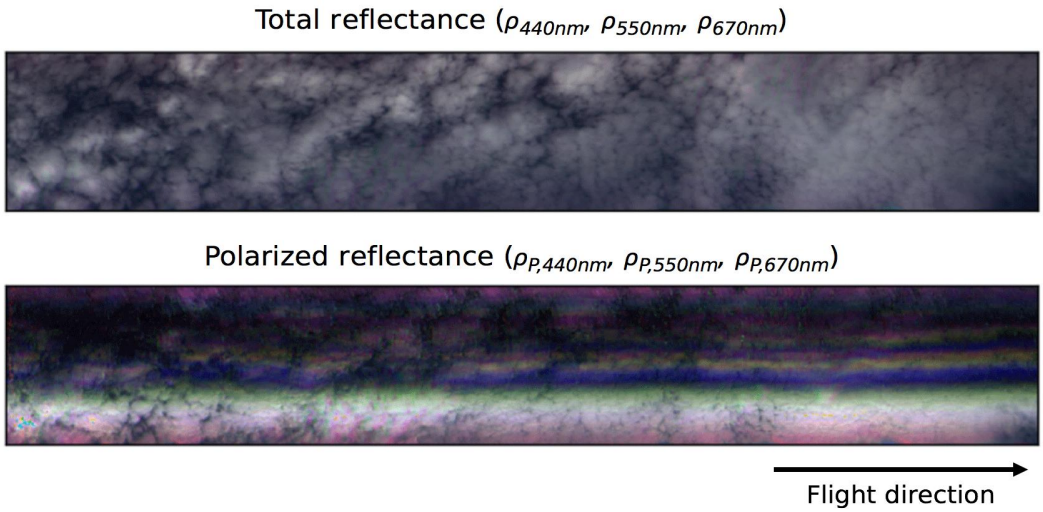

Figure 29. AirHARP forward pushbroom (~38° nadir VZA) RGB composite for total reflectance (top) and polarized reflectance (bottom) for the June 19, 2017 LMOS cloud case.. The scene stretches approximately 37km along-track and 5 km cross track, with a 50m pixel resolution. This figure is reprinted from McBride et al. (2020) under the CC-BY-4.0 license.

the pushbroom segments the Figure 28b simulation. The polarized reflectance image shows a wavelength separation in the cloudbow, which does not appear in total reflectance. Also, the appearance of the cloudbow in this push broom is highly variable compared to the simulation in Figures 27 and 28. This is due to heterogeneity and the 3D nature of the cloud field.

Figure 30 shows several examples of an AirHARP 200 m superpixel retrieval of different regions of the LMOS cloud field shown in Figure 29 using hyper-angular, co-located information. Error bars represent two times the standard deviation of the polarized reflectance in the superpixel. Superpixels are constructed from finer-resolution native pixels to increase SNR and mitigate other potential artifacts in the data. These artifacts will be discussed in Section 6. Note that Figure 30a and b represent narrow DSDs, though the difference in CDR causes a shift in the location of the observed supernumerary bows. Figure 30c and 37d are wider DSDs with higher CDV values. Note the absence of supernumerary bows in Figure 30c and d. The CDR values retrieved in Figure 30 are typical of non-precipitating stratocumulus cloud fields (Pawlowska et al., 2006), and CDV values are like those found by Alexandrov et al. (2015) using RSP measurements over marine stratocumulus.

The hyper-angle data used in this AirHARP cloud retrieval is captured over a short time window: it takes time for the AirHARP backward angles to image the same location on the ground as the forward angles. The differences in time depend on the instrument-level flight speed and the difference in altitude between the instrument and target. For the LMOS campaign, the difference between ±57° observations were 112 s (~2 min) for a nominal UC-12 flight speed of 133 m s^{-1} at 4.85 km of altitude above the cloud deck. Note that the actual aboveground altitude was 8 km, but the cloud deck was geolocated to a 3150 m height on average. Therefore, the hyper-angular retrieval requires cloud constancy over this time interval. The time interval between views with the largest angular separation is reduced to a minute, if

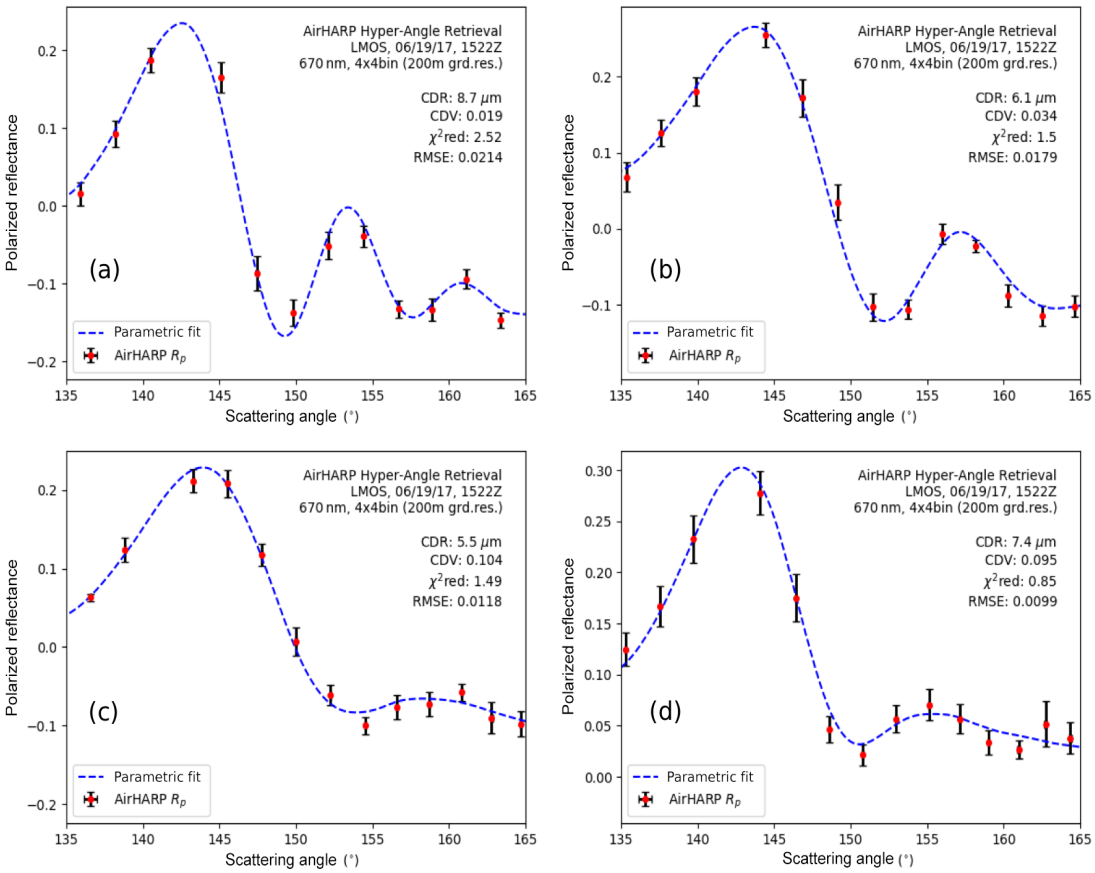

Figure 30. Several examples of the parametric fit retrieval applied to AirHARP cloudbow measurements at 200m superpixel resolution. Panels (a) and (b) are narrow DSDs and (c) and (d) are wider DSDs. Errorbars represent 2-sigma standard deviation of measurements in the superpixel. This figure is reprinted from McBride et al. (2020) under the CC-BY-4.0 license.

only the angles used in the cloudbow retrival are considered. A study with the HARP CubeSat at an estimated 400 km orbital altitude and 7.66 km s^{-1} ISS speed requires ~160 s (~2.5 min) for the same full-angular coverage over the same cloud target. In this way, the HARP hyper-angular retrieval assumes that the cloud DSD does not change significantly within this short time window.

Furthermore, any liquid water cloud pixel in the AirHARP wide FOV that samples scattering angles between 135 and 165° can be used to retrieve CDR and CDV. This constraint is used in several other polarimetric studies, though with a slight discrepancy on the start of the lower bound (Di Noia et al., 2019; Alexandrov et al., 2015). Shang et al. (2015) found that using a 137–165° scattering angle range as opposed to the operational POLDER 145–165° improved many of the CDR and CDV retrievals, specifically for CDR>15 µm (Shang et al., 2019). The upper bound of 165° is consistent between studies dating back to Breon and Goloub (1998): the bulk of the microphysical information lies in the

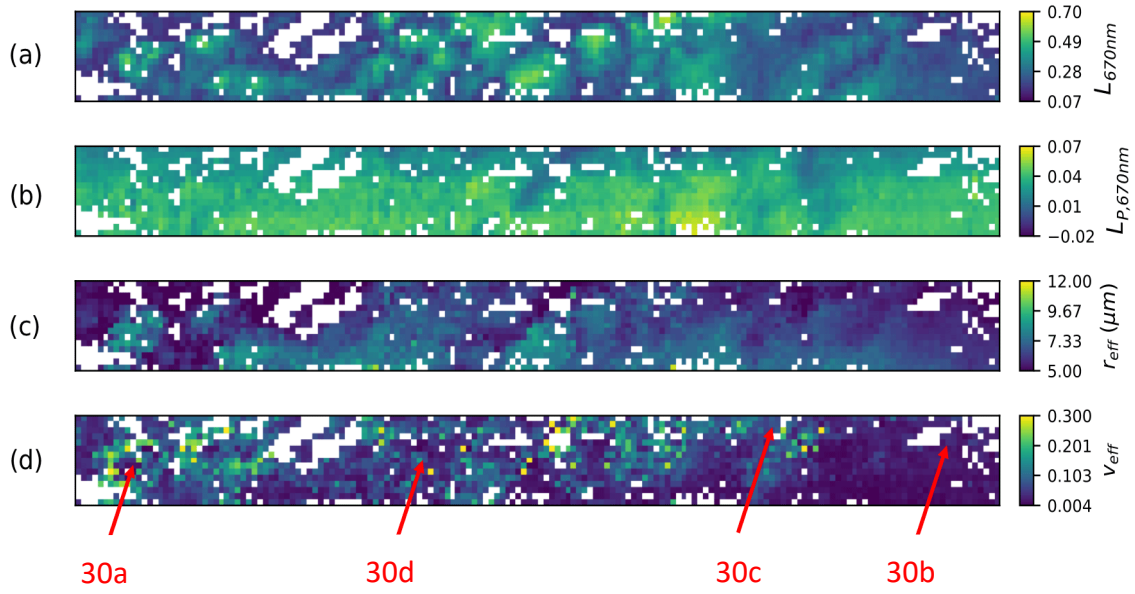

Figure 31. Nadir pushbroom images for 670 nm of total intensity (a) and polarized intensity (b), as well as the retrieved CDR (c) and CDV (d) for 200 m (4x4) gridded superpixels with the requisite scattering angle geometry. The four red arrows show the locations of the retrievals in Figure 30 (a-d). This figure is adapted from McBride et al. (2020) under the CC-BY-4.0 license. Modifications: red labels.

supernumerary bows, and the assumption of a structureless U_{sca} breaks down after this point (Alexandrov et al., 2012a). Figure 31 shows how individual pixel retrievals generate a spatial distribution of CDR and CDV for those that access this cloudbow scattering angle range. Each pixel is first conservatively masked for non-clouds using the nadir 670 nm intensity push broom (−0.003° VZA along the flight track) using a conservative threshold of 0.06 W m^{-2} sr^{-1} nm^{-1}. This was done to avoid cloud holes, thin cloud that could contribute more noise than useful signal, and views of Lake Michigan below. After masking, all pixels are aggregated to 4×4 resolution (200 m), and the polarized radiances ($L_{P,670\,nm}$) are converted into polarized reflectances via Eq. (32) before entering the retrieval process. The portion of the image capable of retrieval stretches 34 km along-track and 3 km cross-track.

Section 4: Retrieval validation

The distribution of CDR and CDV in AirHARP data is consistent with prior studies and physical phenomena. Because the cloud case observed during LMOS was heterogenous, there are several examples of how cloud substructure can give different retrievals. Figure 32 takes a few areas from Figure 31 and zooms in on their retrieval results. Figure 32b shows a uniform sector of the cloud field, described this way because of its visual homogeneity in both intensity and CDR as well as the small and consistent CDV retrievals (<0.1) over many pixels. The results here suggest that the supernumerary bows are well-defined and the cloud pixels have narrow size distributions (see Figure 30 for individual superpixel examples). Figure 32a shows a region of the same leg that is heterogeneous in CDV. The intensity and CDR distribution suggest that this area is a region of convection. Figure 32a shows larger CDR in the cloud core, or the region of the cloud with higher intensity, and smaller CDR retrieved on the periphery, where the intensity is lower. These definitions of cloud core and periphery use the connection between intensity and COT (Najakima and King 1990). In this work, intensity is used as a proxy for COT when discussing cloud core and periphery areas. This phenome-

non will be explored in more detail in the AirHARP data in the sections below. Large-eddy simulations (LESs) of similar heterogenous clouds show similar spatial distributions of intensity, CDR, and CDV (Miller et al., 2018), with one representative case shown in Figure 32c. Miller et al. (2018) simulate LES clouds using vertical weighting functions that consider the distribution of reflectance at the edges of the cloud (Platnick 2000).

While these simulations can assume any resolution, the AirHARP retrievals are performed at 200 m in this study and even coarser resolutions from space. The small-scale variability could be missed in current radiometric studies using MODIS or VIIRS data, for example, which assume constant CDV in their droplet size retrieval. This is one of the strongest benefits of polarized cloud retrievals: a quantitative measurement of heterogeneity through CDV information. This has serious implications for climate in terms of quantifying cloud de-

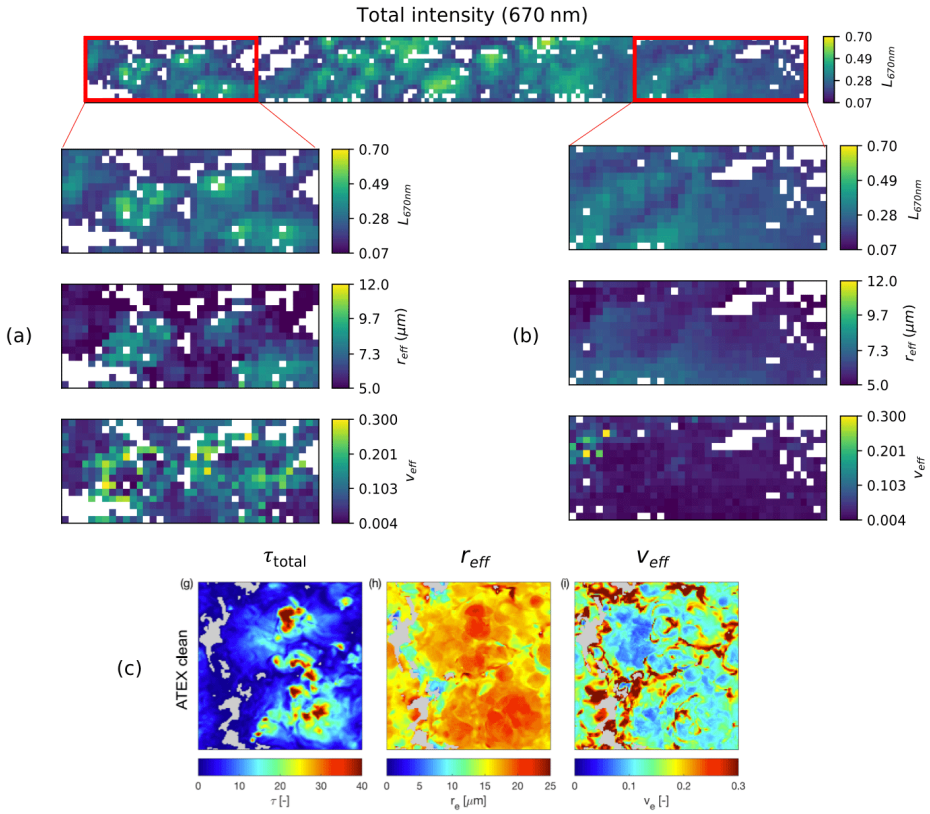

Figure 32. A zoom of heterogeneous (a) and homogeneous (b) sectors of the LMOS cloud field observed by AirHARP, compared to retrievals of the same properties performed on large-eddy simulations of similar clouds from Miller et al. 2018 (c). This figure is reprinted from McBride et al. 2020 and sub-figure (c) is adapted from Miller et al. (2018), both under the CC-BY-4.0 license.

velopment, brightness, and lifetime, aerosol–cloud interaction, and reducing the uncertainty in global radiative forcing due to clouds and aerosols. In the following section, the AirHARP spatial retrievals of CDR and CDV will be analyzed for correlations along the cloud field and to evaluate the impact of resolution on the retrieval itself.

Section 5: Resolution and scale analysis of retrieval products

Subsection 5.1: Spatial correlations between intensity, CDR, and CDV

Because the AirHARP retrievals of CDR and CDV are images, any sector of the cloud field can be analyzed by taking a transect of pixels along- or cross-track. Figure 33 shows a 34 km pixel transect of the cloud field (shown in the inset intensity image with a black line). compare the anomaly from the mean along the track for intensity (~COT), CDR, and CDV. These anomalies are labeled COTa, CDRa, and CDVa in this section, respectively.

The CDVa is log-scaled to capture several orders of magnitude. Positive CDRa are larger droplet sizes, and positive CDVa are wider distributions. Any position along the transect of the cloud field lines up exactly with three unique points in the plot, and any correlation between the three curves suggests information about the nature of the cloud field. In some locations in the plot, COTa and CDRa are correlated with each other and anticorrelated with CDVa. Blue blocks define unambiguous locations in the cloud field where COTa and CDRa have positive anomalies while the CDVa is negative. Orange blocks show the opposite: COTa and CDRa are negative and CDVa is positive. If cloud cores are defined as the pixels brightest in COTa (blue) and cloud peripheries as darkest in COTa (orange) then cloud cell sizes appear to be of the order 1–4 km, both comparable to and slightly larger than traditional MODIS cloud droplet size retrieval products (1 km). Comparison to the traditional cloud product resolution is notable because the 1 km resolution is adequate to resolve cloud microphysics of the cloud cores. However, when cores and peripheries are found in the same

1 km pixel, issues in separating DSDs will arise. Since AirHARP is an aircraft instrument and flies beneath 20 km, its resolution will be better than an equivalent AirHARP instrument in space, so this fine-scale variability will likely not be captured by HARP CubeSat or HARP2 with the unimodal retrieval described in Section 3. More advanced methods, such as the *rainbow Fourier transform* or a multi-spectral hyper-angle retrieval, may get around these scale limitations. Regardless, this result emphasizes the importance of small-scale sub-kilometer sampling of cloud fields because cloud heterogeneity and microphysical processes may be blurred by the large spatial resolutions of spaceborne instruments.

This result does not invalidate the need for a space HARP, however. This retrieval can be used as an independent check on radiometric CDR retrievals, regardless of resolution, and provide an unprecedented, direct, and global CDV measurement. A HARP-like instrument in space over decadal periods could also provide globally resolved *operational* Level-2

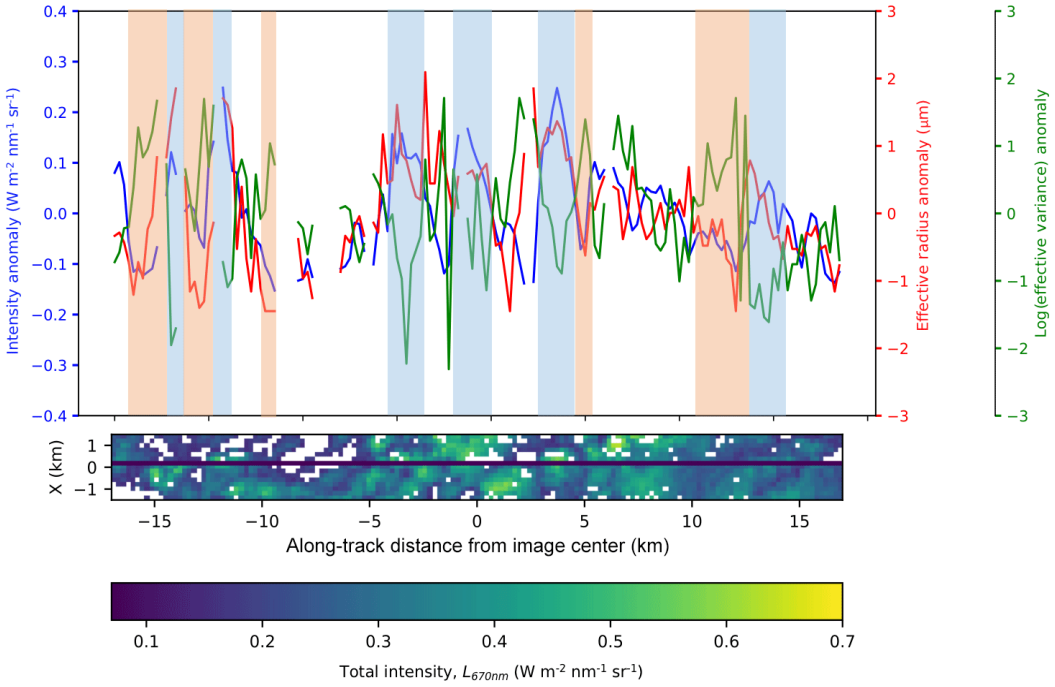

Figure 33. Analysis of intensity (blue), CDR (red), and log(CDV) (green) anomalies from the mean along the black transect for a segment of the cloud field measured by AirHARP (bottom). Light blue blocks represent ”cloud cores” and orange blocks represent ”cloud periphery” areas. This figure is reprinted from McBride et al. (2020) under the CC-BY-4.0 license.

CDR and CDV cloud products. This would be the first polarimetric contribution to our climate record and would advance studies of precipitation onset, aerosol-cloud interaction, and cloud development beyond what is currently possible with radiometric, spectrometer, and lidar measurements (NASA 2015, NAMES 2017, Dubovik et al. 2019). Further details are discussed in Section 7.

There are physical explanations for the relationships between intensity, CDR, and CDV on the spatial scales of Figure 33. Liquid water droplets that form at the base of adiabatic clouds, such as cumulus and stratocumulus, grow to their largest sizes at cloud top (Platnick 2000) and further grow by longwave radiative cooling, small-scale turbulence, and collisional processes (de Lozar and Muessle, 2016). On the periphery, evaporation removes smaller droplets, and at the same time, the entrainment of warm air and/or aerosol may enhance droplet growth. There are many competing theories as to the net effect of aerosol entrainment on droplet growth (Small et al., 2009, and references therein), but these two opposing effects may create a larger DSD variance on the periphery. Alexandrov et al. (2015) and Platnick (2000) also suggest that CDR changes occur vertically in the cloud periphery. Therefore, multi-angle polarimeters that can sample deeper into the periphery could retrieve a larger CDV in these areas. The above LES study of broken marine stratocumulus by Miller et al. (2018) also shows higher CDV (lower CDR) in the cloud periphery and lower CDV (higher CDR) in cloud cores, as shown in Figure 32c. In the present study, these processes cannot be decoupled, but these results show that AirHARP retrievals are consistent with current research and theories of cloud microphysics.

Furthermore, the AirHARP pixel resolution can be degraded and used to understand the effect of sub-pixel variability on the DSD retrieval itself, as shown in Figure 34. Figure 34a and b are repeated from Figure 31a and b, and both represent the 200 m CDR retrieval, while Figure 34c shows the CDR product at 600 m resolution. To calculate the 600 m product, the gridded polarized reflectance data at the original 50 m resolution is aver-

aged over a 12x12 box. Next, the superpixels pass through an intensity-based screening process that eliminates cloud holes and marginal situations. Third, the superpixels enter the retrieval process. Thus, Figure 34c is not a resampling of Figure 34b but a new retrieval using the same input data at different spatial resolution. This study does not examine the effect of cloud screening at the different resolutions, only the effect of the degraded resolution on the retrieval products.

The plots on the left-hand side of Figure 34d–f are the retrieved P_{12} curves, which emphasize how the nine 200 m retrievals, shown as gray lines, compare to the single 600 m retrieval, which is shown as a red line. The two boxes to the right of each of the retrieved P_{12} curve plots in Figure 34d–f represent the retrieved CDR (middle column) and CDV (right column) for the colored superpixel boxes located in Figure 34a–c. The 600 m CDR or CDV result is given in the title above each box and represents the retrieval for the entire nine-box square underneath, whereas the 200 m CDR or CDV results are shown inside each colored sub-box.

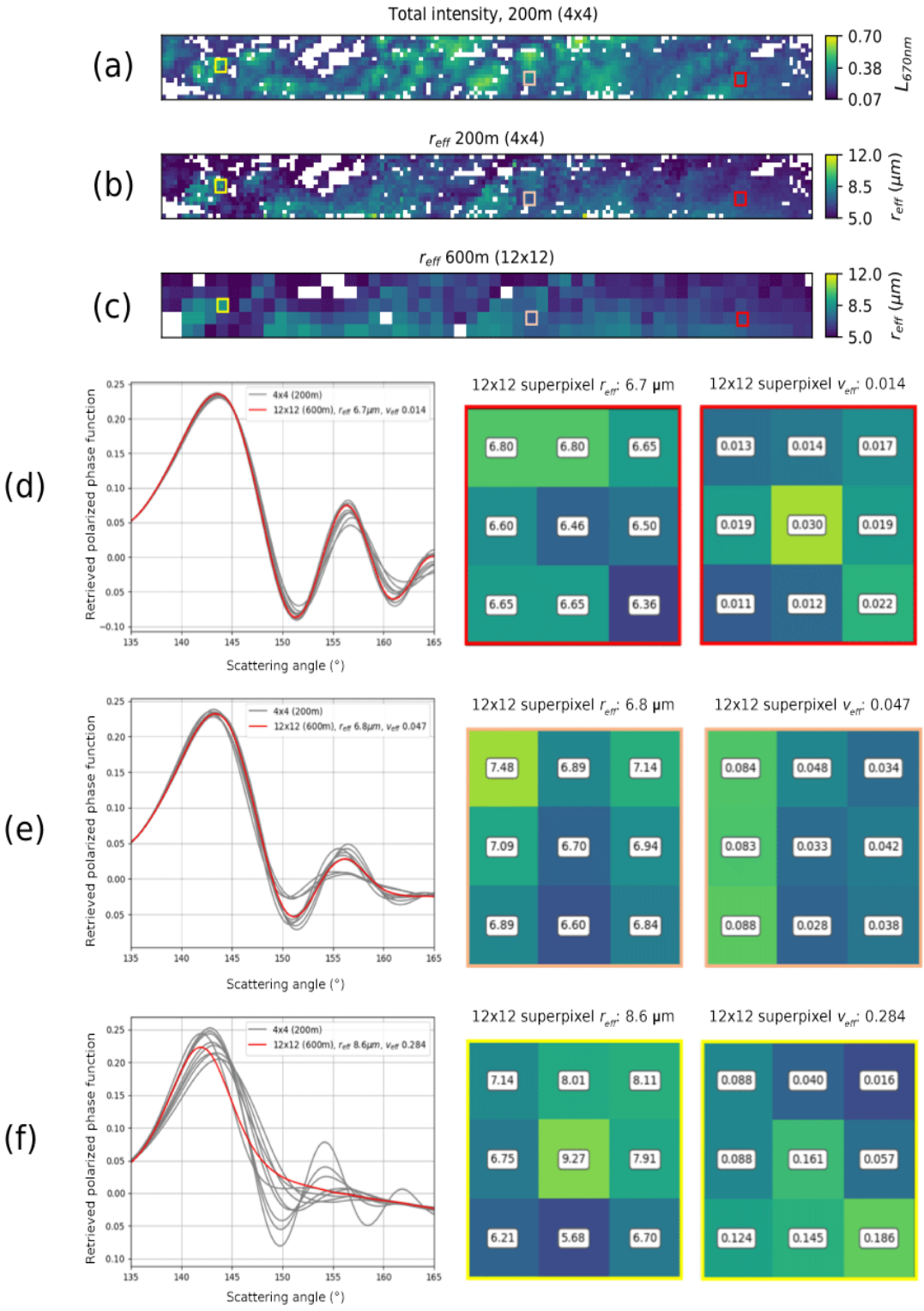

Figure 34. Scale analysis for the scene in Figure 31 at 200 m (b) and 600 m (c) resolutions. Retrieved Mie P_{12} curves shown on the left in (d, e, f – 200 m in grey, 600 m in red) and their CDR and CDV retrieval products at the two resolutions, for the red, beige, and yellow pixel locations in (c). This figure is reprinted from McBride et al. (2020) under the CC-BY-4.0 license.

Subsection 5.2: Information content retrieved at different scales

Figure 34d shows that the narrow DSD retrievals are robust against resolution degradation; if the 200 m retrievals can be considered "ground truth", the 600 m result agrees within community standards (10 % σ_{CDR} and 50 % σ_{CDV}; Mishchenko et al., 2004). The 600 m P_{12} resembles the 200 m P_{12} curves, both in the location of supernumerary peaks and overall structure. Figure 34e shows a retrieval that appears to represent the cloud periphery, as the intensity image shows the appearance of a cloud cell near the superpixel. Here, the CDR retrieval gives higher values in the center of the structure and smaller values on the sides, consistent with prior studies. Figure 34e shows two conflicting P_{12} regimes. Here, 200 m DSDs with CDR between 6.6 and 7.5 μm separate into two modes: CDV>0.08 and CDV between 0.048 and 0.028. While the primary bow around 143◦ is preserved between retrieval scales, the 600 m retrieval gives a CDV of 0.047, a value that appears to represent the mean of the nine pixels but satisfies neither regime. Shang et al. (2015) and Miller et al. (2018) show similar results in theoretical and observational mixed DSDs.

Figure 34f shows another retrieval done close to the cloud periphery, but this time, the retrieved 200 m P_{12} curves show a wider spread of CDV values compared to the results shown in Figure 34d–e. The retrieved 600 m fit generates a curve that represents a broad DSD, but notably all the supernumerary bows present in sub-pixel retrievals are gone at larger resolution. The 600 m CDV is also larger than those the nine sub-pixels, at 0.284, while the nine individual pixels return values 0.086 to 0.186. Interestingly, the primary bow region at 600 m seems to prefer the P_{12} structure of the widest of the 200 m retrievals (CDR 9.27um, CDV 0.161). It is possible that there are other impacts at play here, including microphysical and sampling differences at the periphery vs. the cloud core as mentioned above. Overall, Fig, 44f emphasizes that retrieval resolution is an extremely important aspect to consider and that cloud properties can appear significantly different at 200 m, 600 m, and 1 km+ scales common to current satellite instruments.

It is important to note that the combination of gamma distributions inside a superpixel does not necessarily combine to make a gamma distribution. Homogeneous areas of cloud will converge on a gamma DSD with little dependence on scale (Figure 34d). However, retrievals that contain sub-pixel heterogeneity in the DSD still attempt to infer gamma distribution properties from a signal that may not represent one (Shang et al., 2015, and Figures 34e, f). The rainbow Fourier transform method (Alexandrov et al., 2012b) applied to AirHARP may distinguish the two modes in Figure 34e at the 600 m scale, but this is outside the scope of this work. The interpretation of CDR and CDV at large pixel sizes is still widely debated, but fine-resolution spatial data provided by AirHARP and its retrievals can provide a meaningful advancement in this direction.

Unfortunately, there were no suitable cross-validation opportunities during LMOS with any similar spaceborne or aircraft instruments. Therefore, the results can only be compared to the current literature or intuition from Mie simulations. In the next section, an AirHARP cloud retrieval simulator is developed to validate these results over visually similar LES cloud fields. With realistic bin microphysical DSDs at the target pixels, 200 m and 600 m cloudbow retrievals are simulated and results are reported similarly to Figure 34 for cloud core and periphery areas.

Section 6: Validation using large-eddy-simulated clouds and an AirHARP measurement simulator

To address the lack of quantitative validation opportunities during the LMOS campaign, an AirHARP simulator was developed to demonstrate these results over similar, large-eddy-simulated (LES) marine stratocumulus cloud fields. Due to the differences in the LES fields used in this chapter and the LMOS datasets, this section will focus on demonstrating this cloud retrieval from the standpoint of AirHARP's angular density and resolution. Because of this, some of the results here may not be attributable to other polarimetric instruments with other sampling schemes, angular density and resolution, or other spectral channels.

The LES cloud domains used in this work are simulated using inputs from the Second Dynamics and Chemistry of Marine Stratocumulus (DYCOMS-II) field measurements. Figure 35 shows an example domain with a grid cell size of 25 m, domain of 3 km, and a layer thickness of 10 m (Yao-sheng Chen, NOAA/CSL, private communication). Over nine days in 2005, marine stratocumulus clouds were observed and sampled by a variety of instruments, including droplet sizers, aerosol backscatter LIDAR, cloud radars, radiosondes, and passive radiometers on the NASA C-130 research aircraft. This campaign hoped to improve LES

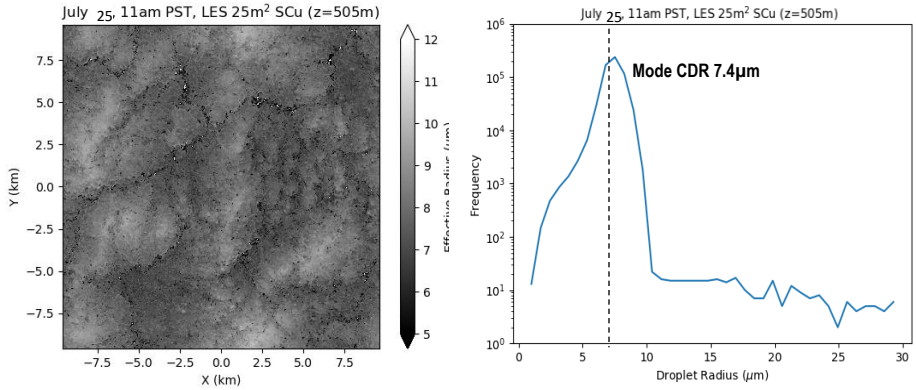

Figure 35. DYCOMS-II bulk microphysical cloud field simulated off the coast of California (center at 35 N, 125 W) with constant geometric standard deviation 1.105 (left). Grid size is 25m^2 and thickness 10m. The histogram of the cloud field shows a mode effective radius of 7.4um (right).

simulations of marine stratocumulus clouds and study the impact of aerosol entrainment and drizzle on cloud development (Stevens et al. 2003). In this study, the aerosol impact on clouds is not considered or measured and non-precipitating cases are selected to match the LMOS observation.

The Figure 35 simulation uses bulk microphysics, which prescribes a lognormal droplet size distribution to each pixel. The geometric mean radius and geometric standard deviation shape parameters in the LES simulation can be converted to the effective radius and variance used in this work via $r_{eff} = r_m \exp\left(\frac{5}{2}\ln^2\sigma\right)$ and $v_{eff} = \exp(\ln^2\sigma) - 1$, where r_m is the geometric mean radius and σ is the geometric standard deviation. Even though this cloud field is relatively homogeneous, CDR variability exists, and the similar distributions seen in Figure 34b are present here. Because the polarimetric cloud retrieval is only sensitive to single scattering (COT ~3), the 10m thickness of the layer is also appropriate. The bulk microphysics cases above were used to develop the AirHARP simulator for eventual application over *bin* microphysics LES cloud fields. The difference between bulk and bin microphysics is in how the DSD is prescribed. Instead of defining a smooth DSD to the pixel, bin DSDs allocate droplet number and mass concentration of a cloud target to a specific range of droplet radii. The entire DSD contains many of these number or mass bins and can take on a realistic and multi-modal shape. Bulk DSDs lead to faster simulations of cloud properties, but they typically lack the information content found in bin DSD simulations. The trade-off is that bin DSD simulations are computationally expensive.

The bin-DSD domains used in this work were generated using a 8-hr System for Atmospheric Modeling (SAM) simulation based off the second research flight (RF02) of the DYCOMS-II campaign. This marine stratocumulus snapshot (9600s into the simulation) shows a closed cell cloud field (shown in Figures 47 and 48), with similar striations and clustering as the more heterogenous areas of the LMOS case above. As in the bulk simulation, a

10 m layer thickness was used (layer 60) and here, the target resolution was 50 m to balance computation and data volume.

In this work, because non-cloud contaminations were relatively small during the 1522Z AirHARP LMOS observation, the algorithm can be streamlined. The measured AOD values by Aqua MODIS along the western coast of Michigan (the closest valid retrieval) on June 19, 2017 at 1834Z are ~0.05 (source: NASA Worldview), which is considered clean. Terra MODIS, which flew over at 1651Z, lacks retrieval coverage in the region due to sun-glint and cloud cover. On June 18, Terra MODIS AOD retrievals at 1610Z show ~0.05 value over the lake. The LMOS campaign had a dedicated Aerosol Robotic Network (AERONET) sun photometer at Zion, Illinois (42.468º N, 87.810º W) that retrieved AOD as well from June 5-22, 2017. The version 2.0 AOD retrieved on June 19 is among the lowest of the month, and the average value for the 675nm band, the closest spectral match to AirHARP's 670 nm, is 0.041 (Pierce 2017). This agrees in general with the nearby Aqua and Terra MODIS results around this time. Furthermore, Alexandrov et al. (2012) simulated the impact of AOD on the polarized reflectances inside the rainbow region for a given CDR and CDV (17.5 and 0.01) and found that though large AOD can impart a slope on the polarized reflectance with angle, this slope nearly disappears for AOD values < 0.1. The difference between a clean case (AOD = 0) and AOD ~0.05 is less than 0.01 in polarized reflectance across the entire cloudbow range in this example.

Furthermore, there is evidence to suggest the scene contained no other contaminations, such as cirrus or surface reflectance (optically thin pixels in the LMOS case are screened). The Terra MODIS effective radius product from June 19 2017 at 1651Z agrees, with only liquid water phase retrievals over the measurement area (42.3 N, 87.1 W). Overall, the observational conditions suggest that these impacts can be neglected, and the radiative transfer simplified with no loss of generality in our study. However, a VRT model should be used to model the polarized reflectance in the presence of heavy aerosol loading, strong sur-

face reflectance, cirrus, or low optical thickness clouds. Significant contaminations can modify the polarized signal significantly relative to the Mie P_{12} (Alexandrov et al. 2016).

Rayleigh scattering cannot be neglected, though. The impact of Rayleigh polarization is dependent on geometry and height of observation and is present regardless of other atmospheric effects. Rayleigh polarization can be simulated with an analytic polarized phase function and an attenuation term and will impart a slope to the polarized reflectances (Q_{sca}). The model in Diner et al. (2013) was used to simulate polarized reflectance at cloudbow geometries:

$$Q_{sca} = \frac{1}{4\,(\mu_0 + \mu)}\left[P_{12,Mie}(\lambda, \vartheta_{scat})\,A(\mu_0, \mu) + P_{12,Rayl}(\lambda, \vartheta_{scat})\left(1 - A(\mu_0, \mu)\right)\right], \quad (36)$$

where $P_{12,Rayl}(\lambda, \vartheta_{scat})$ is $-\frac{3}{4}\left(\frac{1-\delta}{1+\frac{1}{2}\delta}\right) sin^2\vartheta_{scat}$ and $A(\mu_0, \mu)$ is an attenuating factor equal to $exp\left(-\tau_r\left(\frac{1}{\mu_0} + \frac{1}{\mu}\right)\right)$, a term that represents the attenuation of Rayleigh-scattered light in the sun (μ_0) and sensor (μ) directions. The δ term represents the Rayleigh depolarization ratio, which is approximately 0.029 for air (Xu et al. 2017). Diner et al. (2013) also use an attenuating factor for ozone, but its impact is negligible in LMOS conditions. The Rayleigh optical thickness (τ_r) is simulated from using the height of the LMOS cloud layer (3.15km) and UC-12 height (8km) using the following (Bodhaine et al. 1999):

$$\tau_r = \frac{p}{p_0} * 0.00877 * \lambda^{-4.05} \quad (37)$$

where p_0 is the pressure at sea level (1013.25 hPa) and p is the pressure at the observation level. The Rayleigh optical thickness between the cloud and aircraft can be found by calculating Eq. (37) for both heights and subtracting the results. This approximation is valid for 0.67 μm and other optical wavelengths outside the ultraviolet.

The LES simulation does not include any geometry, so it is important to simulate what this cloud field may have looked like to AirHARP if it were a real scene during LMOS.

A range and density of solar and viewing angles that represent an AirHARP cloudbow observation were modeled and a suitable cloudbow range was chosen for the geometry of the LES pixel. The Mie P_{12} in Eq. (36) are derived by using the bin DSDs for *n(r)* and the simulated AirHARP geometry at the target. Therefore, this produces an AirHARP-like Q_{sca} measurement at the 50 m LES pixel over a range of scattering angles. The error on each 200 m Q_{sca} measurement is compatible with the LMOS study above, using a quadrature sum of the superpixel standard deviation from the LES target P_{12} and an additional 0.01 to simulate other impacts in the live data. The result are errorbars on each simulated measurement that are compatible with the LMOS retrievals in Figure 30.

This Q_{sca} is aggregated at the same 200 m and 600 m scales as the actual LMOS retrievals. Using the Q_{sca} data at these resolutions, Eq. (36) is inverted for $P_{12,Mie}$ and CDR and CDV are retrieved, assuming the Q-field represents a unimodal modified gamma DSD using Eq. (29). The polarized signal from Rayleigh scattering is included in the calculation of Q_{sca}, and removed in the retrieval itself with the cosine squared term in Eq. (33). Note that depending on the DSD heterogeneity of the sub-pixels in the 200 m or 600 m aggregates, the 200 m and/or 600 m Q_{sca} may represent a DSD that wholly different from any of the lower-resolution DSDs. Figure 32d shows an example of this on live data. Successful fits will be judged using the two-factor authentication as described above (RMSE and reduced chi-square). This simulates the LMOS retrieval study well and allows us to compare the model and measurement results.

Figure 36a shows a similar setup to Figure 34d-f, a comparison of 200 m and 600 m DSDs retrieved using the AirHARP simulator on the LES bin domain of a non-precipitating marine stratocumulus cloud layer. On the left, the retrieved DSDs from a 600 m superpixel (red) overlaid on the retrieved DSDs from all nine 200 m sub-pixels inside the bounding box of the 600 m domain (gray). The target chosen was in the “cloud core”, which is now defined as a region of larger cloud droplet number concentration (> 80 drops/cm^3) relative to its sur-

roundings that is consistent with neighboring vertical layers in the LES dataset. Here, like in Figure 34d, the DSDs are compatible and narrow between 200 m and 600 m resolutions. The resulting polarized reflectance at 600 m has a compatible shape and structure as the nine 200m retrievals. Live AirHARP data (Figure 34) and prior LES studies in the literature (Figure 32) suggest that homogeneity over a specific domain is preserved at smaller resolutions inside that domain.

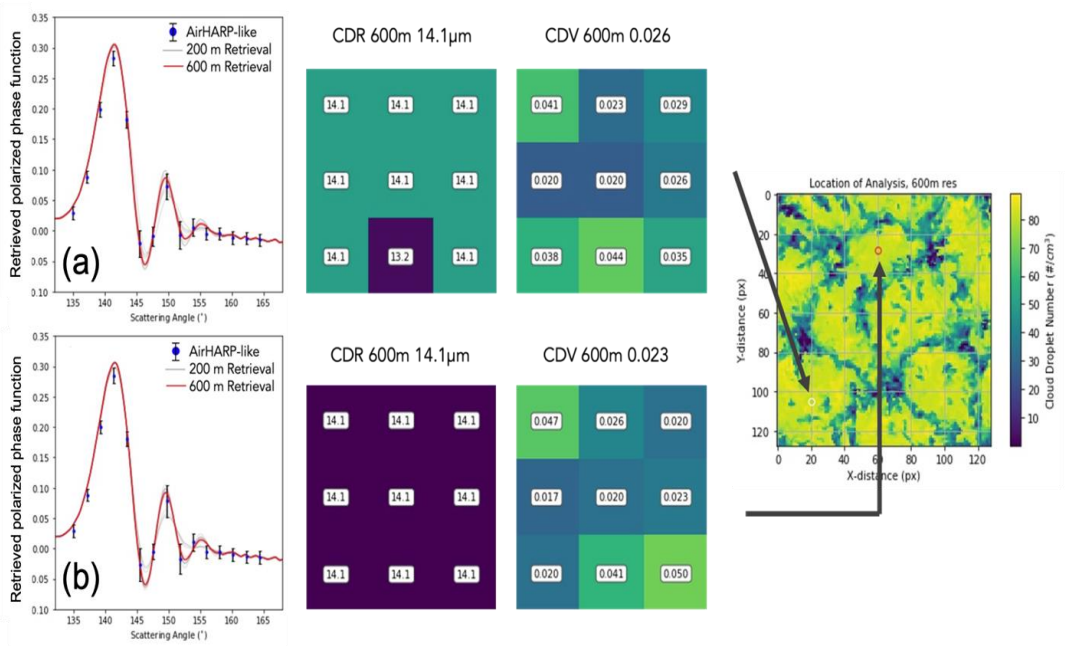

Figure 36a-b. Example 'cloud core' DSD retrievals over a DYCOMS-II marine stratocumulus cloud simulation with bin microphysics. The retrieved polarized phase function is shown in (a,b, left), derived from polarized reflectance simulations. For the two locations shown in the domain (far right), a 600 m DSD retrieval and independently, the DSD of the nine 200 m subpixels were also retrieved. The values of CDR for the 200 m retrievals are shown in the second column images with units of micrometers, and CDV in the third column. The 600 m retrieved values are given as titles above these images. At the far left, the retrieved P12 fits for these cases are shown – the nine 200 m fits in grey, the 600 m fit in red, and the multi-angle AirHARP-like data simulated at 600 m is shown in blue dots with errorbars.

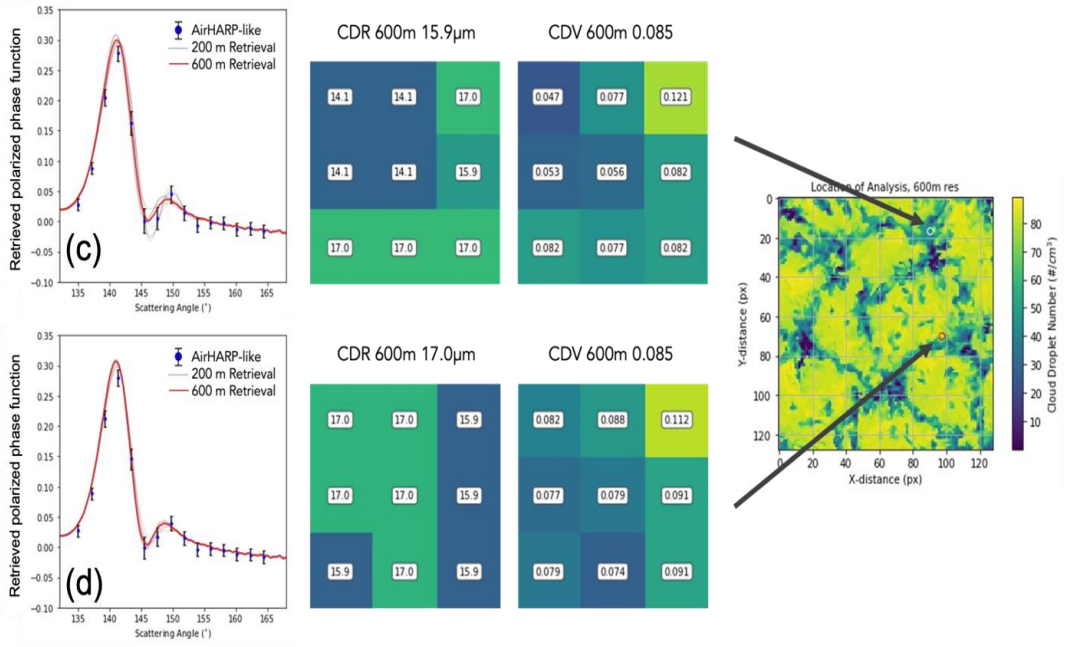

Figure 36c-d. Example 'cloud side' DSD retrievals over the same domain as Figure 36a-b.

Figure 36b examines a more complicated "cloud core" case that includes more than one significantly unique DSD at the 200 m scale. Notably, the 600m DSD retrieval appears to favor one of the regimes of the 200 m sub-pixels, specifically the ones with the larger values of effective radius. This can be explained because the effective radius is the mean droplet size weighted by cross-sectional area. DSD from larger effective radii (and therefore larger surface area) may have a larger weighting on the overall superpixel Q_{sca} than DSDs led by smaller effective radii. Like Figure 34e, this simulated retrieval shows that in cases of well-defined bi-modal DSD regimes, the superpixel Q_{sca} can favor one of them. Unfortunately, details about sub-pixel heterogeneity may be lost when using a unimodal DSD retrieval for "cloud side" cases like this at specific resolutions. This result, in tandem with Figure 34e, emphasizes the need for high resolution polarized sampling of liquid water cloud DSDs *and* improved algorithms that can tease out multiple DSDs, such as the RFT (Alexandrov et al. 2016).

Figure 36c shows a "cloud side" case, which is defined in this work as a region of the cloud domain with relatively lower cloud droplet number concentration than those in Figure 36 (50-70 drops/cm^3). Similar to Figure 36b, this target shows two distinct DSD regimes in CDR and CDV. The retrieved DSD at 600 m appears to split the difference, though results in a P12 fit that blur some of the subpixel detail. Ultimately, only one of the subpixel DSDs agrees with the 600 m result. Again, like Figure 34f, this 600 m result tells us there is heterogeneity in the subpixel but not the extent or where the heterogeneity exists.

Figure 36d examines a visually borderline case between the 'cloud core' and 'cloud side' targets shown above. Interestingly, all the 200 m DSDs represent wider distributions and the 600 m retrieval agrees in CDR and CDV value and P_{12} fit curve, relative to the uncertainty of the simulated measurement. These cases are particularly interesting to climate science and instrument development going forward because the retrieval shows that unresolved DSD heterogeneity exists even below 200 m. In all cases presented in the LES study above,

the simulated AirHARP data led to successful narrow and wide DSD retrievals comparable to those found from LMOS datasets.

Section 7: Discussion and conclusions

Overall, retrievals on AirHARP datasets agree with prior LES studies in the literature. Simulations of AirHARP sampling over bin LES domains produces compatible retrieval results, as well. These studies are not without limitations, however. First, the parametric retrieval used in this work assumes a single-mode DSD that can be described by CDR and CDV alone. Situations that do not fit this assumption may not be retrievable, as mentioned above. For the purposes of our demonstration, the assumptions of the retrieval are met in the live data examples.

The possibility of optically thin upper-level liquid water clouds ($\tau_{cld}<1$) moving over the geolocated cloud deck in the LMOS granule cannot be ignored. If these clouds exist, they will appear to "move" from angle to angle. This could be missed by our current geolocation algorithm, which focuses on the layer of clouds that is producing the dominant signal. The impact on the cloud retrieval will change from angle to angle but will likely affect only two or three view sectors at most. Therefore, this is not expected to significantly contribute to the overall cloudbow fit. All fits shown in this work lie beneath our successful RMSE threshold, however, other retrieval methods could tease out the signals from both cloud layers when properly geolocated (Alexandrov et al., 2016).

Mapping the different angular measurements to a target elevation is a challenge with AirHARP cloud data. Clouds also appear at a range of altitudes and are not always easily predictable in height, distribution, time, or space. Therefore, an iterative method determines the altitude of zero parallax in the cloud field, within a gridded pixel. Well-defined cloud features, observed from at least two view sectors, are used to determine the average cloud height of the dataset. Currently, this estimate is applied to the entire dataset during the geolocation

process. Because there is no such thing as a plane-parallel cloud, both the parallax method and the assumption of constant cloud-top height adds uncertainty in the retrieval. Where possible, the altitude of the scene is verified with heights retrieved from data from other relatively coincident instruments, such as MODIS and VIIRS. Conservative cloud identification and binning pixels to 200 m (4×4) resolution further mitigates the error introduced by using this mean height. In the case shown in Figure 29, the derived height is (3150±50) m and the uncertainty is the resolution that guarantees no movement from view sector to view sector. A self-check on these assumptions is the goodness of fit of each retrieval. In our example, while the RMSE of the cloud field varies, all retrievals shown successfully fit the RMSE threshold defined above. Therefore, errors in our geolocation do not contribute significantly to the results shown at 200 or 600 m resolutions. However, when studying broken or popcorn cumulus clouds, a proper 3D geolocation of the cloud will be required. The HARP science team is currently developing an optimized pixel-level topographic algorithm to mitigate any multi-layer or cloud projection biases in future retrieval studies.

Maintaining calibration accuracy in flight, despite variable temperature, pressure, vibration, and humidification is also challenging. AirHARP did not have an in-flight calibration mechanism during LMOS, so vicarious and model validations are important. Furtehrmore, it was found in lab testing that AirHARP generates internal optical etaloning. Etaloning produces weak, concentric fringes on the raw image, which transform into linear bands at the push-broom level. Typically, a lab flatfield fully corrects for this effect, but some extraneous etaloning appears in some LMOS granules. Because the cloudbow also transforms from a concentric to linear space at the push-broom level, cloudbow cases are especially tricky to correct. Luckily, the effect of the fringes on the hyper-angular retrieval is nearly random. Because the retrieval uses angular data that covers many unique positions in the detector and the etaloning does not have a cloudbow-like phases or amplitudes, it can be modeled as a decrease in SNR (extra 1σ error contribution). Due to the well-resolved retrievals in Figures 30-

34, the etaloning does not contribute significantly to the CDR and CDV products. The fringe contribution would make it difficult to retrieve non-cloud signals within the measurement, though. For this reason, a new correction algorithm is under development to remove the fringing from AirHARP datasets and an internal calibrator for HARP2 on the PACE mission. With frequent flat-field calibrations, the etaloning can be immediately corrected in a variety of environments. Also, there is evidence that the cloudbow retrieval itself could be used to remove the fringe signal from AirHARP data. This is a promising correction technique that may be explored in future work.

Finally, the results from the LMOS study are challenging to validate and even difficult to compare with other retrievals. The MODIS Terra and Suomi-NPP VIIRS radiometers (and MODIS Aqua) passed over the same location on the ground as our example over an hour (three hours) after the AirHARP observation. Both instruments are sampling a statistically different cloud than AirHARP, though AOD and cloud effective radius retrievals can be used to make general conclusions about the state of the local atmosphere around the AirHARP measurement time. While the GOES-R Advanced Baseline Imager (ABI) radiometer is coincident, its 1–2 km CDR retrieval resolution is difficult to reconcile with the variability observed in the cloud field at finer AirHARP resolution, as suggested by Figure 34. AirHARP was also the only Earth-observing polarimeter present on aircraft or in space during LMOS with these capabilities for cloud retrieval. None of the field experiments in which AirHARP has flown (LMOS or ACEPOL in 2017) focused on clouds, and if clouds were captured, they contained sub-optimal cloudbow geometry or limited matchups between instruments. For example, the LMOS observation was the only one in which AirHARP achieved full angular coverage over a continuous cloud field and one that could be geolocated to a constant height over the full push broom with little impact to the retrieval. A dedicated future aircraft campaign for clouds, specifically one that allows coincident AirHARP observations with other compatible cloud-measuring or -retrieving sensors at similar spatial resolution, is needed.

Optimally, coincident HARP space and AirHARP aircraft observations would greatly improve our ability to validate. The differences in retrieval resolution for cloud cores and peripheries, across a wide swath, and for unique global locations and aerosol source regions are of interest in these future campaigns.

Furthermore, the LES case used in the Section 6 study is visually like parts of the LMOS cloud case but has a larger CDR distribution. This allows us to validate the Figure 34 results in general for different DSDs and study how well this retrieval resolves larger CDR cloudbows with AirHARP's angular density. Miller et al. (2018) suggests the Nyquist resolution for AirHARP at 670 nm would limit cloud retrievals to around 24um in CDR, and Figures 47 and 48 show successful simulated 200 m and 600 m DSD retrievals up to 17um. While these retrievals still succeed, the density of the oscillations relative to the multi-angle points suggest the retrieval is nearing an efficiency limit. In a separate sensitivity study using the same LES domain at a timestep an hour later, the AirHARP simulator had difficulty resolving DSDs with CDR of 20um+. These results suggest that this AirHARP retrieval may not be sensitive to drizzle or rain mode droplet sizes at 670 nm. However, with changes to the HARP design to include hyper-angular SWIR channels, this retrieval may access CDR values up to ~50um if they exist (see Chapter 5 for more discussion). The DYCOMS-II domains are well-documented in the literature, but there is a limit in how closely these clouds can match the LMOS case. In future study, it would be useful to generate a cloud field that mirrors the LMOS environment more closely. Using proxy inputs about the atmosphere from the LMOS campaign itself and simulating a Lake Michigan-like environment for the cloud to grow in would be optimal.

In some cases, the microphysics of the cloud field is still heterogeneous beneath 200 m, the lowest resolution presented in this work. This has interesting repercussions to aircraft and spaceborne cloud-measuring instruments, especially those that publish their cloud products at 1km resolutions or larger. These products may blur the subpixel heterogeneity of the

target and potentially average out microphysical processes. These impacts that may change the perceived DSD over time, space, and contribute significantly to radiative forcing. It is important to note that a spaceborne HARP, including HARP CubeSat and the upcoming HARP-2, will not achieve AirHARP-like resolutions, but the ability to derive effective variance directly, with global coverage, and at the lowest spatial resolutions of any spaceborne imaging polarimeter will advance the ability to understand and track cloud growth processes. The conclusions from Section 5 show that regions of the cloud (and therefore developmental processes) can be identified via correlations in reflectance, CDR, and CDV. These retrievals are unique to AirHARP-like imaging polarimeter measurements that are dense in along-track, co-located angular coverage, at narrow resolution, and over wide spatial scales. These studies are also possible with these LES bin domains, which may be assessed in future work.

In the next chapter, future applications of the work presented in Chapters 3 and 4 will be discussed. The cloud retrieval scheme in this chapter is useful beyond this work, as well. The information content in the polarized cloudbow could be used for instrument calibration or expanded to multiple spectral channels to characterize multiple modes or non-cloud-contamination over homogenous scenes. In general, the calibration scheme developed in Chapter 3 could be used to trend and characterize any pixel in the sensor for any stable Earth target, including the polarized cloudbow over homogenous cloud scenes and/or in tandem with a vector radiative transfer model.

Section 8: Acknolwedgements

This chapter is adapted from a publication in Atmospheric Measurement Techniques, available in open access format here:

McBride, B. A., Martins, J. V., Barbosa, H. M. J., Birmingham, W., and Remer, L. A.: *Spatial distribution of cloud droplet size properties from Airborne Hyper-Angular Rainbow Po-*

larimeter (AirHARP) measurements, Atmos. Meas. Tech., 13, 1777–1796, https://doi.org/10.5194/amt-13-1777-2020, 2020.

I would like to personally thank Graham Feingold, Jan Kazil, Michael Garay, and Daniel Miller for their insights on various aspects of this chapter and the related publication in AMT. The LES models used in the above validation were developed by Yao-sheng Chen, Tak Yamaguchi, and Graham Feingold at the NOAA Chemical Sciences Laboratory (NOAA/CSL). NASA LMOS principal investigators Jassim Al-Saadi, Charles Stanier, and R. Bradley Pierce were instrumental in providing AirHARP the opportunity to participate in the LMOS campaign. I also thank Laura Judd for supporting AirHARP in the UC-12 during research flights on days I was not permitted in the plane. The work shown here would not be possible without the engineering, planning, and calibration support from J. Vanderlei Martins, J. Dominik Cieslak, Roberto Fernandez-Borda, and Palkpoom Pongsuphat during the LMOS campaign.

The portions of this chapter that are in the AMT publication were supported by the National Oceanic and Atmospheric Administration – Cooperative Science Center for Earth System Sciences and Remote Sensing Technologies (NOAA-CESSRST) (grant no. NA16SEC4810008, 2019-2021). This work was also supported by the NASA Earth and Space Science Fellowship (grant no. 18-EARTH18R-40) under the NASA Science Mission Directorate from 2016 to 2019.

Chapter 5: Summary and Outlook

The HARP instrument, in all its forms, is a new and ambitious wide field-of-view, multi-angle imaging polarimeter. It can sample a ground target from up to 120 different along-track views and generate long stretches of data from individual view directions in a single live capture. After all 120 HARP pushbrooms are registered to a common grid, HARP data can provide the scientific community a three-dimensional framework to study Earth targets as a function of latitude, longitude, viewing angle, spectral channel, and in reflectance or polarization. A HARP instrument in space may achieve global coverage in 2 days, which is a useful revisit period that may allow for a continuation of our climate record into the future (in the scenario of a decadal mission). HARP can continue accurate and heritage measurements from legacy climate platforms like MODIS, MISR, POLDER-3, and AVHRR and expand the information content possible in a single pixel, relative to these instruments. The HARP instrument advances Earth science in these ways, but also the three major takeaways from this work: (1) HARP meets community accuracy requirements for modern aerosol and cloud retrievals, (2) HARP provides an unprecedented dataset for new cloud property science, and (3) HARP is a compelling example of high science quality at a low taxpayer burden. Because of these advancements, the HARP concept is attractive for a variety of current and future Earth science applications.

Section 1: Calibration and validation

In Chapter 3, a simple, physics-driven calibration for HARP was developed. This framework can be easily adapted to a variety of environments. Starting from the CCD detector specs, the images are corrected for background, flatfield, and non-linearity. The detectors are mechanically and digitally co-aligned to ensure all three images are spatially identical. Using a calibrated polarization state generator, a broad range of possible states of Q and U

were produced and used to derive a calibration matrix for each spectral channel. These coefficients are spread to the entire FOV using the detector flatfields. This is possible because the instrument is telecentric in the image space. There are no focus- or AOI-related biases in any detector images taken beyond a focal distance of three meters. The detector flatfields can correct the entire internal scattering of the instrument and any defects in the images, alone. In the lab, field, or in space, as long as the flatfields are maintained, the polarization matrix can be derived and trended at any location in the active science area of the detector. These values can be spread to all other FOVs with assistance of the flatfields. This also ensures the mechanism of polarization separation and imaging is accurate, stable, and consistent throughout the lifetime of the mission.

The HARP instrument is radiometrically calibrated using a NIST-traceable source, in all spectral bands. This requires knowledge of the HARP spectral response function (SRF), which is independently measured using a monochromator and a separate integrating sphere setup. The output of the calibration process is a *characteristic matrix* for each channel. This matrix translates detector counts to calibrated Stokes radiances, I, Q, and U. In post-processing, the characteristic matrix contains 9-values per channel, and an image-size flatfield auxiliary file for each detector is used to spread those coefficients to all FOVs. This calibration assumes that the SRF is the same in all detectors, which is not the case for AirHARP at 440 nm. The same issue does not appear in HARP CubeSat or HARP2. Therefore, our results suggest this is a manufacturer issue in the either the splitting coatings or detector stripe filters in the AirHARP instrument.

This calibration is validated in the lab and using intercomparisons with other like instruments during field campaigns. In the lab, a Frensel polarization state generator called a "POLBOX" that creates various levels of DoLP with two rotatable glass blades, was used. The DOLP generated by the POLBOX was retrieved by calibrated, polarized AirHARP measurements within 0.5% of theory (0.25% RMS) in all bands. Therefore, AirHARP meets

the current community accuracy benchmark for modern aerosol microphysical retrievals. AirHARP field campaign measurements of ocean and desert targets from NASA ACEPOL were compared to co-located measurements from the RSP instrument. “Single pixel” co-located targets were selected and compared over all compatible view angles over that target. This method evaluates how well AirHARP reproduces the angular signal of the target relative to RSP. While RSP was considered “ground truth” in this section, this study cannot say which instrument is correct, just how well both instruments agree with each other. In both methods, AirHARP data matches RSP within 1% for intensity and DOLP across all bands for most viewing angles < ±35°.

For view angles > ±35°, it is challenging to compare the instruments meaningfully. The AirHARP data is more susceptible to pitch surfing oscillations, geolocation differences, interpolation errors, and other limitations discussed in Chapter 3, Section 5. The pointing knowledge of the RSP instrument may also impact far forward/aft angles moreso than nadir and complicate single-target intercomparisons with imagers. For this reason and others, the SPEX science team used a temporal value-matching approach when comparing with RSP (Smit et al. 2019). This method was also attempted with AirHARP data, and while the results are reasonable, and sometimes better than those shown here, the definition of a co-located ground target was sometimes lost. The methods presented in Chapter 3 show that AirHARP and RSP are reasonably comparable over co-located angles and what both instruments consider to be the same targets, given all potential error sources and sampling differences.

These lab and field validations together demonstrate that AirHARP (and the HARP concept in general) can achieve climate-relevant accuracy benchmarks set by the community. This is crucially important for upcoming space missions that will continue our climate record, such as NASA PACE and AOS. HARP2 on PACE, for example, is expected to be the primary cloud-retrieving polarimeter. This includes cloudbow DSDs, as demonstrated in Chapter 4, but also thermodynamic phase and stereo cloud height. Recent work by Puthukuddy et al.

(2021) verified that AirHARP data can produce spatial maps of aerosol optical thickness, real and imaginary refractive indicies, spherical fraction, and single-scattering albedo, as well. Therefore, this high polarization accuracy on HARP2 can also benefit studies of aerosol-above-cloud and help "remove the atmosphere" from OCI measurements of dark ocean scenes.

The success of the telecentric calibration is an advance in Earth remote sensing. The HARP calibration coefficients can be maintained, updated, and trended in space using any part of the wide FOV, without needing an internal calibrator. This offsets mission cost and removes the risk of having an essential moving part inside of the instrument or necessitating solar slew maneuvers. HARP2 will have an internal diffuser for solar calibration, but if this element fails, the system can recover the calibration using a variety of Earth views, vector radiative transfer simulations, and intercomparisons with other instruments.

The constant co-incidence of SPEXone, HARP2, and OCI on PACE also means that SPEXone polarized and OCI radiometer measurements can be used together to calibrate HARP over a wide variety of Earth scenes, wherever they appear in the FOV. These measurements could stand in for the I, Q, and U that are otherwise typically generated by a vector radiative transfer model. With at least three unique SPEXone polarized measurements (and one OCI intensity) over the same target, the characteristic matrix can be re-derived using the similar process as Chapter 3, Section 3. The constant co-incidence also allows for comparisons over typically challenging targets. Clouds, for example, are constantly moving and growing. Because simultaneous nadir overpasses between instruments can be on the order of 5, 10, or even 30 minutes, cloud scenes are not often used for intercalibration. However, HARP2 and OCI observe the same clouds at the same time over the span of years. Recent work using MODIS Aqua and POLDER-3 data over marine stratocumulus clouds showed that the polarized reflectance of the cloudbow may be used to evaluate the polarization sensitivity of a co-located radiometer (McBride et al. 2022, SPIE). Algorithms like this are optimal

on a platform like PACE, where the radiometer-polarimeter pair are simultaneously co-incident.

Section 2: Spatial distributions of cloud properties, interpretation, and validation

In Chapter 4, AirHARP calibrated reflectances were used to retrieve cloud droplet size distribution properties for the first time, across a spatial field, at sub-40 km resolution, and with no empirical assumptions or assistive radiative transfer models. Liquid water droplets that are comparable in size to the interacting wavelength of light will scatter this light with specific resonances that are related to the DSD. The polarized reflectance (Q) of the cloud field scales proportionally to polarized phase functions (P_{12}) for liquid water droplets that are simulated using Mie theory. These curves are functions of CDR and CDV. Using a two-factor cost function (RMSE and reduced chi-square), CDR and CDV were retrieved at the pixel from the best fitting Mie P_{12} in the scattering angle range of 135 – 165°. The 60 unique views at 670 nm allow for characterization of droplet sizes up to 20um and if the cloud field is a large-scale, marine stratocumulus, there will be a swath of pixels in the AirHARP data that are eligible for retrieval. Therefore, the AirHARP retrieval can produce a highly resolved, spatial map of cloud DSD properties along this valid swath.

A 37 x 5 km cloud domain from the NASA Lake Michigan Ozone Study (LMOS), captured on June 19, 2017, was used to demonstrate this retrieval. This cloud field contained both homogeneous, narrow DSD regions as well as areas of closed-cell convection and subsidence. The domain was masked for non-clouds and the retrieval was performed at 200 m superpixel resolution over the eligible 30 x 3 km swath of pixels that contained the the scattering angle range of 135 – 165°. This allowed for a spatial map of CDR and CDV at 200 m that compared well against LES models of similar clouds in the literature. With these maps, the “cloud core” was defined as bright cloud regions with relatively larger CDR and smaller CDV and “cloud periphery” areas as the opposite: relatively dimmer regions with smaller

CDR and larger CDV. These results support the idea that collision and coalescence processes grow cloud droplets as they rise toward cloud top in updrafts and competing entrainment and evaporation processes create mixed DSDs on the cloud periphery. This study cannot decouple these processes from the measurement, however.

A 1.5 km x 30 km transect of the cloud domain was examined to study correlations between reflectance, CDR, and CDV. After taking the mean of each parameter along the transect, it was demonstrated that reflectance and CDR correlate, but CDV anti-correlates in the cloud "core" and "periphery". These correlations were so consistent and significant in certain areas of the transect that they were used to define "core" and "periphery" areas. Given the 5 – 12 um CDR retrievals, correlations in the cloud "core" may be indicative of condensation processes that narrow the DSD on the way toward cloud top, though more study is needed. These correlations were occurring on the order of 1 km, meaning that instruments like MODIS and VIIRS that produce CDR products at this resolution may be blurring information content about the cloud field. Also, this study shows the importance of a direct measurement of CDV, which is currently assumed to be 0.1 in current radiometric retrievals of cloud properties. Because the value of CDV appears to be tied to certain areas of the cloud, this discrimination may allow us to better understand cloud growth patterns and feedbacks, let alone discriminate the properties of clouds retrieved in different areas of the world.

The resolution of the images was degraded to study the impact of scale on the retrieval itself. In a second study, the reflectance and polarization data for this LMOS cloud domain was degraded to 600 m and independently ran the cloud retrieval again. The result of the 600 m retrieval was compared to the individual results of its nine 200 m sub-pixels to see how well the 600 m retrieval represented the sub-pixel information content. For visually homogeneous areas of the cloud domain, the 200m and 600 m results agree. However, when multiple DSD regimes exist at the 200 m level, the 600 m retrieval has difficulty representing them. In a cloud "periphery" case, two distinct DSD regimes existed at 200 m. However, the

600 m retrieval appeared to favor the DSD regime with the most representation at 200 m. This issue is exacerbated when the sub-pixel DSDs are well-mixed. The final case, also from the cloud "periphery", showed that the 600 m retrieval produces a wide DSD, but cannot describe the extent or the location of the heterogeneity. This result, along with the transect study described above, emphasize the need for high-resolution cloud measurement going forward. They also suggest current cloud products produced at 1 km+ resolutions may be blurring climate-relevant cloud information in the sub-pixel.

Unfortunately, there were no validation opportunities for AirHARP data during LMOS. Therefore, an AirHARP simulator was developed to evaluate the viability of this cloud retrieval over modeled clouds. In a collaboration with the NOAA Chemical Sciences Laboratory (NOAA/CSL), a large-eddy simulation of a marine stratocumulus cloud using DYCOMS-II campaign inputs was used. The properties of the cloud field, such as the geometric radius and geometric standard deviation, were used to calculate the polarized reflectance at the cloud top and Rayleigh reflectance was superimposed over the domain to simulate an LMOS-style atmosphere. Typically, these retrievals may include aerosol, cirrus, and surface properties, though these was neglected due to the lack of aerosol, cirrus, and the presence of high optical thickness clouds during LMOS. Finally, the data was averaged to 200 m resolutions to simulate the LMOS retrieval scale.

Each cloud target was observed by "AirHARP" at multiple angles to produce a simulated along-track measurement of polarized reflectance. This structure was put through the same retrieval process as the actual LMOS data. The three fit parameters, CDR, and CDV were derived for each eligible pixel in the domain. This retrieval was done on a bulk microphysical domain, which uses a single prescribed DSD for each cloud target, before applying AirHARP to a similar domain with bin DSDs. The bin DSDs assign a droplet mass and number to discrete bins along the droplet radius range, which allows for a wider and more realistic range of DSD shapes and modes. Because bin DSD domains are more computationally ex-

pensive to study, specific cloud targets, “cores” and “periphery” areas that were like those found in the LMOS clouds, were used. The retrieval was done for these targets at 200 m, then independently again at 600 m, like the LMOS scale study in Figure 34. The ultimate purpose of this validation was to test the credibility of the AirHARP retrieval results.

Four unique cases were studied: two cloud cores and two periphery areas. In the first case, at the top of a cloud “core”, the nine simulated 200 m retrievals agreed with the 600 m result. This expectedly matched the invariance seen in the similar LMOS retrieval. A two-regime case at 200 m in both “core” and “periphery” areas also agreed with the LMOS result in that the 600 m retrieval tended to favor the DSD regime with more representation at 200 m. The final case was a unique one: a region of heterogeneous DSDs at 200 m in a cloud “periphery” area. The 600 m retrieval reproduced the 200 m result well, but this case shows that unresolved cloud microphysics can also exist below 200 m. Again, this suggests the importance of high-resolution cloud measuring instruments going forward, even if current instruments can still make useful cloud microphysical retrievals at larger 200 m, 600 m, and 1 km sizes. Ultimately, our simulation study shows that the AirHARP sampling over marine stratocumulus-type clouds during LMOS data produces DSD retrievals and polarized reflectances that are compatible with those found in a simulated study using LES cloud domains. These results also show that AirHARP is sensitive to and can retrieve CDR nearing 24um, consistent with Miller et al. (2018).

Section 3: Legacy and extensions of this work

The calibration and cloud research discussed in this dissertation has many applications and extensions in future work. Some of these include involving multiple wavelengths in the cloud retrieval, cross-calibration with other polarimeters, and expanding the sensitivity of the current cloud retrieval scheme to multiple DSD modes or larger CDR.

Subsection 3.1: Cross-track retrieval of cloud properties

Subsection 3.1.1: Joint spectral application

The hyper-angular along-track cloud DSD retrieval described in Chapter 4 is not the only way to retrieve DSD properties using HARP polarization data. When HARP observes the cloudbow, there is always one or more pushbroom that contains pixels that span the full 135 - 165º scattering angle range in the cross-track direction (see Chapter 4, Figure 28). Following the same procedure explained in Chapter 4, CDR and CDV can be derived along a cross-track *line-cut* of suitable pixels. A similar method is used to retrieve DSDs in AirMSPI continuous sweep data (Xu et al. 2018) and is possible whenever the full cloudbow appears in a single image (i.e. POLDER-3 wide FOV, see Breon and Boucher 2005). However, this version is less attractive because the retrieval represents a larger region of the cloud and therefore, possibly several DSD regimes. This retrieval is limited to clouds that span large distances, such as marine stratocumulus, and is therefore not applicable on global data.

The major advantage of this retrieval is that all four HARP wavelengths can be used equally. Along-track, the 60 views for the 670 nm band can characterize cloudbows with effective radii up to around 24um (see Figure 41). Up to this limit, the oscillations in the cloud signal with scattering angle are wider than the 2-degree angular separation between view sectors (Miller et al. 2018). However, because the other three channels have a 6-degree separation between view sectors, they cannot resolve oscillations any wider than 6 degrees (i.e.,

CDR < 5um). These channels may not contribute meaningfully to a retrieval when combined with 670 nm data either. However, because this retrieval is done cross-track, there are no angular limitations. This requires separate pre-computed Mie P12 LUTs for all four channels, though the core retrieval framework is the same as in Chapter 4. However, instead of each data point representing a unique along-track view, they now represent a group of cross-track pixels binned in scattering angle (Xu et al. 2018).

Figure 37 shows one example of a joint spectral retrieval of the same LMOS cloud domain used in Chapter 4 (Figure 29). The pushbrooms used in the DOLP RGB composite (Figure 37, left) are those closest to the 38º forward view sector (shown in Chapter 4, Figure 27). Pixels inside the white region delineated in Figure 37 (left) are binned 3x3 (150m) cross-track and compared to a wavelength-specific Mie P_{12} LUT. The RMSE and reduced chi-

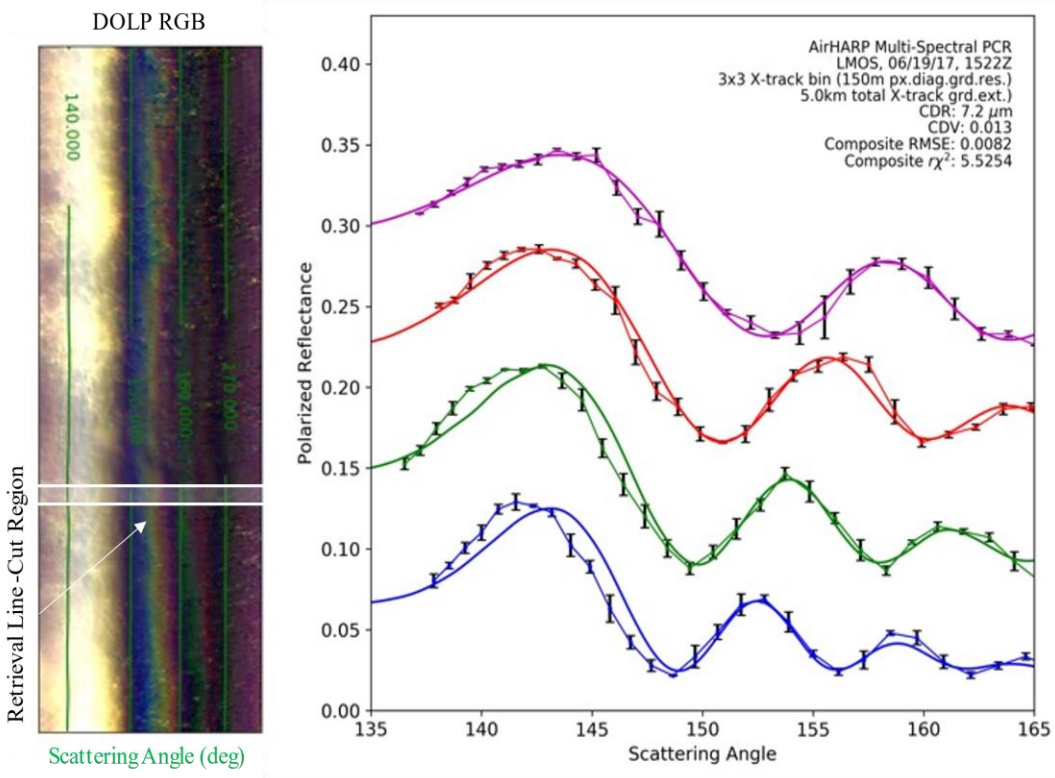

Figure 37. Joint spectral retrieval of cloud DSD properties for a cross-track line-cut of pixels in the AirHARP observation of the LMOS cloud field. Data and fits for 870 (magenta), 670 (red), 550 (green) are offset by a constant value for clarity. The 440 nm (blue) data and fit are not altered. Composite RMSE and reduced chi-square ($r\chi^2$) are a joint index of all four retrievals. This retrieval represents a 5km stretch of the cloud.

square ($r\chi^2$) is calculated for each the fits for a given wavelength, CDR, and CDV. A composite RMSE and $r\chi^2$ is derived from the quadrature sum of the RMSE and $r\chi^2$ maps for each channel, and successful fits are subject to the same criteria in Chapter 4, Section 3. The minimized composite RMSE and $r\chi^2$ gives the retrieved CDR and CDV for all channels in the Figure 37 example, though all fits could be done as individual retrievals if desired.

Figure 37 shows that the cross-track retrieval can achieve a higher data density than the along-track version, even for 670 nm. The along-track version is limited by the 2º angular separation between 670 nm view sectors. Here, the only limitation is the size of the scattering angle bin. In the Figure 1 example, the cloudbow is well-resolved in the supernumerary area in all four channels, but notably deviates in the primary bow area at shorter wavelengths. Breon and Goloub (1998) discussed that secondary and tertiary scattering may contribute to the polarized reflectance in some cases, which may broaden the primary bow relative to P_{12}. This effect may be tied to Rayleigh scattering as well, since the effect disappears at longer wavelengths.

Subsection 3.1.2: Application to flatfield characterization

The cross-track retrieval may also be useful for characterizing the detector flatfield on-orbit. The AirHARP instrument creates optical etaloning on the detector surface, which is a weak, stable ring-like structure that covers a large portion of the detector. Etaloning occurs when photons scatter inside of a narrow region of space between two interfaces. It is currently unknown why this occurs in AirHARP, but it is properly and fully corrected in the lab using a traditional flatfield (see Chapter 3). On-orbit, this etaloning may shift location on the FPA due to temperature changes, which will require monitoring. HARP2, for example, will have an internal diffuser for taking on-orbit flatfields and will be able to capture the etaloning state whenever a solar observation is possible. However, these opportunities are infrequent. A trending during the interim between solar measurements is optimal.

Like the cloudbow, the etaloning structure transforms from a circular space to a linear space when the AirHARP raw image is reconstituted into pushbrooms. The etaloning appears like a cross-track ripple and is much dimmer than the signal from the Earth scene. It is stable across the full pushbroom in the along-track direction. The signal from the etaloning is not correlated to the signal from the cloudbow oscillations, which means the retrieval may be used to "remove the signal" from the data. In doing so, this may reveal the etaloning structure whenever a suitable retrieval is possible. Like before, this technique is only possible over wide-spanning clouds like marine stratocumulus, though there are several areas across the globe, such as the coasts of California, Australia, South America, and Africa, where these clouds appear year-round.

Subsection 3.2: Cross-comparison with SPEXone for cloud retrievals

The NASA PACE mission will be the first major climate payload to include two polarimeters, the wide FOV hyper-angle imager HARP2, and the multi-angle, hyper-spectral imager SPEXone. Both instruments will measure the calibrated I and DOLP signals from the same Earth targets at the same time, which will lead to many compatible cloud, aerosol, ocean, and atmospheric retrievals. As Chapter 4 explained, HARP is well-suited for cloudbow measurement due to the hyper-angular along-track coverage at 670 nm. Of the two, SPEXone is less suited for cloudbows and may not be able to retrieve CDR and CDV at all, outside of special geometries. Unlike HARP, SPEXone will view the Earth from five angles: nadir (0°), ± 20°, and ± 58°. The separation between view angles is more than twice that of POLDER-3, meaning that a useful along-track retrieval is not likely. However, the cloudbow is also a spectral signal. SPEXone will sample at 109 discrete bands in the visible from 400 to 700 nm, which means that for certain geometries, scientists may be able to retrieve CDR and CDV using the difference in cloudbow signal by spectra at a specific scattering angle.

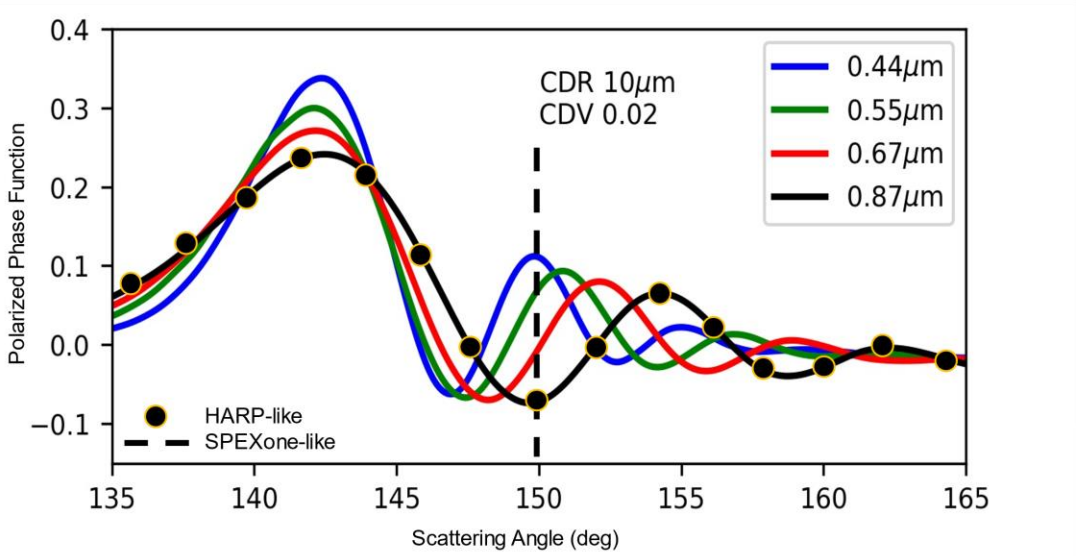

Figure 38. Schematic of HARP-like and SPEXone-like cloudbow sampling. While HARP2 typically observes the same cloud pixel from up to 15 view angles in one wavelength (black dots), SPEXone may only acquire a single geometry (dotted line). However, the spectral separation in the cloudbow signal may allow for a DSD retrieval on SPEXone data.

The following is a theoretical sensitivity study in preparation for HARP2 cloud retrieval validation. Figure 38 shows an example of HARP-like and SPEXone-like cloudbow sampling. As discussed in Chapter 4, HARP observes the same cloud pixel from up to 15 angles in the cloudbow scattering angle range (black dots), and so can retrieve the polarization signal in a single wavelength. SPEXone, however, may only observe the cloudbow from a single geometry due to the wide separation between viewing angles (dotted line), as shown in Figure 38. However, if the cloudbow has significant spectral differentiation at this geometry, a DSD retrieval may still be possible on SPEXone data. SPEXone data could be compared to a Mie P_{12} LUT in a similar manner as the parametric fit from Chapter 4, though the comparison would be done over spectra instead of along-track scattering angles. Additional terms for Rayleigh scattering and non-cloud contaminants as a function of wavelength may take the place of angular terms in Eq. (33). This retrieval leverages the idea that the *relative structure* of P_{12}, not the absolute values, contains all the cloud information content (i.e. largely independent of cloud optical depth and number concentration) and that single-scattering from polarization dominates the signal. Therefore, a cloud target measured at a single, suitable geometry over a

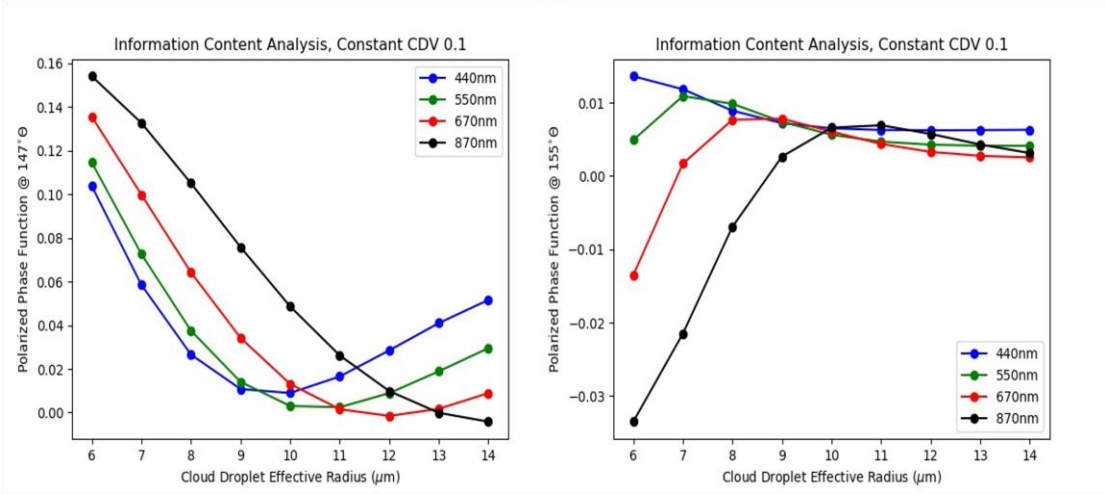

Figure 39. Spectral separation typical of cloudbow signals at a single geometry. The wavelengths chosen are the same as HARP, with 440 (blue), 550 (green), 670 (red) and 870 nm (black) The plots show the expected polarized phase function for a given CDR (x-axis), for a narrow DSD cloudbow signal observed at 147°(left) and 155° (right).

wide range of wavelengths may yield a cloud DSD retrieval that is compatible with one performed using hyper-angular information in a single channel. In the Figure 38 example, the 150° scattering angle geometry (dotted line) has a clear differentiation by spectra, as does 142° (primary bow peak). Spectral DSD retrievals at a single angle may not be possible at 144°, where all the curves meet, or past 155°, where the signal might compete with measure-

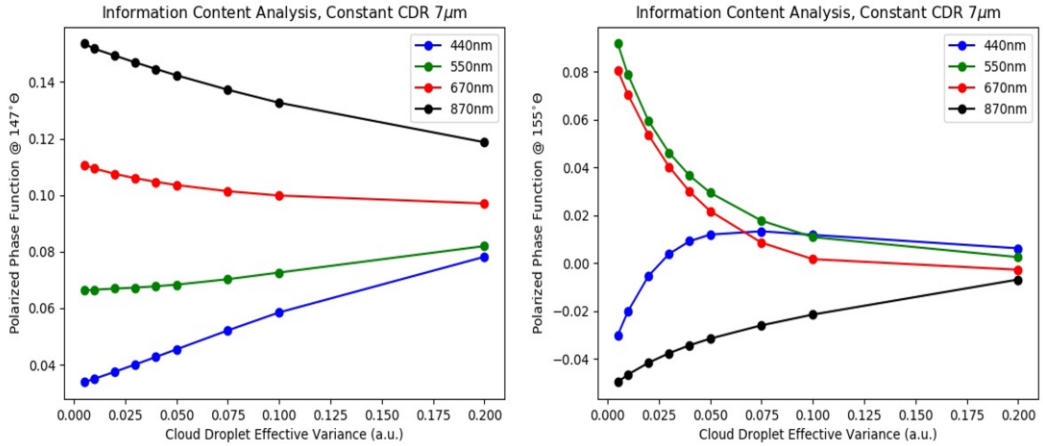

Figure 40. Same study as Figure 39 but the expected polarized phase function for a given CDV (x-axis), for a narrow DSD cloudbow signal observed at 147°(left) and 155° (right). CDR is constant (7um).

ment noise. Because the combination of CDR, CDV, and wavelength make a unique cloudbow signal, the retrievable geometries for SPEXone will also change with the DSD. Figure 39 shows a sensitivity study done for a constant CDV (0.1) cloudbow measured at 147° (left) and 155° (right) across a HARP-like spectral range. Note that each CDR value in the 147° observation corresponds to a unique combination of P_{12} values by wavelength. The 155° measurement is trickier to parse at larger CDR, however. The dynamic range of the P_{12} is small because the cloudbow oscillations shift toward the primary bow with increasing CDR.

Figure 40 shows the same sensitivity study, though with constant CDR (7um) and a varying CDV. The information content is dramatically different compared to Figure 39 for both geometries, but the takeaway is the same: certain geometries are better for retrievals than others. Again, the 147° has the stronger spectral separation (left). This work is still preliminary, though synergistic and co-located cloud retrievals with all three PACE instruments is anticipated when the mission launches in 2023.

Subsection 3.3: Extensions on the along-track cloud DSD retrieval

As clouds begin to precipitate, their effective radius exceeds 20 μm at cloud top (Rosenfeld and Lensky 1998). HARP measurements could be used to indicate the onset of precipitation if it can sense rain mode sizes (current limit is ~24 μm, Figure 41), though this study has not been done as of this work. This result would enhance the synergy with other satellite instruments, such as the Atmospheric Infrared Sounder (AIRS) and the Global Precipitation Measurement (GPM) Microwave Imager. These instruments generate precipitation metrics using infrared and microwave channels from space that can penetrate deep into the clouds (Bolvin et al. 2009, Hou et al. 2014). If HARP can support these metrics with a polarized cloud top measurement, this may be a unique independent validation. If HARP can do so with global coverage and over spatial fields as described in Chapter 4, it would be a considerable advance for Earth remote sensing. HARP is also under consideration for the NASA AOS space mission, which has a precipitation focus and interest in a multi-angle imaging polarimeter system as one of the payloads (NASA 2019). The following discussion uses micron (μm) instead of nanometer

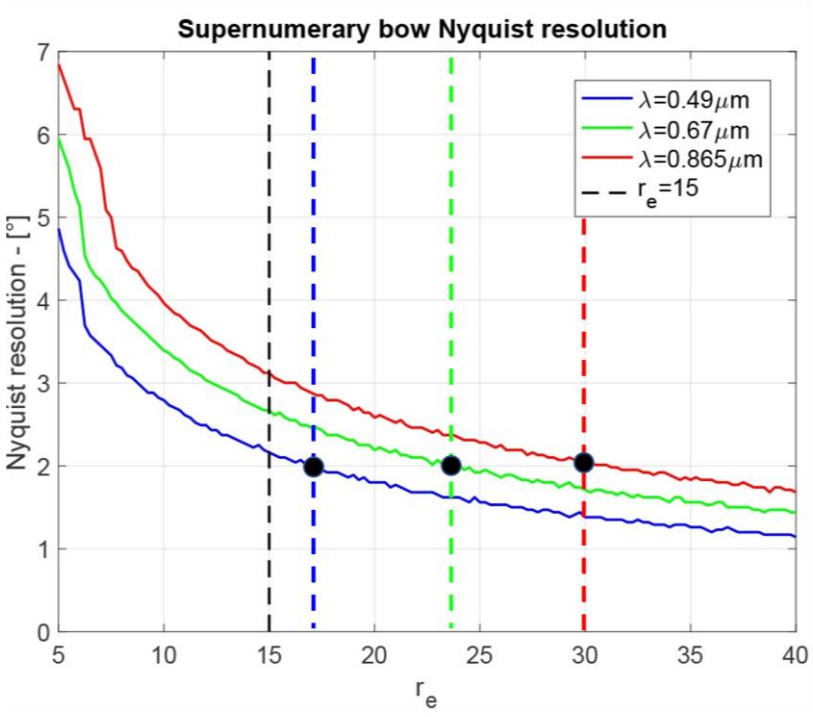

Figure 41. Sampling resolution required to resolve cloudbow signals for a given CDR and wavelength**.** A HARP-like 2° along-track sampling density (black dots) may not be able to consistently retrieve CDR larger than 24 um at 670 nm (green dotted line). This figure is adapted from Miller et al. (2018), under the CC-BY-4.0 license. Modifications: cropped, black dots, colored vertical dashed lines.

(nm) as a more convenient unit of wavelength when analyzing SWIR bands.

A sensitivity study was performed to support this idea, using Mie simulations of cloudbows that are "observed" in 0.67 μm and 1.64 μm channels with HARP-like angular sampling. For CDR where the Nyquist resolution for 0.67 μm is suitable for retrieval (8 and 15 μm), both channels could be used in a joint retrieval (akin to Section 3.1.1) or alone to retrieve DSD properties (Figure 30a-d). Note that Figure 42e shows the difficulty in retrieving large CDR at 0.67 μm with HARP-like angular sampling density. The supernumerary bows are too narrow to be resolved for the CDV 0.01 case, and the data suggests that the retrieval may fail to distinguish either CDV, especially if measurement error is large or compatible to the difference between the curves. However, Figure 42f shows that the 1.64 μm channel is still capable of resolving the supernumeraries at 30um CDR.

The capability to sense larger CDR modes was demonstrated in Sinclair et al. (2021) using RSP data over clouds during the NASA ORACLES campaign. The authors followed the development of a cloud over the course of a research flight and tracked the movement of the DSD modes toward larger CDR as the cloud droplets grew. In this study, the authors used a single channel (0.865 μm) and the RFT method to infer multiple modes of the DSD. RSP has 2.5 more along-track angles over a single cloud target as compared to the HARP 0.670 μm, so retrievals on RSP data at 0.67 μm are sensitive to CDR > 40 μm (off the right side of the Figure 41 plot). Without changing the HARP design, the only way to match this capability is to add a hyper-angular SWIR channel, like 1.64 μm or larger, or subsample each view sector.

As of this work, the RFT method has not been attempted on HARP 0.67 μm data, but according to Alexandrov et al. (2016), it may be viable. If successful, may allow HARP retrievals of multiple modes without any design changes to the instrument. The authors consider a 2° angular separation the upper limit for an accurate RFT retrieval, given that the RFT is

highly sensitive to measurement noise. RFT retrieval sensitivity studies on AirHARP and HARP CubeSat data in preparation for future HARP instrument development are anticipated.

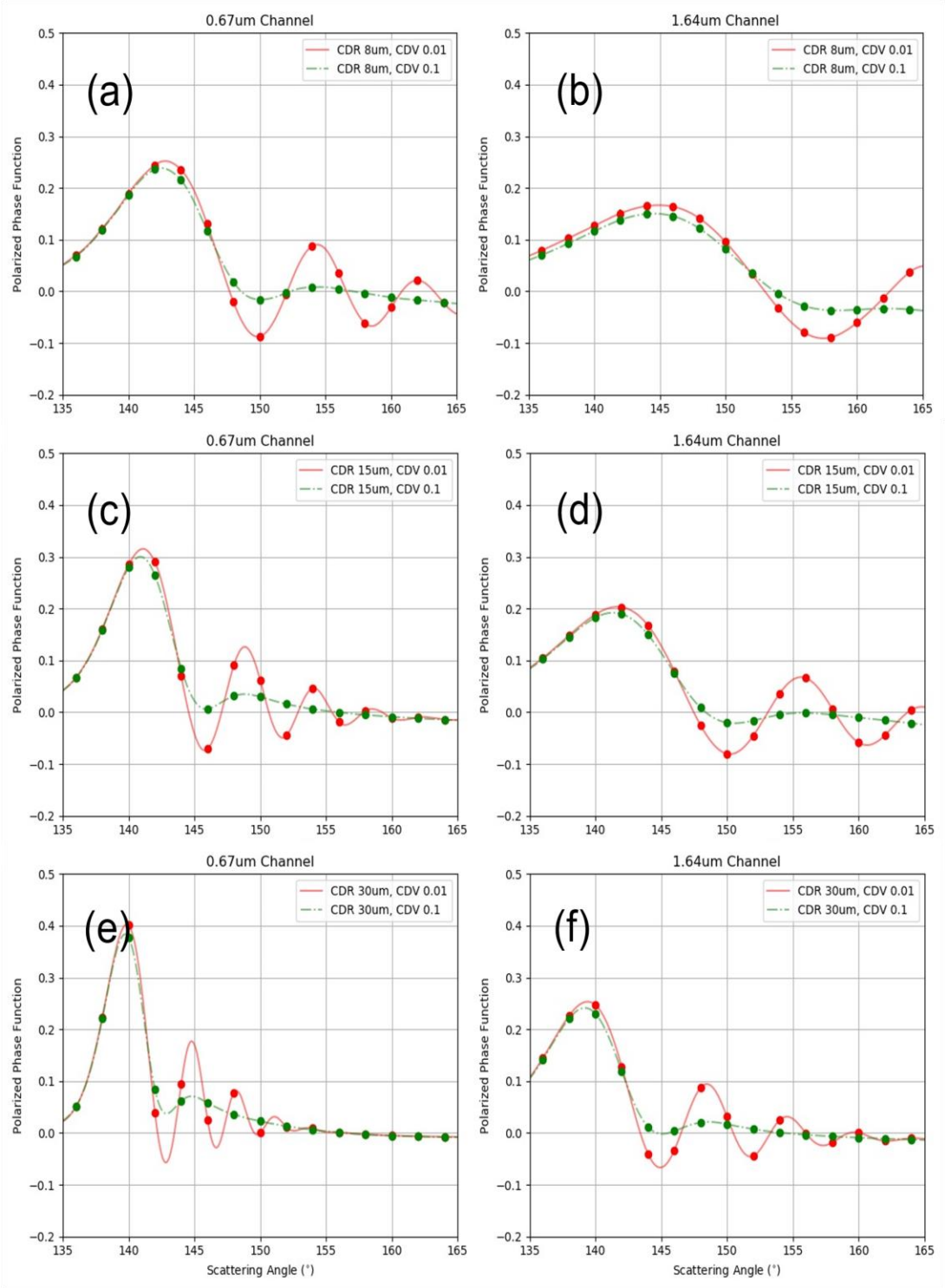

Figure 42. Mie simulations for 0.67 μm (left column) and 1.64 μm (right column) cloudbow observations for increasing CDR 8 μm (top row), 15 μm (middle row), and 30 μm (bottom row). The curves correspond to CDV of 0.01 (red) and 0.1 (green). The dots represent a HARP-like 2° angular sampling density. The "data" in both channels capture the cloudbow information content for 8 and 15 μm cases, though the 0.67 μm channel may not be able to discriminate either CDV in the 30 μm CDR case (e). Here, the 1.64 μm "data" continues to capture the oscillations (f).

Section 4: Conclusions

HARP is a wide FOV polarimetric imager, capable of highly accurate measurements of the Earth's atmosphere. The HARP concept has a wide swath, hyper-angular coverage on the same target, narrow ground resolution, 2-day global coverage from space (HARP2), and high socio-economic value (<5M USD development) for the science quality and information content in its measurements. These advancements are supported by a simple, physics-based calibration that is accurate to community benchmarks, produces comparable measurements to other like instruments, and is adaptable in a variety of lab, field, and space environments. On-orbit, this calibration is maintained through extensive vicarious studies (AirHARP, HARP CubeSat), planned lunar/solar calibrations and constant coincidence with SPEXone and OCI (HARP2). These advancements also allow highly resolved retrievals of liquid water cloud DSDs, as well as aerosol optical properties and loading and land surface reflectance (McBride et al. 2020, IAC). To date, HARP is the only instrument capable of liquid water cloud DSD retrievals using polarized light, at high co-located angular and spatial resolution, and across a wide FOV from space and aircraft.

In the case of clouds, the hyper-angular wide swath measurement provides the foundation for spatial maps of cloud droplet effective radius and variance for HARP resolutions < 1km from aircraft and < 5 km from space. AirHARP DSD retrievals from a heterogeneous stratocumulus cloud field during the NASA LMOS campaign demonstrated that context is essential to understanding the correlation between reflectance, CDR, and CDV for cloud core and periphery regions. These correlations may directly connect to microphysical and radiative processes, but more study is needed. The wide FOV of HARP can access a broad scattering angle range as well, which may extend <90° for some observations. These angles are typically inaccessible to narrow FOV instruments and HARP measurements may not only increase our capability for cloud retrievals, but BRDF/BPDF models that typically struggle at extreme

angles. The HARP 670 nm channel, with 60 views on the same pixel, also provides a nearly uninterrupted scattering profile for any target. This angular sampling is also useful for stereogrammetry: when comparing the parallax from the same target, the altitude of the cloud top, aerosol layer, or surface feature can be derived. HARP multi-angle data can be used to generate topographic maps of atmospheric and surface features and assist with geolocation of co-located instruments, such as SPEXone and OCI on NASA PACE. All these capabilities, combined, is unprecedented for any spaceborne Earth remote sensor thus far. The AirHARP and HARP CubeSat instruments missions demonstrated this technology from aircraft and space inside a compact, 10x10x15cm volume. This compact size is suitable for small-sat constellations as well, which could boost the spatial, angular, and temporal coverage for cloud, aerosol, ocean, and land retrievals than current standalone HARP concepts presented in this work.

With the upcoming launch of the NASA PACE mission and the release of HARP CubeSat L1B data to the scientific community, the same calibration and cloud retrieval concepts discussed in this work may be used to help connect cloud microphysical properties to global radiative forcings. This is a major step in reducing climate change uncertainties related to clouds and aerosols. Current and future HARP datasets may provide strong science and economic rationale for including high-resolution, hyper-angle imaging polarimetry and small satellite technology on future major Earth science space missions.

Appendix

The RSP error model is provided in Knobelspiesse (2015). The overall error in reflectance and DOLP is described below:

$$\sigma_\rho^2 = \left(\frac{r^2\sigma_{floor}}{\mu_s}\right)^2 + \frac{a\,R_I r^2}{\mu_s} + \frac{\sigma_{lnK}^2 R_P^2}{16} + \sigma_{a_c}^2 R_I^2 \tag{38}$$

$$\sigma_{DOLP}^2(noise) = 4\left(1 + \frac{DOLP^2}{2}\right)\left(\frac{r^2\sigma_{floor}}{\mu_s R_I}\right)^2 + 2\left(1 - \frac{DOLP^2}{2}\right)\left(\frac{a\,r^2}{\mu_s R_I}\right) \tag{39}$$

$$\sigma_{DOLP}^2(cal) = \frac{\sigma_{lnK}^2}{2}\left[1 - DOLP^2 + \frac{DOLP^4}{2}\left(1 - \frac{1}{2}\sin^2 4\chi\right)\right] + \sigma_{lna}^2 DOLP^2 \tag{40}$$

$$\sigma_{DOLP}^2 = \sigma_{DOLP}^2(noise) + \sigma_{DOLP}^2(cal) \tag{41}$$

Several parameters are prescribed, based on Knobelspiesse (2015):

- Solar distance in AU, r: 1
- Noise floor, σ_{floor} (x 10^{-5}): 2.5 (550 nm), 2.2 (670 nm), and 2.0 (865 nm)
- Shot noise parameter, *a* (x 10^{-9}): 4.5 (550 nm), 3.7 (670 nm), 3.7 (865 nm)
- Relative gain coefficient cal uncertainty, σ_{lnK}: 0.005
- Absolute radiometric uncertainty, σ_{a_c}: 0.03
- Polarimetric characterization uncertainty, σ_{lna}: 0.001

Other parameters are given in the field datasets and are a function of observational geometry and Earth scene:

- Cosine of the solar zenith angle, μ_s
- Intensity reflectance, R_I
- Polarized reflectance, R_P
- Degree of Linear Polarization, *DOLP*

Finally, the RSP DOLP uncertainty depends on the angle of polarization, χ, in Eq. (27). In a sensitivity study with the above parameters and field data, we found that the intercomparison with AirHARP did not vary meaningfully when χ varied between 0 and 180°. Therefore, $\sin^2 4\chi$ was set to its expectation value, 0.5, which represents any angle $\chi = (45n + 11.25)^\circ$ for n in $\mathbb{Z}$.

A simplified version of the AirHARP error model uses both systematic and random terms:

$$\sigma_\rho^2 = (0.03\rho)^2 + \left(\frac{\Delta\rho}{\sqrt{B}}\right)^2 \tag{42}$$

$$\sigma_{DOLP}^2 = (0.0025)^2 + \left(\frac{\Delta DOLP}{\sqrt{B}}\right)^2 \tag{43}$$

where the 0.03 in Eq. (42) is an estimate of the radiometric transfer calibration of the NASA GSFC "Grande" sphere (Butler and Cooper 2015, using Slick data as a reference), $\Delta\rho$ is the standard deviation of the superpixel reflectance measurement, and B is the number of binned pixels (B=64). 0.0025 in Eq. (43) is derived from the POLBOX measurements in Figure 21 and is the same for all channels. $\Delta DOLP$ is the standard deviation of the superpixel DOLP measurement.

In Eq. (23), the polarized reflectance is defined as P and the reflectance as R:

$$P = \sqrt{Q^2 + U^2} = DOLP * R \tag{44}$$

The polarized reflectance uncertainty can be derived via error propogation on Eq. (44):

$$\sigma_P^2 = (DOLP\ \sigma_R)^2 + (R\ \sigma_{DOLP})^2 \tag{45}$$

Bibliography

Section 1: Complete Reference List

[1] Harding, R. Kwok, M. Lefsky, T. Markus, A. Marshak, T. Neumann, S. Palm, B. Schutz, B. Smith, J. Spinhirne and C. Webb, Proceedings of the IEEE **98** (5), 735-751 (2010).

[2] A. S. Ackerman, O. B. Toon, D. E. Stevens, A. J. Heymsfield, V. Ramanathan and E. J. Welton, Science **288** (5468), 1042-1047 (2000).

[3] B. A. Albrecht, Science **245** (4923), 1227-1230 (1989).

[4] E. J. Aldoretta, A. Angal, K. A. Twedt, H. Chen, Y. Li, D. O. Link, Q. Mu, K. Vermeesch and X. Xiong, *The MODIS RSB calibration and look-up table delivery process for collections 6 and 6.1*. (SPIE, 2020).

[5] M. D. Alexandrov, B. Cairns, C. Emde, A. S. Ackerman, M. Ottaviani and A. P. Wasilewski, Remote Sensing of Environment **177**, 144-152 (2016).

[6] M. D. Alexandrov, B. Cairns, C. Emde, A. S. Ackerman and B. van Diedenhoven, Remote sensing of environment **125**, 92-111 (2012).

[7] M. D. Alexandrov, B. Cairns and M. I. Mishchenko, Journal of Quantitative Spectroscopy and Radiative Transfer **113** (18), 2521-2535 (2012).

[8] M. D. Alexandrov, B. Cairns, B. Van Diedenhoven, A. S. Ackerman, A. P. Wasilewski, M. J. McGill, J. E. Yorks, D. L. Hlavka, S. E. Platnick and G. T. Arnold, Remote Sensing of Environment **181**, 96-110 (2016).

[9] M. D. Alexandrov, B. Cairns, A. P. Wasilewski, A. S. Ackerman, M. J. McGill, J. E. Yorks, D. L. Hlavka, S. E. Platnick, G. T. Arnold and B. Van Diedenhoven, Remote Sensing of Environment **169**, 20-36 (2015).

[10] O. Altaratz, I. Koren, L. A. Remer and E. Hirsch, Atmospheric Research **140**, 38-60 (2014).

[11] Oxford Instruments, *Optical Etaloning in Charge Coupled Devices*, last accessed at https://andor.oxinst.com/learning/view/article/optical-etaloning-in-charge-coupled-devices on 14 January 2020.

[12] T. L. Anderson, R. J. Charlson, N. Bellouin, O. Boucher, M. Chin, S. A. Christopher, J. Haywood, Y. J. Kaufman, S. Kinne and J. A. Ogren, Bulletin of the American Meteorological Society **86** (12), 1795-1810 (2005).

[13] M. O. Andreae, D. Rosenfeld, P. Artaxo, A. A. Costa, G. P. Frank, K. M. Longo and M. A. F. d. Silva-Dias, science **303** (5662), 1337-1342 (2004).

[14] R. F. Arduini, P. Minnis, W. L. Smith Jr, J. K. Ayers, M. M. Khaiyer and P. Heck, (2005).

[15] D. Baumgardner, L. Avallone, A. Bansemer, S. Borrmann, P. Brown, U. Bundke, P. Y. Chuang, D. Cziczo, P. Field and M. Gallagher, Bulletin of the American Meteorological Society **93** (2), ES29-ES34 (2012).

[16] T. L. Bell, D. Rosenfeld and K. M. Kim, Geophysical Research Letters **36,** (2009).

[17] R. Bhatt, D. R. Doelling, B. R. Scarino, A. Gopalan, C. O. Haney, P. Minnis and K. M. Bedka, Journal of Atmospheric and Oceanic Technology **33** (11), 2499-2515 (2016).

[18] B. A. Bodhaine, N. B. Wood, E. G. Dutton and J. R. Slusser, Journal of Atmospheric and Oceanic Technology **16** (11), 1854-1861 (1999).

[19] D. T. Bolvin, R. F. Adler, G. J. Huffman, E. J. Nelkin and J. P. Poutiainen, Journal of Applied Meteorology and Climatology **48** (9), 1843-1857 (2009).

[20] P. Bontempi, B. Edwards, H. Maring, W. Turner, *Pre-Aerosol, Clouds, and ocean Ecosystem (PACE) mission*, NRC Space Science Week, Spring 2015 Meeting of the CESAS. Last retrieved at https://sites.nationalacademies.org/cs/groups/ssbsite/documents/webpage/ssb_160751.pdf on 28 September 2022.

[21] O. Boucher, D. Randall, P. Artaxo, C. Bretherton, G. Feingold, P. Forster, V.-M. Kerminen, Y. Kondo, H. Liao, U. Lohmann, P. Rasch, S.K. Satheesh, S. Sherwood, B. Stevens and X.Y. Zhang, Clouds and Aerosols. In: *Climate Change 2013: The Physical Science Basis. Contribution of Working Group I to the Fifth Assessment Report of the Intergovernmental Panel on Climate Change* [Stocker, T.F., D. Qin, G.-K. Plattner, M. Tignor, S.K. Allen, J. Boschung, A. Nauels, Y. Xia, V. Bex and P.M. Midgley (eds.)]. Cambridge University Press, Cambridge, United Kingdom and New York, NY, USA, (2013).

[22] R. M. Bowers, C. L. Lauber, C. Wiedinmyer, M. Hamady, A. G. Hallar, R. Fall, R. Knight and N. Fierer, Applied and environmental microbiology **75** (15), 5121-5130 (2009).

[23] F. M. Bréon and M. Doutriaux-Boucher, IEEE Transactions on Geoscience and Remote Sensing **43** (8), 1796-1805 (2005).

[24] F. M. Breon and F. Maignan, Earth System Science Data **9** (1), 31-45 (2017).

[25] F. M. Bréon and P. Goloub, Geophysical Research Letters **25** (11), 1879-1882 (1998).

[26] S. M. Burrows, C. Hoose, U. Pöschl and M. G. Lawrence, Atmospheric Chemistry and Physics **13** (1), 245-267 (2013).

[27] B. Cairns, E. E. Russell and L. D. Travis, *Research scanning polarimeter: calibration and ground-based measurements*. (SPIE, 1999).

[28] K. K. Chandrakar, W. W. Grabowski, H. Morrison and G. H. Bryan, Journal of the Atmospheric Sciences **78** (9), 2983-3005 (2021).

[29] D. M. Chate, P. S. P. Rao, M. S. Naik, G. A. Momin, P. D. Safai and K. Ali, Atmospheric Environment **37** (18), 2477-2484 (2003).

[30] S. Chen, M.-K. Yau, P. Bartello and L. Xue, Atmospheric Chemistry and Physics **18** (10), 7251-7262 (2018).

[31] J. Chowdhary, B. Cairns, F. Waquet, K. Knobelspiesse, M. Ottaviani, J. Redemann, L. Travis and M. Mishchenko, Remote Sensing of Environment **118**, 284-308 (2012).

[32] O. M. Coddington, P. Pilewskie, J. Redemann, S. Platnick, P. B. Russell, K. S. Schmidt, W. J. Gore, J. Livingston, G. Wind and T. Vukicevic, Journal of Geophysical Research: Atmospheres **115** D10 (2010).

[33] D. L. Coffeen, JOSA **69** (8), 1051-1064 (1979).

[34] J. Cooper and J. Butler, *NASA GSFC Code 618 Calibration Facility*, 2020. Last retrieved from https://cl.gsfc.nasa.gov/ on 28 September 2022.

[35] C. Cornet, L. C-Labonnote, F. Waquet, F. Szczap, L. Deaconu, F. Parol, C. Vanbauce, F. Thieuleux and J. Riédi, Atmospheric Measurement Techniques **11** (6), 3627-3643 (2018).

[36] C. Cox and W. Munk, JOSA **44** (11), 838-850 (1954).

[37] J. P. Craven, R. E. Jewell and H. E. Brooks, Weather and Forecasting **17** (4), 885-890 (2002).

[38] A. da Silva, *The Atmosphere Observing System (AOS): Synergistic Aerosol, Cloud, Convection and Precipitation Measurement and Modeling Systems*, (AGU, 2021).

[39] A. M. Da Silva Jr, H. Maring, F. Seidel, M. Behrenfeld, R. Ferrare and G. Mace, 2020.

[40] R. Davies, V. M. Jovanovic and C. M. Moroney, Journal of Geophysical Research: Atmospheres **122** (7), 3975--3986 (2017).

[41] A. de Lozar and L. Muessle, Atmospheric Chemistry and Physics **16** (10), 6563-6576 (2016).

[42] P. J. DeMott, Atmospheric Research **38** (1-4), 63-99 (1995).

[43] P. J. DeMott, O. Möhler, O. Stetzer, G. Vali, Z. Levin, M. D. Petters, M. Murakami, T. Leisner, U. Bundke and H. Klein, Bulletin of the American Meteorological Society **92** (12), 1623-1635 (2011).

[44] P. Y. Deschamps, F. M. Bréon, M. Leroy, A. Podaire, A. Bricaud, J. C. Buriez and G. Seze, IEEE Transactions on Geoscience and Remote Sensing **32** (3), 598-615 (1994).

[45] B. J. Devenish, P. Bartello, J. L. Brenguier, L. R. Collins, W. W. Grabowski, R. H. A. Ijzermans, S. P. Malinowski, M. W. Reeks, J. C. Vassilicos and L. P. Wang, Quarterly Journal of the Royal Meteorological Society **138** (667), 1401-1429 (2012).

[46] A. Di Noia, O. P. Hasekamp, B. van Diedenhoven and Z. Zhang, Atmospheric Measurement Techniques **12** (3), 1697-1716 (2019).

[47] M. Diamond, M., H.M. Director, R. Eastman, A. Possner, and R. Wood, AGU Advances **1** (1), (2020).

[48] D. J. Diner, J. C. Beckert, T. H. Reilly, C. J. Bruegge, J. E. Conel, R. A. Kahn, J. V. Martonchik, T. P. Ackerman, R. Davies and S. A. W. Gerstl, IEEE Transactions on Geoscience and Remote Sensing **36** (4), 1072-1087 (1998).

[49] D. J. Diner, S. W. Boland, M. Brauer, C. Bruegge, K. A. Burke, R. Chipman, L. Di Girolamo, M. J. Garay, S. Hasheminassab and E. Hyer, Journal of Applied Remote Sensing **12** (4), (2018).

[50] D. J. Diner, F. Xu, M. J. Garay, J. V. Martonchik, B. E. Rheingans, S. Geier, A. Davis, B. R. Hancock, V. M. Jovanovic and M. A. Bull, Atmospheric Measurement Techniques **6** (8), 2007-2025 (2013).

[51] N. Ding, J. Shao, C. Yan, J. Zhang, Y. Qiao, Y. Pan, J. Yuan, Y. Dong and B. Yu, Remote Sensing **13** (10), (2021).

[52] M. S. Djellali, J. Riedi, S. Marcq, B. Fougnie, S. Hioki and J.-M. Nicolas, *Development of calibration methods using specular reflection over the ocean for the multiviewing, multichannel, multipolarization imager (3MI) of the Eumetsat polar system--second generation (EPS-SG)*. (SPIE, 2019).

[53] J. P. do Carmo, G. de Villele, K. Wallace, A. Lefebvre, K. Ghose, T. Kanitz, F. Chassat, B. Corselle, T. Belhadj and P. Bravetti, Atmosphere **12** (1) (2021).

[54] O. Dubovik, M. Herman, A. Holdak, T. Lapyonok, D. Tanré, J. L. Deuzé, F. Ducos, A. Sinyuk and A. Lopatin, Atmospheric Measurement Techniques **4** (5), 975-1018 (2011).

[55] O. Dubovik, Z. Li, M. I. Mishchenko, D. Tanré, Y. Karol, B. Bojkov, B. Cairns, D. J. Diner, W. R. Espinosa and P. Goloub, Journal of Quantitative Spectroscopy and Radiative Transfer **224**, 474-511 (2019).

[56] O. Dubovik, G. L. Schuster, F. Xu, Y. Hu, H. Bösch, J. Landgraf and Z. Li, Frontiers **2**, 612673-616187 (2021).

[57] M. Ed Chaves, M. Ca Picoli and I. D Sanches, Remote Sensing **12** (18), 3062 (2020).

[58] Z. A. Eitzen, K.-M. Xu and T. Wong, Journal of Climate **22** (22), 5983-6000 (2009).

[59] M. Endemann, *The ADM-Aeolus mission*. (SPIE, 2017).

[60] H. Erives, X. Xiong, J. Sun, J. A. Esposito, S. Xiong and W. L. Barnes, *Terra MODIS RSB on-orbit calibration and performance: Four years of data*. (SPIE, 2004).

[61] V. Eyring, N.P. Gillett, K.M. Achuta Rao, R. Barimalala, M. Barreiro Parrillo, N. Bellouin, C. Cassou, P.J. Durack, Y. Kosaka, S. McGregor, S. Min, O. Morgenstern, and Y. Sun, 2021: Human Influence on the Climate System. In *Climate Change 2021: The Physical Science Basis. Contribution of Working Group I to the Sixth Assessment Report of the Intergovernmental Panel on Climate Change* [Masson-Delmotte, V., P. Zhai, A. Pirani, S.L. Connors, C. Péan, S. Berger, N. Caud, Y. Chen, L. Goldfarb, M.I. Gomis, M. Huang, K. Leitzell, E. Lonnoy, J.B.R. Matthews, T.K. Maycock, T. Waterfield, O. Yelekçi, R. Yu, and B. Zhou (eds.)]. Cambridge University Press, Cambridge, United Kingdom and New York, NY, USA, 423–552 (2021)

[62] J. Fan, L. R. Leung, D. Rosenfeld, Q. Chen, Z. Li, J. Zhang and H. Yan, Proceedings of the National Academy of Sciences **110** (48), E4581-E4590 (2013).

[63] D. K. Farmer, C. D. Cappa and S. M. Kreidenweis, Chemical Reviews **115** (10), 4199-4217 (2015).

[64] G. Feingold, W. R. Cotton, S. M. Kreidenweis and J. T. Davis, Journal of the Atmospheric Sciences **56** (24), 4100-4117 (1999).

[65] G. Feingold and Z. Levin, Journal of Climate and Applied Meteorology, 1346-1363 (1986).

[66] G. Feingold, L. A. Remer, J. Ramaprasad and Y. J. Kaufman, Journal of Geophysical Research: Atmospheres **106** (D19), 22907-22922 (2001).

[67] R. Fensholt, K. Rasmussen, T. T. Nielsen and C. Mbow, Remote sensing of Environment **113** (9), 1886-1898 (2009).

[68] R. Fernandez-Borda, E. Waluschka, S. Pellicori, J. V. Martins, L. Ramos-Izquierdo, J. D. Cieslak and P. L. Thompson, *Evaluation of the polarization properties of a Philips-type prism for the construction of imaging polarimeters*. (SPIE, 2009).

[69] L. Flynn, C. Long, X. Wu, R. Evans, C. T. Beck, I. Petropavlovskikh, G. McConville, W. Yu, Z. Zhang and J. Niu, Journal of Geophysical Research: Atmospheres **119** (10), 6181-6195 (2014).

[70] P. Forster, T. Storelvmo, K. Armour, W. Collins, J.-L. Dufresne, D. Frame, D.J. Lunt, T. Mauritsen, M.D. Palmer, M. Watanabe, M. Wild, and H. Zhang, The Earth's Energy Budget, Climate Feedbacks, and Climate Sensitivity. In *Climate Change 2021: The Physical Science Basis. Contribution of Working Group I to the Sixth Assessment Report of the Intergovernmental Panel on Climate Change* [Masson-Delmotte, V., P. Zhai, A. Pirani, S.L. Connors, C. Péan, S. Berger, N. Caud, Y. Chen, L. Goldfarb, M.I. Gomis, M. Huang, K. Leitzell, E. Lonnoy, J.B.R. Matthews, T.K. Maycock, T. Waterfield, O. Yelekçi, R. Yu, and B. Zhou (eds.)]. Cambridge University, United Kingdom and New York, NY, USA, 923-1054 (2021).

[71] B. Fougnie, G. Bracco, B. Lafrance, C. Ruffel, O. Hagolle and C. Tinel, Applied optics **46** (22), 5435-5451 (2007).

[72] B. Fougnie, T. Marbach, A. Lacan, R. Lang, P. Schlüssel, G. Poli, R. Munro and A. B. Couto, Journal of Quantitative Spectroscopy and Radiative Transfer **219**, 23-32 (2018).

[73] B. Fox-Kemper, H.T. Hewitt, C. Xiao, G. Aðalgeirsdóttir, S.S. Drijfhout, T.L. Edwards, N.R. Golledge, M. Hemer, R.E. Kopp, G. Krinner, A. Mix, D. Notz, S. Nowicki, I.S. Nurhati, L. Ruiz, J.-B. Sallée, A.B.A. Slangen, and Y. Yu, Ocean, Cryosphere and Sea Level Change. In *Climate Change 2021: The Physical Science Basis. Contribution of Working Group I to the Sixth Assessment Report of the Intergovernmental Panel on Climate Change* [Masson-Delmotte, V., P. Zhai, A. Pirani, S.L. Connors, C. Péan, S. Berger, N. Caud, Y. Chen, L. Goldfarb, M.I. Gomis, M. Huang, K. Leitzell, E. Lonnoy, J.B.R. Matthews, T.K. Maycock, T. Waterfield, O. Yelekçi, R. Yu, and B. Zhou (eds.)]. Cambridge University Press, Cambridge, United Kingdom and New York, NY, USA, 1211–1362 (2021).

[74] D. Francis, R. Fonseca, N. Nelli, J. Cuesta, M. Weston, A. Evan and M. Temimi, Geophysical Research Letters **47** (24), (2020).

[75] R. J. Frouin, B. A. Franz, A. Ibrahim, K. Knobelspiesse, Z. Ahmad, B. Cairns, J. Chowdhary, H. M. Dierssen, J. Tan and O. Dubovik, Frontiers in Earth Science **7**, 145 (2019).

[76] G. Fu and O. Hasekamp, Atmospheric Measurement Techniques **11** (12), 6627-6650 (2018).

[77] G. Fu, O. Hasekamp, J. Rietjens, M. Smit, A. Di Noia, B. Cairns, A. Wasilewski, D. Diner, F. Seidel and F. Xu, Atmospheric Measurement Techniques **13** (2), 553-573 (2020).

[78] B. C. Gao and Y. J. Kaufman, Journal of Atmospheric Sciences **52** (23), 4231-4237 (1995).

[79] M. Gao, B. A. Franz, K. Knobelspiesse, P.-W. Zhai, V. Martins, S. Burton, B. Cairns, R. Ferrare, J. Gales and O. Hasekamp, Atmospheric Measurement Techniques **14** (6), 4083-4110 (2021).

[80] M. J. Garay, O. V. Kalashnikova and M. A. Bull, Atmospheric Chemistry and Physics **17** (8), 5095-5106 (2017).

[81] B. Gérard, J. L. Deuzé, M. Herman, Y. J. Kaufman, P. Lallart, C. Oudard, L. A. Remer, B. Roger, B. Six and D. Tanré, Journal of Geophysical Research: Atmospheres **110**, (2005).

[82] S. Ghan, M. Wang, S. Zhang, S. Ferrachat, A. Gettelman, J. Griesfeller, Z. Kipling, U. Lohmann, H. Morrison and D. Neubauer, Proceedings of the National Academy of Sciences **113** (21), 5804-5811 (2016).

[83] S. Glienke, A. Kostinski, J. Fugal, R. A. Shaw, S. Borrmann and J. Stith, Geophysical Research Letters **44** (15), 8002-8010 (2017).

[84] P. Goloub, M. Herman, H. Chepfer, J. Riédi, G. Brogniez, P. Couvert and G. Sèze, Journal of Geophysical Research: Atmospheres **105** (D11), 14747-14759 (2000).

[85] B. Gorbunov, A. Baklanov, N. Kakutkina, H. L. Windsor and R. Toumi, Journal of Aerosol Science **32** (2), 199-215 (2001).

[86] E. Gryspeerdt, J. Quaas, S. Ferrachat, A. Gettleman, S. Ghan, U. Lohmann, H. Morrison, D. Neubauer, D. G. Partridge, P. Stier, T. Takemura, H. Wang, M. Wang, and K. Zhang, Proceedings of the National Academy of Sciences, **114** (19), 4899–4904 (2017)

[87] S. K. Gulev, P.W. Thorne, J. Ahn, F.J. Dentener, C.M. Domingues, S. Gerland, D. Gong, D.S. Kaufman, H.C. Nnamchi, J. Quaas, J.A. Rivera, S. Sathyendranath, S.L. Smith, B. Trewin, K. von Schuckmann, and R.S. Vose, Changing State of the Climate System. In *Climate Change 2021: The Physical Science Basis. Contribution of Working Group I to the Sixth Assessment Report of the Intergovernmental Panel on Climate Change* [Masson-Delmotte, V., P. Zhai, A. Pirani, S.L. Connors, C. Péan, S. Berger, N. Caud, Y. Chen, L. Goldfarb, M.I. Gomis, M. Huang, K. Leitzell, E. Lonnoy, J.B.R. Matthews, T.K. Maycock, T. Waterfield, O. Yelekçi, R. Yu, and B. Zhou (eds.)]. Cambridge University Press, Cambridge, United Kingdom and New York, NY, USA, 287–422, (2021)

[88] J. W. Hair, C. A. Hostetler, A. L. Cook, D. B. Harper, R. A. Ferrare, T. L. Mack, W. Welch, L. R. Izquierdo and F. E. Hovis, Applied Optics **47** (36), 6734-6752 (2008).

[89] J. E. Hansen and L. D. Travis, Space Science Reviews **16** (4), 527-610 (1974).

[90] D. L. Hartmann and K. Larson, Geophysical Research Letters **29** (20), (2002).

[91] O. P. Hasekamp, G. Fu, S. P. Rusli, L. Wu, A. Di Noia, J. aan de Brugh, J. Landgraf, J. M. Smit, J. Rietjens and A. van Amerongen, Journal of Quantitative Spectroscopy and Radiative Transfer **227**, 170-184 (2019).

[92] O. P. Hasekamp, E. Gryspeerdt, and J. Quaas, Nature Communications, **10** (1), 1–7 (2019).

[93] O. P. Hasekamp and J. Landgraf, Applied Optics **46** (16), 3332-3344 (2007).

[94] J. Haywood and O. Boucher, Reviews of Geophysics **38** (4), 513-543 (2000).

[95] A. A. Hill, G. Feingold and H. Jiang, Journal of the Atmospheric Sciences **66** (5), 1450-1464 (2009).

[96] S. Hioki, J. Riedi and M. S. Djellali, Atmospheric Measurement Techniques **14** (3), 1801-1816 (2021).

[97] A. Y. Hou, R. K. Kakar, S. Neeck, A. A. Azarbarzin, C. D. Kummerow, M. Kojima, R. Oki, K. Nakamura and T. Iguchi, Bulletin of the American meteorological Society **95** (5), 701-722 (2014).

[98] Y. Hu, D. Winker, M. Vaughan, B. Lin, A. Omar, C. Trepte, D. Flittner, P. Yang, S. L. Nasiri and B. Baum, Journal of Atmospheric and Oceanic Technology **26** (11), 2293-2309 (2009).

[99] W. H. Hunt, D. M. Winker, M. A. Vaughan, K. A. Powell, P. L. Lucker and C. Weimer, Journal of Atmospheric and Oceanic Technology **26** (7), 1214-1228 (2009).

[100] E. Im, C. Wu and S. L. Durden, *Cloud profiling radar for the CloudSat mission*. (IEEE, 2005).

[101] J. Jackson, Classical Electrodynamics. Wiley, New York, NY, 3rd edition, 1999.

[102] B. T. Johnson, K. P. Shine and P. M. Forster, Quarterly Journal of the Royal Meteorological Society **130** (599), 1407-1422 (2004).

[103] R. A. Kahn, W. H. Li, C. Moroney, D. J. Diner, J. V. Martonchik and E. Fishbein, Journal of Geophysical Research: Atmospheres **112** (2007).

[104] O. V. Kalashnikova, M. J. Garay, A. B. Davis, D. J. Diner and J. V. Martonchik, Journal of Quantitative Spectroscopy and Radiative Transfer **112** (13), 2149-2163 (2011).

[105] Y. J. Kaufman, I. Koren, L. A. Remer, D. Rosenfeld and Y. Rudich, Proceedings of the National Academy of Sciences **102** (32), 11207-11212 (2005).

[106] J. E. Kay, T. L'Ecuyer, H. Chepfer, N. Loeb, A. Morrison and G. Cesana, Current Climate Change Reports **2** (4), 159-169 (2016).

[107] J. Kazil, T. Yamaguchi and G. Feingold, Journal of Advances in Modeling Earth Systems **9** (5), 2214-2229 (2017).

[108] A. Khain, D. Rosenfeld and A. Pokrovsky, Quarterly Journal of the Royal Meteorological Society, **131** (611), 2639- (2005).

[109] A. M. Khan, P. C. Stoy, J. T. Douglas, M. Anderson, G. Diak, J. A. Otkin, C. Hain, E. M. Rehbein and J. McCorkel, Biogeosciences **18** (13), 4117-4141 (2021).

[110] M.-H. Kim, A. H. Omar, J. L. Tackett, M. A. Vaughan, D. M. Winker, C. R. Trepte, Y. Hu, Z. Liu, L. R. Poole and M. C. Pitts, Atmospheric Measurement Techniques **11** (11), 6107-6135 (2018).

[111] M. D. King, S.-C. Tsay, S. E. Platnick, M. Wang and K.-N. Liou, MODIS Algorithm Theoretical Basis Document (1997).

[112] S. Kinne, U. Lohmann, J. Feichter, M. Schulz, C. Timmreck, S. Ghan, R. Easter, M. Chin, P. Ginoux and T. Takemura, Journal of Geophysical Research: Atmospheres **108** (2003).

[113] S. A. Klein, A. Hall, J. R. Norris and R. Pincus, Shallow clouds, water vapor, circulation, and climate sensitivity, 135-157 (2017).

[114] D. S. Kliger, J. W. Lewis and C. E. Randall, Boston: Academic Press (1990).

[115] E. J. Knight and G. Kvaran, Remote sensing **6** (11), 10286-10305 (2014).

[116] K. Knobelspiesse, RSP Uncertainty Model, 2015. Last accessed at https://airbornescience.nasa.gov/sites/default/files/documents/rsp_unc.pdf on 28 September 2022.

[117] K. Knobelspiesse, B. Cairns, M. Ottaviani, R. Ferrare, J. Hair, C. Hostetler, M. Obland, R. Rogers, J. Redemann and Y. Shinozuka, Atmospheric Chemistry and Physics **11** (14), 7045-7067 (2011).

[118] K. D. Knobelspiesse, A. Ibrahim, B. A. Franz, S. W. Bailey, Z. Ahmad, J. M. Gales, M. J. Garay and R. C. Levy, *Information content analysis of multi-angle, polarimetric instruments for Ocean Color remote sensing atmospheric correction*. (AGU, 2018).

[119] K. Knobelspiesse, H. M. J. Barbosa, C. Bradley, C. Bruegge, B. Cairns, G. Chen, J. Chowdhary, A. Cook, A. Di Noia and B. van Diedenhoven, Earth System Science Data **12** (3), 2183-2208 (2020).

[120] K. Knobelspiesse, B. Cairns, M. Mishchenko, J. Chowdhary, K. Tsigaridis, B. van Diedenhoven, W. Martin, M. Ottaviani and M. Alexandrov, Optics express **20** (19), 21457-21484 (2012).

[121] K. Knobelspiesse, Q. Tan, C. Bruegge, B. Cairns, J. Chowdhary, B. Van Diedenhoven, D. Diner, R. Ferrare, G. Van Harten and V. Jovanovic, Applied optics **58** (3), 650-669 (2019).

[122] H. Köhler, Transactions of the Faraday Society **32**, 1152-1161 (1936).

[123] A. A. Kokhanovsky and G. Leeuw, *Satellite aerosol remote sensing over land*. (Springer, 2009).

[124] M. Komurcu, T. Storelvmo, I. Tan, U. Lohmann, Y. Yun, J. E. Penner, Y. Wang, X. Liu and T. Takemura, Journal of Geophysical Research: Atmospheres **119** (6), 3372-3400 (2014).

[125] I. Koren, Y. J. Kaufman, L. A. Remer and J. V. Martins, Science **303** (5662), 1342-1345 (2004).

[126] A. Korolev, G. McFarquhar, P. R. Field, C. Franklin, P. Lawson, Z. Wang, E. Williams, S. J. Abel, D. Axisa and S. Borrmann, Meteorological Monographs **58**, 5.1-5.50 (2017).

[127] A. Kosowsky, arXiv preprint astro-ph/9501045 (1995).

[128] T. S. L'Ecuyer and J. H. Jiang, Phys. Today **63** (7), 36-41 (2010).

[129] J. Latham, K. Bower, T. Choularton, H. Coe, P. Connolly, G. Cooper, T. Craft, J. Foster, A. Gadian and L. Galbraith, Philosophical Transactions of the Royal Society A: Mathematical, Physical and Engineering Sciences **370** (1974), 4217-4262 (2012).

[130] J.-Y. Lee, J. Marotzke, G. Bala, L. Cao, S. Corti, J.P. Dunne, F. Engelbrecht, E. Fischer, J.C. Fyfe, C. Jones, A. Maycock, J. Mutemi, O. Ndiaye, S. Panickal, and T. Zhou, Future Global Climate: Scenario-Based Projections and NearTerm Information. In *Climate Change 2021: The Physical Science Basis. Contribution of Working Group I to the Sixth Assessment Report of the Intergovernmental Panel on Climate Change* [Masson-Delmotte, V., P. Zhai, A. Pirani, S.L. Connors, C. Péan, S. Berger, N. Caud, Y. Chen, L. Goldfarb, M.I. Gomis, M. Huang, K. Leitzell, E. Lonnoy, J.B.R. Matthews, T.K. Maycock, T. Waterfield, O. Yelekçi, R. Yu, and B. Zhou (eds.)]. Cambridge University Press, Cambridge, United Kingdom and New York, NY, USA, 553–672 (2021)

[131] P. F. Levelt, J. Joiner, J. Tamminen, J. P. Veefkind, P. K. Bhartia, D. C. Stein Zweers, B. N. Duncan, D. G. Streets, H. Eskes and R. van der A, Atmospheric Chemistry and Physics **18** (8), 5699-5745 (2018).

[132] A. Levis, Y. Y. Schechner and A. B. Davis, *Multiple-scattering microphysics tomography*. (IEEE,2017).

[133] R. C. Levy, L. A. Remer, D. Tanré, Y. J. Kaufman, C. Ichoku, B. N. Holben, J. M. Livingston, P. B. Russell and H. Maring, Journal of Geophysical Research: Atmospheres **108** (2003).

[134] Z. Li, W. Hou, J. Hong, F. Zheng, D. Luo, J. Wang, X. Gu and Y. Qiao, Journal of Quantitative Spectroscopy and Radiative Transfer **218**, 21-37 (2018).

[135] Z. Li, K. Li, L. Li, H. Xu, Y. Xie, Y. Ma, D. Li, P. Goloub, Y. Yuan and X. Zheng, Applied Optics **57** (5), 1011-1018 (2018).

[136] J. A. Limbacher and R. A. Kahn, Atmospheric Measurement Techniques **10** (4), 1539-1555 (2017).

[137] Y. Liu, D. Chen, R. A. Kahn and K. He, Science in China Series D: Earth Sciences **52** (1), 132-144 (2009).

[138] Z. Liu, A. Omar, M. Vaughan, J. Hair, C. Kittaka, Y. Hu, K. Powell, C. Trepte, D. Winker and C. Hostetler, Journal of Geophysical Research: Atmospheres **113** (2008).

[139] B. Lockwood and M. Lockwood, Global Environmental Politics, 1-26 (2022).

[140] U. Lohmann, J. Feichter, J. Penner and R. Leaitch, Journal of Geophysical Research: Atmospheres **105** (D10), 12193-12206 (2000).

[141] M. L. Lu and J. H. Seinfeld, Journal of Geophysical Research: Atmospheres **111** (2006).

[142] A. Lyapustin, Y. Wang, X. Xiong, G. Meister, S. Platnick, R. Levy, B. Franz, S. Korkin, T. Hilker and J. Tucker, Atmospheric Measurement Techniques **7** (12), 4353-4365 (2014).

[143] G. G. Mace, D. O. C. Starr, R. Marchand, S. A. Ackerman, S. E. Platnick, A. Fridlind, S. Cooper, D. G. Vane and G. L. Stephens, *Contemplating synergistic algorithms for the NASA ACE mission*. (SPIE, 2013).

[144] R. T. Marchand, T. P. Ackerman and C. Moroney, Journal of Geophysical Research: Atmospheres **112** (2007).

[145] A. Marshak, J. V. Martins, V. Zubko and Y. J. Kaufman, Atmospheric Chemistry and Physics **6** (12), 5295-5305 (2006).

[146] J. V. Martins, R. Fernandez-Borda, B. McBride, L. Remer and H. M. J. Barbosa, *The harp hyperangular imaging polarimeter and the need for small satellite payloads with high science payoff for earth science remote sensing*. (IEEE, 2018).

[147] B. A. McBride, J. V. Martins, H. M. J. Barbosa, W. Birmingham and L. A. Remer, Atmospheric Measurement Techniques **13** (4), 1777-1796 (2020).

[148] B. A. McBride, J.V. Martins, J. D. Cieslak, R. Fernandez-Borda, A. Puthukkudy, X. Xu, N. Sienkiewicz, B. Cairns, and H. M. J. Barbosa, *Pre-launch calibration and validation of the Hyper-Angular Rainbow Polarimeter (HARP) instruments*, 2023 (in prep).

[149] B. A. McBride, J.V. Martins, A. Puthukkudy, X. Xu, R. Fernandez-Borda, H. M. J. Barbosa, O. Hasekamp, and L. A. Remer. *The Hyper-Angular Rainbow Polarimeter-2 (HARP2): a wide FOV polarimetric imager for high resolution spatial and angular characterization of aerosol and cloud microphysics.* (Proceedings of the 70th International Astronautical Congress 2019).

[150] B. A. McBride, X. Xiong, A. Wu. *Assessment of polarization sensitivity of Aqua-MODIS using co-located POLDER-3 polarized measurements over marine stratocumulus clouds.* (SPIE 2022).

[151] S. C. McClain, C. L. Bartlett, J. L. Pezzaniti and R. A. Chipman, *Depolarization measurements of an integrating sphere*. (SPIE, 1994).

[152] T. McCoy, I. Tan, D. L. Hartmann, M. D. Zelinka and T. Storelvmo, Journal of Advances in Modeling Earth Systems **8** (2), 650-668 (2016).

[153] W. P. Menzel, R. A. Frey and B. A. Baum, Cloud top properties and cloud phase algorithm theoretical basis document, (2015).

[154] N. L. Miles, J. Verlinde and E. E. Clothiaux, Journal of the atmospheric sciences **57** (2), 295-311 (2000).

[155] J. Miller, Z. Zhang, S. Platnick, A. S. Ackerman, F. Werner, C. Cornet and K. Knobelspiesse, Atmospheric Measurement Techniques **11** (6), 3689-3715 (2018).

[156] M. I. Mishchenko, B. Cairns, J. E. Hansen, L. D. Travis, R. Burg, Y. J. Kaufman, J. V. Martins and E. P. Shettle, Journal of Quantitative Spectroscopy and Radiative Transfer **88** (1-3), 149-161 (2004).

[157] M. I. Mishchenko and L. D. Travis, Journal of Geophysical Research: Atmospheres **102** (D14), 16989-17013 (1997).

[158] A. Mitra, L. Di Girolamo, Y. Hong, Y. Zhan and K. J. Mueller, Journal of Geophysical Research: Atmospheres **126** (9), (2021).

[159] J. Murray, K. S. Carslaw and P. R. Field, Atmospheric Chemistry and Physics **21** (2), 665-679 (2021).

[160] G. Myhre, B. H. Samset, M. Schulz, Y. Balkanski, S. Bauer, T. K. Berntsen, H. Bian, N. Bellouin, M. Chin and T. Diehl, Atmospheric Chemistry and Physics **13** (4), 1853-1877 (2013).

[161] T. Nakajima and M. D. King, Journal of Atmospheric Sciences **47** (15), 1878-1893 (1990).

[162] National Academies of Sciences, Engineering, and Medicine, *Thriving on Our Changing Planet: A Decadal Strategy for Earth Observation from Space*. Washington, DC: The National Academies Press, (2018).

[163] NASA, *Aerosols and Clouds-Convection-Precipitation Study, Science and Applications Traceability Matrix*, 2009. Last retrieved from https://science.nasa.gov/science-red/s3fs-public/atoms/files/ACCP_SATM_Rel_E_TAGGED.pdf on 28 September 2022.

[164] NASA, *AQUA Press Kit*, 2002. Last retrieved from https://aqua.nasa.gov/sites/default/files/references/Aqua_Press_Kit.pdf on 28 September 2022.

[165] NASA, *Chem Matters: Demystifying Everyday Chemistry, Special Edition*, 2005. Last retrieved from https://aura.gsfc.nasa.gov/images/outreach/cm_0905.pdf on 28 September 2022.

[166] NASA, AtmOS Polarimeter Instrumentation, 2021. Last retrieved from https://aos.gsfc.nasa.gov/docs/ATMOS_Polarimeter_210602_final_revised.pdf on 28 September 2022.

[167] NASA, FY 2021 Budget Estimates, 2021. Last retrieved from https://www.nasa.gov/sites/default/files/atoms/files/fy_2021_budget_book_508.pdf on 28 September 2022.

[168] NASA, Orbiting Carbon Observatory-2 Launch, Press Kit/July 2014,2014. Last retrieved from https://www.jpl.nasa.gov/news/press_kits/oco2-launch-press-kit.pdf on 28 September 2022.

[169] NASA, *Polarimetry in the PACE Mission Science Team Consensus Document*, 2015. Last retrieved at https://pace.oceansciences.org/docs/PACE_polarimetry_final.pdf on 28 September 2022.

[170] NASA LARC Data Archive, ACEPOL - Aerosol Characterization from Polarimeter and Lidar, 2018. Last retrieved from https://www-air.larc.nasa.gov/missions/acepol/index.html on 28 September 2022.

[171] C. M. Naud, B. A. Baum, M. Pavolonis, A. Heidinger, R. Frey and H. Zhang, Remote Sensing of Environment **107** (1-2), 200-210 (2007).

[172] NOAA National Centers for Environmental Information, State of the Climate: Global Climate Report for Annual 2020, 2021. Last retrieved from https://www.ncdc.noaa.gov/sotc/global/202013 on 28 September 2022.

[173] C. O'Neill, C. Tebaldi, D. P. Van Vuuren, V. Eyring, P. Friedlingstein, G. Hurtt, R. Knutti, E. Kriegler, J.-F. Lamarque and J. Lowe, Geoscientific Model Development **9** (9), 3461-3482 (2016).

[174] NREL, *2000 ASTM Standard Extraterrestrial Spectrum Reference E-490-00*, 2000. Last retrieved from https://www.nrel.gov/grid/solar-resource/spectra-astm-e490.html on 28 September 2022.

[175] Paris Agreement to the United Nations Framework Convention on Climate Change, Dec. 12, 2015, T.I.A.S. No. 16-1104

[176] F. Parol, J. Riedi, C. Vanbauce, C. Cornet, S. Zeng, F. Thieuleux and N. Henriot, *Climatology of POLDER/PARASOL cloud properties*. (American Institute of Physics, 2013).

[177] F. Parol, J.-C. Buriez, C. Vanbauce, J. Riédi, M. Doutriaux-Boucher, M. Vesperini, G. Sèze, P. Couvert, M. Viollier and F. M. Bréon, Advances in Space Research **33** (7), 1080-1088 (2004).

[178] M. J. Pavolonis, A. K. Heidinger and T. Uttal, Journal of Applied Meteorology **44** (6), 804-826 (2005).

[179] H. Pawlowska, W. W. Grabowski and J. L. Brenguier, Geophysical Research Letters **33** (2006).

[180] J. E. Penner, X. Dong and Y. Chen, Nature **427** (6971), 231-234 (2004).

[181] R. J. Peralta, C. Nardell, B. Cairns, E. E. Russell, L. D. Travis, M. I. Mishchenko, B. A. Fafaul and R. J. Hooker, *Aerosol polarimetry sensor for the Glory Mission*. (SPIE, 2007).

[182] M. D. Petters and S. M. Kreidenweis, Atmospheric Chemistry and Physics **7** (8), 1961-1971 (2007).

[183] B. Pierce, Aerosol Optical Depth Data Display Interface, LMOS Zion Site, 2017. Last retrieved from https://aeronet.gsfc.nasa.gov/cgi-bin/data_display_aod_v3 on 20 November 2022.

[184] M. B. Pinsky and A. P. Khain, Quarterly Journal of the Royal Meteorological Society **128** (580), 501-533 (2002).

[185] S. Platnick, Journal of Geophysical Research: Atmospheres **105** (D18), 22919-22935 (2000).

[186] S. Platnick, M. D. King, S. A. Ackerman, W. P. Menzel, B. A. Baum, J. C. Riédi and R. A. Frey, IEEE Transactions on Geoscience and Remote Sensing **41** (2), 459-473 (2003).

[187] S. Platnick, K. G. Meyer, M. D. King, G. Wind, N. Amarasinghe, B. Marchant, G. T. Arnold, Z. Zhang, P. A. Hubanks and R. E. Holz, IEEE Transactions on Geoscience and Remote Sensing **55** (1), 502-525 (2016).

[188] S. Platnick and L. Oreopoulos, Journal of Geophysical Research: Atmospheres **113** (2008).

[189] J. P. Putaud, R. Van Dingenen, A. Alastuey, H. Bauer, W. Birmili, J. Cyrys, H. Flentje, S. Fuzzi, R. Gehrig and H.-C. Hansson, Atmospheric Environment **44** (10), 1308-1320 (2010).

[190] A. Puthukuddy, J. V. Martins, B. A. McBride, X. Xu, N. Sienkiewicz, R. Fernandez-Borda, O. Dubovik, and L. A. Remer, *HARP: A 3U CubeSat for aerosol and cloud observations*, (Proceedings of the 72nd International Astronautical Congress, 2022)

[191] A. Puthukkudy, J. V. Martins, L. A. Remer, X. Xu, O. Dubovik, P. Litvinov, B. McBride, S. Burton and H. M. J. Barbosa, Atmospheric Measurement Techniques **13** (10), 5207-5236 (2020).

[192] X. Qu, A. Hall, S. A. Klein and A. M. DeAngelis, Geophysical Research Letters **42** (18), 7767-7775 (2015).

[193] C. Rajapakshe and Z. Zhang, UMBC Joint Center for Earth Systems Technology (JCET) (2020).

[194] C. R. Rao, (1987).

[195] L. A. Remer, Y. J. Kaufman, D. Tanré, S. Mattoo, D. A. Chu, J. V. Martins, R. R. Li, C. Ichoku, R. C. Levy and R. G. Kleidman, Journal of the Atmospheric Sciences **62** (4), 947-973 (2005).

[196] L. A. Remer, K. Knobelspiesse, P.-W. Zhai, F. Xu, O. V. Kalashnikova, J. Chowdhary, O. Hasekamp, O. Dubovik, L. Wu and Z. Ahmad, Frontiers in Environmental Science **7**, 94 (2019).

[197] M. S. Richardson, P. J. DeMott, S. M. Kreidenweis, D. J. Cziczo, E. J. Dunlea, J. L. Jimenez, D. S. Thomson, L. L. Ashbaugh, R. D. Borys and D. L. Westphal, Journal of Geophysical Research: Atmospheres **112** (2007).

[198] J. Riedi, B. Marchant, S. Platnick, B. A. Baum, F. Thieuleux, C. Oudard, F. Parol, J. M. Nicolas and P. Dubuisson, Atmospheric Chemistry and Physics **10** (23), 11851-11865 (2010).

[199] D. Rosenfeld, M. O. Andreae, A. Asmi, M. Chin, G. de Leeuw, D. P. Donovan, R. Kahn, S. Kinne, N. Kivekäs and M. Kulmala, Reviews of Geophysics **52** (4), (2014).

[200] D. Rosenfeld and I. M. Lensky, Bulletin of the American Meteorological Society **79** (11), 2457-2476 (1998).

[201] D. Rosenfeld, U. Lohmann, G. B. Raga, C. D. O'Dowd, M. Kulmala, S. Fuzzi, A. Reissell and M. O. Andreae, Science **321** (5894), 1309-1313 (2008).

[202] M. Saint-Lu, S. Bony and J. L. Dufresne, Geophysical Research Letters **47** (14), (2020).

[203] B. H. Samset, G. Myhre, M. Schulz, Y. Balkanski, S. Bauer, T. K. Berntsen, H. Bian, N. Bellouin, T. Diehl and R. C. Easter, Atmospheric Chemistry and Physics **13** (5), 2423-2434 2013).

[204] C. B. Schaaf, F. Gao, A. H. Strahler, W. Lucht, X. Li, T. Tsang, N. C. Strugnell, X. Zhang, Y. Jin and J.-P. Muller, Remote Sensing of Environment **83** (1-2), 135-148 (2002).

[205] C. Schär, O. Fuhrer, A. Arteaga, N. Ban, C. Charpilloz, S. Di Girolamo, L. Hentgen, T. Hoefler, X. Lapillonne and D. Leutwyler, Bulletin of the American Meteorological Society **101** (5), E567-E587 (2020).

[206] G. P. Schill, K. Genareau and M. A. Tolbert, Atmospheric Chemistry and Physics **15** (13), 7523-7536 (2015).

[207] J. S. Schlosser, S. Stamnes, S. P. Burton, B. Cairns, E. Crosbie, B. van Diedenhoven, G. Diskin, S. Dmitrovic, R. Ferrare, J. W. Hair, C. A. Hostetler, Y. Hu, X. Liu, R. H. Moore, T. Shingler, M. A. Shook, K. L. Thornhill, E. Winstead, L. Ziemba, and A. Sorooshian, Frontiers in Remote Sensing, **3** (2022).

[208] T. J. Schmit, M. M. Gunshor, W. P. Menzel, J. J. Gurka, J. Li and A. S. Bachmeier, Bulletin of the American Meteorological Society **86** (8), 1079-1096 (2005).

[209] J. R. Schott, *Fundamentals of polarimetric remote sensing*. (SPIE press, 2009).

[210] A. Schucknecht, S. Erasmi, I. Niemeyer and J. Matschullat, European Journal of Remote Sensing **46** (1), 40-59 (2013).

[211] S. Scollo, A. Folch, M. Coltelli and V. J. Realmuto, Journal of Geophysical Research: Atmospheres **115** (2010).

[212] Semiconductor Components Industries, LLC, *KAI-04070 2048 (H) x 2048 (V) Interline CCD Sensor*, 2015. Last retrieved from https://www.imperx.com/wp-content/uploads/2017/08/KAI-04070-D.pdf on 28 September 2022.

[213] H. Shang, L. Chen, F.-M. Breon, H. Letu, S. Li, Z. Wang and L. Su, Atmospheric Measurement Techniques **8** (11), 4931-4945 (2015).

[214] H. Shang, H. Letu, F.-M. Bréon, J. Riedi, R. Ma, Z. Wang, T. Y. Nakajima, Z. Wang and L. Chen, Remote Sensing of Environment **228**, 61-74 (2019).

[215] K. Sinclair, B. van Diedenhoven, B. Cairns, M. Alexandrov, A. M. Dzambo and T. L'Ecuyer, Geophysical Research Letters **48** (10), (2021).

[216] J. D. Small, P. Y. Chuang, G. Feingold and H. Jiang, Geophysical Research Letters **36** (2009).

[217] J. M. Smit, J. H. H. Rietjens, G. van Harten, A. Di Noia, W. Laauwen, B. E. Rheingans, D. J. Diner, B. Cairns, A. Wasilewski and K. D. Knobelspiesse, Applied Optics **58** (21), 5695-5719 (2019).

[218] T. M. Smith, V. Lakshmanan, G. J. Stumpf, K. L. Ortega, K. Hondl, K. Cooper, K. M. Calhoun, D. M. Kingfield, K. L. Manross and R. Toomey, Bulletin of the American Meteorological Society **97** (9), 1617-1630 (2016).

[219] S. Stamnes, C. Hostetler, R. Ferrare, S. Burton, X. Liu, J. Hair, Y. Hu, A. Wasilewski, W. Martin and B. Van Diedenhoven, Applied Optics **57** (10), 2394-2413 (2018).

[220] W. Steffen, P. J. Crutzen, J. R. McNeill, AMBIO: A Journal of the Human Environment, **36** (8), 614-621, (2007)

[221] G. L. Stephens and J. M. Haynes, Geophysical Research Letters **34** (20), (2007).

[222] G. L. Stephens, D. G. Vane, S. Tanelli, E. Im, S. Durden, M. Rokey, D. Reinke, P. Partain, G. G. Mace and R. Austin, Journal of Geophysical Research: Atmospheres **113** (2008).

[223] G. Stephens, D. Winker, J. Pelon, C. Trepte, D. Vane, C. Yuhas, T. L'Ecuyer and M. Lebsock, Bulletin of the American Meteorological Society **99** (3), 569-581 (2018).

[224] B. Stevens, D. H. Lenschow, G. Vali, H. Gerber, A. Bandy, B. Blomquist, J. L. Brenguier, C. S. Bretherton, F. Burnet and T. Campos, Bulletin of the American Meteorological Society **84** (5), 579-594 (2003).

[225] B. Stevens, C.-H. Moeng, A. S. Ackerman, C. S. Bretherton, A. Chlond, S. de Roode, J. Edwards, J.-C. Golaz, H. Jiang and M. Khairoutdinov, Monthly Weather Review **133** (6), 1443-1462 (2005).

[226] C. J. Stubenrauch, W. B. Rossow, S. Kinne, S. Ackerman, G. Cesana, H. Chepfer, L. Di Girolamo, B. Getzewich, A. Guignard and A. Heidinger, Bulletin of the American Meteorological Society **94** (7), 1031-1049 (2013).

[227] D. Sulla-Menashe and M. A. Friedl, USGS: Reston, VA, USA **1**, 18 (2018).

[228] S. C. Sullivan, D. Lee, L. Oreopoulos and A. Nenes, Proceedings of the National Academy of Sciences **113** (21), 5791-5796 (2016).

[229] S. Szopa, V. Naik, B. Adhikary, P. Artaxo, T. Berntsen, W.D. Collins, S. Fuzzi, L. Gallardo, A. Kiendler-Scharr, Z. Klimont, H. Liao, N. Unger, and P. Zanism, Short-Lived Climate Forcers. In *Climate Change 2021: The Physical Science Basis. Contribution of Working Group I to the Sixth Assessment Report of the Intergovernmental Panel on Climate Change* [Masson-Delmotte, V., P. Zhai, A. Pirani, S.L. Connors, C. Péan, S. Berger, N. Caud, Y. Chen, L. Goldfarb, M.I. Gomis, M. Huang, K. Leitzell, E. Lonnoy, J.B.R. Matthews, T.K. Maycock, T. Waterfield, O. Yelekçi, R. Yu, and B. Zhou (eds.)]. Cambridge University Press, Cambridge, United Kingdom and New York, NY, USA, 817–922, (2021).

[230] S. Tanelli, S. L. Durden, E. Im, K. S. Pak, D. G. Reinke, P. Partain, J. M. Haynes and R. T. Marchand, IEEE Transactions on Geoscience and Remote Sensing **46** (11), 3560-3573 (2008).

[231] W. K. Tao, S. Lang, J. Simpson, C. H. Sui, B. Ferrier and M. D. Chou, Journal of the atmospheric sciences **53** (18), 2624-2651 (1996).

[232] A. Thompson, Scientific American, (2017). Last retrieved from https://www.scientificamerican.com/article/trump-budget-cuts-ldquo-critical-rdquo-nasa-climate-missions/ on 28 September 2022.

[233] C. Tomasi, A. A. Kokhanovsky, A. Lupi, C. Ritter, A. Smirnov, N. T. O'Neill, R. S. Stone, B. N. Holben, S. Nyeki and C. Wehrli, Earth-Science Reviews **140**, 108-157 (2015).

[234] K. Twedt, E. Aldoretta, A. Angal, H. Chen, X. Geng, Y. Li, Q. Mu, K. Vermeesch and X. Xiong, *MODIS reflective solar bands calibration improvements for Collection 7*. (SPIE, 2021).

[235] S. Twomey, Atmospheric Environment (1967) **8** (12), 1251-1256 (1974).

[236] S. Tyo, D. L. Goldstein, D. B. Chenault and J. A. Shaw, Applied optics **45** (22), 5453-5469 (2006).

[237] USGCRP, 2017: Climate Science Special Report: Fourth National Climate Assessment, Volume I [Wuebbles, D.J., D.W. Fahey, K.A. Hibbard, D.J. Dokken, B.C. Stewart, and T.K. Maycock (eds.)]. U.S. Global Change Research Program, Washington, DC, USA, (2017).

[238] A. van Amerongen, J. Rietjens, J. Campo, E. Dogan, J. Dingjan, R. Nalla, J. Caron and O. Hasekamp, *SPEXone: a compact multi-angle polarimeter*. (SPIE, 2019).

[239] B. Van Diedenhoven, B. Cairns, A. M. Fridlind, A. S. Ackerman and T. J. Garrett, Atmospheric Chemistry and Physics **13** (6), 3185-3203 (2013).

[240] B. Van Diedenhoven, B. Cairns, I. V. Geogdzhayev, A. M. Fridlind, A. S. Ackerman, P. Yang and B. A. Baum, Atmospheric Measurement Techniques **5** (10), 2361-2374 (2012).

[241] G. van Harten and D. J. Diner, *AirMSPI radiometric/polarimetric uncertainties*, 2015. Last retrieved at https://airbornescience.nasa.gov/sites/default/files/documents/AirMSPI_uncertainty_model_15Aug2017.pdf on 28 September 2022.

[242] G. van Harten, D. J. Diner, B. J. S. Daugherty, B. E. Rheingans, M. A. Bull, F. C. Seidel, R. A. Chipman, B. Cairns, A. P. Wasilewski and K. D. Knobelspiesse, Applied optics **57** (16), 4499-4513 (2018).

[243] T. Várnai and A. Marshak, Journal of the Atmospheric Sciences **59** (9), 1607-1618 (2002).

[244] E. F. Vermote, N. Z. El Saleous and C. O. Justice, Remote Sensing of Environment **83** (1-2), 97-111 (2002).

[245] A. Walther and A. K. Heidinger, Journal of Applied Meteorology and Climatology **51** (7), 1371-1390 (2012).

[246] F. Waquet, C. Cornet, J. L. Deuzé, O. Dubovik, F. Ducos, P. Goloub, M. Herman, T. Lapyonok, L. C. Labonnote and J. Riedi, Atmospheric Measurement Techniques **6** (4), 991-1016 (2013).

[247] P. J. Werdell, M. J. Behrenfeld, P. S. Bontempi, E. Boss, B. Cairns, G. T. Davis, B. A. Franz, U. B. Gliese, E. T. Gorman and O. Hasekamp, Bulletin of the American Meteorological Society **100** (9), 1775-1794 (2019).

[248] M. Wiegner and J. Gasteiger, Atmospheric Measurement Techniques **8** (9), 3971-3984 (2015).

[249] D. M. Winker, M. A. Vaughan, A. Omar, Y. Hu, K. A. Powell, Z. Liu, W. H. Hunt and S. A. Young, Journal of Atmospheric and Oceanic Technology **26** (11), 2310-2323 (2009).

[250] T. P. Wright and M. D. Petters, Journal of Geophysical Research: Atmospheres **118** (9), 3731-3743 (2013).

[251] A. Wu, X. Geng, A. Wald, A. Angal and X. Xiong, IEEE Transactions on Geoscience and Remote Sensing **55** (7), 4168-4176 (2017).

[252] A. Wu, X. Xiong, C. Cao and A. Angal, *Monitoring MODIS calibration stability of visible and near-IR bands from observed top-of-atmosphere BRDF-normalized reflectances over Libyan Desert and Antarctic surfaces*. (SPIE, 2008).

[253] A. Wu, O. Hasekamp, B. Van Diedenhoven and B. Cairns, Atmospheric Measurement Techniques **8** (6), 2625-2638 (2015).

[254] L. Wu, O. Hasekamp, B. van Diedenhoven, B. Cairns, J. E. Yorks and J. Chowdhary, Geophysical Research Letters **43** (16), 8783-8790 (2016).

[255] X. Xiong and J. J. Butler, Remote Sensing **12** (16), 2523 (2020).

[256] X. Xiong, A. Wu and B. N. Wenny, Journal of Applied Remote Sensing **3** (1), 033520 (2009).

[257] F. Xu, G. van Harten, D. J. Diner, A. B. Davis, F. C. Seidel, B. Rheingans, M. Tosca, M. D. Alexandrov, B. Cairns and R. A. Ferrare, Journal of Geophysical Research: Atmospheres **123** (6), 3175-3204 (2018).

[258] F. Xu, G. van Harten, D. J. Diner, O. V. Kalashnikova, F. C. Seidel, C. J. Bruegge and O. Dubovik, Journal of Geophysical Research: Atmospheres **122** (13), 7004-7026 (2017).

[259] P. Yan, R. Schroeder, and S. Stier, Information, Communication & Society **25** (10), 1400-1439 (2021).

[260] P. Yang, L. Bi, B. A. Baum, K.-N. Liou, G. W. Kattawar, M. I. Mishchenko and B. Cole, Journal of the Atmospheric Sciences **70** (1), 330-347 (2013).

[261] P. Yang, S. Hioki, M. Saito, C.-P. Kuo, B. Baum, and K.-N. Liou, Atmosphere, **9** (12), 499, (2018).

[262] Y. Yin, Z. Levin, T. G. Reisin and S. Tzivion, Atmospheric research **53** (1-3), 91-116 2000).

[263] J. E. Yorks, M. J. McGill, S. P. Palm, D. L. Hlavka, P. A. Selmer, E. P. Nowottnick, M. A. Vaughan, S. D. Rodier and W. D. Hart, Geophysical Research Letters **43** (9), 4632-4639 (2016).

[264] A. T. Young, Applied Optics **20** (4), 533-535 (1981).

[265] M. D. Zelinka, S. A. Klein and D. L. Hartmann, Journal of Climate **25** (11), 3736-3754 (2012).

[266] M. D. Zelinka, C. Zhou and S. A. Klein, Geophysical Research Letters **43** (17), 9259-9269 (2016).

[267] Z. Zhang and S. Platnick, Journal of Geophysical Research: Atmospheres **116** (2011).

Section 2: Figure Licensing Statements and Notices

Several figures in this dissertation are reprinted or reasonably adapted under the CC-BY-4.0 license at https://creativecommons.org/licenses/by/4.0/, as noted. The reader may find all original figures in the papers that are sourced in the text caption, with a full reference in the Bibliography.

I acknowledge the use of imagery from the NASA Worldview application (https://worldview.earthdata.nasa.gov), part of the NASA Earth Observing System Data and Information System (EOSDIS).

This Bibliography uses the American Institute of Physics style, in its relevant formats. If the AIP does not provide a format for a certain product or work, a consistent one is used across the Bibliography.